

MÖSSBAUER SPECTROSCOPIC STUDIES OF SOME GLASS-CERAMICS, METALLIC GLASSES AND PYRITE MINERALS

A Thesis Submitted
in Partial Fulfilment of the Requirements
for the Degree of

DOCTOR OF PHILOSOPHY

By

AKHILESH PRASAD

to the

DEPARTMENT OF PHYSICS

INDIAN INSTITUTE OF TECHNOLOGY KANPUR

DECEMBER, 1983

24 JUN 1983

12 11 1983

CENTRAL LIBRARY

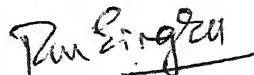
87522

600 Pa. Ave. N.W.

PMY-1983-D-PRA-MOS

CERTIFICATE

This is to certify that the work presented in this thesis entitled "'Mössbauer Spectroscopic Studies of Some Glass-Ceramics, Metallic Glasses and Pyrite Minerals'" by Akhilesh Prasad has been done under my supervision and it has not been submitted elsewhere for a degree or diploma.



R. M. Singru
Professor of Physics
Indian Institute of Technology
KANPUR - 208016, INDIA

December 1983.

ACKNOWLEDGEMENTS

I am highly grateful to Professor R.M. Singru for his most inspiring and valuable guidance, encouragement and help throughout the course of this research work. I am equally grateful to him for his constant help and useful advice in my personal problems.

I wish to express my sincere thanks to Professor T.R. Ramachandran for providing the samples of metallic glass and for communicating the results of transmission electron microscopy and differential thermal analysis measurements. I am grateful to him for valuable discussions regarding the planning and interpretation of the present studies on metallic glasses.

I am equally grateful to Dr. D. Bahadur for helping me at all stages of my research work and particularly for the useful discussions about the study of glass-ceramic samples. I am thankful to Professor D. Chakravorty and Dr. D. Bahadur for providing me with the glass-ceramic samples and for other research facilities offered in their laboratory.

I am grateful to Dr. A.K. Biswas for providing me with the pyrite mineral samples and for his valuable suggestions during the course of this work.

I am thankful to Professor G.K. Mehta for his kind cooperation throughout my stay here. My thanks are also

due to Professor D.C. Khan for providing me the facility of using his furnace for heat-treatment of our samples. I am also thankful to Dr. E.C. Subbarao and Dr. R. Hasegawa for supplying the metallic glass samples.

I am particularly thankful to the staff of the Central Nuclear Laboratory, Mr. K.M.L. Jha, Mr. A.R. Korde, Mr. R.S. Rajput, Mr. K. Masood, Mr. M.M. Gupta and Mr. V.K. Sharma, who have provided able technical help, without which it would have been impossible for me to complete my experimental work. I should also thank Mr. Shiv Prakash and Mr. Ram Nath for their willing help.

I express my sincere thanks to the staff of the Physics Workshop, X-Ray Laboratory and Glass Blowing Section for their willing help.

I am thankful to Mrs. Vijayalaxmi for helping in the leaching of pyrite samples and for useful discussions and Mr. S.C.D. Arora for help in roasting of pyrite samples.

I sincerely thank Dr. A.K. Singh, Dr. K.R.K. Gandhi, Dr. N.V. Nair, Dr. H.C. Verma, Dr.(Mrs.) V.R. Joshi, Mr. Virendra Kumar, Mr. J.P. Singh, Mr. M.M. Sharma, Mr. G.S. Raghuvanshi, Mr. S.C. Prasad, Dr. Premchand, Mr. Atul Sen, Mr. O.P. Rama and all other friends who kept good company with me and helped me in one way or another.

I am sincerely thankful to the families of Dr. A.K. Singh, Mr. J.P. Singh, Mr. G.S. Raghuvanshi and Mr. S.C. Prasad.

I am thankful to Mr. D.S. Panesar for the neat tracings prepared by him for this thesis and Mr. Dilip Kumar

for making the photocopies of the figures.

I express my thanks to Mr. L.S. Bajpai for neat typing and Mr. Lallu Singh Rathor and Mr. H.K. Panda for cyclostyling this thesis.

The partial financial support provided by the Department of Science and Technology, Government of India is gratefully acknowledged.

This work would not have been possible without emotional support from my parents and I wish to express my profound regards to them.

Finally I would like to express my deepest appreciation to my wife, Asha, and my sons, Umesh and Rakesh who provided inspiration during this work.

I might have missed some names but I remain thankful to all those who have helped me in one way or another during this work.

Akhilesh Prasad

LIST OF CONTENTS

	<u>Page</u>
LIST OF TABLES	x
LIST OF FIGURES	xii
SYNOPSIS	xxiii
CHAPTER 1 : INTRODUCTION	1
1.1 Mössbauer Effect	1
1.2 Hyperfine Interaction	9
1.3 Isomer Shift	10
1.4 Quadrupole Splitting	20
1.5 Magnetic Hyperfine Splitting	23
1.6 Motivation Behind the Present Work	27
REFERENCES	32
CHAPTER 2 : EXPERIMENTAL METHODS	34
2.1 Introduction	34
2.2 Radioactive Source	37
2.3 Mössbauer Spectrometer	38
2.4 Absorber	41
2.4.1 Standard absorber for calibration	41
2.4.2 Sample preparation	43
2.4.3 Optimization of the absorber thickness	43
2.4.4 Effect of geometry	47
2.5 Cryostat and Furnace	50
2.5.1 Introduction	50
2.5.2 Cryostat	50

	<u>Page</u>
2.5.3 Furnace	53
2.6 Detector and Storage System	55
2.7 Analysis of Data	56
2.8 Hyperfine Field Distribution	58
2.8.1 Introduction	58
2.8.2 Computational method	59
2.9 Other Measurements	60
REFERENCES	64
CHAPTER 3 : MÖSSBAUER AND OTHER STUDIES OF SOME GLASS-CERAMIC SYSTEM CONTAINING YIG	66
3.1 Introduction	66
3.2 Study of $\text{Na}_2\text{O}-\text{SiO}_2-\text{Fe}_2\text{O}_3-\text{Y}_2\text{O}_3$ Glass System	71
3.2.1 Introduction	71
3.2.2 Experimental method	72
(a) Sample preparation	72
(b) Mössbauer measurements	72
(c) Other measurements	73
3.2.3 Results and discussion	76
3.2.4 Summary	99
3.3 Study of the Effect of Nucleating Agents on the YIG Crystallization in $\text{Na}_2\text{O}-\text{SiO}_2-\text{Fe}_2\text{O}_3-\text{Y}_2\text{O}_3$ Glass System	100
3.3.1 Introduction	100

	<u>Page</u>
3.3.2 Experimental method	101
(a) Sample Preparation	101
(b) Measurements	103
3.3.3 Results and discussions	103
3.3.4 Summary	125
3.4 Study of $\text{PbO-B}_2\text{O}_3\text{-Al}_2\text{O}_3\text{-Fe}_2\text{O}_3\text{-Y}_2\text{O}_3$ Glass System	126
3.4.1 Introduction	126
3.4.2 Experimental method	127
(a) Sample preparation	127
(b) Measurements	127
3.4.3 Results and discussion	127
REFERENCES	143
CHAPTER 4 : MÖSSBAUER SPECTROSCOPIC STUDIES OF THE METALLIC GLASS SYSTEM	
$\text{Fe}_{100-x}\text{B}_x$	145
4.1 Introduction	145
4.2 Review of Mössbauer Studies of $\text{Fe}_{100-x}\text{B}_x$ ($13 \leq x \leq 26$)	150
4.3 Experimental	154
4.3.1 Introduction	154
4.3.2 Sample preparation	154
4.3.3 Measurement technique	155
(a) Transmission electron microscopy	155
(b) Differential thermal analysis	156

	<u>Page</u>
(c) Mössbauer spectroscopic measurements	156
4.4 Results and discussion	156
4.4.1 Results of transmission electron microscopy	156
4.4.2 Differential thermal analysis	160
4.4.3 Dynamical temperature X-ray diffraction	161
4.4.4 Mössbauer studies	162
REFERENCES	190
 CHAPTER 5 : STUDY OF THE ROASTING AND LEACHING PROCESS OF PYRITE MINERALS BY MÖSSBAUER SPECTROSCOPY	 193
5.1 Study of the Roasting Process of Pyrite Mineral	193
5.1.1 Introduction	193
5.1.2 Experiment	195
(a) Sample preparation	195
(b) Mössbauer measurements	196
(c) Other measurements	196
5.1.3 Results and discussion	200
5.2 Study of the Leaching Process of the Pyrite minerals	208
5.2.1 Introduction	208

	<u>Page</u>
5.2.2 Experimental	211
(a) Micro-organism	211
(b) Substrate	211
(c) Estimation of iron	212
(d) Experimental procedure	212
(e) Mössbauer measurements	212
5.2.3 Results and discussion	213
REFERENCES	219

LIST OF TABLES

Table No.	Caption	Page
1.1	Parameters for the 14.4 keV Mössbauer transition in ^{57}Fe .	.. 8
1.2	Isomer shift and quadrupole splitting for iron in various electron configuration d^n .	.. 16
1.3	Relationship between variables measured using Mössbauer spectroscopy and various research fields.	.. 28
3.1	X-ray diffraction data for heat-treated samples.	.. 74
3.2	Mössbauer parameters for sample Y6 showing quadrupole splitting only.	.. 80
3.3	Mössbauer parameters for the samples showing magnetic hyperfine splitting as well as quadrupole splitting.	.. 82
3.4	EPR results for the Y6 sample.	.. 96
3.5	Composition of the glasses studied. Molecular percentage values are given.	.. 102
3.6	X-ray diffraction data for heat-treated sample Y9P.	.. 106
3.7	Mössbauer parameters of as-prepared sample.	.. 1112

Table No.	Caption	Page
3.8	Mössbauer parameters for the sample with two-stage heat-treatment at temperature $720^{\circ}\text{C} + 820^{\circ}\text{C}$ for 2 h each.	115
3.9	Sample Y9P : heat-treatment at different temperatures. Percentage of the intensities of the A site and B site.	123
3.10	X-ray diffraction data of the samples with different heat-treatment. T denotes the heat-treatment temperature.	129
3.11	Mössbauer parameters of as-prepared sample as well as samples heat-treated at different temperatures.	135
4.1	Classification of glass-forming alloy systems.	149
4.2	Summary of the results obtained by the TEM, DTA, DTXD and Mössbauer studies of the $\text{Fe}_{100-x}\text{B}_x$ samples.	158
4.3	Behaviour of internal magnetic field, H_{int} , in the $\text{Fe}_{100-x}\text{B}_x$ alloys as a function of x at different heat-treatment temperatures.	174
5.1	X-ray data for pyrite roasted for different time intervals.	197
5.2	Mössbauer parameters of pyrite sample roasted for different time intervals at temperature $610 \pm 5^{\circ}\text{C}$.	204
5.3	Mössbauer parameters of pyrite samples leached for different days by using two different source of bacteria.	214

LIST OF FIGURES

Figure No.	Caption	Page
1.1	Overlap of the emission and absorption lines showing the relation between E_o , E_γ^s , E_γ^a and for two cases : (a) optical case, $R \ll \Gamma$ and (b) nuclear case, $R \gg \Gamma$.	.. 4
1.2	Radioactive decay scheme of ^{57}Co .	.. 7
1.3	(a) Effect of monopole interaction on the energy levels of source and absorber. (b) Mössbauer spectrum showing monopole interaction.	.. 12
1.4	Review of ^{57}Fe isomer shift data of iron in various ionization states [10].	.. 17
1.5	Review of ^{57}Fe Mössbauer parameters (a) IS (isomer shift) and (b) ΔE (quadrupole splitting) for iron plotted against the coordination number for 'ionic' high spin and low spin compounds and minerals. Arrows indicate that the values outside the range of boxes have been observed [11].	.. 18

Figure No.	Caption	Page
1.6	Data for the ^{57}Fe isomer shift with respect to natural iron ($\alpha\text{-Fe}$) at room temperature. Units of the IS values are mm sec^{-1} and the signs of the velocity for the source are to be read from the top row while the signs of the velocity for the absorber are to be read from the bottom row. To take an example, for a source in Rh host matrix, the IS of $\alpha\text{-Fe}$ absorber will be $-0.0888 \text{ mm sec}^{-1}$ (with respect to metallic $\alpha\text{-Fe}$). The IS values are taken from Stevens and Gettys [12].	.. 19
1.7	Isomer shifts (relative of $\alpha\text{-Fe}$) for some crystals and glasses [13].	.. 21
1.8	Effect of the quadrupole interaction on the nuclear energy levels of source/absorber and the resulting Mössbauer spectrum showing the quadrupole splitting and isomer shift.	.. 22
1.9	Effect of the magnetic hyperfine interaction on the nuclear energy levels of the source/absorber.	.. 25
2.1	Schematic block diagram of various instruments involved in a Mössbauer effect experiment.	.. 36

Figure No.	Caption	Page
2.2	Schematic block diagram of the Mössbauer spectrometer used by us.	.. 39
2.3	Schematic block diagram of the electro-mechanical transducer used in the Mössbauer spectrometer.	.. 42
2.4	Design of the cryostat used in the Mössbauer experiments carried out in the temperature range 80-300 K.	.. 51
2.5	Design of the furnace with resistance heating assembly.	.. 54
2.6	Hyperfine field distribution for α -Fe (absorber) at room temperature. The top figure shows the $p(H)$ distribution while the bottom figure shows the corresponding Mössbauer spectrum of α -Fe.	.. 61
2.7	EFG distribution in sodium nitroprusside (absorber) at room temperature. The top figure shows the $(p V)$ distribution while the bottom figure shows the fitted Mössbauer spectrum.	.. 62
3.1	DTA plot of the as-prepared $\text{Na}_2\text{O-SiO}_2\text{-Fe}_2\text{O}_3\text{-Y}_2\text{O}_3$ glass sample (hereinafter called as the Y6 sample).	.. 77

Figure No.	Caption	Page
3.2	Room-temperature Mössbauer spectra of glass sample Y6 heat-treated at different temperatures. The zero of the velocity scale refers to the centroid of the double spectrum from sodium nitroprusside absorber.	.. 78
3.3	Room-temperature Mössbauer spectra of Y6 samples heat-treated at (a) 700 °C for 40 h, (b) 810 °C for 4 h, (c) 850 °C for 4 h and (d) 600 and 750 °C for 4 h each. The zero of the velocity scale refers to the centroid of the doublet spectrum from sodium nitroprusside absorber.	.. 79
3.4	Plot of the isomer shift (IS) determined for the spectra showing quadrupole splitting against heat-treatment temperature. The IS values are given with respect to sodium nitroprusside absorbers. Point marked as Δ refers to the as-prepared sample.	.. 83
3.5	The Mössbauer spectra measured at liquid nitrogen temperature (LNT) 80 K, for samples described in Fig. 3.2. The labels a,b,c..... etc. of the samples correspond to those shown in Fig. 3.2.	.. 86

Figure No.	Caption	Page
3.6	Plot of the quadrupole splitting (ΔE) against the heat-treatment temperatures. Point marked as Δ refers to the as-prepared sample.	.. 89
3.7	EFG distribution of the as-prepared (Y6) at room temperature. The top figure shows the results for the ($p V $) distribution while the bottom figure shows the resulting fitted Mössbauer spectrum.	.. 90
3.8	Same as Fig. 3.7 but for the sample heat-treated at 750 °C for 4 h.	.. 92
3.9	Plot of the magnetic susceptibility against the heat-treatment temperature, treatment time being 4 h for each.	.. 93
3.10	Typical EPR spectra measured at room temperature for the as-prepared (Y6) sample and the sample heat-treated at 650 °C.	.. 95
3.11	Typical electron micrograph of the as-prepared sample.	.. 97
3.12	Typical (a) electron and (b) optical micrograph of the sample heat-treated at 650 °C.	.. 98
3.13	DTA plot of the as-prepared Y9P sample. Scan rate is 10 °C per minute.	.. 104

Figure No.	Caption	Page
3.14	Plot of magnetization <u>versus</u> temperature for the two-stage heat-treated samples (a) Y9, (b) Y9T and (c) Y9P.	.. 108
3.15	Plot of magnetization <u>versus</u> field for the two-stage heat-treated samples (a) Y9, (b) Y9P, (c) Y9T and (d) Y6P at room temperature.	.. 109
3.16	Room temperature Mössbauer spectra of the as-prepared samples Y9, Y6P, Y9T and Y9P. The zero of the velocity scale refers to the centroid of the α -Fe (absorber) Mössbauer spectrum.	.. 111
3.17	Room temperature Mössbauer spectra of the samples Y9, Y6P, Y9T heat-treated at 720° and 820°C for 2 h each and sample Y9P heat-treated at 800°C for 40 h.	.. 113
3.18	Room temperature Mössbauer spectra of the samples Y9P heat-treated at different growing temperature (a) $720^{\circ} + 750^{\circ}\text{C}$, (b) $720^{\circ} + 775^{\circ}\text{C}$, (c) $720^{\circ} + 800^{\circ}\text{C}$ and (d) $720^{\circ} + 820^{\circ}\text{C}$ for 2 h each.	.. 114
3.19	EFG distribution for the as-prepared samples Y9, Y6P, Y9T and Y9P.	.. 117

Figure No.	Caption	Page
3.20	Behaviour of the Mössbauer parameters, isomer shift (IS) and quadrupole splitting (ΔE), for the sample Y6, Y9, Y6P, Y9T and Y9P. The results for the sample Y6 have been taken from the previous section.	.. 119
3.21	DTA plot of the as-prepared sample $\text{PbO-B}_2\text{O}_3\text{-Al}_2\text{O}_3\text{-Fe}_2\text{O}_3\text{-Y}_2\text{O}_3$.	.. 128
3.22	Plot of magnetization versus magnetic field for the (a) as-prepared sample (b) sample heat-treated at 300 °C for 4 h and (c) sample heat-treated at 660 °C for 4 h.	.. 131
3.23	Plot of magnetization versus temperature for the sample heat-treated at 660 °C for 4 h.	.. 132
3.24	Room temperature Mössbauer spectra of the sample $\text{PbO-B}_2\text{O}_3\text{-Al}_2\text{O}_3\text{-Fe}_2\text{O}_3\text{-Y}_2\text{O}_3$ heat-treated at different temperatures.	.. 133
3.25	Plot of the isomer shift (IS) against heat-treatment temperature. The isomer shift values are given relative to the sodium nitroprusside absorber. Point marked as Δ refers to the as-prepared sample.	.. 136
3.26	EFG distribution for the as-prepared samples $\text{PbO-B}_2\text{O}_3\text{-Al}_2\text{O}_3\text{-Fe}_2\text{O}_3\text{-Y}_2\text{O}_3$.	.. 138

Figure No.	Caption	Page
3.27	Plot of the quadrupole splitting (ΔE) against the heat-treatment temperatures. Point marked as Δ refers to the as-prepared sample. 139
3.28	Electron micrograph of the heat-treated sample at 660 °C. 141
4.1	Mössbauer spectra of $\text{Fe}_{87}\text{B}_{13}$ at room temperature. Spectrum a represents the results for the as-prepared sample while spectra b,c,d,e and f refer to samples heat-treated at $T = 100, 200, 300, 350$ and 400 °C for 1 h each. The zero of the velocity scale refers to the centroid of the inner peaks of the α -Fe Mössbauer spectrum. The lines at the top indicate the characteristic peak positions in the Mössbauer spectra of α -Fe, Fe_2B and Fe_3B (three sextets for Fe_3B). 163
4.2	Same as Fig. 4.1 but for $\text{Fe}_{84}\text{B}_{16}$ 164
4.3	Same as Fig. 4.1 but for $\text{Fe}_{82}\text{B}_{18}$ 165
4.4	Same as Fig. 4.1 but for $\text{Fe}_{80}\text{B}_{20}$ 166
4.5	Same as Fig. 4.1 but for $\text{Fe}_{78}\text{B}_{22}$ 167
4.6	Same as Fig. 4.1 but for $\text{Fe}_{74}\text{B}_{26}$ 168

Figure No.	Caption	Page
4.7	Mössbauer spectra of $\text{Fe}_{100-x}\text{B}_x$ samples heat-treated for 4 h at different temperatures, T. $\text{Fe}_{87}\text{B}_{13}$: (a) 400 °C, (b) 350 °C; $\text{Fe}_{84}\text{B}_{16}$: (c) 400 °C, (d) 350 °C and $\text{Fe}_{82}\text{B}_{18}$: (e) 400 °C, (f) 350 °C. 169
4.8	Same as Fig. 4.7 but for $\text{Fe}_{80}\text{B}_{20}$: (a) 400 °C, (b) 350 °C; $\text{Fe}_{78}\text{B}_{22}$: (c) 400 °C, (d) 350 °C and $\text{Fe}_{74}\text{B}_{26}$: (e) 400 °C, (f) 350 °C. 170
4.9	Plots of the p(H) distributions determined from the Mössbauer spectra of the as-prepared samples of $\text{Fe}_{100-x}\text{B}_x$ (taken at room temperature) for different x. 172
4.10	Plots of the p(H) distribution determined from the Mössbauer spectra of the $\text{Fe}_{74}\text{B}_{26}$ sample (taken at room temperature) heat-treated at 100, 200, 300 and 400 °C for 1 h. 173
4.11	Plot of the isomer shift data for $\text{Fe}_{100-x}\text{B}_x$ samples against the heat-treatment temperature, T. a : x = 26, b : x = 22, c : x = 20, d : x = 18, e : x = 16 and f : x = 13. 177

Figure No.	Caption	Page
4.12	Plot of the H_{int} data for $\text{Fe}_{100-x}\text{B}_x$ samples against the heat-treatment temperature, T. a : $x = 26$, b : $x = 22$, c : $x = 20$, d : $x = 18$, e : $x = 16$, f : $x = 13$ 178
4.13	Plot of the IS data for $\text{Fe}_{100-x}\text{B}_x$ samples against the boron concentration x. a : as-prepared, b : $T = 100^\circ\text{C}$, c : $T = 200^\circ\text{C}$, d : $T = 300^\circ\text{C}$ and e : $T = 350^\circ\text{C}$. (In each case $t = 1$ h). 179
4.14	Same as Fig. 4.13 but for the H_{int} data. 180
5.1	Room temperature Mössbauer spectrum of pyrite roasted at $610 \pm 5^\circ\text{C}$ for different time intervals. a) 0.0 min, b) 0.5 min, c) 1.0 min, d) 2.0 min, e) 5.0 min, f) 15.0 min, g) 30.0 min and h) 60.0 min. The zero of the velocity of the inner peaks of α -Fe Mössbauer spectrum. The lines at the top indicate the characteristic peak positions in the Mössbauer spectra γ - Fe_2O_3 , α - Fe_2O_3 , Fe_3O_4 , α -Fe, FeS and pyrrhotite. 201

Figure No.	Caption	Page
5.2	Room temperature Mössbauer spectrum of a) pyrrhotite. Spectrum b shows the expansion of the inner peaks of the spectrum (a). The zero of the velocity scale refers to the centroid of the sodium nitroprusside Mössbauer spectrum. In (b) 1 and 2 denote unidentified peaks [2]. 206
5.3	Room temperature Mössbauer spectrum of $\gamma\text{-Fe}_2\text{O}_3$, Fe_3O_4 , FeS and $\text{FeSO}_4 \cdot 2\text{H}_2\text{O}$ 207
5.4	Room temperature Mössbauer spectrum of (a) pyrite and (b) pyrite sample leached for 15 days. 215

SYNOPSIS

MÖSSBAUER SPECTROSCOPIC STUDIES OF SOME GLASS-CERAMICS, METALLIC GLASSES AND PYRITE MINERALS

AKHILESH PRASAD

Department of Physics
Indian Institute of Technology, Kanpur

November 1983

Mössbauer effect or recoil-free nuclear resonance absorption was discovered in 1957 and its early applications were in the studies of fundamental problems. During the last 25 years, however, the experimental technique of Mössbauer spectroscopy has been applied to a variety of problems, in the field of solid state physics and chemistry, biochemistry, metallurgy and geological sciences. Of special interest are the studies of different glass systems using Mössbauer effect. As a result of the hyperfine interaction, the parameters like isomer shift, quadrupole splitting and magnetic hyperfine splitting determined from the observed Mössbauer spectra provide valuable information about electronic structure in the sample being studied and these data can be corroborated by using other experimental techniques. Recently, glass-ceramics and metallic glasses (or amorphous metallic alloys) form two classes of materials which have invoked tremendous research interest. The present thesis describes the study of the glass ceramic systems $\text{Na}_2\text{O-SiO}_2\text{-Fe}_2\text{O}_3\text{-Y}_2\text{O}_3$ and $\text{PbO-B}_2\text{O}_3\text{-Al}_2\text{O}_3\text{-Fe}_2\text{O}_3\text{-Y}_2\text{O}_3$ and the amorphous metallic alloy (metal glass) $\text{Fe}_{100-x}\text{B}_x$ using Mössbauer

spectroscopic and other techniques. The thesis also reports study of the roasting and leaching processes of pyrite minerals by Mössbauer spectroscopy.

The thesis is divided into five Chapters. In Chapter 1 a brief introduction to the subject of Mössbauer effect and hyperfine interactions is given. The three parameters, isomer shift, electric quadrupole splitting and magnetic hyperfine splitting are discussed and this is followed by a brief description of the motivation behind the present work.

Chapter 2 describes the experimental details. Different aspects of the Mössbauer effect methodology like the radioactive source, Mössbauer spectrometer, absorber, cryostat and furnace, detector and storage system are discussed in some detail. Methods used for the analysis of data and for the determination of hyperfine field distribution are discussed. In the present work, data obtained from Mössbauer spectroscopy were corroborated by using data obtained by other experimental techniques such as X-ray powder diffraction, optical and electron microscopy, differential thermal analysis (DTA), electron paramagnetic resonance (EPR) and magnetization measurements. Brief working details of these techniques are given.

The experimental results of our studies of the glass-ceramic systems are presented and discussed in Chapter 3. Today glass-ceramics form an important class of materials because of their interesting mechanical, thermal and

abrasion-resistant properties. In particular the glass-ceramics containing magnetic phases can be studied usefully with Mössbauer spectroscopy. In the glass-ceramic $\text{Na}_2\text{O-SiO}_2\text{-Fe}_2\text{O}_3\text{-Y}_2\text{O}_3$, yttrium iron garnet (YIG) can be precipitated by suitable heat-treatment. The results of the Mössbauer, EPR and magnetization measurements of this glass composition (labelled Y6) are presented first. Measurements were carried out on the as-quenched Y6 sample as well as the Y6 samples heat-treated for 4 h at 400, 500, 600, 650, 700, 750, 810 and 850 °C. The Mössbauer spectra from the as-quenched sample as well as the first six samples showed a quadrupole splitting while the last two samples as well as the sample heat-treated first (i) by a two-stage process at 600 °C and then at 750 °C for 4 h each, and (ii) at 700 °C for 40 h showed a hyperfine as well as quadrupole splitting. The behaviour of the isomer shift (IS) and quadrupole splitting (ΔE) with the heat-treatment temperature show significant changes at the glass transition and crystallization temperature. The Mössbauer data have been found to be consistent with optical and electron micrographs which show a large variation in the particle size of the precipitated magnetic phase. This has been further correlated with EPR and magnetization data. This work has provided a characterization of the magnetic phases precipitated in the samples after different heat-treatments.

It is well known that the crystallization kinetics of the YIG phase precipitated in the $\text{Na}_2\text{O-SiO}_2\text{-Fe}_2\text{O}_3\text{-Y}_2\text{O}_3$ glass (Y6) can be enhanced by using suitable nucleating agents such as the oxides P_2O_5 or TiO_2 . The effect of the nucleating agents on the crystallization of YIG was studied by X-ray and Mössbauer spectroscopic studies by selecting samples of different compositions and by subjecting them to various heat-treatment schedules in the temperature range 720-820 °C. These studies have indicated that P_2O_5 is more favourable for crystallization of YIG. Analysis of the results suggested an optimum growth-temperature for the crystallization of the YIG phase to be 800 °C in the sample with P_2O_5 as the nucleating agent. The sample heat-treated at the growth-temperature for 40 h was found to be not as favourable for crystallization of the YIG phase as the sample heat-treated at two temperatures.

Last part of Chapter 3 describes the Mössbauer spectroscopic, X-ray and magnetization studies of the magnetic properties of the glass-ceramic system $45\text{PbO-35B}_2\text{O}_3\text{-4Al}_2\text{O}_3\text{-10Fe}_2\text{O}_3\text{-6Y}_2\text{O}_3$. Data from the as-prepared samples and samples heat-treated at 330, 500, 560 and 660 °C (for 4 h each) were analyzed and they indicated the presence of large $\alpha\text{-Fe}_2\text{O}_3$ particles surrounded by smaller spinel particles. A compensation temperature observed at 180 °C has been ascribed to an exchange interaction of the surface ions of $\alpha\text{-Fe}_2\text{O}_3$ with the surrounding spinel phase.

Chapter 4 describes the Mössbauer spectroscopic and other studies of the metallic glass (or amorphous metallic alloy) system $\text{Fe}_{100-x}\text{B}_x$. During the last decade the metallic glass systems have been widely studied because of the theoretical and technological interest in these materials. Although several Mössbauer spectroscopic studies of the $\text{Fe}_{100-x}\text{B}_x$ glass system have been reported in the literature, the kinetics of the crystallization process in these glasses ~~is~~^{are} not clearly understood yet. In order to obtain more information about the crystallization process in $\text{Fe}_{100-x}\text{B}_x$ we have studied this system by selecting samples having the boron content $x = 13, 16, 18, 20, 22$ and 26 . The as-prepared samples as well as samples heat-treated at $100, 200, 300, 350$ and 400°C for 1 h each and at 350 and 400°C for 4 h each were studied with Mössbauer spectroscopy, DTA and transmission electron microscopy (TEM) techniques. Systematic behaviour of the Mössbauer parameters like isomer shift (IS) and hyperfine magnetic field (H_{int}) for each temperature for different x is presented and analyzed. Observed Mössbauer spectra were analyzed to obtain the hyperfine magnetic field distribution $p(H)$ using Window's method. The Mössbauer spectra for various samples were carefully examined to identify contributions from Fe_3B , Fe_2B and $\alpha\text{-Fe}$ with an aim of determining at what temperature, for different x , the various phases get crystallized in the amorphous alloy $\text{Fe}_{100-x}\text{B}_x$. The results

of Mössbauer spectroscopy were compared with those obtained from DTA and TEM measurements with an aim of seeking corroborative evidence. Such a combined analysis led to a better understanding of the crystallization of the $\text{Fe}_{100-x}\text{B}_x$ glass.

Chapter 5 describes the study of the roasting and leaching processes of pyrite minerals by Mössbauer spectroscopy. Pyrite mineral contains iron sulphide (FeS_2) and iron can be extracted from it by using different methods of ore dressing of which roasting and leaching are two different methods. As a result of roasting pyrite transforms into pyrrhotite (Fe_{1-x}S) and magnetic oxides of iron such as $\alpha\text{-Fe}_2\text{O}_3$ and/or $\gamma\text{-Fe}_2\text{O}_3$. The latter kinds of magnetic oxides can be separated out by magnetic methods for subsequent extraction. It is, therefore, important to know the kinetics of the roasting of pyrite and to determine how and when the different magnetic oxides are formed. We have studied these kinetics by observing Mössbauer spectra of pyrite mineral roasting at $610 \pm 5^\circ\text{C}$ at time periods $t = 0.0, 0.5, 1.0, 2.0, 5.0, 15.0, 30.0$ and 60.0 mins. These studies have helped to determine optimum time period for efficient transformation into the magnetic oxides $\alpha\text{-Fe}_2\text{O}_3$ and $\gamma\text{-Fe}_2\text{O}_3$.

In recent years bacterial leaching of pyrite minerals has been carried out using the microorganism T. ferrooxidans. This process of bacterial leaching of

pyrite minerals has been studied by us using Mössbauer spectroscopy. These results are discussed towards the end of Chapter 5. The observed results are analyzed to establish the phases containing iron and the valency states of iron. It is felt that these two types of studies of pyrite minerals provide a novel application of Mössbauer spectroscopy in the area of extraction metallurgy.

CHAPTER 1

INTRODUCTION

1.1 Mössbauer Effect

Mössbauer effect is the name given to the phenomenon of recoilless emission and absorption of the nuclear radiation when the radiating system is embedded in a solid. It was discovered by the German physicist, R.L. Mössbauer [1] in 1958 and it rapidly developed into a sensitive spectroscopic technique which has been applied to the study of a variety of interesting problems in solid state physics, solid state chemistry, metallurgy, material science and many other areas. Several excellent reviews of the techniques of Mössbauer spectroscopy exist in the literature [2-7] and in view of this no attempt will be made here to describe this technique in detail. However, for the sake of completeness we shall briefly outline the basic principle, methodology and applications of Mössbauer spectroscopy in this Chapter.

Let us consider a system of mass M (which may be a nucleus or an atom) having two levels A and B, separated by an energy E_0 . Considering the transition of the system from level B to level A by the emission of a photon of energy E_γ^s and applying the law of conservation of momentum we can write the recoil energy R of the system as

$$R = \frac{p^2}{2M} = \frac{p^2}{2Mc^2} = \frac{(E_\gamma^s)^2}{2Mc^2} \quad (1.1)$$

where p and P are the linear momenta of the photon and the recoiling system respectively and c is the velocity of light. Remembering that $Mc^2 \gg E_0$, we can write

$$R = E_0^2 / 2Mc^2 \quad (1.2)$$

Conservation of energy leads us to

$$E_0 = E_\gamma^s + R \quad \text{or} \quad E_\gamma^s = E_0 - R \quad (1.3)$$

In a similar manner we can consider the excitation of the system from the level A to B and realise that the energy E_γ^a of the incident photon should provide an extra amount of recoil energy E_0 over and above the transition energy E_0 . We thus have

$$E_\gamma^a = E_0 + R \quad (1.4)$$

Further it is well known that the excited state B does not possess single energy E_0 but is characterised by a spectral lineshape $\omega(E)$ centred around E_0 such that

$$\omega(E) = \frac{1}{1 + 4(E - E_0)^2 / \Gamma^2} \quad (1.5)$$

where Γ , the natural linewidth of the state, is related to the mean lifetime, τ through Heisenberg's uncertainty principle

$$\Gamma \cdot \tau = h/2\pi \quad (1.6)$$

where h is the Planck's constant. The energy of the stable ground state is very sharp because it has $\tau \rightarrow \infty$ and $\Gamma \rightarrow 0$. As a result, the energy of the photon emitted in the transition from level B to A displays a natural lineshape similar to (1.5) but centred around E_γ^s which is given by (1.3). Similarly the energy of the photon which can induce a transition from level A to B also displays a distribution similar to (1.5) but centred around E_γ^a . An emission of photon will be followed by a resonant absorption when $E_\gamma^a = E_\gamma^s$ and is determined by the overlap of the two distributions

$$\begin{aligned}\omega_s(E) &= \left[1 + \frac{4(E - E_\gamma^s)^2}{\Gamma^2}\right]^{-1} \quad \text{and} \\ \omega_a(E) &= \left[1 + \frac{4(E - E_\gamma^a)^2}{\Gamma^2}\right]^{-1}\end{aligned}\tag{1.7}$$

In Fig. 1.1 we show the nature of this overlap for two cases : (a) the atomic system (emission of an optical photon) where $R \ll \Gamma$ and (b) the nuclear system (emission of a gamma ray) where $R \gg \Gamma$. It may be noticed that the overlap is very small in the case of a nuclear system.

Mössbauer discovered that in the case of nuclear gamma rays the overlap of the emission and absorption lineshape spectra can be increased by significant amount if the emitting and absorbing atoms are sufficiently tightly bound inside a solid lattice, thus increasing the efficiency of the resonant absorption.

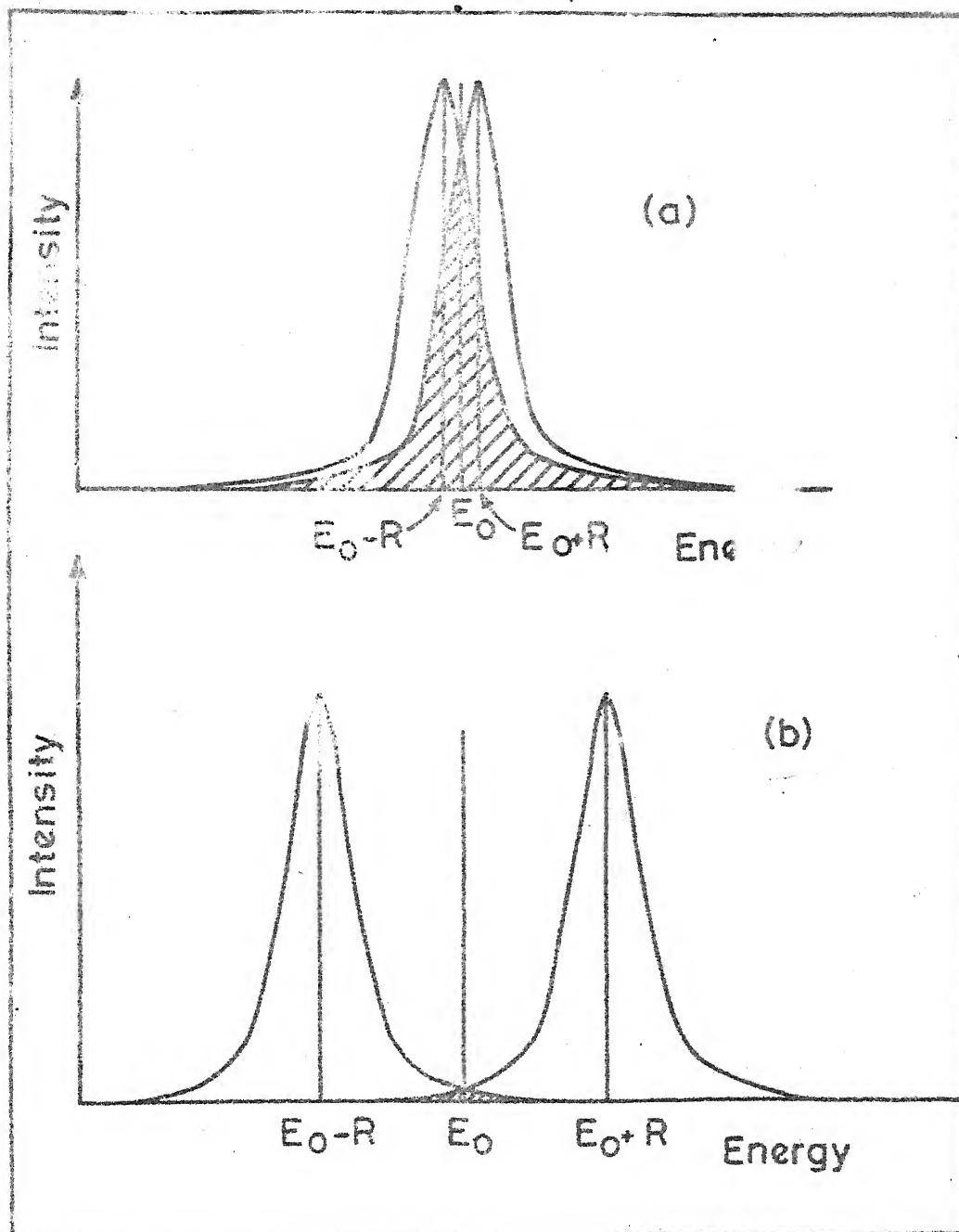


Fig. 1.1 Overlap of the emission and absorption lines showing the relation between E_0 , E_Y^S , E_Y^A and for two cases : (a) optical case, and (b) nuclear case.

The above discussion is based on classical arguments. In terms of quantum mechanics we can describe Mössbauer effect by saying that it consists of an enhancement of the probability for observing the zero phonon events (i.e. events in which there is no transfer of energy to or from lattice) over one phonon, two phonon or higher events.

It has been shown that the probability, f , for zero phonon event (f is usually termed as the recoil-free fraction) for a Debye solid at $T = 0$ K is given by

$$f = \exp(-3R/2k\theta_D) \quad (1.8)$$

where k is the Boltzmann constant and θ_D is the Debye temperature of the solid.

The above discussion makes it clear why the Mössbauer effect can be observed only for a small number of nuclides. For the observation of the Mössbauer effect f must be significantly large and this means that $R \ll k\theta_D$. Since $R \propto E_0^2$, we may think that the solution lies in using very low-energy gamma rays. However, very low energy gamma rays will have a poor emission yield and will need very thin absorbers. In most of the practical cases Mössbauer effect is observed in the range $10 \text{ keV} < E_0 < 150 \text{ keV}$, depending on the θ_D value of the element involved.

One nucleus in which the Mössbauer effect is most often observed is ^{57}Fe and most of the studies in Mössbauer spectroscopy have been carried out in solids containing ^{57}Fe .

It is well known that at room temperatures iron exists in fcc cubic lattice structure and the ^{57}Fe nucleus has a ground state with spin $I = (1/2)^-$ and an excited state at 14.4 keV with spin $I = (3/2)^-$. The radioactive source ^{57}Co decays to ^{57}Fe with a half-life of about 270 d via electron capture (Fig. 1.2) and can be conveniently prepared through the nuclear reaction $^{56}\text{Fe}(d,n)^{57}\text{Co}$. As seen in Fig. 1.2, the radioactive decay of ^{57}Co leads to the excited states of ^{57}Fe and the transition from the $(3/2)^-$ state to the $(1/2)^-$ state provides the gamma ray for studying the Mössbauer effect in the ^{57}Fe nucleus. Some interesting data [8,9] about ^{57}Fe is given in Table 1.1. Besides ^{57}Fe , there are many other nuclei in which Mössbauer effect is studied and their detailed properties are reviewed in the literature [2-9]. We have discussed the properties of ^{57}Fe alone because the present study used only the ^{57}Fe Mössbauer transition.

The experimental methodology that is used in observing the Mössbauer effect will be summarised in the next Chapter. In the next three sections we describe how the quantitative information about the hyperfine interaction between the ^{57}Fe nucleus and its surroundings is obtained through the parameters like isomer shift, quadrupole splitting, effective magnetic field etc.

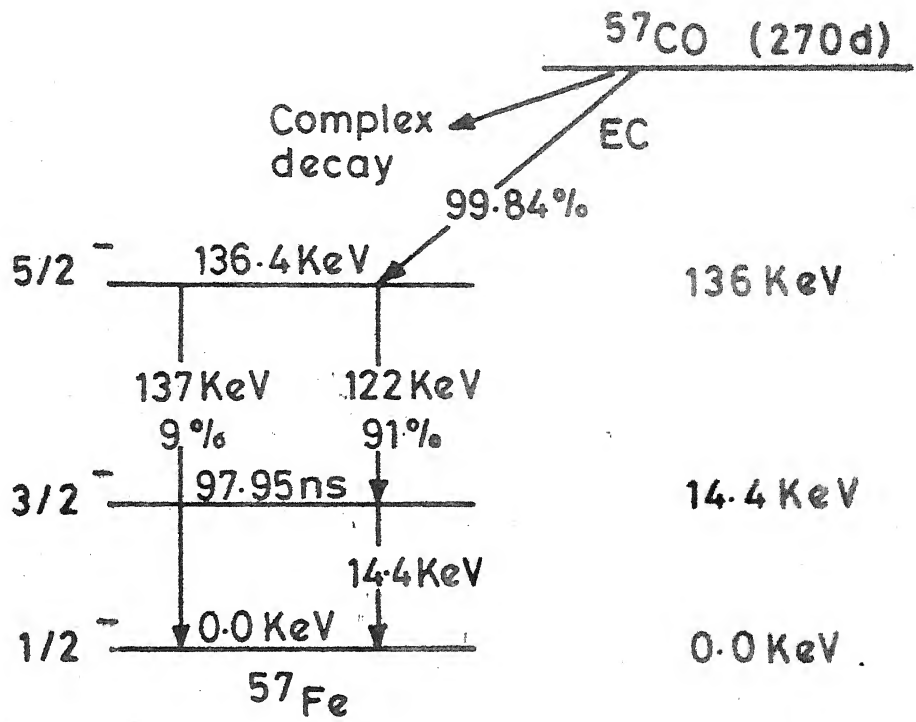


Fig. 1.2 Radioactive decay scheme of ^{57}Co .

TABLE 1.1

Parameters for the 14.4 keV Mössbauer transition in ^{57}Fe [8,9]

- 1) Isotopic abundance = 2.14 %
- 2) Energy $E_\gamma = 14.41303$ (8) keV
- 3) Half-life, $t_{1/2} = 97.81$ (14) ns
- 4) Ratio of the excited and ground state nuclear magnetic moments, $R_\mu = -1.7145$ (5)
- 5) Nuclear magnetic dipole moment of the excited state = $\mu = -0.15534$ (5) nm
- 6) Nuclear electric quadrupole moment of the excited state = $Q = +0.209$ (15) barns
- 7) Total internal conversion coefficient, $\alpha_T = 8.21$ (12)
- 8) Debye temperature, $\Theta_D = 440$ K
- 9) Mössbauer cross section = $256(3) \times 10^{-20} \text{ cm}^{-2}$
- 10) Mössbauer linewidth (theoretical full width at half maximum) = $0.1940 \text{ mm sec}^{-1}$
- 11) Recoil energy, $E_R = 1.957 \times 10^{-3} \text{ eV}$
- 12) Conversion factor $1 \text{ mm sec}^{-1} = 11.6248$ (1) MHz.

1.2 Hyperfine Interactions

The nature of the Mössbauer spectrum and the number and positions of the peaks observed in a Mössbauer spectrum are sensitive to the extranuclear environment and as a result different spectra are observed from different compounds of ^{57}Fe . To understand these differences in the spectra, one has to understand the effects of the so-called hyperfine interactions on Mössbauer spectra. These hyperfine interactions include the interactions between the charge (and current) distributions of the Mössbauer nucleus (e.g. ^{57}Fe) and the extranuclear electric and magnetic fields.

These hyperfine interactions can be described in terms of the Hamiltonian

$$H = E_0 + M_1 + E_2 + \dots \quad (1.9)$$

where E_0 describes the electric monopole interaction between nucleus and the surrounding electrons, M_1 describes the magnetic dipole interaction between the nuclear magnetic dipole moment and the surrounding extranuclear magnetic field and E_2 describes the electric quadrupole interaction between the nuclear electric quadrupole moment and the electric field gradient of the surrounding electrons. Terms higher than E_2 are small and can be usually neglected.

The first term, E_0 , causes a change in the energy separation between the ground and the excited states of

the nucleus (e.g. ^{57}Fe). Depending on the chemical state of the compound containing ^{57}Fe the amount of this change will be different for the absorber and the source. As a result the position of the peak in the Mössbauer lineshape is shifted and the amount of the shift is known as isomer shift (IS) or chemical shift.

The presence of other two terms M_1 and E_2 , singly or jointly, causes a splitting of the energy levels and this gives rise to multiple lines in the Mössbauer spectra. The peak positions and intensities of these lines provide valuable information about the hyperfine interaction as discussed in the following sections. The aim of the present work is to use the Mössbauer parameters like isomer shift, electric quadrupole splitting, magnetic hyperfine splitting etc. for characterizing different compounds of iron and the magnetic, non-magnetic phases etc. rather than studying these parameters in a fundamental manner. In view of this the discussion in the following sections will be given in its barest outline. The subject of hyperfine interaction is discussed in detail in many excellent reviews and monographs [2-7,10].

1.3 Isomer Shift

Isomer shift is one of the important Mössbauer parameters and it measures the difference between the Mössbauer transition energy in the source and absorber when both of them are at the same temperature. Isomer shift is

usually quoted in terms of the relative velocity between the source and absorber. It arises out of the electrostatic interaction (electric monopole interaction) between the charge distribution of the nucleus and those surrounding electrons which have a finite probability of being found in the volume of the nucleus. As a result of this interaction, the nuclear energy levels do not show any splitting but there is a small but measurable shift of Mössbauer energy levels in a compound compared to that in a free atom. This effect is illustrated in Fig. 1.3a, where this shift is shown to be different in source and absorber. The energy of the Mössbauer gamma ray in the source is denoted by E_{γ}^S while that in the absorber is shown by E_{γ}^a and the difference between E_{γ}^S and E_{γ}^a is typically of the order of 10^{-9} eV. In order to observe the resonance in this case, therefore, one will have to provide a Doppler velocity v , to the source (or absorber) so that $[E_{\gamma}^S + (v/c) E_{\gamma}^S] = E_{\gamma}^a$. In the absence of electric quadrupole or magnetic dipole interaction, isomer shift manifests itself as the shift of the single resonance from the zero velocity (Fig. 1.3b). If the electric quadrupole or magnetic dipole interactions are also present, the isomer shift is determined from the centre of gravity of the Mössbauer spectrum and it gives a measure of the strength of the electric monopole interaction.

The subject of isomer shift has been discussed in detail in several reviews [3-10] and we shall not go into

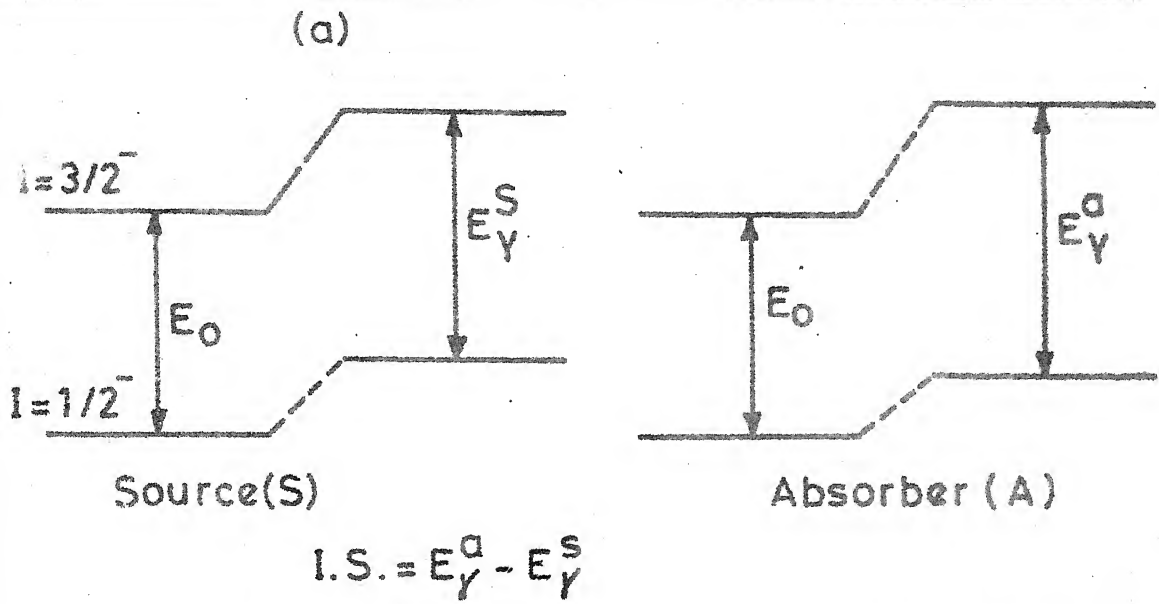


Fig.1.3 - Effect of monopole interaction on the energy levels of source and absorber.

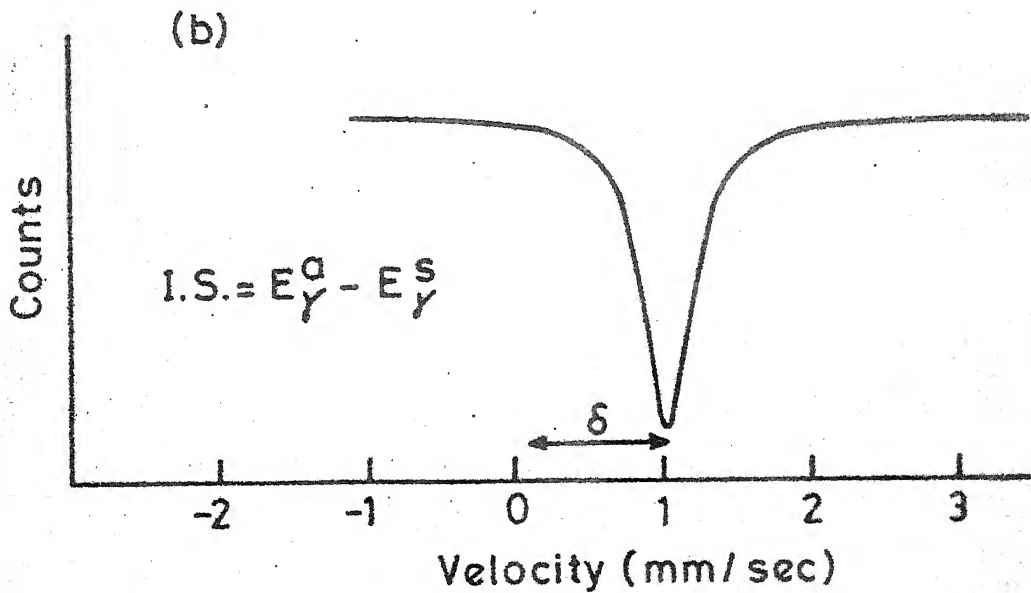


Fig.1.3 - Mössbauer spectrum showing monopole interaction.

these finer details here. We shall, however, outline a simple calculation of the isomer shift using a classical treatment [11]. Let us consider the effect of the overlap between the nuclear charge density and the s-electron density by assuming the nucleus to be a uniformly charged sphere of radius R . We denote the s-electron density at the nucleus by $[\Psi(0)_s]^2$ and assume it to be constant over the nuclear volume. Let δE denote the energy difference between the electrostatic interaction of a point nucleus with $[\Psi(0)_s]^2$ and the electrostatic interaction of a finite-size nucleus having a radius R with $[\Psi(0)_s]^2$. It can be shown that

$$\delta E = K [\Psi(0)_s]^2 R^2$$

where K is a nuclear constant. The value of δE will be different for the excited and ground nuclear states because the R values are different for these two states. Using the subscripts e and g for the excited and ground nuclear states respectively, we have

$$\delta E_e - \delta E_g = K [\Psi(0)_s]^2 (R_e^2 - R_g^2) \quad (1.10)$$

For a given nucleus (e.g. ^{57}Fe) the R -values will be constant but the values of $[\Psi(0)_s]^2$ will vary from one compound of iron to another. Comparison of the nuclear transition energy in a source (E_γ^s) with that in an absorber (E_γ^a) involves the above energy difference which can be

measured in a Mössbauer experiment. As mentioned earlier the isomer shift (IS) can be expressed in terms of the Doppler velocity which is to be given to the source to observe the resonance. An expression for IS can be obtained by writing the difference of eq. (1.10) for source and absorber to obtain

$$IS = K (R_e^2 - R_g^2) \left\{ [\Psi(0)_s]_a^2 - [\Psi(0)_s]_s^2 \right\} \quad (1.11)$$

where the subscripts a and s correspond to the absorber and source respectively. In usual practice, one uses a standard source material, e.g. ^{57}Co in Rh for Fe Mössbauer spectra or BaSnO_3 for Sn Mössbauer spectra. If we write $\delta R = (R_e - R_g)$ and recognise that δR is very small, we can write

$$IS = 2K R^2 \frac{\delta R}{R} \left\{ [\Psi(0)_s]_a^2 - C \right\} \quad (1.12)$$

where C is a constant whose value depends on the source used. It is thus seen from (1.12) that the IS depends on two factors, the first one being the nuclear factor δR while the second one is an extranuclear factor $[\Psi(0)_s]^2$. For a given nucleus like ^{57}Fe , the value of δR is a constant and the value of IS is directly proportional to the s-electron density at the nucleus. In the case of ^{57}Fe , δR is negative and thus the IS-value becomes more negative with an increase in the s-electron density at the absorber nucleus (^{57}Fe). In this way a variation in

the s-electron density leads to changes in the IS. In addition changes in the p or d electron density also induces changes in the IS value even though the p or d electrons do not directly interact with the nuclear charge density.

Study of Mössbauer spectra of the different compounds of iron has shown that the range of values of IS falls in different classes depending on the oxidation states of iron. This is brought by the data presented in Table 1.2 and in Fig. 1.4 for compounds in which iron ion has a high-spin configuration. In this way the oxidation state of iron in a solid can be determined from the examination of the measured IS value.

In Fig. 1.5a we have plotted the ^{57}Fe isomer shifts against the coordination number for ionic high spin and low spin compounds and minerals. The arrows marked on the boxes indicate that values outside the ranges shown (boxed areas) have also been observed. Similar data for the quadrupole splitting are shown in Fig. 1.5b.

Different authors quote their results for the IS relative to different sources or to different absorbers. In order to have a universal comparison, it is necessary to have a ^{57}Fe isomer shift scale for sources (or absorber) as shown in Fig. 1.6.

In the present work we have studied different glass-systems, minerals and other materials by Mössbauer spectroscopy and have analyzed the results for the IS values in

TABLE 1.2

Isomer shift and quadrupole splitting for iron in various
electron configuration d^n . (+)

d^n	Oxidation State	IS* [10] (mm sec ⁻¹)	ΔE [4] (mm sec ⁻¹)
d^7	+ 1	1.90	-
d^6	+ 2	1.20	1.5 - 3.7
d^5	+ 3	0.45	0.0 - 1.0
d^4	+ 4	0.0	-
d^2	+ 6	-0.9	-

(+) IS = Isomer shift, ΔE = Quadrupole splitting

*With respect to α -Fe.

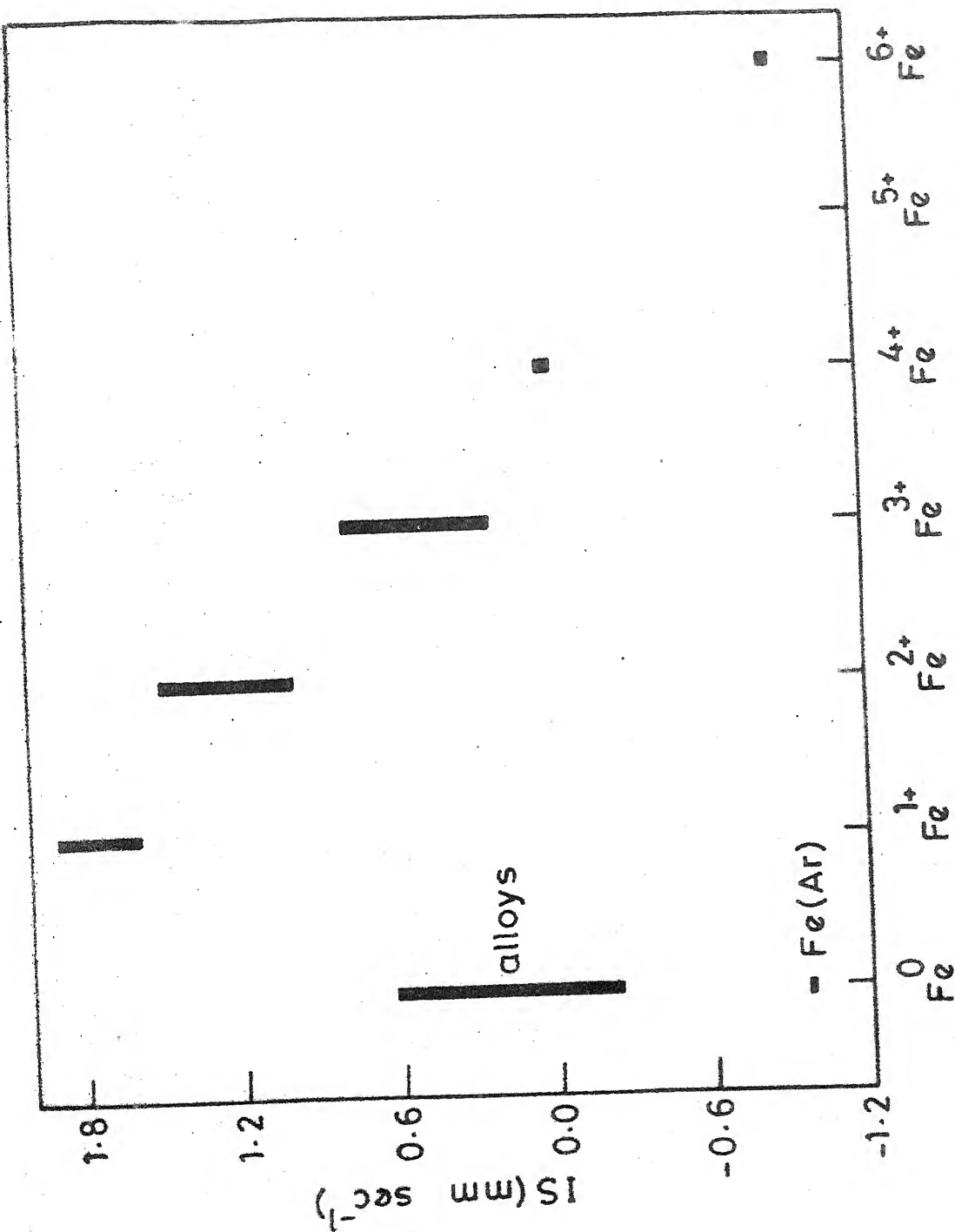


Fig. 1.4 Review of ⁵⁷Fe isomer shift data of iron in various ionization states [10].

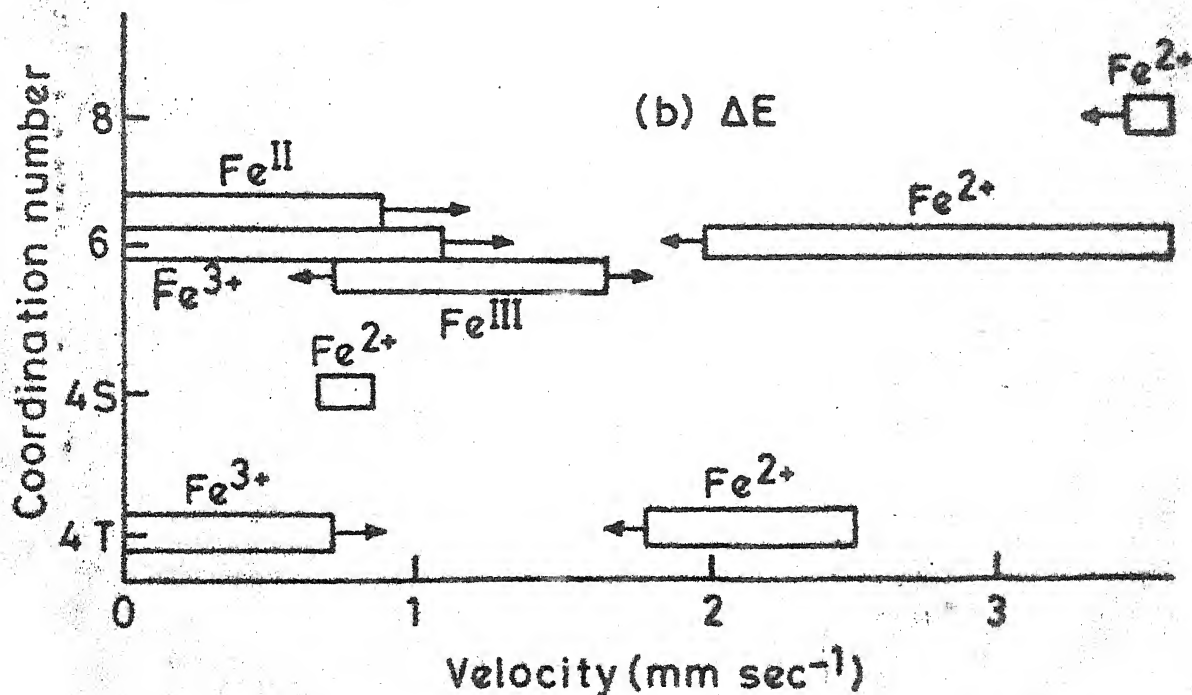
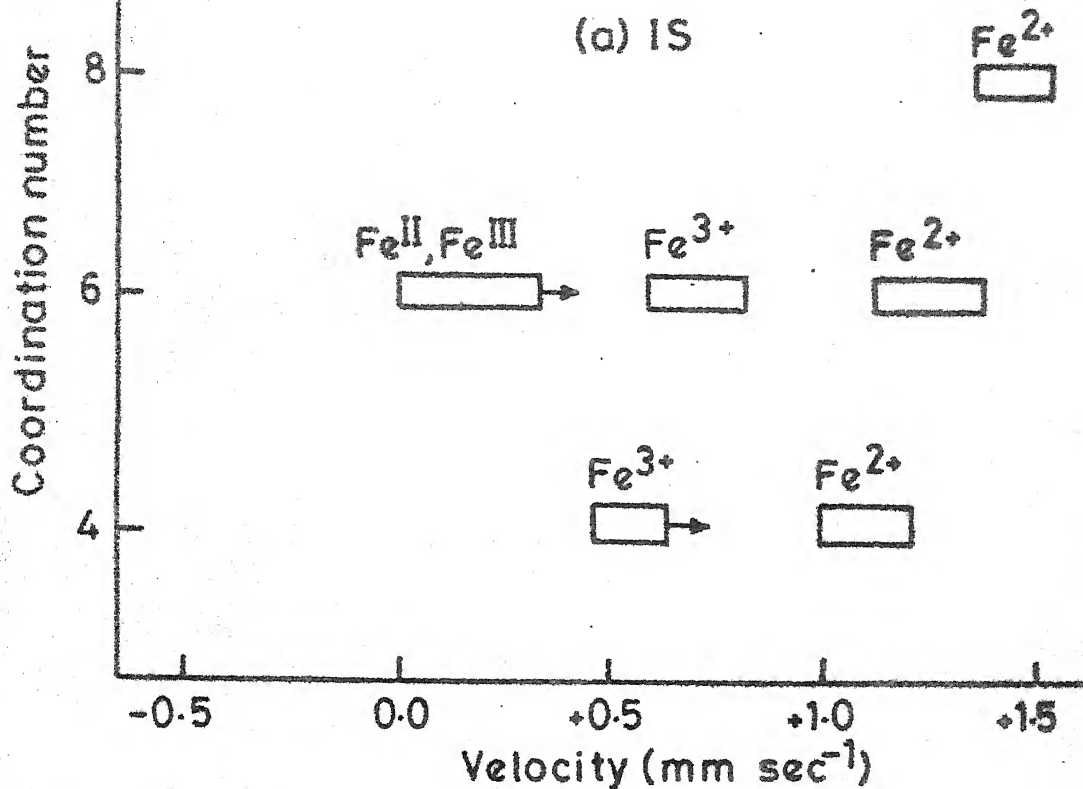
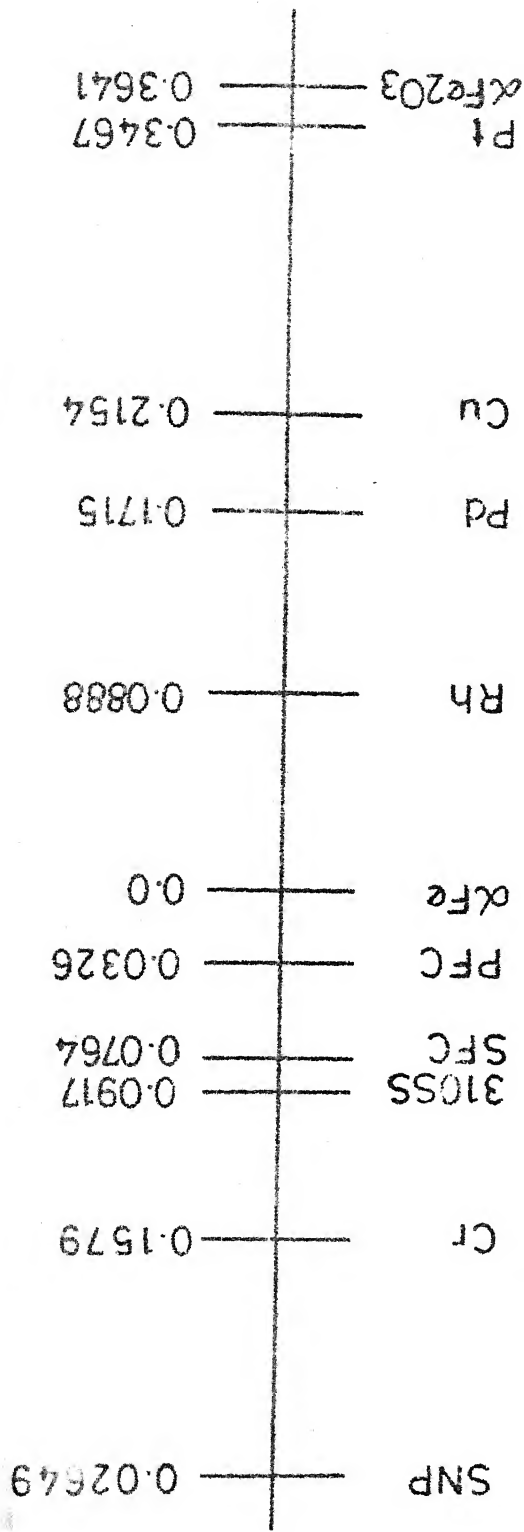


Fig. 1.5 Review of ^{57}Fe Mössbauer parameters (a) IS (isomer shift) and (b) ΔE (quadrupole splitting) for iron plotted against the coordination number for 'ionic' high spin and low spin compounds and minerals. Arrows indicate that the values outside the range of boxes have been observed [11].

Positive

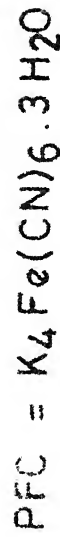
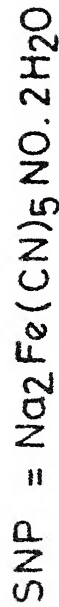
Negative



Absorber

Negative

Positive



SS = Stainless steel

Fig. 1.6 Data for the ^{57}Fe isomer shift with respect to natural iron ($\alpha\text{-Fe}$) at room temperature. Units of the IS values are mm sec^{-1} and the signs of the velocity for the source are to be read from the top row while the signs of the velocity for the absorber are to be read from the bottom row. To take an example, for a source in Rh host matrix, the IS of $\alpha\text{-Fe}$ absorber will be $-0.0888 \text{ mm sec}^{-1}$ (with respect to metallic $\alpha\text{-Fe}$). The IS values are taken from [12].

terms of the octahedral/tetrahedral coordination. We have reproduced in Fig. 1.7 results for the IS values for some crystals and glasses classified according to octahedral/tetrahedral symmetry [13].

The results shown in Table 1.2 and Figs. 1.4-1.7 will be useful when the results of our measurements are analyzed in Chapters 3 to 5.

1.4 Quadrupole Splitting

In the last section the treatment of isomer shift was based on the assumption that nucleus is spherical and that it has a uniform charge density. In case these assumptions are not valid and if the nuclear spin $I > 1/2$, there will be an interaction of the nuclear charge density with the extranuclear electric field. More precisely the Z-components of the electric field gradient (EFG) tensor will interact with the electric quadrupole moment of the nucleus. Such an electric quadrupole interaction leads to a splitting of the nuclear energy levels. Let us consider the case of ^{57}Fe nucleus for which the spins of the excited and the ground states are $I_e = 3/2$ and $I_g = 1/2$ respectively. The higher level ($I_e = 3/2$) splits into two levels ($m_I = \pm 3/2$, $m_I = \pm 1/2$) while the $I = 1/2$ level remains unsplit (or degenerate) as shown in Fig. 1.8. Selection rules allow both the transitions $m_I^e = \pm 3/2 \rightarrow m_I^g = \pm 1/2$ and $m_I^e = \pm 1/2 \rightarrow m_I^g = \pm 1/2$ (Fig. 1.8). This results in a doublet

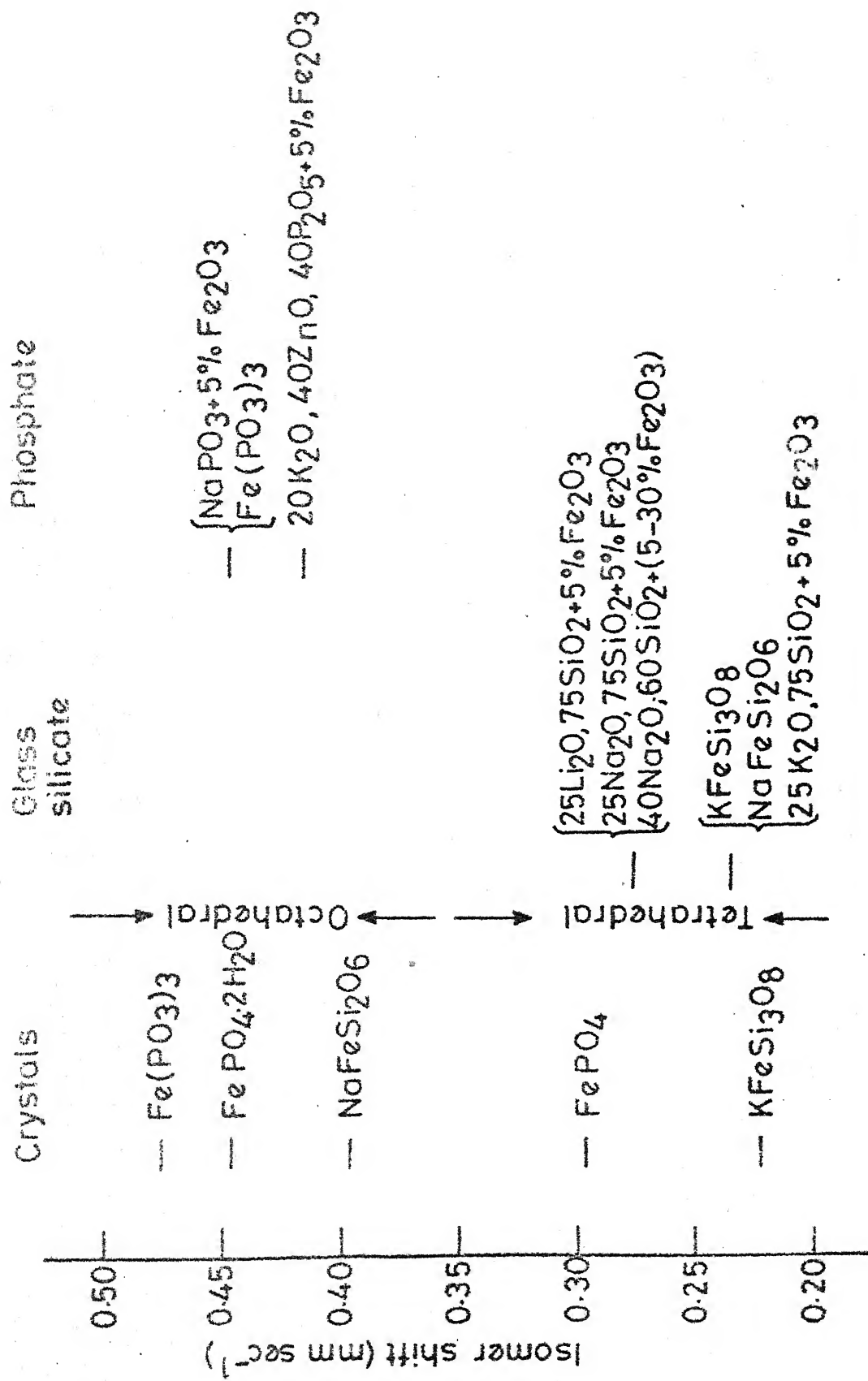


Fig. 1.7 Isomer shifts (relative of α-Fe) for some crystals and glasses [13].

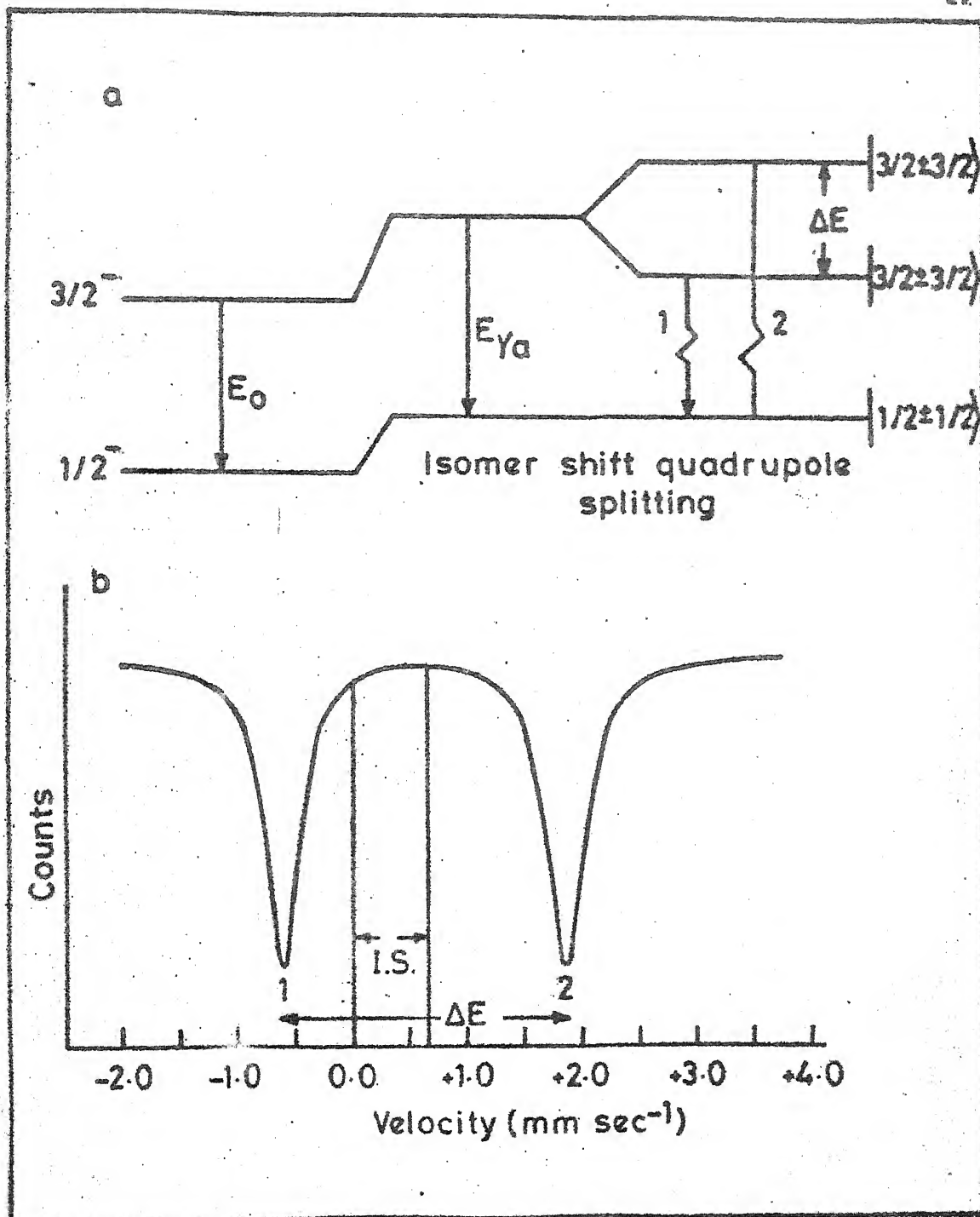


Fig. 1.8 Effect of the quadrupole interaction on the nuclear energy levels of source/absorber and the resulting Mössbauer spectrum showing the quadrupole splitting and isomer shift.

or two-line Mössbauer spectrum from which the quadrupole splitting (QS or ΔE) is obtained as the separation of the two peaks while the isomer shift is obtained from the separation of the centroid of the two peaks from the zero of the velocity scale for the source.

The theory of quadrupole splitting is discussed in many texts [2-9]. In the case of ^{57}Fe (which has $I = 3/2$) the quadrupole splitting (ΔE) can be expressed as

$$\text{QS} = \Delta E = 1/2 e^2 q Q [1 + \eta^2/3]^{1/2} \quad (1.13)$$

where Q is the electric quadrupole moment of the nucleus, and

$e q = V_{ZZ}$ = the negative of the Z-component of the electric field gradient (EFG)

e = protonic charge

η = the asymmetry parameter = $(V_{XX} - V_{YY})/V_{ZZ}$.

Analysis of the ΔE (or QS) values determined from the observed Mössbauer spectra provide valuable information for studying the solid. In Fig. 1.5b we have plotted the ΔE values against the coordination number for different ionic high spins.

1.5 Magnetic Hyperfine Splitting

Detailed discussion of the magnetic hyperfine splitting of Mössbauer spectra is given in literature [2-9]. We give

here a brief outline of the magnetic hyperfine splitting in the case of ^{57}Fe because it will be used in the interpretation of our results for different samples presented in Chapter 3 to 5.

The magnetic dipole moment μ_N of a nucleus having spin I is given by

$$\mu_N = g_N \beta_N I \quad (1.14)$$

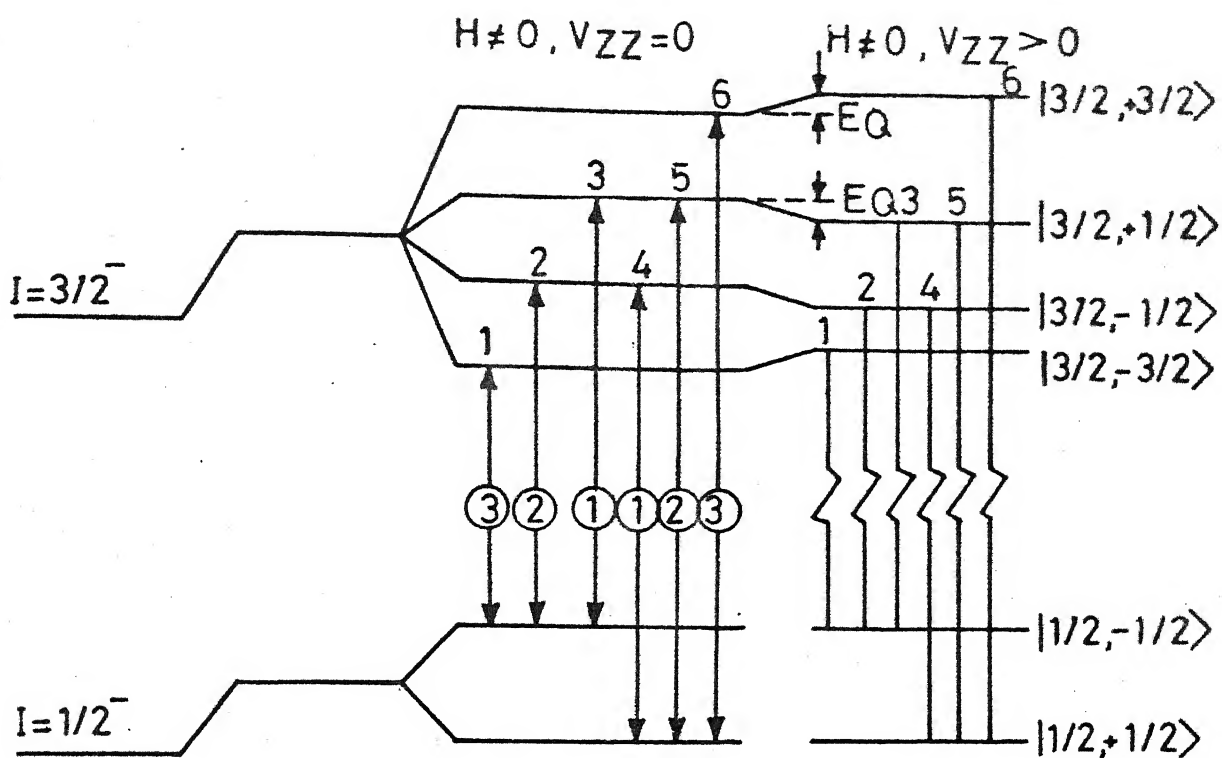
As a result of the magnetic interaction between this magnetic dipole moment and the applied or local (extranuclear) magnetic fields at the nucleus, the degeneracy of the nuclear energy levels is completely removed (Fig. 1.9). Taking into account the different g_N values of the ground and excited states and the selection rules $\Delta m_I = 0, \pm 1$, it can be shown that a symmetric six-line Mössbauer spectrum will be observed. The isomer shift is determined by the centre of gravity of the six peaks. Although the line-widths of the six peaks are in general equal, their intensities are different, being given by the following equations :

$$I_1 = I_6 = 3(1 + \cos^2 \theta) \quad (1.15a)$$

$$I_2 = I_5 = 4 \sin^2 \theta \quad (1.15b)$$

$$I_3 = I_4 = (1 + \cos^2 \theta) \quad (1.15c)$$

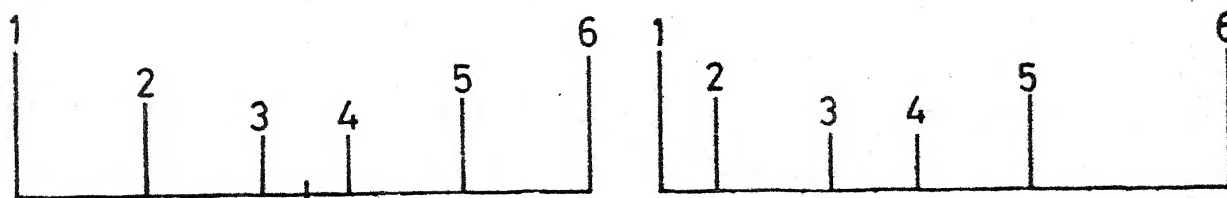
where θ is the angle between the direction of propagation of the radiation and the effective magnetic field H_{int} . In



Isomer shift Magnetic dipole
splitting

Magnetic dipole
splitting + electric

Quadrupole
perturbation



Velocity (mm sec⁻¹)

Fig. 1.9 Effect of the magnetic hyperfine interaction on the nuclear energy levels of the source/absorber.

the case of a sample for which the magnetic domains are randomly oriented, the ratio of the areas of the six lines is 3:2:1:1:2:3.

In the case of many magnetic substances, the electric quadrupole and magnetic dipole interaction will be present concurrently. This makes the spectra more complicated and such situations are discussed in the literature [2-9].

One of the important applications of the magnetic hyperfine splittings is for the calibration of the Mössbauer spectrometer. One usually records a Mössbauer spectrum of natural Fe (as absorber) at room temperature and obtains a spectrum similar to the one shown in Fig. 1.9. The position of the six lines of Fe are as follows : - 5.328, -3.083, -0.838, +0.838, +3.083 and +5.328 mm sec⁻¹ relative to Fe source.

The determination of the effective magnetic field H_{int} for a given sample can be done with the help of the following equations.

$$E_{(3/2, +1/2) \rightarrow (1/2, +1/2)} - E_{(3/2, +1/2) \rightarrow (1/2, -1/2)} =$$

$$\frac{E_0}{c} [V_{(3/2, +1/2) \rightarrow (1/2, +1/2)} - V_{(3/2, +1/2) \rightarrow (1/2, -1/2)}]$$

$$= (\mu_g H) / (1/2) \quad (1.16)$$

and

$$\begin{aligned}
& E(3/2, 3/2) \rightarrow (1/2, 1/2) - E(3/2, +1/2) \rightarrow (1/2, +1/2) = \\
& \frac{E_0}{c} [V(3/2, 3/2) \rightarrow (1/2, 1/2) - V(3/2, 1/2) \rightarrow (1/2, 1/2)] = \\
& (\mu_e H) / (3/2) \quad (1.17)
\end{aligned}$$

where E represent the energy state of corresponding level.

The value of H from these two equations (1.16) and (1.17) can be found out if the value of μ_g and μ_e are known. The value of μ_g obtained by Ludwig and Woodbury [14] by using the nmr technique is $+0.0903 \pm 0.0007$ nm. Using the value of μ_g and $E_0 = 14.4$ keV the magnetic hyperfine field H_{int} is given by

$$\begin{aligned}
H_{int} &= 0.843 \times 10^5 [V(3/2, +1/2) \rightarrow (1/2, +1/2) \\
&\quad - V(3/2, +1/2) \rightarrow (1/2, -1/2)] \text{ Oe} \\
&= 0.843 \times 10^5 [L_5 - L_3] \times \text{Calibration constant Oe}
\end{aligned}$$

where L_3 and L_5 are the position of third and fifth line. By using this value one can also find out the value of μ_e .

1.6 Motivation Behind the Present Work

In Table 1.3 we have summarized the relationship between variables measured using Mössbauer spectroscopy and various research fields.

As outlined in the Synopsis the present work describes Mössbauer spectroscopic and other studies of

TABLE 1.3

Relationship between variables measured using Mössbauer spectroscopy and various research

Measured Variable	Nuclear Physics	Solid State Physics	Chemistry	Metallurgy	Biology	Analytical
Isomer shift	Nuclear radius change	Electronic structure	Valence state and covalency	Electronic structure	Valence change	-
Magnetic hyperfine structure	Nuclear moment	Magnetic structure, Electronic configuration of magnetic ions	Electronic configuration of magnetic ions	Order disorder precipitation identification	Ligand configuration	Particle size information via superparamagnetism
Electric quadrupole hyperfine structure		Electronic configuration	Ligand symmetry, bonding orbitals			
Recoil free fraction		Phonon spectrum, anisotropic binding	Anisotropic binding	Force constants and anharmonic binding	Free or bound complex	-

three kinds of solids, namely, glass ceramics, amorphous metallic alloys (or metallic glasses) and pyrite minerals. Although the background and motivation behind these research problems will be discussed in detail in Chapter 3 to 5, we outline here, a brief discussion of the problems studied by us.

Today glass ceramics form an important class of materials in view of their superior mechanical, thermal and abrasion-resistant properties. Among these, the glass ceramics containing magnetic phases hold a special interest. Mössbauer spectroscopic studies can provide valuable information about glass ceramics and such studies along with differential thermal analysis, electron paramagnetic resonance, magnetization, optical and electron microscopic and X-ray diffraction studies allow us to have a better understanding of the physical properties of the glass ceramic systems. In the present work we have chosen the glass ceramic $\text{Na}_2\text{O-SiO}_2\text{-Fe}_2\text{O}_3\text{-Y}_2\text{O}_3$ in which yttrium iron garnet (YIG) can be precipitated by suitable heat-treatment. This particular composition has been studied by taking the as-prepared samples as well as samples heat-treated for different time periods and at different temperatures in the range $400\text{-}850^\circ\text{C}$ with a view of characterizing the magnetic phases precipitated in the samples. In the next stage of study the effect of the nucleating agents on the crystallization of YIG in the above glass ceramic ($\text{Na}_2\text{O-SiO}_2\text{-Fe}_2\text{O}_3\text{-Y}_2\text{O}_3$)

was investigated since it is known that the crystallization kinetics of the YIG phase can be enhanced by using suitable nucleating agents such as the oxides P_2O_5 or TiO_2 . One more glass ceramic having a composition $45PbO-35B_2O_3-4Al_2O_3-10Fe_2O_3-6Y_2O_3$ was also studied with an aim of studying the magnetic properties of this system.

In the recent years metallic glasses (amorphous metallic alloys) have invoked tremendous research interest in view of their interesting technological applications. Among these metallic glasses the system $Fe_{100-x}B_x$ had been well studied with Mössbauer spectroscopy and other techniques by different workers for different concentrations (x) of boron by measuring their properties at different temperatures. Although such studies in the past have provided valuable information about the crystallization process in the metallic glasses, the kinetics of crystallization are not clearly understood yet. In the present work we have aimed to further characterize the crystallization process by selecting samples of amorphous $Fe_{100-x}B_x$ ($x = 13$ to 26) alloys and subjecting them to heat-treatments over different time periods and at different temperatures. The heat-treatment schedule was programmed so as to follow the kinetics of crystallization upto a temperature where the crystallization is more or less complete. Various samples have been studied by employing Mössbauer spectroscopy, differential thermal analysis and transmission electron

microscopy so that corroborating results could be obtained.

In the present work we have also studied the roasting and leaching process of pyrite minerals by Mössbauer spectroscopy. Pyrite contains iron sulphide (FeS_2) and can be beneficiated by different methods of ore dressing prior to extraction of iron. Roasting of pyrite mineral leads to pyrrhotite and magnetic oxides of iron such as $\alpha\text{-Fe}_2\text{O}_3$ and/or $\gamma\text{-Fe}_2\text{O}_3$. The latter types of oxides, being magnetic, can be separated out by magnetic methods for subsequent extraction. It is therefore important to know the kinetics of the roasting of pyrite and to determine how and when the different magnetic oxides are formed. We have studied these kinetics by observing Mössbauer spectra of pyrite mineral roasted at $610 \pm 5^\circ\text{C}$ at different time periods ranging from $t = 0$ to $t = 60$ mins.

Recently the micro-organism T. ferrooxidans has been used for bacterial leaching of pyrite minerals. We have studied these bacterial leaching process of pyrite minerals by Mössbauer spectroscopy with an aim to establish the phases containing iron and the valency states of iron. We feel that these two types of studies of pyrite minerals provide a novel application of Mössbauer spectroscopy in the area of extraction metallurgy.

REFERENCES

1. R.L. Mössbauer, Z. Physik 151, 124 (1958); Z. Naturforsch. 14a, 211 (1959).
2. H. Frauenfelder, ''The Mössbauer Effect'' W.A. Benjamin, New York (1962).
3. G.K. Wertheim, ''Mössbauer Effect : Principles and Applications'' Academic Press, New York and London (1964).
4. V.I. Goldanskii and R.H. Herber, Editors, ''Chemical Application of Mössbauer Spectroscopy'', Academic Press, New York and London (1968).
5. N.N. Greenwood and T.C. Gibb, ''Mössbauer Spectroscopy'', Plenum Press, New York-London (1971).
6. L. May, Editor, ''An Introduction to Mössbauer Spectroscopy'', Plenum Press, New York-London (1971).
7. V.G. Bhide, ''Mössbauer Effect and its Applications'', Tata McGraw-Hill Publishing Co. Ltd. New Delhi (1973).
8. J.G. Stevens and L.H. Bowen, Analy. Chemistry 48, 232R (1976).
9. U. Gönser, Editor, ''Mössbauer Spectroscopy'', Springer-Verlag - Berlin (1975), p. 7.
10. G.K. Shenoy and F.E. Wagner, Editor, ''Mössbauer Isomer Shifts'', North-Holland - Amsterdam (1978).
11. G.M. Bancroft, ''Mössbauer Spectroscopy'', McGraw-Hill Book Co. England (1973).

12. J.G. Stevens and W.L. Gettys "'Int. Conf. on the Appl. of the Mössbauer Effect'" Jaipur, India Dec. 14-18, (1981).
13. C.R. Kurkijan and E.A. Sigety, "'Physics and Chemistry of Glasses'" 9, 73 (1968).
14. G.W. Ludwig and H.H. Woodbury, Phys. Rev. 117, 1286 (1960).
15. R.L. Cohen, Editor, Applications of Mössbauer Spectroscopy, Vol. I, Academic Press, New York and London (1976).

CHAPTER 2

EXPERIMENTAL METHODS

2.1 Introduction

The following instruments form the basic units in a Mössbauer spectroscopy experiment. In the experiments carried out by us and described in this work we have used only the 14.4 keV gamma-ray in the ^{57}Fe nuclei for observing Mössbauer effect. We shall, therefore, limit ourselves to the case where ^{57}Co is the radioactive source and ^{57}Fe is the absorber used in Mössbauer experiment. These instruments are shown in the block diagram of Fig. 2.1 and they are :

- (i) Radioactive source which can emit gamma ray (e.g. 14.4 keV gamma ray emitted in the electron capture decay of ^{57}Co to ^{57}Fe nucleus) suitable for observing Mössbauer effect.
- (ii) Mössbauer spectrometer having an electromechanical transducer for providing either constant or accelerated relative velocity between the source and absorber.
- (iii) Sample to be studied (containing ^{57}Fe nuclei) as an absorber.

- (iv) In some studies it is necessary to carry out measurements not only at room temperature but also at lower (e.g. liquid nitrogen) or higher (e.g. 800 K) temperatures. Correspondingly a cryostat or an oven is required for housing the absorber or the source as required by the objectives of the experiment.
- (v) Nuclear radiation detector for counting the gamma-rays.
- (vi) Electronic instruments. Two types of such instruments are required. First kind consists of instruments required to process the gamma-ray signal, i.e. stabilised high voltage power supply, preamplifier, amplifier, single channel analyzer etc. The second type of instruments consists of electronics required to drive the transducer and to pick up and analyze the signal in the multichannel analyzer according to the velocity information.

In this Chapter we shall provide brief description of the apparatus used in the present experimental work. This description is divided according to the different parts shown in Fig. 2.1. Detailed description of the general methodology of Mössbauer effect has been reported in literature [1-8] and will not be given here.

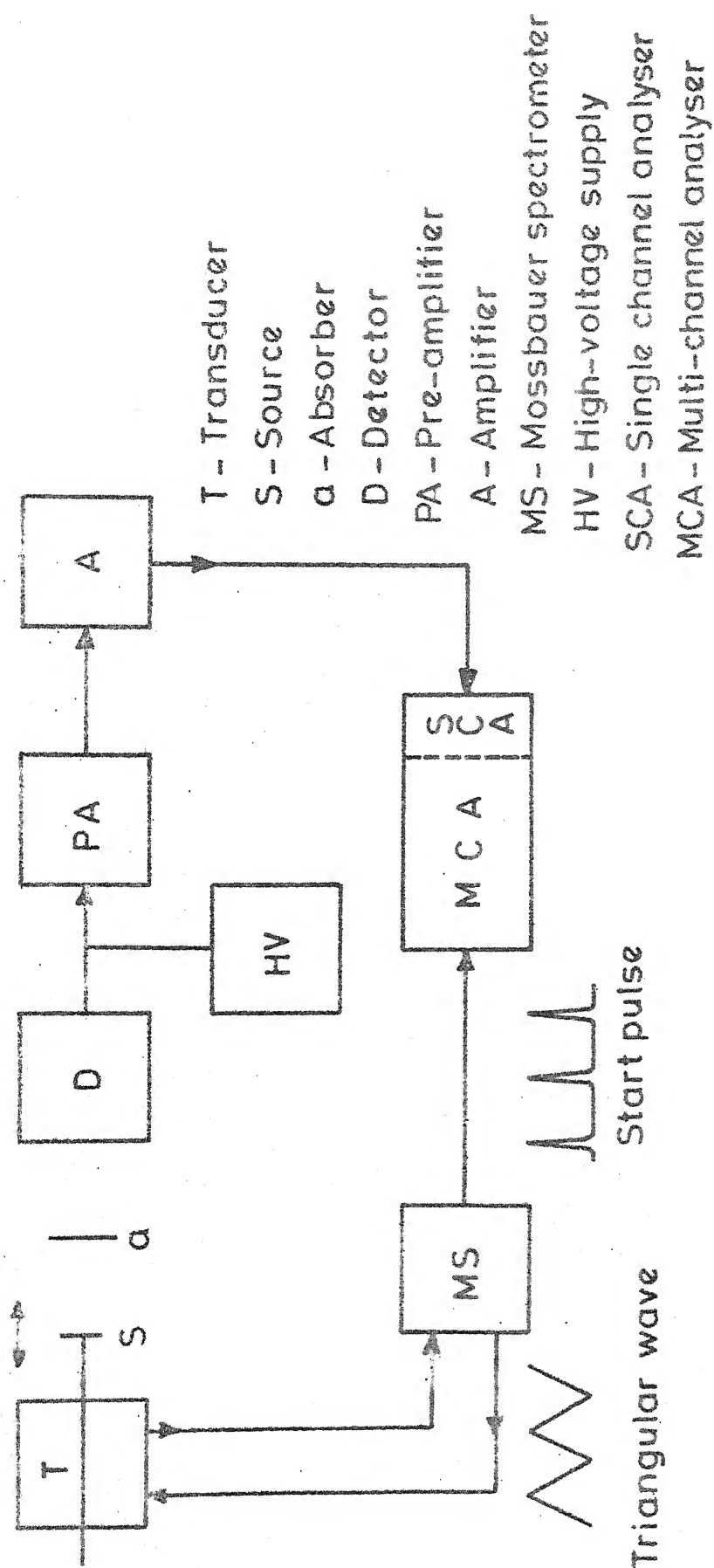


Fig. 2.1 Schematic block diagram of various instruments involved in a Mossbauer effect experiment.

2.2 Radioactive Source

The desirable properties of the radioactive source used in Mössbauer spectroscopy are follows:

- (i) The source material should be deposited in a host matrix which should be chemically stable.
- (ii) The emitted gamma-ray should provide a single line (in the energy spectrum). In other words there should be no electric field gradient or Zeeman splitting due to internal magnetic field at the site of the ^{57}Fe nuclei in the Mössbauer source.
- (iii) Recoil-free fraction in the source matrix should be large.
- (iv) Line broadening introduced by the effects of self-absorption, thickness etc. should be minimum.
- (v) Radiation not contributing to the Mössbauer effect such as characteristic X-rays, gamma-rays and X-rays arising out of Compton scattering, photoelectric effect etc. should have low intensity. The energy of the 'interfering' radiation should be such that they can be clearly separated from the 'resonant' gamma ray (14.4 keV) in the energy spectrum.

In our experiments we used the radioactive source of ^{57}Co deposited in Rh metal (host matrix) foil. The source was purchased from Amersham International Ltd., Amersham, U.K. and its initial activity was 24 mCi. The recoil-free

fraction of this source as specified by the supplier was 0.76. The characteristic X-rays of Rh have energies in the range 22-23.2 keV (which is quite high compared to 14.4 keV, the energy of the Mössbauer gamma ray) and could be filtered out easily. The source gave a single Mössbauer line observed with our Mössbauer spectrometer using potassium ferrocynide absorber (at room temperature) with a full-width-at-half-maximum (FWHM) of 0.22 mm sec^{-1} . The linewidth observed with sodium nitroprusside as absorber (at room temperature) was 0.22 mm sec^{-1} .

2.3 Mössbauer Spectrometer

The Mössbauer spectrometer used in the present work was designed and developed in this Institute [9] and built by M/s Encardio-Rite, Lucknow, India. This spectrometer could be run in three modes (a) constant velocity (b) constant accelerator and (c) sinusoidal velocity. In our experiments we had run the spectrometer in constant accelerator mode throughout. In the spectrometer a precision velocity drive was realized by generating a signal with highly stable amplitude, frequency and phase and placing the transducer in a feedback loop. The resulting velocity is sensed by a pick-up coil and the pick-up voltage is compared with the reference signal representing the desired velocity. The block diagram of the circuit is shown in Fig. 2.2.

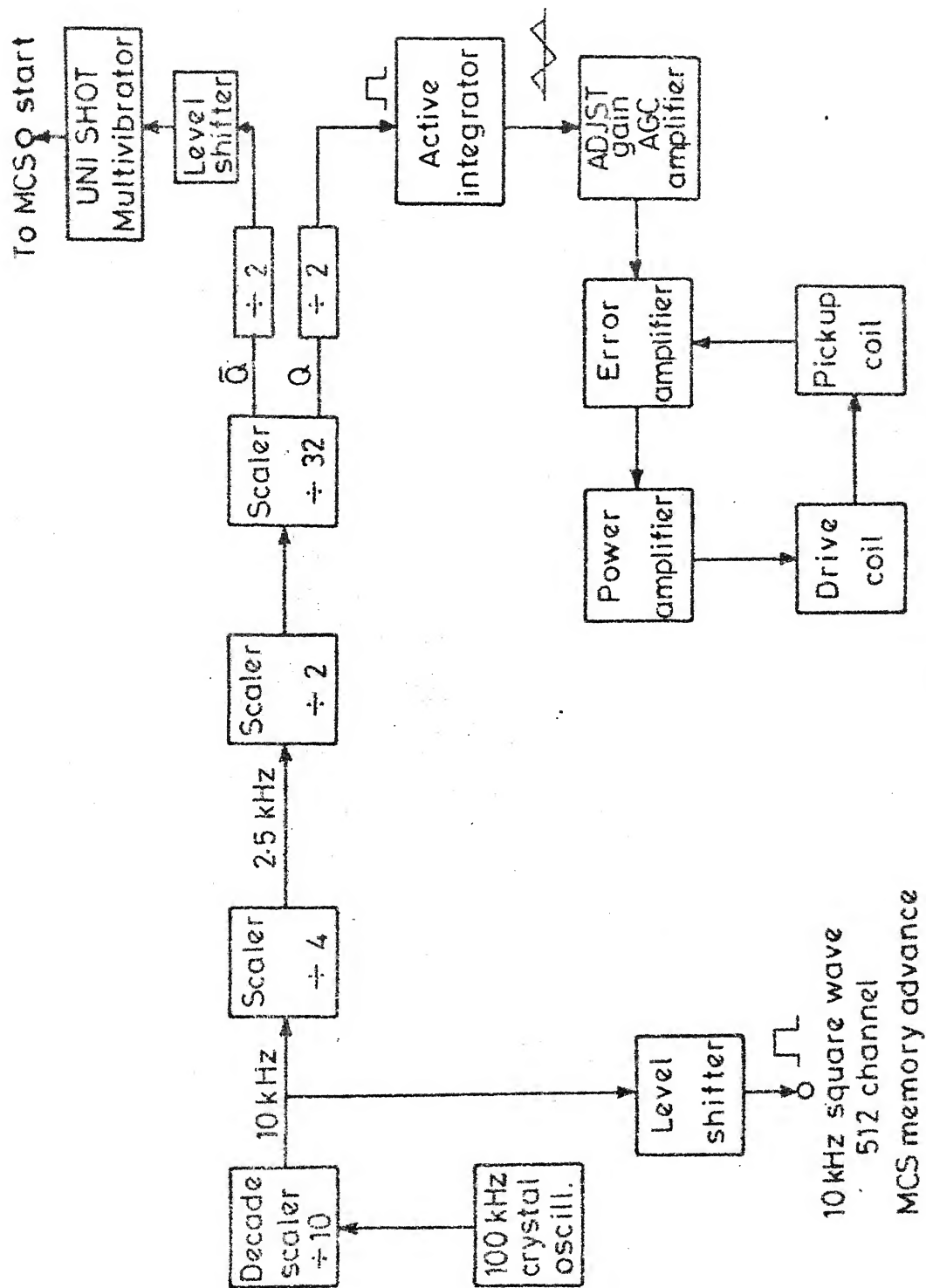


Fig. 2.2 Schematic block diagram of the Keeshaer spectrometer used by us.

The transducer is driven at a frequency of 20 Hz. A crystal oscillator is used as a basic frequency standard to ensure a stable frequency and amplitude of the transducer. This crystal oscillates at a frequency of 100 kHz and its output is scaled down by JK flip-flop to a 20 Hz square wave. The reference signal was a triangular wave generated by integrating a square wave with the help of an active integrator consisting of IC 741.

The transducer consists of a conventional double speaker arrangement having a drive coil and pick-up coil. The velocity is monitored by comparing the pick-up signal with the reference signal in an error amplifier. The difference between the two signals, called the error signal is a measure of the deviation from the designed velocity. Error amplifier output is fed to the power amplifier which drives the transducer (Fig. 2.2). There is a synchronization between the transducer velocity and reference signal in amplitude as well as in phase.

Starting of the multi-channel analyzer (MCA) is effected by a pulse which is obtained by scaling down the complementary output of the penultimate $\div 2$ stage by a factor of 2 which is again applied to monostable multivibrator (IC 74121) through a level shifter to get a narrow pulse of width 10 μ S. This complementary output synchronises the opening of the first channel of the multichannel analyzer (MCA) with the negative maxima of

the velocity reference signal.

The construction of the transducer used is shown in Fig. 2.3. Impedance of both the power amplifier and the transducer are matched to each other. The magnetic field and the number of turns on the coil is chosen in such a way that the conversion of the electrical energy to the mechanical energy is reasonably efficient.

The transducer is designed in such a way that the frequency of the external vibration is far away from the resonance frequency. The drive coil and the pick-up coil are wound in grooves, at the two ends of a common holder, having diameter of 38 mm which is made out of perspex. Each coil has a length of 7.8 mm which is subdivided into three coils of length 2.6 mm each. The three pick-up coils are connected in series and the drive coils are in parallel in the normal operation for impedance matching of the drive coil and to improve the linearity.

2.4 Absorber

2.4.1 Standard absorber for calibration

In our experiment we have used the following standard absorbers for calibrating the Mössbauer spectrometer : (a) natural iron (α -Fe) foil 25 μm thick, (b) enriched iron foil (1.9 mg/cm^2 of ^{57}Fe) and (c) sodium nitroprusside (5 mg/cm^2 of iron). All these absorbers were obtained from the Amersham International Limited, Amersham, U.K.

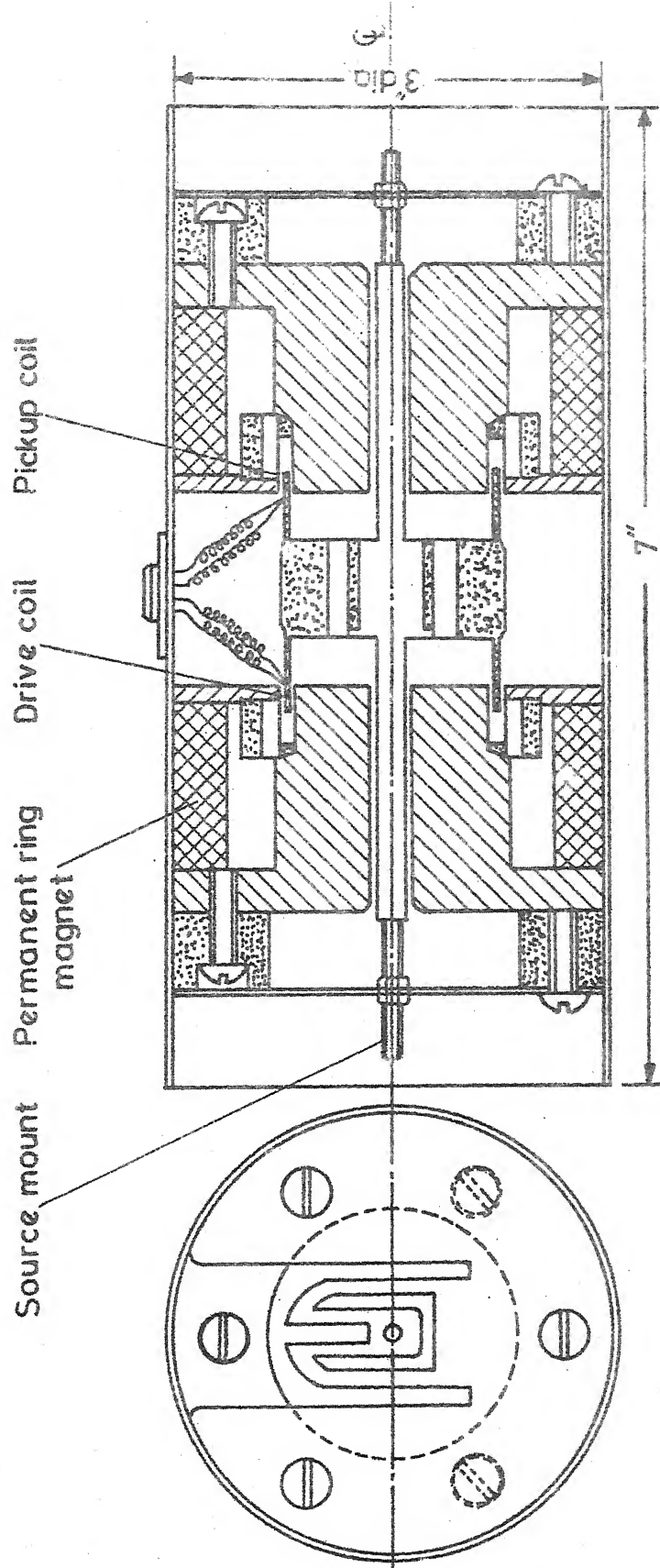


Fig. 2.3 Schematic block diagram of the electromechanical transducer used in the Rutherford spectrometer.

2.4.2 Sample preparation

For each measurement the Mössbauer absorber was prepared according to the nature of the problem to be studied. The method used for preparation of each of the sample absorber is given in the following Chapter at the appropriate place.

2.4.3 Optimization of the absorber thickness

In Mössbauer spectroscopy the recoilless emission and absorption resonance is affected by the thickness of the absorber and source. The Mössbauer line is broadened out due to the thickness of both the absorber and the source. A number of studies made to analyze these effects on the Mössbauer spectrum have been reported [10-13]. The area as well as peak-width is affected. The area of the Lorentzian as well as Gaussian is given by

$$A = \left(\frac{\pi}{2}\right) f_s \Gamma L(t) \quad \text{or} \quad (2.1)$$

$$A = \left(\frac{1}{2}\right) f_s \Gamma [\pi/\Gamma^2]^{1/2} G(t) \quad (2.2)$$

where f_s is recoilless fraction of the gamma ray source and Γ is natural width of the absorption spectrum and $L(t)$ and $G(t)$ is the respective Lorentzian and Gaussian function dependent on t , thickness of the absorber.

The thickness, t , is defined by the relation

$$t = \sigma \eta f_a \quad (2.3)$$

where σ is the resonance cross-section of the absorber nuclei and η is the number of the absorbing nuclei in unit area in the path of the gamma rays and f_a is the recoilless fraction of the gamma ray in the absorber.

The number of transmitted gamma rays at the resonance dip as a function of thickness, t , is given by the equation [14]

$$N(t, v_0) = (1 - f) N + N_f \exp(-t/2) J_0(it/2) \quad (2.4)$$

where t is the thickness of the absorber, N and v_0 are the number of the gamma rays emitted and the Doppler velocity respectively. The intensity (i.e. peak amplitude) of the Mössbauer line is given by

$$N - N(t, v_0) = fN [1 - \exp(t/2) J_0(it/2)] \quad (2.5)$$

where $J_0(x)$ is the zeroth order Bessel function of an imaginary argument.

Equation (2.5) tells that peak intensity (i.e. resonance absorption amplitude) is a function of Doppler velocity v_0 . It also shows that intensity increases with the thickness of the absorber due to the fact that active nuclei in the path is more. But at some thickness above the limit the non-resonant gamma rays will increase the damping and background noise. As a result there is an increase of width and distortion of the Mössbauer spectrum.

On the other hand when the thickness is very small the number of active particles (i.e. which give the absorbing resonance) is very small and the peak intensity is very poor. This means that very thin absorber is also not suitable for good spectrum. The optimum thickness which gives good resonance spectrum will be obtained by a compromise. The amplitude, when non-resonant [13] absorption is considered, is given by

$$N-N(d, \nu_0) = fN[1 - \exp(-\mu_r d/2) J_0(i\mu_r d/2)] \exp(-\mu_a d) \quad (2.6)$$

where μ_a and μ_r are maximum non-resonant and resonant absorption coefficients respectively. The relation between resonant and absorption cross-section is given by

$$\mu_r = (n/d) \sigma f_a \quad (2.7)$$

where d is the actual thickness of the sample and n/d is the density of the active nuclei.

The optimum thickness to get a highest peak for a given N is given by Shimony [15]

$$\mu_r/\mu_a = \frac{\exp(\mu_r d_0/2) - J_0(i\mu_r d_0/2)}{J_0(i\mu_r d_0/2) + J_1(i\mu_r d_0/2)} \quad (2.8)$$

where $J_1(x)$ is the negative of the first derivative of $J_0(x)$ i.e.

$$J_1(x) = - \frac{d J_0(x)}{dx}$$

Another consideration for choosing a thickness is the ratio of the amplitude of peak and the statistical uncertainty in the counts and is defined by α

$$\alpha = \frac{\text{Amplitude of absorption spectrum}}{\text{Statistical uncertainty in the counts}}$$

The counts at velocity which is very high compared to v_0 is given by

$$N(d, \infty) = N \exp(-\mu_a d) \quad (2.9)$$

If the absorption is not too large the statistical uncertainty is given by

$$\Delta N = [N(d, \infty)]^{1/2} \quad (2.10)$$

$$= [N \exp(-\mu_a d)]^{1/2}$$

$$\therefore \alpha(d) = \frac{1}{\sqrt{N}} [1 - \exp(-\mu_r d/2) J_0(i\mu_r d/2)] \exp(-\mu_a d/2) \quad \dots\dots (2.11)$$

Equating the derivative of $\alpha(d)$ (with respect to d) to zero, one can get

$$\frac{\mu_r}{\mu_a} = \frac{\exp(\mu_r d_0/2) - J_0(i\mu_r d_0/2)}{J_0(i\mu_r d_0/2) + J_1(i\mu_r d_0/2)} \quad (2.12)$$

and using this equation d_0 can be calculated if μ_r and μ_a are known.

The above considerations were kept carefully in mind when we designed the thickness of the sample absorber.

2.4.4 Effect of geometry

The shape and width of the peak in the Mössbauer spectrum is affected by the geometry between the source, the absorber and the detector. There are mainly two effects which give rise to distortion in the Mössbauer spectra.

i) The distance between the source and the detector is continuously changed in the acceleration mode. The counting of the gamma rays depend upon this distance. The counting rate of the gamma rays varies as $(1/r)^2$ where r is the distance between source and the detector. This results in the baseline being non-flat.

Considered mathematically the velocity $V(t)$, is given by the expression

$$V(t) = -V_0 + \frac{4V_0}{T} t \quad \text{for } 0 \leq t \leq T/2 \quad (2.13)$$

$$= 3V_0 - \frac{4V_0}{T} t \quad \text{for } T/2 \leq t \leq T \quad (2.14)$$

where V_0 , is the amplitude of velocity and, T , its time period. The distance between source and detector can be obtained by integrating eq. 2.13 and 2.14 and is given by

$$X(t) = -V_0 t + \frac{2V_0}{T} t^2 + X_0 \quad 0 \leq t \leq T/2 \quad (2.15)$$

$$= 3V_0 - \frac{2V_0}{T} t^2 + x_0 \quad T/2 \leq t \leq T \quad (2.16)$$

where X_0 is the distance between source and detector at $t = 0$. The two equations for different time period will

be same for $t = T/2$. This gives

$$x_o = X_o - V_o T \quad (2.17)$$

writing $X(t) = X_o + \Delta X(t)$.

The variable distance $\Delta X(t)$ due to the motion of the source is given by

$$\Delta X(t) = -V_o(t) + \frac{2V_o}{T} t^2 \quad 0 \leq t \leq T/2 \quad (2.18)$$

$$= 2V_o(t) - \frac{2V_o}{T} t^2 \quad T/2 \leq t \leq T \quad (2.19)$$

The count rate without absorber is given by

$$C(t) = \frac{K}{[X_o + \Delta X(t)]^2} \quad (2.20)$$

where K is a constant. At the turning point (i.e. when the velocity of the source is zero) at $t = T/4$ and $3T/4$ the maximum displacement is given by

$$\Delta X(t)_{\max} = \frac{V_o T}{8} \quad (2.21)$$

In our experiment the time period of oscillation, $T = 50$ milliseconds and velocity $V_o \approx 10 \text{ mm sec}^{-1}$

$$X(t) = 0.5 \text{ mm}$$

The count rate $C(t)$ (eq. 2.20) expressed by the help of binomial theorem, is

$$C(t) = \frac{K}{X_o^2} \left[1 - \frac{2\Delta X}{X_o} + \dots \right] \quad (2.22)$$

Since $\frac{\Delta X}{X_0}$ is small for $X \gg 5$ cm.

The first term of the equation (2.22) gives the baseline while the second term gives the first order shift in the baseline which is 0.1 %. The other term is very small and that can be neglected. The shift in the baseline is very small and there is no effect in the spectrum if the absorption is much larger. If the absorption is small, care must be taken by folding [16] the spectrum about the maximum velocity point. This procedure can be followed only if the linearity of the velocity cycle is very good in both halves of the velocity cycle and there is no significant phase shift between the advance pulse of the address scaler and velocity waveform. Otherwise, the folding of the spectrum may result in bad quality and poor resolution.

ii) The second effect due to the geometry of the experiment is the well known cosine effect. Since source, absorber and window of the proportional counter has some finite size, the gamma rays which reach the counter have different angles with respect to the experimental axis. The energy of the gamma rays which enter the counter is given by

$$E'(\theta) = E_0(1 - V \cos\theta/c)$$

where θ is the angle of gamma-rays with respect to the optical axis of the experiment. The angle θ varies from 0 to θ_{\max} and hence it is difficult to consider an

effective velocity. If θ is small the peak width will change and if θ is large the spectrum becomes complicated and distorted.

These considerations were kept in mind while deciding the geometry of the experiment.

2.5 Cryostat and Furnace

2.5.1 Introduction

In Mössbauer spectroscopy one needs to study problems like the phase transitions, variation of the hyperfine parameters with temperature, crystallization of amorphous systems etc. Such studies require a system in which one can change the temperature of the absorber (or source). The temperature range required for such studies usually varies from 0 K to 1400 K.

Two types of such facilities were used by us. One was the cryostat used for the temperature range 80 K (liquid nitrogen) to the room temperature while the other one was an oven for the temperature range room temperature to 800 K.

2.5.2 Cryostat

A cryostat designed for measurements in the range 80 K to 300 K (room temperature) and which used liquid nitrogen was fabricated by us in the laboratory. The design is shown in Fig. 2.4. The two concentric cylindrical brass vessels are connected by thin walled stainless

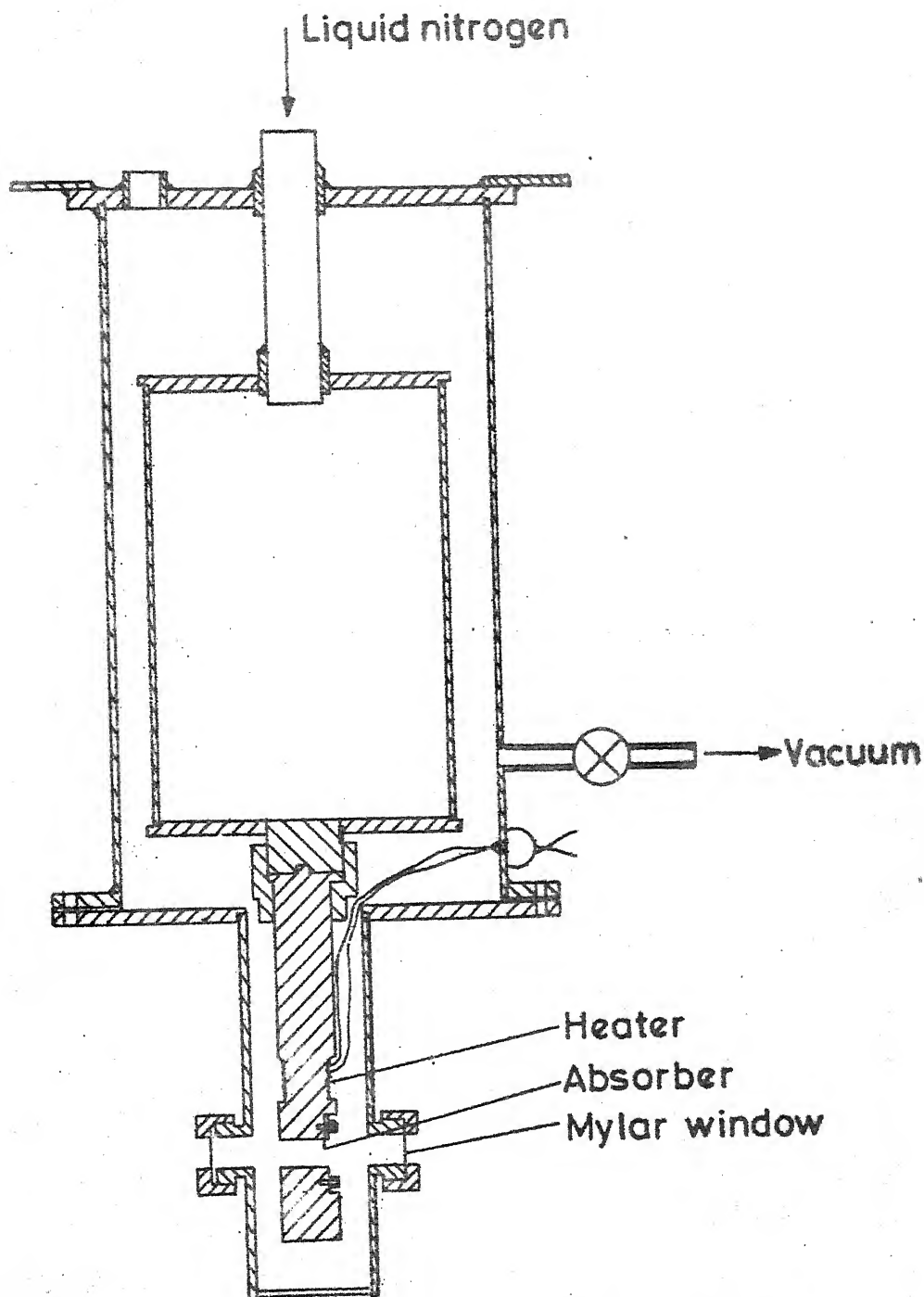


Fig. 2.4 Design of the cryostat used in the Mössbauer experiments carried out in the temperature range 80-300 K.

87522

steel tube. This tube is used for pouring liquid nitrogen in inner vessel. A copper rod of 3 cm dia. is attached to the inner vessel. This rod, called cold finger, can be demounted at any time. The sample i.e. absorber (or source) is passed against the cold finger by flat thick copper square plate. This ensures a better isothermal temperature distribution over the sample. There is space between inner vessel and cold finger for introducing thermal insulation material for stabilizing the temperature of the cold finger at a value higher than 80 K using a heater element. To achieve a thermal insulation the vacuum between the inner vessel and outer vessel can be kept at about 0.03 micron with the help of a diffusion pump and a rotary pump. Flat nichrome wire is wound on the cold finger near the sample with mica sheets as insulator for heating the sample. The temperature of the sample is measured by the help of a copper-constantan-thermocouple. A window made of mylar sheet has been designed for the transmission of the gamma rays.

The sample can be easily changed by opening the bottom flange. A temperature controller for controlling the temperature of the sample was fabricated here. The temperature controller provided an accuracy of the order of 0.4 °C.

2.5.3 Furnace

The Mössbauer study of the sample above room temperature is possible using a furnace having a very good vacuum and variable temperature (upto 1000 K) facility. A furnace has been fabricated in our laboratory by using quartz glass tube as shown in Fig. 2.5. The advantages of this furnace are i) a very good vacuum can be achieved within a short time, ii) The separation between the counter and the source can be kept very small, i.e. the Mössbauer experiment is possible with very weak source also, iii) the handling of the furnace is very easy and iv) power consumption is very small. The furnace consists of quartz tube of 5 cm dia. with length about 8 cm. A stop cock has been connected for evacuating the chamber. One end of the tube is tapered to a diameter of 1.5 cm. This end is sealed with mylar window. The window is shielded from the thermal radiation emitted by the heating coil by the help of thin sheet of beryllium. The other end is in the form of a flange and closed with perspex disc with an O-ring between them. The disc contains a mylar window at the centre for transmitting the gamma rays. The temperature is measured with the help of a thermocouple. Cooling of the furnace is done by a copper tube of 6 mm dia. wound around the outer wall of the furnace. This copper tube can also be used for induction heating.

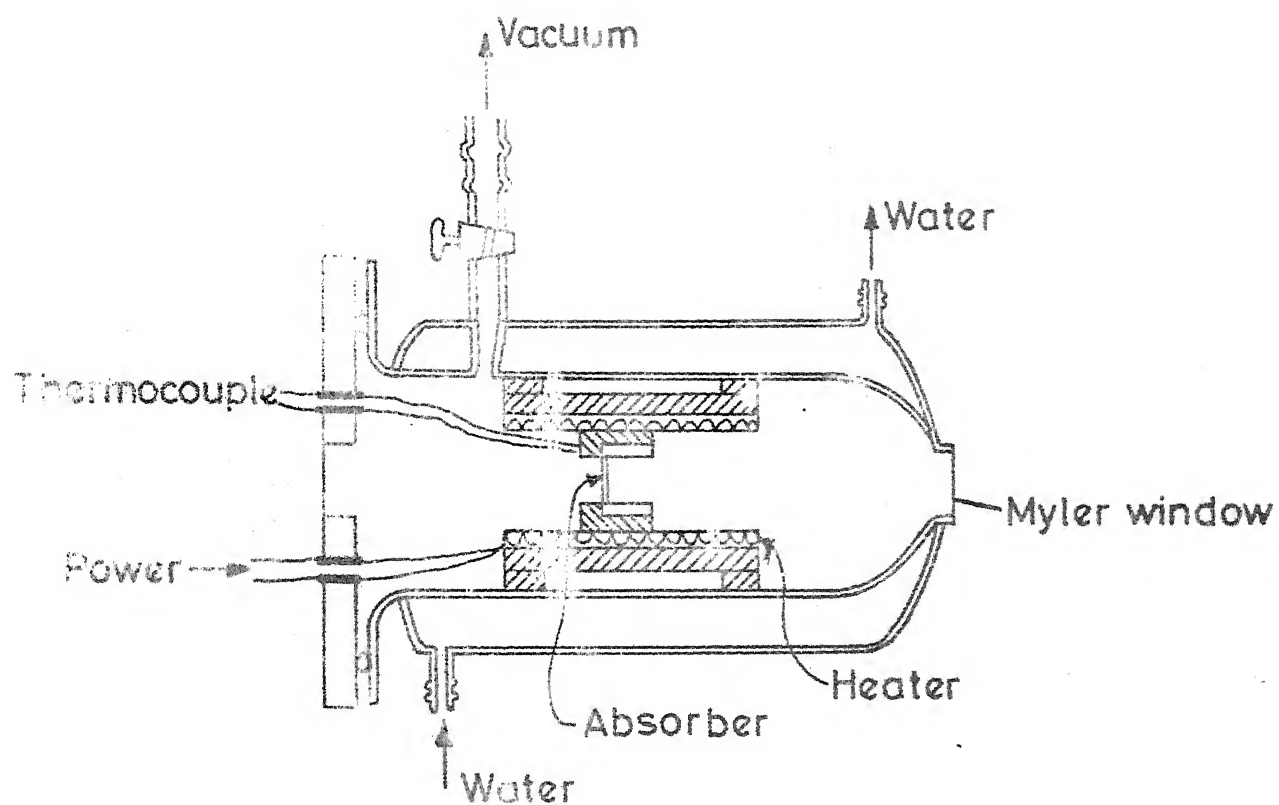


Fig. 2.5 Design of the furnace with resistance heating assembly.

The heating assembly consists of a quartz tube of 3 cm dia. and about 3.5 cm in length. A nichrome wire was wound on it in a way such that there were no induction effects. This wire is fixed by using high temperature cement. Remaining space between quartz tube (furnace) and heating assembly is filled with refractory brick. The sample is put in the heating assembly by the help of copper disc of 2.3 cm dia. and 1.0 cm thickness. The sample between two sheets of mica or aluminium (which is free from iron) is clamped with the help of a groove. The temperature of the sample is controlled by same temperature controller as in the cryostat system.

2.6 Detector and Storage System

The gamma rays after the absorption by sample are detected by an argon gas-filled proportional counter with aluminized mylar window supplied by the Electronic Corporation of India, Hyderabad. During the Mössbauer effect process a large number of X-rays are also produced and energies of these X-rays may be close to the Mössbauer level, thus causing a non-resonance interference. Proper resolution of these X-rays with Mössbauer level is an important feature of the detection system. In our proportional counter this requirement was satisfactorily met since FWHM of the energy resolution was about 2 keV. The proportional counter was run at a high voltage of +1500 V DC using high voltage power supply (Baird Atomic model 318A). It was connected to

preamplifier and a linear amplifier (ECIL Model PA 521). The output of the amplifier is fed to the ND-60 multichannel analyzer.

The ND-60 (microprocessor based 2048 (2K) channel) multichannel analyzer is used in the PHA mode for selecting the Mössbauer gamma ray line, which in the case of ^{57}Fe has an energy of 14.4 keV. The MCS ext mode with a dwell time 100 μsec (for 512 channel operation) and 50 μsec (for 1024 channel operation) was used for recording the Mössbauer spectrum. The efficiency of counting is much higher in the analyzer. The trigger sweep of the MCA is governed by the start pulse from the spectrometer for getting a stable pattern. The data in each subsequent sweep are added continuously to the data stored in preceding sweeps. The data stored in the MCA memory is printed/plotted in a series line printer/X-Y recorder (Hewlett-Packard model 7015A).

2.7 Analysis of Data

The Mössbauer data of the sample is analyzed by the help of a digital computer. The main approximation made in writing computer program for such data analysis is that the relaxation effect is small and the Mössbauer absorption line can be approximated by a Lorentzian curve. A number of computer programs are available for analysis of Mössbauer data. The basic concept is nearly the same in all programs.

The program which we have used is based upon the method developed by Law and Bailey [17,18]. The main purpose of this curve fitting is to find the value of the adjustable parameters (guess values) which provide a close agreement between experimental data and the value predicted by assumed function.

Let the function $\phi_i = \phi_i(B_1, B_2, \dots, B_n)$ be the functional form chosen for the experimental points Y_i . The condition for getting the set of parameter B_k is

$$S^2 = \sum_{i=1}^N S_i^2 = \sum_{i=1}^N (Y_i - \phi_i)^2 \quad (2.23)$$

is minimum. Here N is the number of experimental data points. The condition for minimum of the above equation is

$$\frac{dS^2}{dB_k} = 0$$

With the help of this condition we are able to get n simultaneous equations. By solving these equations one gets a correction in the approximate value ΔB_k . The new parameters $B_k^{i+1} = B_k^i + \Delta B_k$ are then obtained. The superscript i refers to i^{th} iteration.

The new parameters are examined to ensure that S^2 is minimum and this gives better results if the increment of the parameters is restricted i.e.

$$B_k^{i+1} = B_k^i + \alpha \Delta B_k \quad (2.24)$$

where α is less than one. Convergence is assured when successive values differ by an amount less than the pre-assigned tolerances. The goodness of fit is tested by the calculation of the Chi-square.

We are able to calculate the error matrix [19] with the help of the inversion matrix. By the help of the error matrix we are able to calculate the standard error in the fitted parameters B_k .

2.8 Hyperfine Field Distribution

2.8.1 Introduction

The broadening of the Mössbauer line can be explained on the basis of the thickness of the sample and distribution of the hyperfine parameters. As we know that hyperfine parameter in the crystalline sample is unique with a very little variation. However, in glass systems there is a wide variation or distribution of the hyperfine parameters. The hyperfine parameters such as magnetic field, electric field gradient, isomer shift etc. do not possess a unique value but display a distribution. In 1971, B. Window [20] developed a method to calculate the hyperfine field distribution. His assumption is that the field distribution is a Gaussian distribution around the mean value of the hyperfine field. Chien [21] has applied Window's method for determining the hyperfine field distribution in the metallic glass system. Eibschutz et al. [22] interpret the large width of vitreous YIG

(Yttrium Iron Garnet) as the distribution of the electric field gradient at the Fe site.

We also applied Window's method for determining the magnetic field distribution of the metallic glass systems and electric field gradient distribution for the glassy phase of the YIG system. This method is explained below.

2.8.2 Computational method

The basic principle for the two distributions (EFG and hyperfine field) are same. Let the distribution of hyperfine parameter be represented by $p(H)$. The Mössbauer spectrum of ^{57}Fe is defined by

$$Y(E) = \sum_{i=1}^N \int \frac{A_i p(H)}{1+4[(E-E_0)/W]^2} dH \quad (2.25)$$

where A_i is the intensity of the i^{th} peak and E_0 is defined as

$E_0 = V$ principal component of electric field gradient for EFG distribution.

$= a_i H$ Position of the peak for magnetic field distribution.

The value of a_i is given as [21].

$$a_6 = -a_1 = 16.15 \times 10^{-3} \text{ mm/kOe}$$

$$a_5 = -a_2 = 9.34 \times 10^{-3} \text{ mm/kOe}$$

$$a_4 = -a_3 = 2.54 \times 10^{-3} \text{ mm/kOe}$$

and W is the FWHM.

The $p(H)$ is expressed in trigonometric terms

$$p(H) = \sum_{n=1}^N b_n \left[\cos \frac{n\pi H}{H_{\max}} - (-1)^n \right] \quad (2.26)$$

with the condition

$$\left(\frac{d p(H)}{d H} \right)_{H=H_{\min}} = 0 = \left(\frac{d p(H)}{d H} \right)_{H=H_{\max}}$$

The H_{\max} is far away from the real value of H such that $p(H_{\max}) = 0$. The Fourier coefficient b_n is calculated by best fit to the data. If $N \rightarrow \infty$ any $p(H)$ can be represented by eq. (2.26). The coefficient b_n is calculated by solving $N+1$ simultaneous equations. So it is not possible to take N as a very large quantity. More details of this method are explained by Nair [23].

The computer program for these calculations was tested for the standard sample such as natural iron as well as for sodium nitroprusside and the results are shown in Figs. 2.6 and 2.7. These satisfactory results gave us enough confidence to use these programs in our data analysis for the determination of $p(H)$.

2.9 Other Measurements

In order to corroborate the results obtained for various samples with Mössbauer measurements, we have also carried out other measurements using various other methods

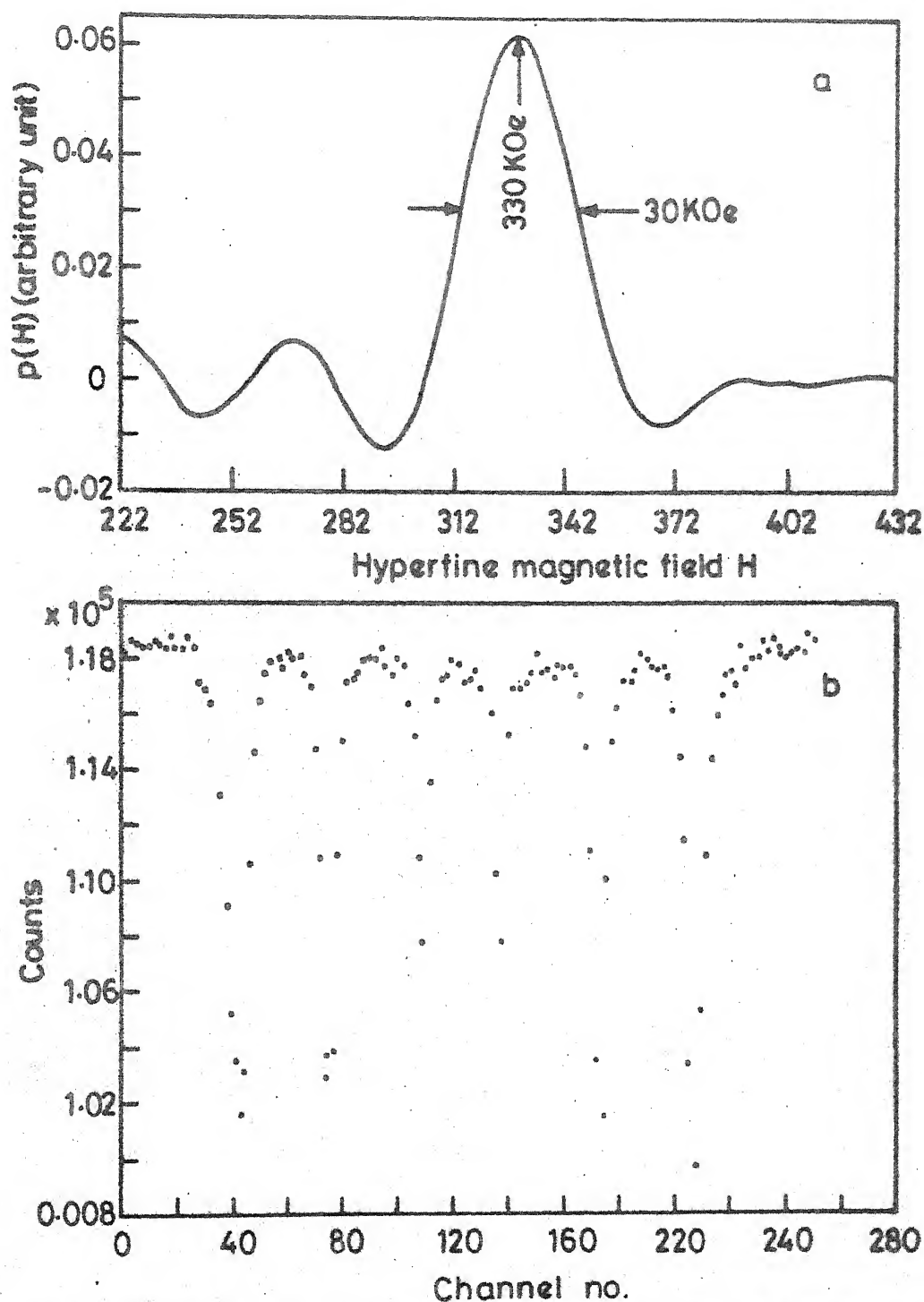


Fig. 2.6 Hyperfine field distribution for α -Fe (absorber) at room temperature. The top figure shows the $p(H)$ distribution while the bottom figure shows the corresponding Mössbauer spectrum of α -Fe.

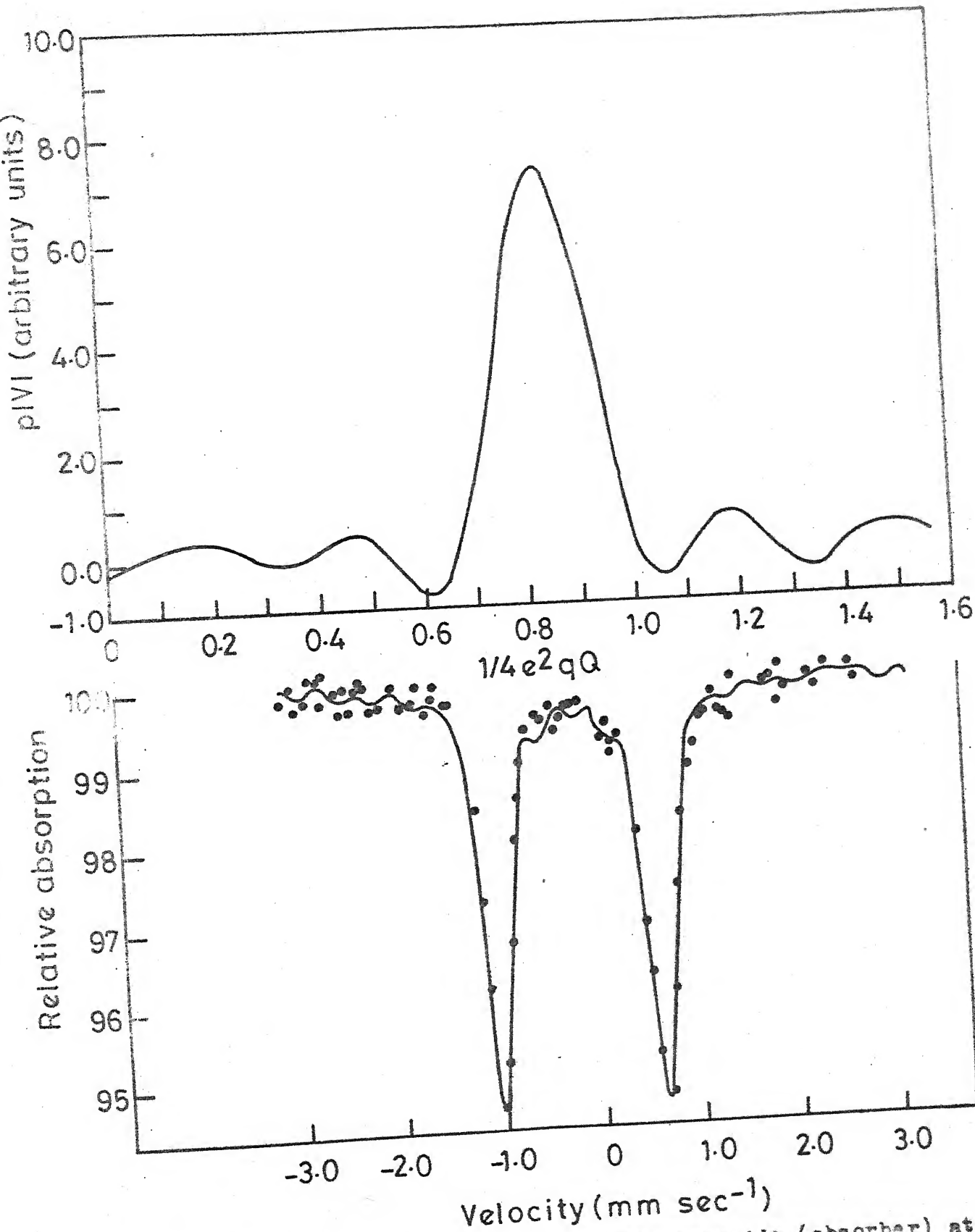


Fig. 2.7 EFG distribution in sodium nitroprusside (absorber) at room temperature. The top figure shows the $(p|V|)$ distribution while the bottom figure shows the fitted Mössbauer spectrum.

like X-ray powder diffraction, optical microscopy, , differential thermal analysis, electron microscopy, electron paramagnetic resonance (EPR) and magnetization measurements.

The X-ray powder diffraction patterns of the samples were recorded by using Rich and Seifert ISO-Debye flex 2002 diffractometer with a Cr K_{α} target. All these studies were performed at room temperature.

After polishing the samples optically and etching the surface, the optical micrographs were taken by a Bauch and Lomb optical microscope.

The differential thermal analysis (DTA) was performed to determine the glass transition temperature and glass crystallization temperature by using MOM Hungary Derivatograph. The transmission electron micrograph of samples were taken on a Phillips EM 301 electron microscope.

The EPR and magnetization measurements were done by using Varian Association Spectrometer (Model V4502-12) in the X-band frequency and with a 100 kHz field modulation and PAR vibrating sample magnetometer (Model 150A) and using a field upto 8 KG respectively. All these measurements were done at room temperature.

REFERENCES

1. N. Benczer-Koller and R.H. Herber in ''Chemical Applications of Mössbauer Spectroscopy'' edited by V.I. Goldanskii and R.H. Herber, Academic Press, New York (1968).
2. U. Gonser in ''Mössbauer Spectroscopy'' edited by U. Gonser, Springer-Verlag, Berlin-Heidelberg, New York (1975).
3. N.N. Greenwood and T.C. Gibb ''Mössbauer Spectroscopy'', Chapman and Hall Ltd., London (1971).
4. G.M. Bancroft ''Mössbauer Spectroscopy, An Introduction for Inorganic Chemists and Geochemists'', McGraw-Hill, London (1973).
5. A. Vertes, L. Korecz and K. Burger ''Mössbauer Spectroscopy'', Elsevier Scientific Publishing Co., Amsterdam (1979).
6. V.G. Bhide ''Mössbauer Effect and its Applications'', Tata McGraw-Hill Publishing Co. Ltd., New Delhi (1973).
7. Mössbauer Effect Methodology, Vol. 1-9 edited by I.J. Gruverman, Plenum Press, New York (1965-74).
8. J.J. Spijkerman in ''An Introduction to Mössbauer Spectroscopy'' edited by L. May, Plenum Press, New York (1971).
9. A.K. Gupta, K.R. Sarma, J.J. Huntzicker and G.N. Rao, Rev. Sci. Instrum. 45, 1423 (1974).

10. S. Margulies and J.R. Ehrman, Nucl. Inst. and Method 12, 131 (1961).
11. D.A. Shirley, M. Kaplan and P. Axel, Phys. Rev. 123, 816 (1961).
12. D.A. O'Connor, Nucl. Inst. and Method 21, 318 (1963).
13. A.J. Stone, Nucl. Inst. and Method 107, 285 (1973).
14. R.M. Housley, N.E. Brickson and J.G. Dash, Nucl. Inst. and Method 27, 29 (1964).
15. U. Shimony, Nucl. Inst. and Method 37, 348 (1965).
16. Takayuki Kobayashi and Kazuko Fukumura, Nucl. Inst. and Method 173, 363 (1980).
17. V.J. Law and R.V. Bailey, Chem. Eng. Sci. 18, 189 (1963).
18. H.C. Verma, Ph.D. Thesis, Indian Institute of Technology, Kanpur India (1980) (unpublished).
19. J.R. Wolberg, 'Prediction Analysis', D. Van Nostrand Company Inc., Princeton (1967).
20. B. Window, J. Physics E4, 401 (1971).
21. C.L. Chien, Phys. Rev. B18, 1003 (1978).
22. M. Eibschutz, M.E. Lines and K. Nassau, Phys. Rev. B21, 3767 (1980).
23. N.V. Nair, Ph.D. Thesis, Indian Institute of Technology, Kanpur, India (1981) (unpublished).

CHAPTER 3

MÖSSBAUER AND OTHER STUDIES OF SOME GLASS-CERAMIC SYSTEMS CONTAINING YIG*

3.1 Introduction

In recent years a new class of materials known as glass-ceramics have evoked considerable interest. Glass ceramics represent polycrystalline solids which are produced by a process involving controlled crystallization of glasses. Such a crystallization is achieved by selecting a suitable glass subjecting it to a carefully regulated schedule of heat-treatment. As a result of this heat-treatment there occurs a nucleation and growth of crystal phases within the glass. The glass ceramics possess outstanding characteristics which render them ideally suitable for fundamental studies as well as for novel technical applications.

Glass-ceramics possess certain special properties which distinguish them from glasses on one hand, and ceramics on the other hand. Whereas glasses are amorphous

*Partial contents of this chapter are published in the following two papers :

(a) Akhilesh Prasad, D. Bahadur, R.M. Singru and D.

Chakravorty, J. Mater. Sci. 17, 2687 (1982).

(b) D. Bahadur, D. Chakravorty, Akhilesh Prasad and R.M.

Singru, J. Magn. and Magn. Materials, 31-34, 1513 (1983).

(or noncrystalline) materials, glass ceramics contain a certain amount of crystals. These crystalline phases in the glass ceramic are entirely produced by crystal growth from a homogeneous glass phase. This process is distinctly different from that in traditional ceramics where most of the crystalline material is introduced at the stage of the preparation of glass-ceramic composition.

In general, the crystal size in the glass-ceramics is considerably smaller than in conventional ceramics made by sintering a pre-shaped powder compact. The glass ceramics as a class are therefore relatively strong materials in general the strength of a polycrystalline ceramic increases as the crystal size is reduced.

The present development of glass-ceramics has been largely brought about by the research and development efforts of private industries (e.g. Corning Glass Works in the U.S.A.) who are interested in the numerous applications of these materials. As a result, published literature on glass-ceramics is rather limited. An excellent monograph by McMillan [1] published in 1979 is still perhaps the best resource book on this subject. The development of the first true glass-ceramic may be attributed to S.D. Stookey [1] of Corning Glass Works (U.S.A.) who selected a photosensitively opacified glass and subjected it to a heat-treatment at a temperature higher than that normally used. He observed that the glass sample did not melt but rather got converted

to an opaque polycrystalline material. This material showed improved mechanical and electrical properties. These changes were attributed to the crystallization in the glass as a result of the small metallic crystals acting as nucleating sites. This development was followed by a search for other types of nucleating catalysts. It was found that titanium dioxide (TiO_2), metallic phosphates (e.g. P_2O_5) and other oxides can be used as nucleating catalysts to promote the controlled crystallization of glasses over a wide range of glass-compositions.

Production of a glass-ceramic sample involves the following stages. In the first stage the particular glass is prepared and then shaped in its molten or plastic state to produce the sample of the desired form. The glass-sample is next taken through a controlled heat-treatment cycle which gives rise to nucleation and crystallization of various phases and results in the required glass-ceramic sample. This process of manufacturing glass-ceramics has two important features. Firstly it is applicable to a wide range of composition and secondly the heat-treatment schedule can be varied in different ways. These features allow one to develop various crystal types in a controlled manner and one can thus control the physical characteristics of the glass-ceramic produced. It is therefore important to study various physical properties of glass-ceramics so produced.

Study of glass ceramics bears scientific importance as well as technological importance. The fundamental or scientific interest in these studies arises from the following :

(i) Study of glass-ceramics provides valuable understanding of the process of nucleation and crystallization of super-cooled liquid. (ii) Such studies provide information about amorphous phase separation. (iii) The wide range of compositions available in a glass-ceramic allows one to study phase changes in widely different chemical environment. (iv) Glass-ceramic systems provide interesting problems in material science and stimulate further interest in the science of glasses and ceramics themselves. (v) Finally the study of glass ceramics is of interest to the mineralogist also because of the possibility of getting materials containing unusual combination of known crystals. More details about this will be found elsewhere [1,2].

The technological interest in the study of glass-ceramics arises from the many interesting applications of these materials. Various actual and potential applications [1] of glass-ceramics are listed below :

- i) General and mechanical engineering applications as in the bearings, pumps valves and pipes, heat exchangers, furnace construction etc.
- ii) Applications in electrical engineering and electronics include glass-ceramic to metal seals, insulators and bushings, high temperature electrical insulation,

performed circuitry for electronics applications, substrates for microelectronics, capacitors, sealing and bonding media, electro-optical materials.

- iii) Lighting and optical applications such as lamp envelopes, components for lasers, telescope mirrors etc.
- iv) Applications in aerospace engineering such as radomes, infrared transparencies etc.
- v) Applications in nuclear engineering such as reactor control rod materials, seals for reactor use, disposal of radioactive wastes etc.

It is thus seen that the study of the physical properties of glass-ceramics is very important. Such studies can be carried out using different methods like X-ray diffraction, differential thermal analysis (DTA), electron paramagnetic resonance (EPR), transmission electron and optical micrographs, magnetization, Mössbauer spectroscopic studies etc. In particular the method of Mössbauer spectroscopy is ideally suited to provide important information about the magnetic phases (e.g. yttrium iron garnet or the YIG phase) involved. In the following sections we have described the results of our Mössbauer spectroscopic studies of the glass-ceramics (i) $\text{Na}_2\text{O}-\text{SiO}_2-\text{Fe}_2\text{O}_3-\text{Y}_2\text{O}_3$ and (ii) $\text{PbO}-\text{B}_2\text{O}_3-\text{Al}_2\text{O}_3-\text{Fe}_2\text{O}_3-\text{Y}_2\text{O}_3$ heat-treated under different schedules and also containing different compositions/nucleating catalysts. To corroborate the results obtained by Mössbauer

spectroscopy we have also studied these glass-ceramics using different other methods like X-rays, EPR, DTA etc.

3.2 Study of $\text{Na}_2\text{O-SiO}_2\text{-Fe}_2\text{O}_3\text{-Y}_2\text{O}_3$ Glass System

3.2.1 Introduction

In recent years there has been considerable interest in development of glass-ceramics containing magnetic phases, as for example, lithium ferrite, barium hexa-ferrite, nickel ferrite and manganese ferrite etc. Glasses containing these ferrites have been produced and their properties have been studied by other authors [3-7]. It is well known that yttrium iron garnet (YIG) and substituted YIG have been widely used in various microwave and memory devices [8]. It should therefore be interesting to develop glass ceramics with YIG as the crystalline phase and to study its physical properties.

In this Institute glass ceramic containing YIG had been developed by Bahadur et al. [9] in the glass composition $\text{Na}_2\text{O-SiO}_2\text{-Fe}_2\text{O}_3\text{-Y}_2\text{O}_3$. This sample will be referred to as Y6 sample (Sec. 3.3). In this glass ceramic YIG can be precipitated by suitable heat treatment. We present here our Mössbauer, EPR and magnetization experiments carried out on such as-quenched (or as-prepared) sample as well as samples heat-treated for 4 h at 400, 500, 600, 650, 700, 750, 810 and 850 °C. The Mössbauer data have been compared

with EPR and magnetization data.

3.2.2 Experimental method

(a) Sample preparation

The composition of the glass used in the present studies was as follows : Na_2O (34 mol %), SiO_2 (50 mol %), Fe_2O_3 (10 mol %) and Y_2O_3 (6 mol %). The glass was prepared from reagent grade chemicals by melting the mixture of chemicals in an alumina crucible at 1350°C in an electrically heated furnace. Glass plates were cast by pouring the melt into an aluminium mould. Wherever necessary, powdered samples were formed from these glass plates. The samples were heat-treated at various temperatures for a time-period mentioned in the following sections. The heated samples were allowed to cool down slowly to room temperature before studying them by various techniques.

(b) Mössbauer measurements

The constant acceleration Mössbauer spectrometer used in the present studies has already been described in Chapter 2. All the Mössbauer spectra presented here were recorded at room temperatures unless mentioned otherwise. The source used in these measurements was a 10 mCi ^{57}Co in Rh matrix obtained from New England Nuclear Inc. U.S.A. The spectrometer was calibrated by using enriched ^{57}Fe absorber and sodium nitroprusside. For Mössbauer spectroscopic studies,

the glass samples were powdered and approximately 50 mg of the powder was sandwiched uniformly on about 1 cm diameter circular area between two layers of sellotape. Observed Mössbauer spectra were analyzed to obtain the Mössbauer parameters by using a least-squares curve-fitting computer program as discussed in Chapter 2.

(c) Other measurements

The EPR measurements were carried out at room temperature with the help of a Varian Associates Spectrometer (Model V 4502-12) in the X-band frequency using a 100 kHz field modulation.

Magnetization measurements of the glass samples were made with the help of a PAR vibrating sample magnetometer (Model 150 A) at room temperature using magnetic fields upto 8 KG.

X-ray powder diffraction patterns for the precipitated glass-ceramic samples were recorded using a Rich and Seifert ISO-Debyeflex-2002 diffractometer with a CrK_α target. As reported by Bahadur et al. [9] the X-ray data for samples heat-treated at 650 and 750 °C indicated (Table 3.1) that the YIG phase had been precipitated in the glass systems studied by us.

In order to estimate the glass transition temperature (T_g) and crystallization temperature (T_c), differential thermal analysis (DTA) of the samples was carried out [9]

TABLE 3.1

X-ray diffraction data for heat-treated samples (a)

Sample heated at 650 °C			Sample heated at 750 °C			YIG [±]	
d (nm)	Intensity ⁺	hkl	d (nm)	Intensity ⁺	hkl	Intensity ⁺	hkl
0.3042	W	400	0.3040	W	400	S	400
			0.2916	VW	330		
0.2772	VS	420	0.2769	VS	420	VS	420
0.2706	VS		0.2706	S			
0.2625	M	332	0.2612	W	322		
0.2517	W	422	0.2515	W	422	S	422
			0.2366	VW			
0.1941	W	620	0.1938	M	620	W	521
0.1774	VW	444	0.1777	VW	440	W	611
						M	444
0.1648	VW	642	0.1642	VW	642	S	640
0.1608	VW		0.1609	VW		S	642
0.1575	W	651	0.1539	W	800	W	800
0.1452	W	653	0.1451	VW	653	W	840
0.1352	VW	842	0.1354	VW	842	W	842

Continued.... 74

TABLE 3.1 (Continued)

(a) Taken from D. Bahadur et al. [9].

*Data obtained from a polycrystalline YIG sample.

⁺VS = very strong; S = strong; M = medium; W = weak ;

VW = very weak.

using a MOM Hungary Derivatograph. An amount of sample weighing 1.6 gm was taken and heated upto 1000 °C at a rate of 10 °C/min. The DTA data are shown in Fig. 3.1. The exothermic and endothermic peaks correspond to the crystallization (T_c) and glass transition (T_g) temperature which are estimated as 750 °C and 650 °C respectively.

A Phillips transmission electron microscope (Model EM 301) was used to record transmission electron micrographs of samples heat-treated at different temperatures.

3.2.3 Results and discussion

Mössbauer spectra observed by us at room temperature (RT) for the as-prepared samples and samples heat-treated for 4 h at temperatures $T = 400, 500, 600, 650, 700$ and 750 °C are shown in Fig. 3.2. All these seven Mössbauer spectra exhibit quadrupole splitting only. In Fig. 3.3 we have shown the Mössbauer spectra observed at RT for the samples heat-treated at (i) $T = 700$ °C for 40 h, (ii) $T = 810$ °C for 4 h, (iii) $T = 850$ °C for 4 h and (iv) $T = 600$ °C for 4 h followed by heat treatment at $T = 750$ °C for 4 h. These four Mössbauer spectra show magnetic hyperfine splitting as well as electric quadrupole splitting. The values of the isomer shift (with respect to sodium nitroprusside) and the quadrupole splitting obtained from the spectra of Fig. 3.2 are listed in Table 3.2. Two sets of values (marked as b and c in Table 3.2) for the quadrupole

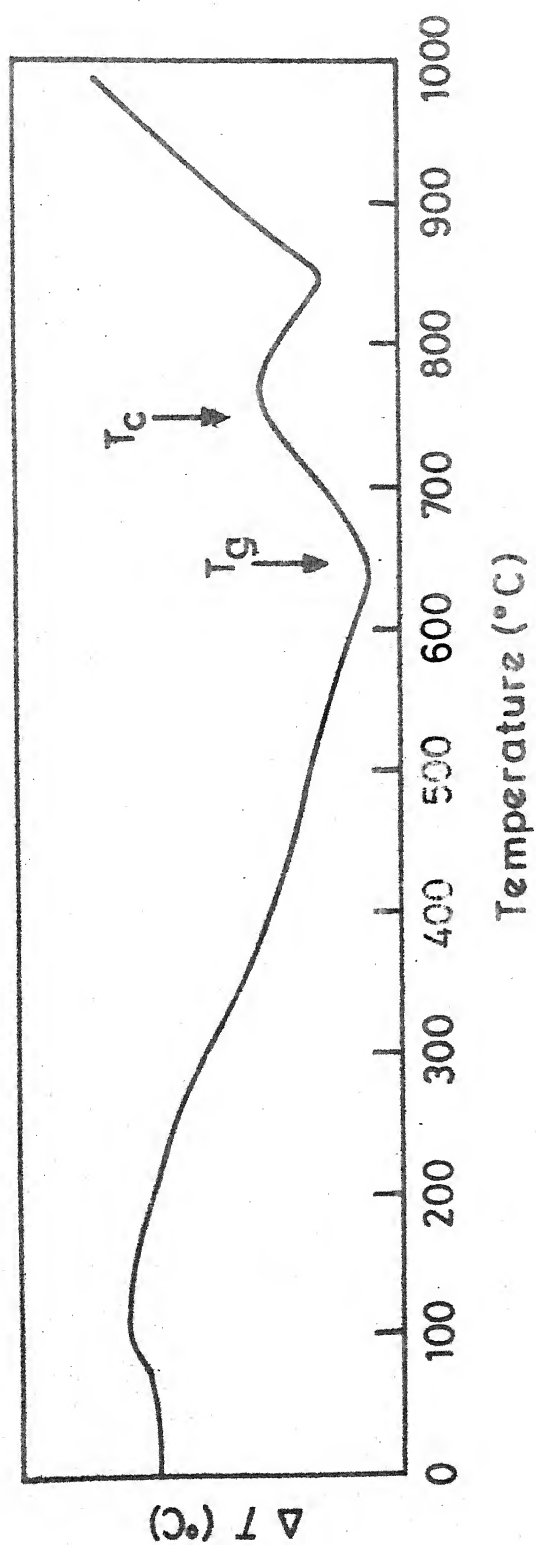


Fig. 3.1 DTA plot of the as-prepared $\text{Na}_2\text{O-SiO}_2\text{-Fe}_2\text{O}_3\text{-Y}_2\text{O}_3$ glass sample (hereinafter called as the Y6 sample).

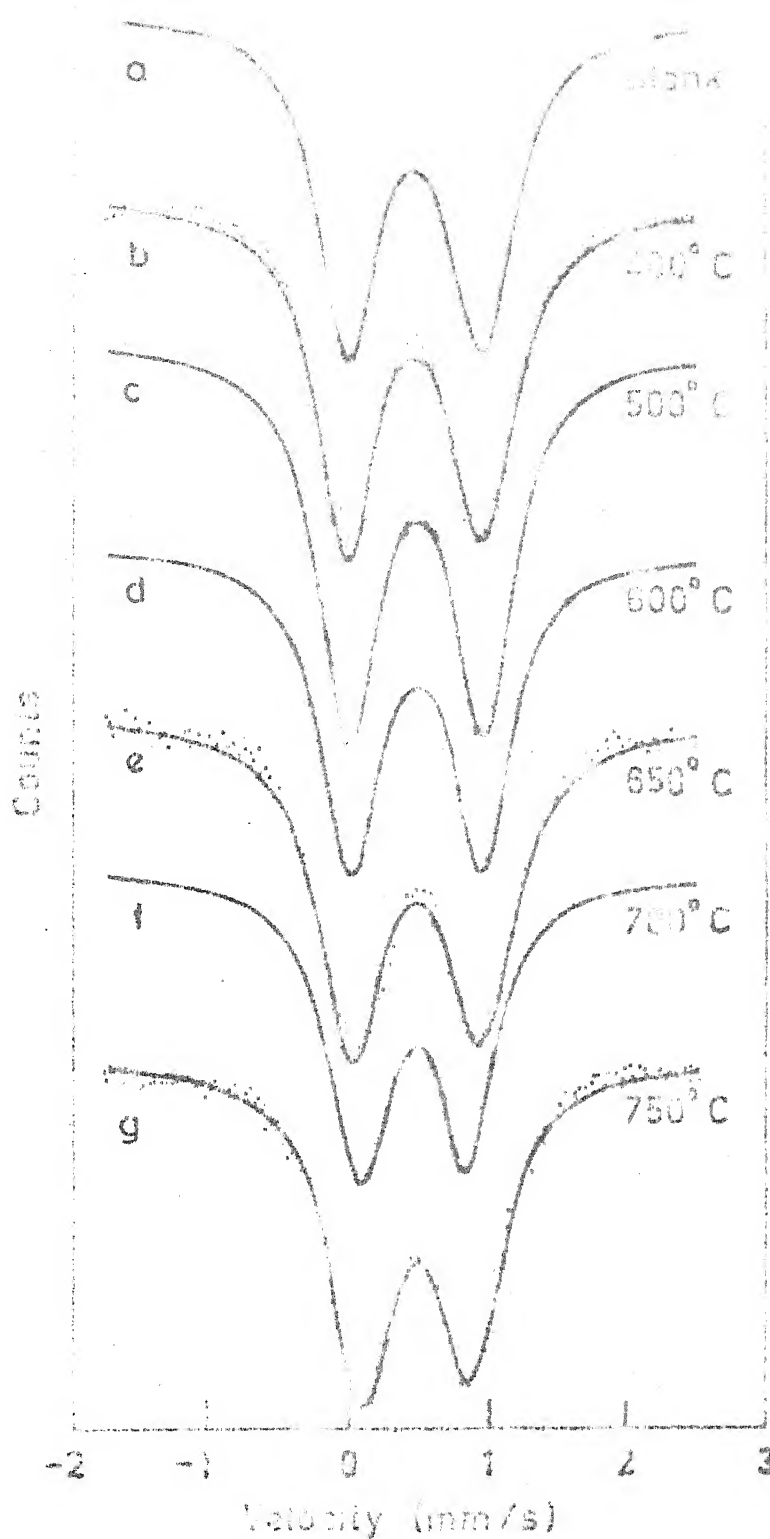


Fig. 3.2 Room-temperature Mössbauer spectra of glass sample Y6 heat-treated at different temperatures. The zero of the velocity scale refers to the centroid of the doublet spectrum from sodium nitroprusside absorber.

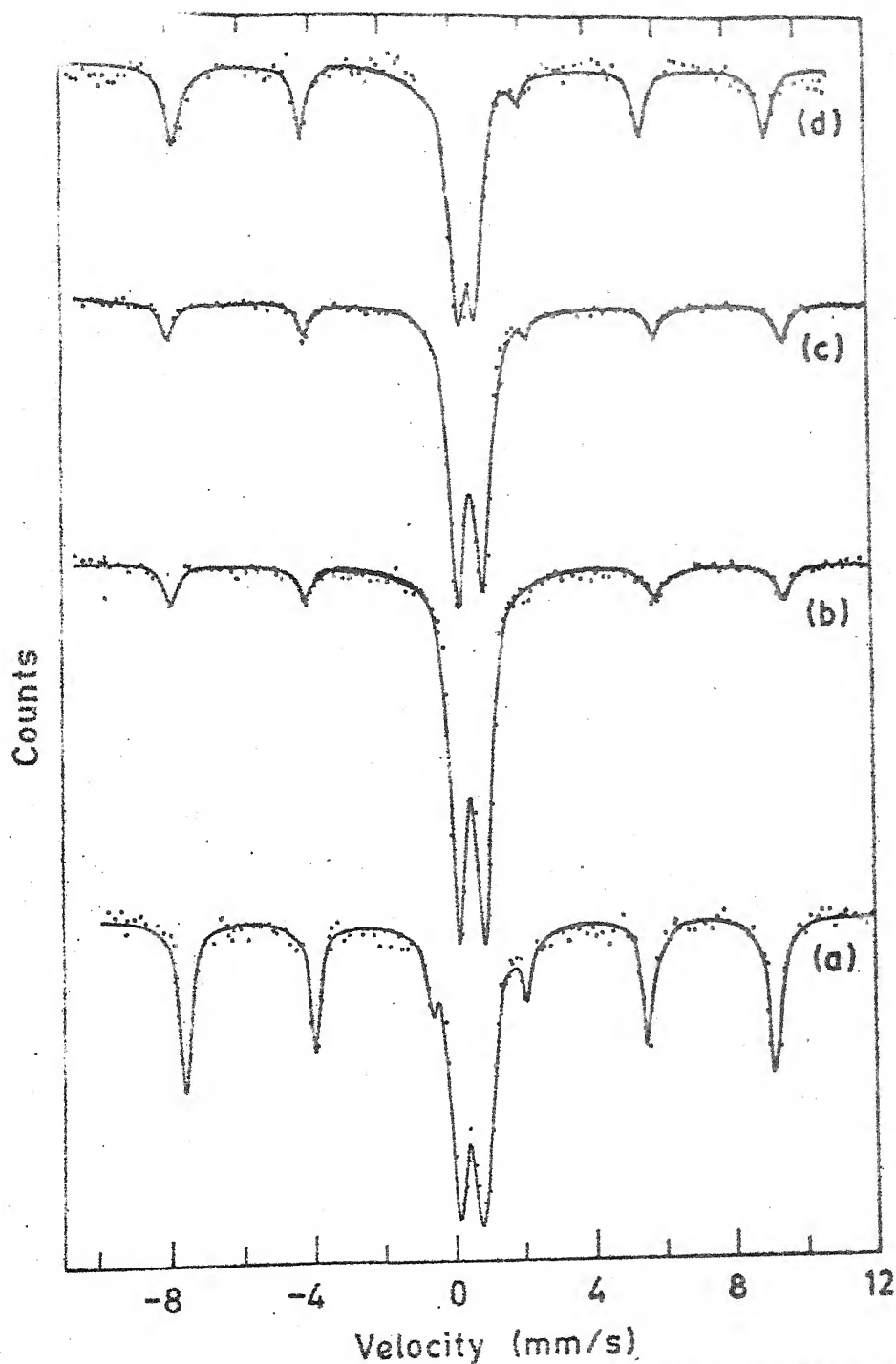


Fig. 3.3 Room-temperature Mössbauer spectra of Y6 samples heat-treated at (a) 700°C for 40 h, (b) 810°C for 4 h, (c) 850°C for 4 h and (d) 600 and 750°C for 4 h each. The zero of the velocity scale refers to the Fig. 3.2.

TABLE 3.2

Mössbauer parameters for sample Y6 showing quadrupole splitting only.

Heat-treatment Temperature °C for 4 h	Isomer Shift (IS) (a) (mm sec ⁻¹)	Isomer Shift (IS) w.r.t. α -Fe (mm sec ⁻¹)	Quadrupole Splitting Δ_E		FWHM (c) of the p(V) distribution (mm sec ⁻¹)
			(b) (mm sec ⁻¹)	(c) (mm sec ⁻¹)	
As-prepared	0.437 \pm 0.007	0.173 \pm 0.007	0.921 \pm 0.007	0.885 \pm 0.012	0.38
400	0.434 \pm 0.006	0.170 \pm 0.006	0.924 \pm 0.008	-	-
500	0.444 \pm 0.007	0.180 \pm 0.007	0.919 \pm 0.007	0.928 \pm 0.012	0.40
600	0.449 \pm 0.004	0.185 \pm 0.004	0.920 \pm 0.004	0.892 \pm 0.012	0.40
650	0.430 \pm 0.006	0.166 \pm 0.006	0.836 \pm 0.006	0.786 \pm 0.015	0.40
700	0.431 \pm 0.007	0.167 \pm 0.007	0.791 \pm 0.007	i) 0.634 \pm 0.015 ii) 1.177 \pm 0.015	0.38 0.38
750	0.470 \pm 0.006	0.206 \pm 0.006	0.713 \pm 0.006	i) 0.576 \pm 0.012 ii) 1.104 \pm 0.012	0.40 0.40

(a) Values with respect to sodium nitroprusside.

(b) Values obtained from a pure Lorentzian least square fit to observed Mössbauer spectra.

(c) Values obtained from a fit of EFG distribution to observed Mössbauer spectra (see text for details).

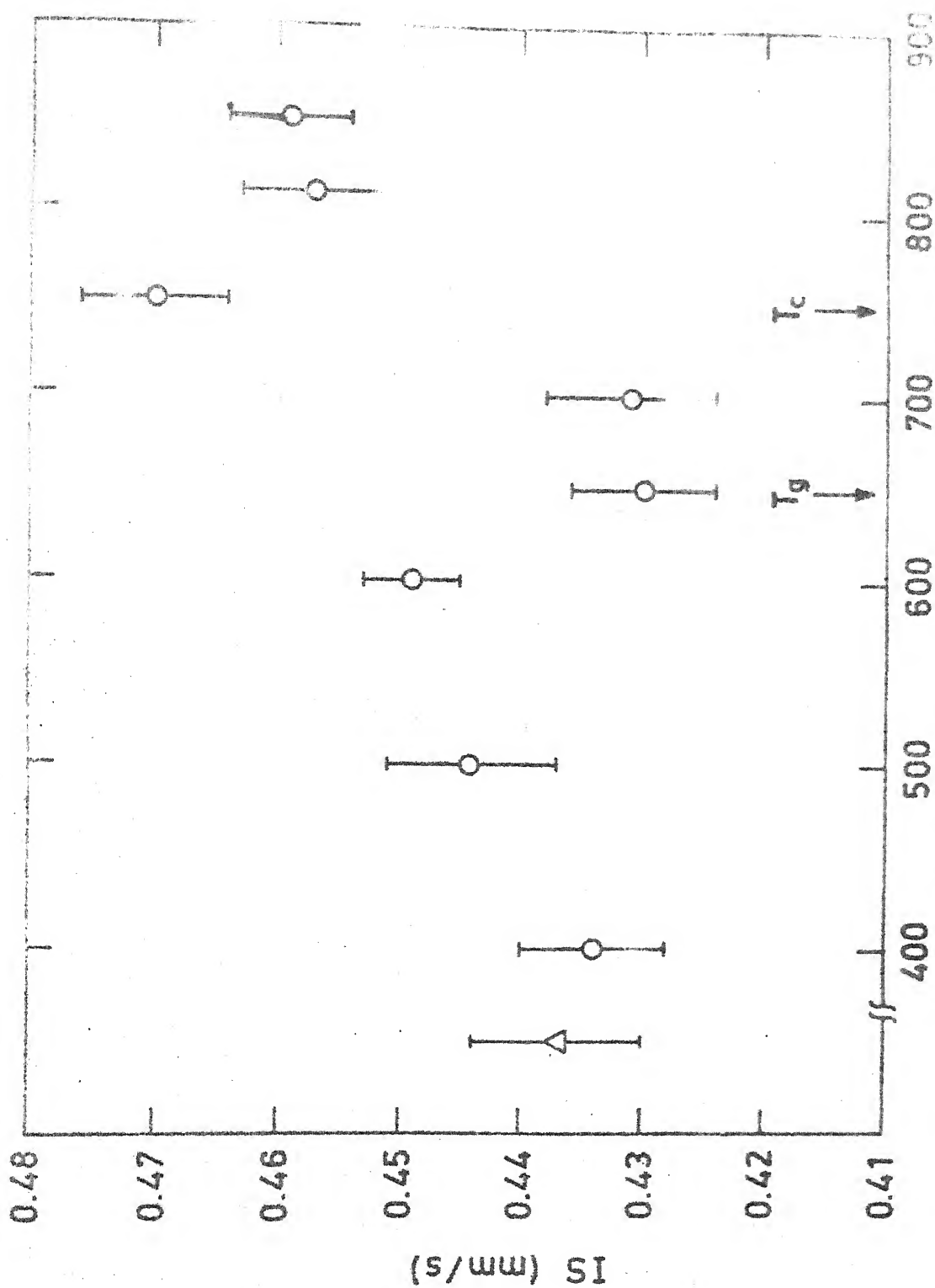
splitting were obtained by us. In the first method, the quadrupole splitting, E , was determined in the conventional way by obtaining a pure Lorentzian least square fit to the observed Mössbauer spectra and using the values of the two peak positions. In the second approach, we applied Window's method [11] for obtaining a fit of the EFG distribution $p(V)$ to the observed spectra. This procedure has been described in section 2.8. In Table 3.3 we have shown the values of the Mössbauer parameters for the spectra of Fig. 3.3.

We shall now discuss our results for the values of isomer shift (IS) observed by us. To facilitate such a discussion we have plotted the IS values against the heat-treatment temperature in Fig. 3.4, where the glass-transition temperature (T_g) and the crystallization temperature (T_c) for the present glass sample (determined earlier, see Fig. 3.1) are also shown. The value of IS for all these samples is characteristic of Fe^{3+} ion [12,13]. It is observed that the value of IS does not change significantly upto the heat-treatment temperature of $600^\circ C$. The IS value, however, shows sharp changes near T_g ($650^\circ C$) and T_c ($750^\circ C$). The sharp decrease of the IS for the sample heated at $650^\circ C$ could be attributed to incipient phase separation occurring at T_g prior to nucleation of the crystalline phase. It is possible that such a phase separation can lead to Fe^{3+} ions being situated in distorted tetrahedra resulting in a

TABLE 3.2

Mössbauer parameters for the samples showing magnetic hyperfine splitting as well as quadrupole splitting.

Heat-treatment Temperature	Period of Heat-treat- ment	Magnetic hyperfine splitting			Quadrupole splitting			Ratio areas der th magnet hyperf and qu upole peaks
		IS wrt SNP (mm sec ⁻¹)	IS wrt α-Fe (mm sec ⁻¹)	H _{int} (kOe)	IS wrt SNP (mm sec ⁻¹)	IS wrt α-Fe ΔE (mm sec ⁻¹)		
(°C)	(h)							
700	40	0.67±0.03	0.41±0.03	496±3	0.443±0.017	0.179±0.017	0.660± 0.017	0.
810	4	0.71±0.05	0.45±0.05	527±9	0.457±0.006	0.193±0.006	0.687± 0.006	0.5
850	4	0.65±0.03	0.39±0.03	526±5	0.459±0.006	0.195±0.006	0.699± 0.005	0.2
Two Stage								
i) 600	4	0.59±0.04	0.33±0.04	494±4	0.460±0.022	0.196±0.022	0.519± 0.022	0.5
ii) 750	4							



Heat-treatment temperature (°C)

Fig. 3.4 Plot of the isomer shift (IS) determined for the spectra showing quadrupole splitting against heat-treatment temperature. The IS values are given with respect to sodium nitroprusside absorbers. Point marked Δ refers to the as-prepared sample.

decrease in the IS value at T_g . The IS value shows a sharp rise as heat-treatment temperature is raised to 750°C (T_c) and it remains high for samples heated at 810°C and 850°C respectively (The IS values for the latter samples were obtained from quadrupole splitting). The observed increase in IS at T_c and beyond could probably be ascribed to generation of some octahedral Fe^{3+} ions which should be present in the garnet phase [8,12]. The sharp changes in IS observed at T_g and T_c also suggest that the nature of $\text{Fe}^{3+} - \text{O}^{2-}$ bond changes at these temperatures [4]. The density of 4s electrons at the tetrahedral site is greater than that at the octahedral sites in various solids. The Fe-O distance for the tetrahedral site is about 5 % smaller than that of the octahedral site. Van Loef [14] has suggested that this difference gives rise to different charge density which could explain the difference in the IS value at the tetrahedral and octahedral sites of iron in ferrites and garnets.

The value of IS observed in the case of as-prepared (blank) glass sample was $0.437 \pm 0.007 \text{ mm sec}^{-1}$. This result indicates that Fe^{3+} ions are mostly in tetrahedral coordination with a small fraction possibly being in octahedral co-ordination. A surprising observation is that only quadrupole splitting appears in the spectra for samples heated upto 750°C (4 h). The Mössbauer spectra for the samples in Fig. 3.2 were also measured at liquid nitrogen (80 K) temperatures (LNT) and these spectra are shown in

Fig. 3.5. It is seen that no magnetic hyperfine splitting is observed for these samples even at LNT. The samples heat-treated at 810 °C and 850 °C show a magnetic hyperfine splitting (in addition to the quadrupole splitting) characterized by IS values of 0.71 ± 0.05 and 0.65 ± 0.03 mm sec⁻¹ respectively (Table 3.3). From the absence of the magnetic hyperfine splitting for the samples heat-treated for 4 h at 650, 700 and 750 °C, we infer that the volume fraction of the crystallized YIG phase (which is magnetic) is very small in them. The corresponding hyperfine field probably gets smeared out because the volume fraction of the YIG phase is small. As a result, the corresponding Mössbauer spectra show only quadrupole splitting.

The Mössbauer spectra in Fig. 3.3 comprise of magnetic hyperfine splitting as well as quadrupole splitting. Values of the corresponding Mössbauer parameters are given in Table 3.3. It is seen that the values of the IS determined for the hyperfine splitting are intermediate between those for octahedral and tetrahedral iron. On the other hand the IS value for the doublet structure (quadrupole splitting) indicates the presence of tetrahedral iron predominantly. It is possible that some other phase (such as α -Fe₂O₃) is also precipitated [15,16]. This possibility is also indicated by the X-ray data [9]. Another possibility is that the precipitated YIG phase consists of distorted octahedral

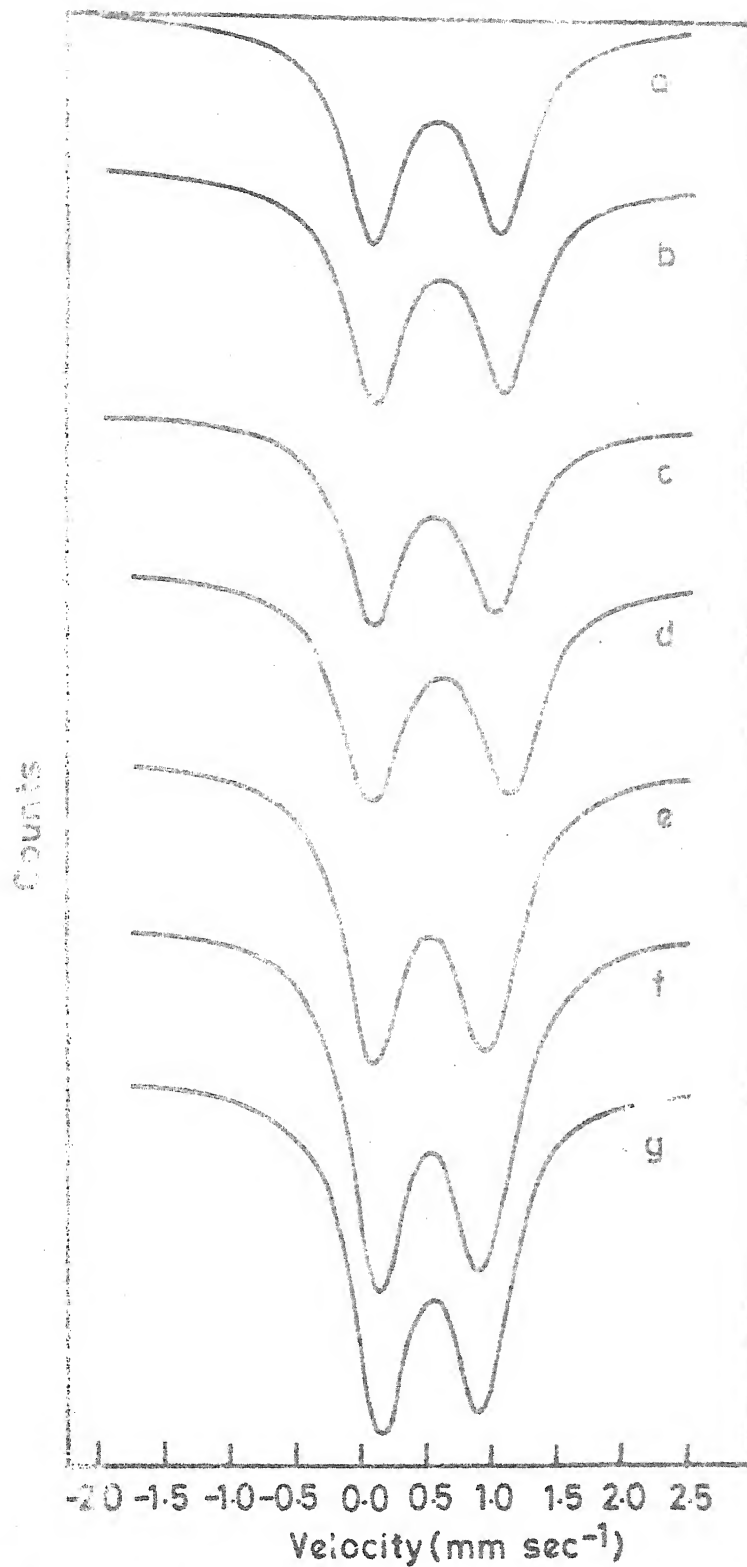


Fig. 3.5 The Mössbauer spectra measured at liquid nitrogen temperature (LNT) 80 K, for samples described in Fig. 3.2. The labels a, b, c.... etc. of the samples correspond to those shown in Fig. 3.2.

and tetrahedral giving rise to the observed behaviour (Table 3.2).

Comparing the Mössbauer spectra of samples heat-treated at 700 °C for 4 h and 40 h respectively, it is observed that the former show only quadrupole splitting whereas the latter show quadrupole as well as magnetic hyperfine splitting. In the case of the sample heat-treated at 700 °C for 40 h, the Mössbauer spectrum was also taken at LNT. These measurements showed that the hyperfine field (H_{int}) observed at LNT is greater than that observed at RT. Further, the ratio of the peak-area for the hyperfine splitting to that for quadrupole splitting changes from LNT to RT for the sample heated at 700 °C. As seen from Table 3.3, this ratio increases as the heat-treatment temperature or the treatment time (at a given temperature) increases. The magnetization data do not show any saturation behaviour upto a field of 8 KG. All these observations suggest a superparamagnetic behaviour. A systematic investigation of these aspects for the present glass system would provide more interesting information.

The value of the quadrupole splitting (ΔE) for the as-prepared glass sample as determined from pure Lorentzian least square fit was 0.912 ± 0.007 mm sec⁻¹. The electron distribution is spherically symmetric in the case of high spin Fe³⁺ ion ($3d^5$, $6s_{5/2}$) and this should

result in an absence of quadrupole splitting. In other words, no quadrupole splitting should be observed, if the normal tetrahedral or octahedral co-ordination is undistorted. It has been suggested by Kurkjian and Sigety [17] that in glasses there is a large number of non-identical sites with a substantial departure from cubic symmetry as compared to the situation existing in crystals. We feel that this explains the large quadrupole splitting observed in the present glass system. A plot of the quadrupole splitting (ΔE), determined from the Lorentzian least square fit, is shown in Fig. 3.6 against the heat-treatment temperature. It is seen that the ΔE value remains essentially constant upto 600 °C after which it decreases. It attains a constant value beyond 750 °C. These results suggest that there is no change in the symmetry upto 600 °C. At T_g (650 °C) and above, however, the ion sites acquire higher symmetry as a result of the nucleation and growth of the crystalline phase. This explains why the ΔE value decreases and finally attains a constant value (Fig. 3.6).

An examination of the values of ΔE determined from a fit of EFG distribution (Fig. 3.7) to the observed Mössbauer spectra (Table 3.2) shows that they differ from the ΔE values obtained from the Lorentzian least square fit. This behaviour is common and has been observed earlier [18]. However the trend of the former set of values (as

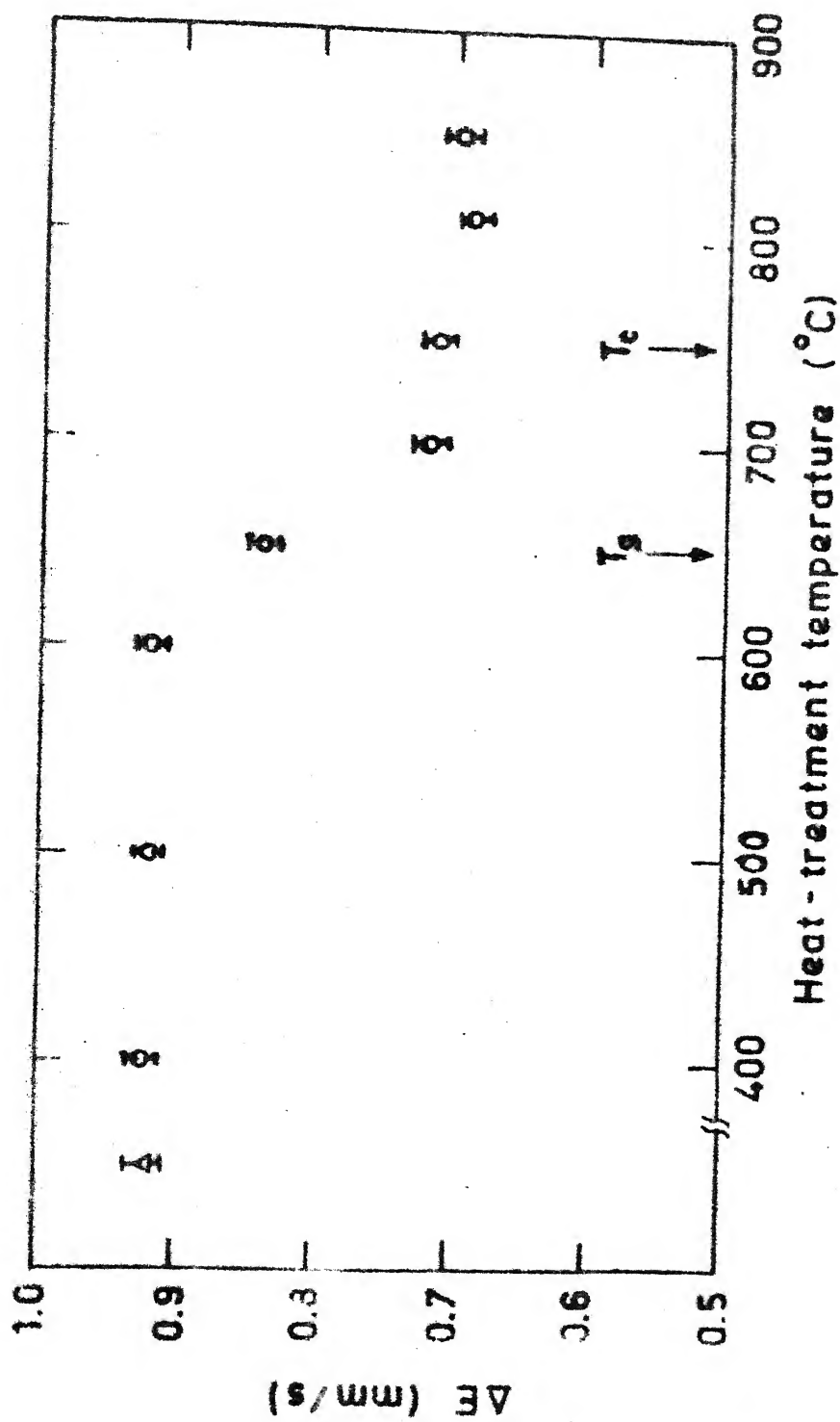


Fig. 3.6 Plot of the quadrupole splitting (ΔE) against the heat-treatment temperatures. Point marked as Δ refers to the as-prepared sample.

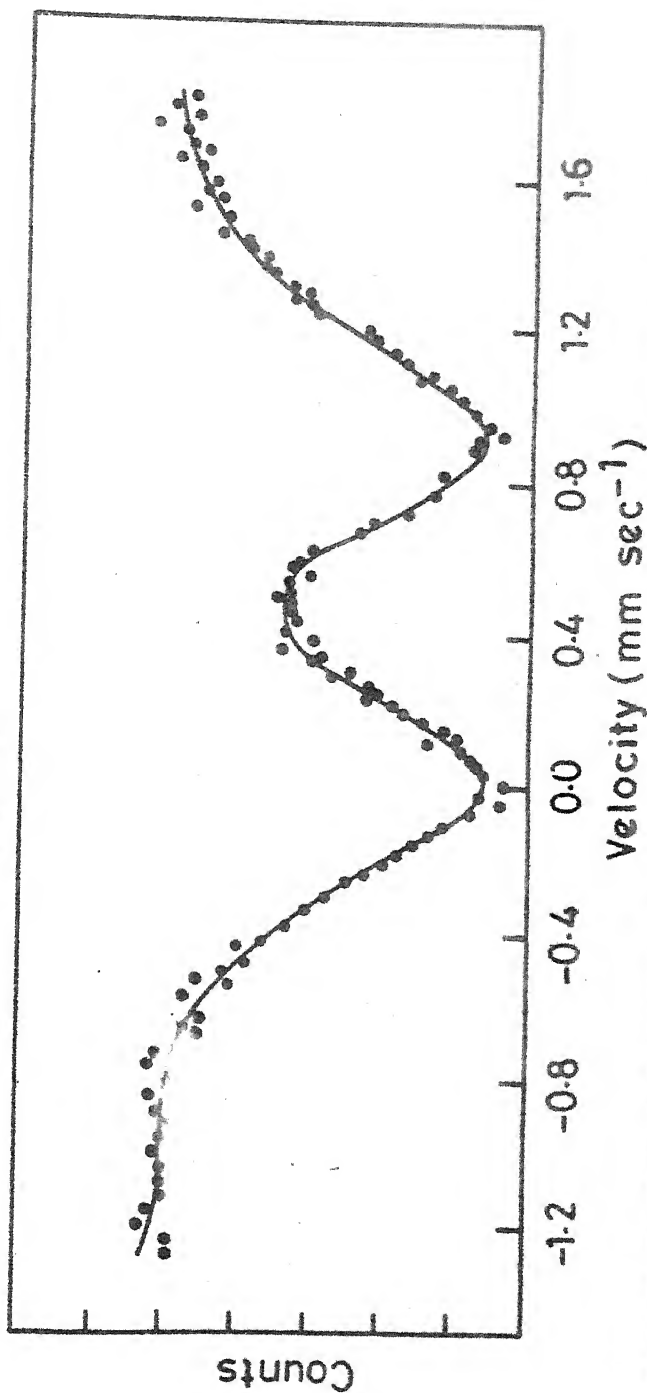
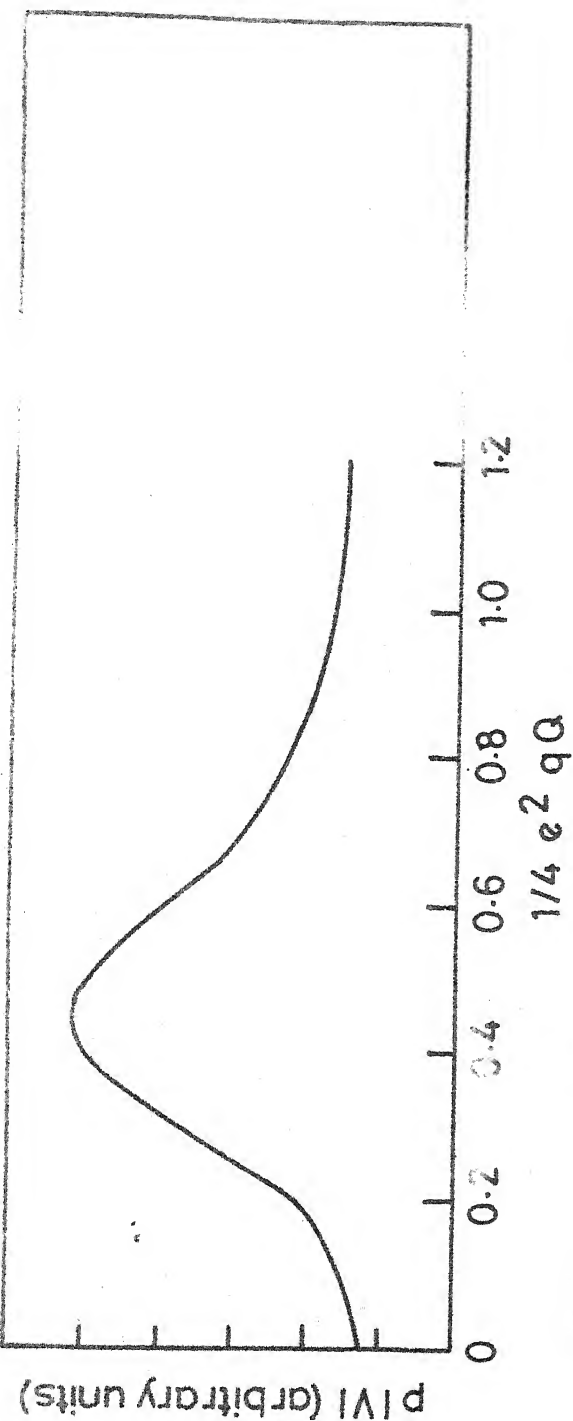


Fig. 3.7 EFG distribution of the as-prepared sample (V6) at room temperature. The top figure shows the results for the $(p(V))$ distribution while the bottom figure shows the resulting fitted Mössbauer spectrum.

a function of the heat-treatment temperature) is similar to that shown in Fig. 3.6. The values of the FWHM (full width at half maximum) of the EFG distribution $p(|V|)$ is also shown in Table 3.2. The FWHM value indicate the amorphous nature of the glass system and the higher values of FWHM observed after 500 °C suggest an onset of long-range order or glass formation in the samples. It is found that the samples heat-treated at 700 °C and 750 °C give rise to two separate EFG distribution (see, for example, Fig. 3.8, for 750 °C) such that one of these two ΔE ($\Delta E = 0.634 \pm 0.015$ mm sec⁻¹) values correspond to the quadrupole splitting characterizing the samples heat-treated below 700 °C while the second ΔE value ($\Delta E = 1.177 \pm 0.015$ mm sec⁻¹) is higher and may be characteristic of the development of the magnetic phase. It is to be noted that the higher ΔE value could not be resolved from a pure Lorentzian least square fit. In this connection we wish to present the data on the variation of magnetic susceptibility with temperature as shown in Fig. 3.9. A sharp rise in the curve is observed at 650 °C and it is attributed to the precipitation of the magnetic phase. A similar result has been reported in the case of basalt glass-ceramics [19].

We carried out EPR measurements on some of the glass samples with an aim to obtain further understanding into the co-ordination and symmetry of iron as well as the relaxation phenomenon. Some typical EPR spectra observed

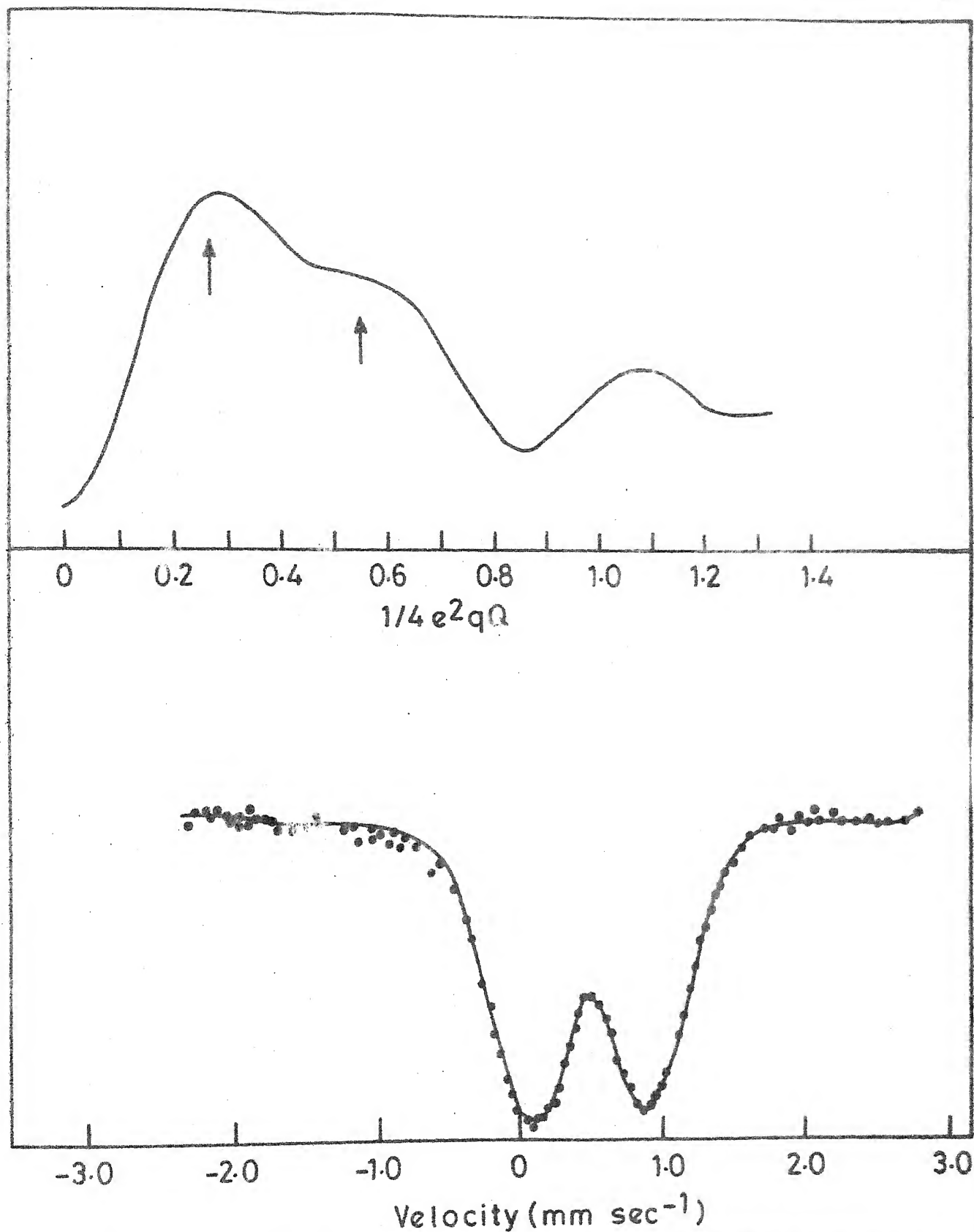


Fig. 3.8 Same as Fig. 3.7 but for the sample heat-treated at 750°C for 4 h.

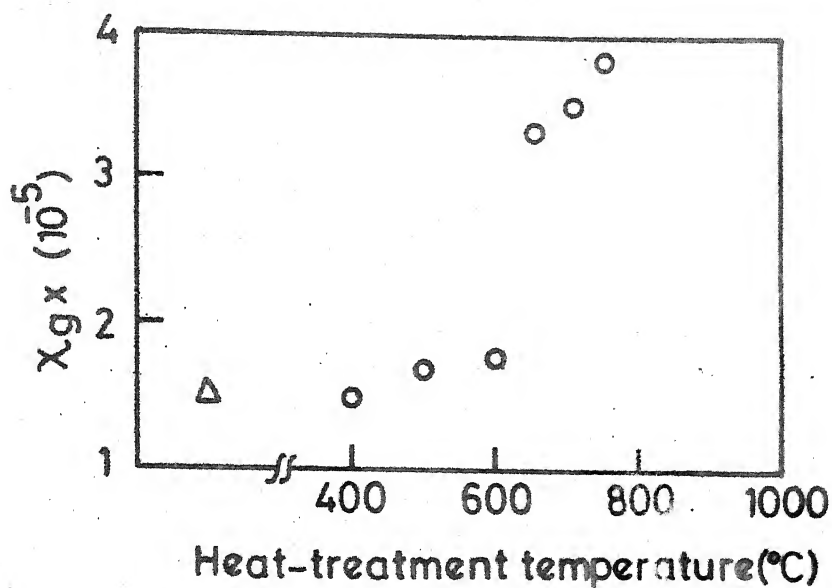
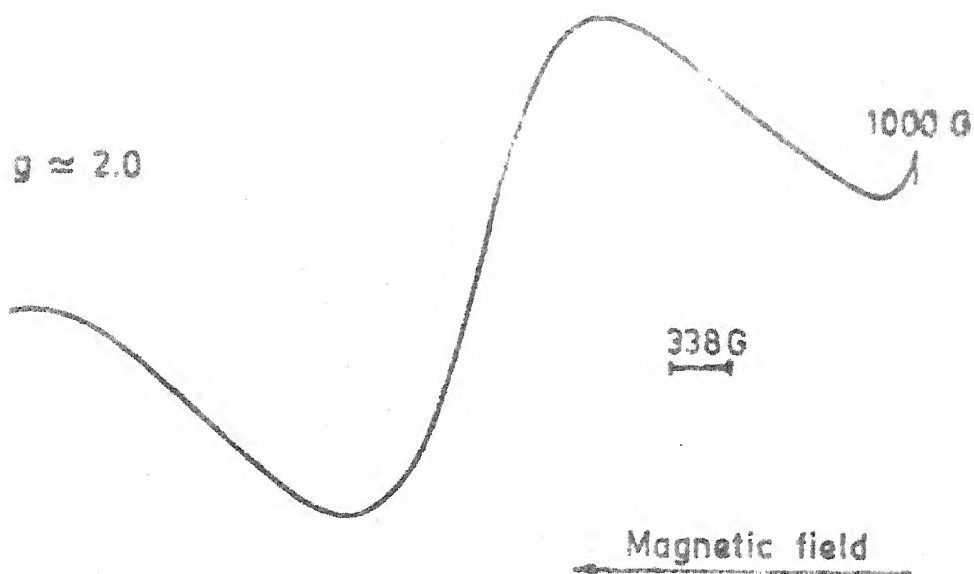


Fig. 3.9 Plot of the magnetic susceptibility against the heat-treatment temperature, treatment time being 4 h for each.

at RT are shown in Fig. 3.10. Values of g and linewidths determined from some of these EPR spectra are given in Table 3.4. The spectra for all the samples show only one resonance which correspond to a value of g around 2.0.

It should be pointed out that the $g = 4.3$ resonance which usually occurs for paramagnetic Fe^{3+} ions [19] was not observed in any of the samples. This behaviour may indicate the presence of some type of super-exchange interaction in all the samples (including the as-prepared sample) which exhibit phase separation. A typical electron micrograph of the as-prepared glass is shown in Fig. 3.11. A super-exchange interaction may exist between the iron ions present in the iron-rich phases of these samples. It is observed that the line-widths for the as-prepared sample and the sample heat-treated at 400°C are nearly identical. However, a sharp decrease in the linewidth is observed in the case of samples heat-treated at 650 and 750°C . Similar behaviour has also been observed in the variation of ΔE (Fig. 3.6). The value of g observed for the sample heat-treated at 650°C agrees with the value observed for YIG [20]. The decrease in the linewidth as a function of heat-treatment temperature may be attributed to an increase in the super-exchange interaction following the precipitation of the magnetic phase within the glass. In order to illustrate the wide range of particle size present in the system we have shown in Fig. 3.12 typical electron and optical micrograph

BLANK GLASS AT 27°C



SAMPLE 650 AT 27°C

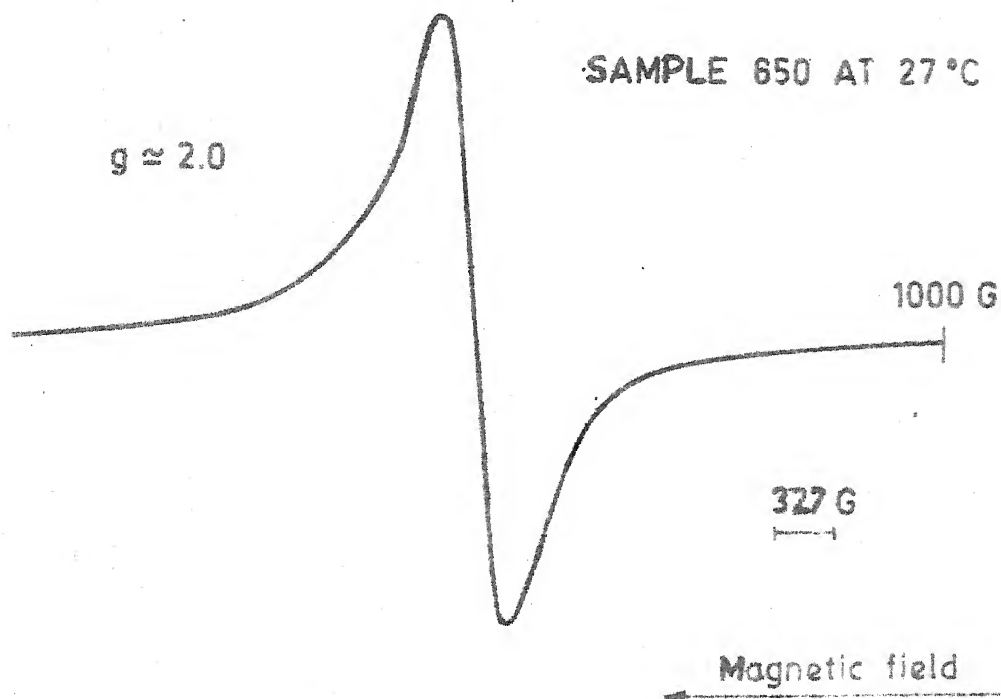


Fig. 3.10 Typical EPR spectra measured at room temperature for the as-prepared (Y6) sample and the sample heat-treated at 650°C.

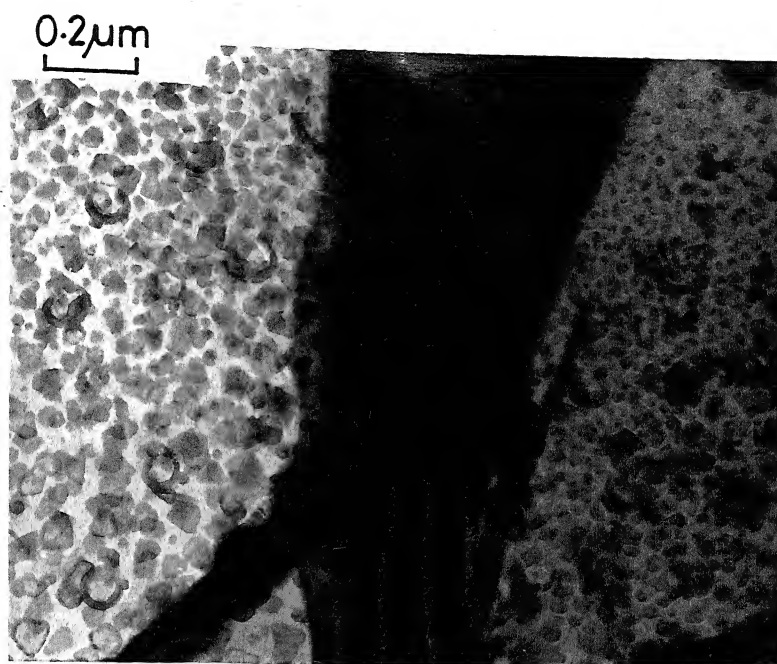
TABLE 3.4

EPR results for the Y6 sample.

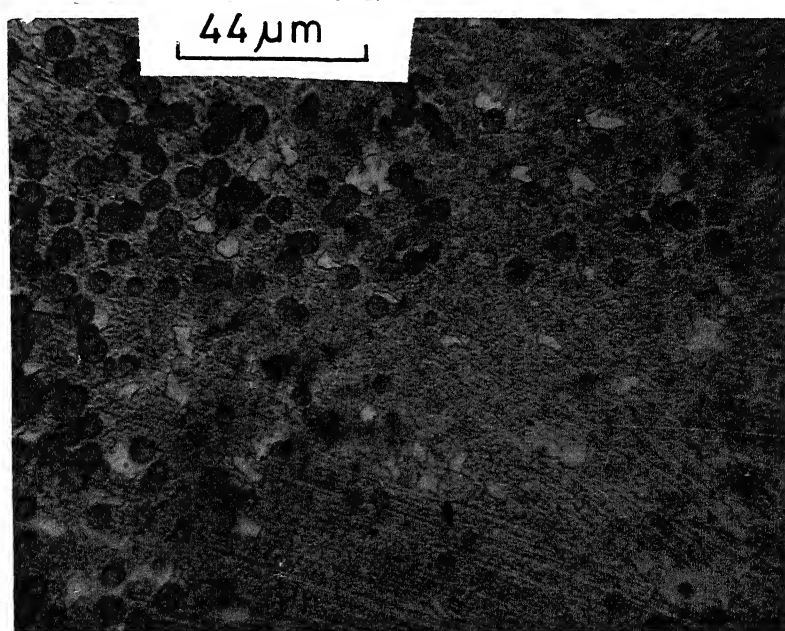
Sample	g	$\Delta H(G)$
As-prepared	1.98 ± 0.02	1283 ± 100
Heat-treated at 400 °C	1.96 ± 0.02	1169 ± 100
Heat-treated at 650 °C	2.02 ± 0.02	277 ± 20
Heat-treated at 750 °C	1.94 ± 0.02	268 ± 20



Fig. 3.11 Typical electron micrograph of the as-prepared sample.



(a)



(b)

Fig. 3.12 Typical (a) electron and (b) optical micrograph of the sample heat-treated at 650°C.

of the sample heated at 650 °C. We have observed similar behaviour in the case of other samples heated above 650 °C and it is observed that the particle size grows with heat-treatment temperature. Such behaviour has also been observed in the case of thin films of garnets heat-treated at various temperatures [21]. The wide range of particle size could have given rise to simultaneous occurrence of magnetic hyperfine structure and quadrupole splitting for samples in Table 3.3..

3.2.4 Summary

Mössbauer, EPR and magnetization experiments have been carried out on the glass composition $\text{Na}_2\text{O}-\text{SiO}_2-\text{Fe}_2\text{O}_3-\text{Y}_2\text{O}_3$ in which yttrium iron garnet (YIG) can be precipitated by suitable heat treatment. The measurements have been carried out on the as-prepared sample as well as samples heat-treated for 4 h at 400, 500, 600, 650, 700, 750, 810 and 850 °C. Mössbauer spectra from the as-prepared samples as well as the samples heat-treated at first set of six temperatures showed a quadrupole splitting while the samples heat-treated at (i) 810 °C for 4 h, (ii) 850 °C for 4 h, (iii) 600 °C for 4 h followed by 750 °C for 4 h (two-stage heat-treatment) and (iv) 700 °C for 40 h showed a hyperfine as well as quadrupole splitting. The behaviour of the isomer shift (IS) and quadrupole splitting (ΔE) with the heat-treatment temperature show significant changes at the

glass transition and crystallization temperature. As discussed earlier these results have been used to characterize the magnetic phases precipitated in the samples after different heat-treatments. The Mössbauer data have been found consistent with optical and electron micrographs which show a large variation in particle size of the precipitated magnetic phase. This has been further correlated with EPR and magnetization data.

3.3 Study of the Effect of Nucleating Agents on the YIG Crystallization in $\text{Na}_2\text{O-SiO}_2\text{-Fe}_2\text{O}_3\text{-Y}_2\text{O}_3$ Glass System.

3.3.1 Introduction

In the previous section we have presented the results of our studies of the glass-ceramic system $\text{Na}_2\text{O-SiO}_2\text{-Fe}_2\text{O}_3\text{-Y}_2\text{O}_3$ in the as-prepared form as well as the samples heat-treated at 400, 500, 600, 650, 700, 750, 810 and 850 °C. This kind of heat-treatment led to the precipitation of the yttrium iron garnet (YIG) phase. It was observed during the studies described in the previous section that the volume fraction of the crystallized YIG phase was rather small. An attempt was made by Bahadur et al. [22] to improve the crystallization kinetics of the YIG phase by using suitable nucleating agent such as the oxides P_2O_5 or TiO_2 which are commonly used in the field of glass-ceramics [1]. It was observed by Bahadur et al. [22] that P_2O_5 acts as a better

nucleating agent than TiO_2 . In addition, the magnetic properties of the glass-ceramic containing P_2O_5 were found to be superior. It was also suggested that the crystallization of the YIG phase is improved if a larger concentration of Fe_2O_3 is used.

We, therefore, decided to study the effect of the nucleating agents (such as P_2O_5 and TiO_2) on the crystallization of the YIG phase in the $\text{Na}_2\text{O}-\text{SiO}_2-\text{Y}_2\text{O}_3-\text{Fe}_2\text{O}_3$ glass system. To this end we used the method of Mössbauer spectroscopy which has already demonstrated its usefulness for such studies. We have also carried out other measurements on this glass system using X-ray and other techniques so that there is a corroboration of results obtained by Mössbauer studies. All these results are presented and discussed in this section.

3.3.2 Experimental method

(a) Sample preparation

The composition of the glasses studied by us is given in Table 3.5. The glasses were prepared from reagent grade chemicals by melting the mixture in alumina crucibles in an electrically heated furnace at temperature between 1300 and 1400 °C. Glass plates were cast by pouring the melt onto an aluminium mould. The glass transition temperature (T_g) and crystallization temperature (T_c) were estimated from

TABLE 3.5

Composition of the glasses studied. Molecular percentage values are given.

Glass	SiO ₂	Na ₂ O	Y ₂ O ₃	Fe ₂ O ₃	P ₂ O ₅	TiO ₂
Y6 (✱)	50	34	6	10	-	-
Y9	50	26	9	15	-	-
Y6P	48	34	6	10	2	-
Y9T	48	26	9	15	-	2
Y9P	48	26	9	15	2	-

(✱) The studies of the glass with this composition have been described in section 3.2 of this chapter.

DTA analysis using MOM Hungary Derivatograph [10]. The estimated values of the glass transition (T_g) and crystallization temperature (T_c) for different compositions were found to be nearly same. Based on this result, all the samples were given a two-stage heat treatment at $T_g = 720^\circ\text{C}$ and $T_c = 820^\circ\text{C}$ for two hours duration each. Since the Y9P glass (Table 3.5) was found to be the most favourable for the crystallization of YIG, we gave a number of different heat treatments for this sample according to the following schedule to find out the right growth temperature for the garnet phase:

- (i) $720^\circ\text{C} + 750^\circ\text{C}$ for 2 h each
- (ii) $720^\circ\text{C} + 775^\circ\text{C}$ for 2 h each
- (iii) $720^\circ\text{C} + 800^\circ\text{C}$ for 2 h each
- (iv) $720^\circ\text{C} + 820^\circ\text{C}$ for 2 h each, and
- (v) 800°C for 40 h .

(b) Measurements

The DTA, X-ray, magnetization and Mössbauer measurements were carried out by methods described earlier in section 3.2.2.

3.3.3 Results and discussions

The DTA plot of the as-prepared Y9P sample recorded by Bahadur et al. [22] is shown in Fig. 3.13 and it is typical for all the samples in Table 3.5. X-ray powder

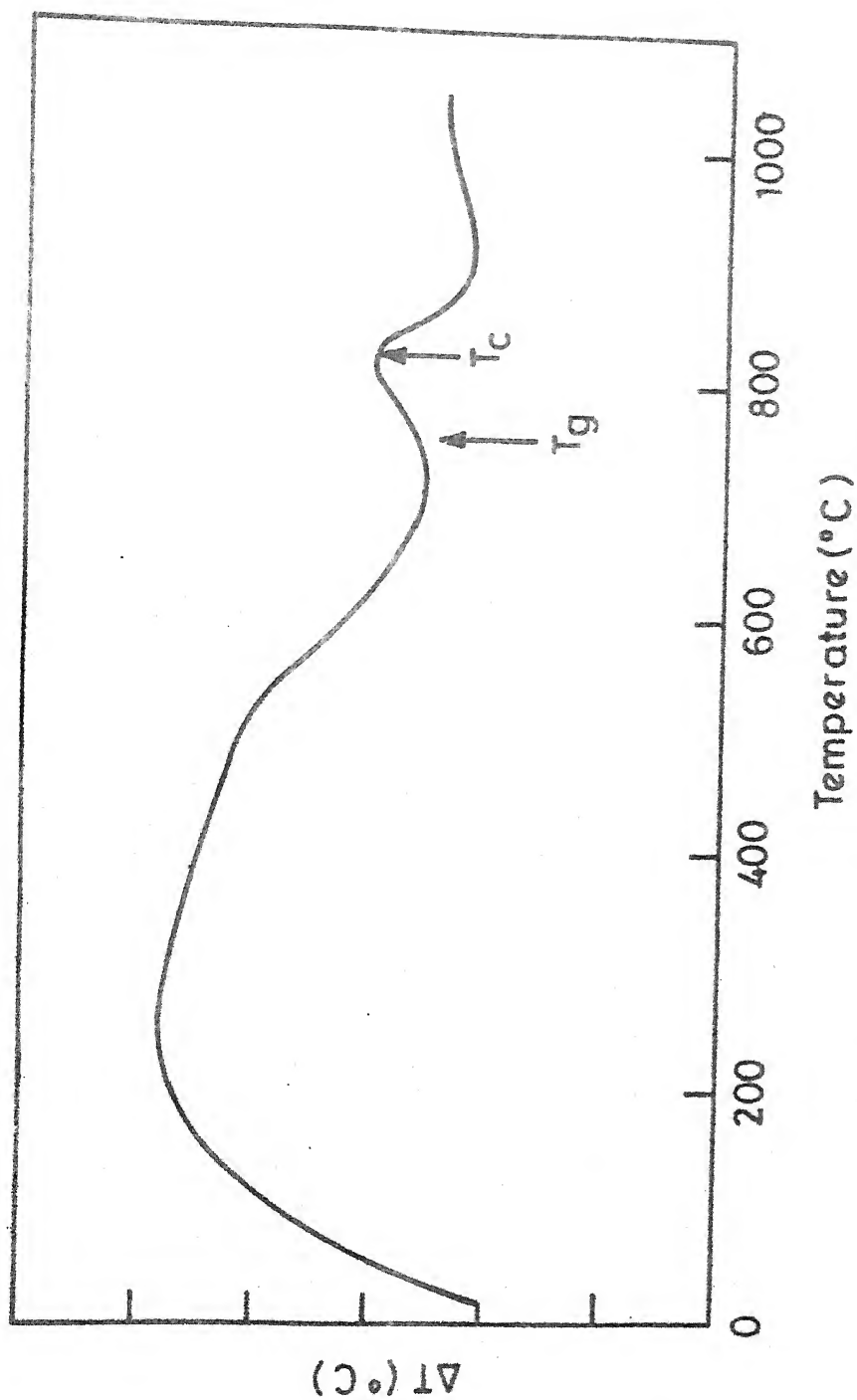


Fig. 3.13 DTA plot of the as-prepared Y9P sample.
Scan rate is 10°C per minute.

diffraction patterns for glass ceramic samples were recorded in Rich and Siefert ISO-Debyeflex 2002 diffractometer with Cr K α target. X-ray diffraction data for the Y9P glass measured by us is given in Table 3.6 while the X-ray data for other glasses were taken from the studies of Bahadur et al. [22]. In the case of all the two-stage heat-treated samples, the results of the X-ray diffractograms show lines due to YIG phase. In addition lines due to different oxidation products of iron which could be either $\gamma\text{-Fe}_2\text{O}_3$, or its derivative, or $\alpha\text{-Fe}_2\text{O}_3$ were also observed. The results for the X-ray diffraction from the Y9P sample indicated that this particular glass ceramic is the most favourable for crystallization of the YIG phase. The lattice constant of this particular YIG phase was found to be 12.31 Å. On the other hand, the sample Y6P having a smaller molar concentration of Fe_2O_3 and Y_2O_3 is not as favourable. The same (Y9P) sample when heat-treated at 800 °C for 40 h was not found to be as favourable as the two-stage heat-treated sample.

Bahadur et al. [22] have reported the magnetization measurements for the two-stage heat-treated samples Y9, Y9T and Y9P. Their plots for the magnetization versus temperature and magnetization versus field are shown in Fig. 3.14 and Fig. 3.15 respectively. Results of Fig. 3.14 indicate the presence of two magnetic phases by a clear break near the Curie temperature (280 °C) of YIG. It should be pointed out that this break is most obvious in samples containing

TABLE 3.6

X-ray diffraction data for heat-treated sample Y9P.

Sample heated at 720 °C + 820 °C for 2 h each			Sample heated at 800 °C for 40 h			YIG*			Assignmen
d (nm)	Intensity ⁺	hkl	d (nm)	Intensity ⁺	hkl	d (nm)	Intensity ⁺	hkl	
			0.4007	VS	-				$\gamma\text{-Fe}_2\text{O}_3$
			0.3657	M	012				$\alpha\text{-Fe}_2\text{O}_3$
0.3043	S	400	0.3036	M	400	0.3088	S	400	
			0.2954	W	220				$\gamma\text{-Fe}_2\text{O}_3$
0.2735	VS	420	0.2724	S	420	0.2764	VS	420	
			0.2679	VS	104				$\alpha\text{-Fe}_2\text{O}_3$
0.2640	S	-				0.2517	W	521	
0.2509	S	422	0.2508	S	422	0.2517	S	422	$\alpha\text{-Fe}_2\text{O}_3$
0.2390	W	521				0.2251	W	521	
			0.2204	M	113				$\alpha\text{-Fe}_2\text{O}_3$
			0.2052	W	202				$\alpha\text{-Fe}_2\text{O}_3$
0.1916	M	-	0.1916	W	-				$\alpha\text{-Fe}_2\text{O}_3$
			0.1837	M	024				$\alpha\text{-Fe}_2\text{O}_3$
0.1811	W	444	0.1806	W	444	0.1779	M	444	
			0.1725	VW	640	0.1710	S	640	$\alpha\text{-Fe}_2\text{O}_3$
0.1698	W	640	0.1691	M	640				

TABLE 3.6 (Continued)

Sample heated at 720 °C + 820 °C for 2 h each		Sample heated at 800 °C for 40 h		YIG*		Assignment
d (nm)	Intensity ⁺	hkl	d (nm)	Intensity ⁺	hkl	
0.1644	W	642	0.1641	W	642	642
			0.1625	VW	211	800
0.1479	W	-	0.1488	W	214	α -Fe ₂ O ₃ γ -Fe ₂ O ₃
			0.1453	VW	300	α -Fe ₂ O ₃ γ -Fe ₂ O ₃
					0.1379	840
					0.1347	842

*Data obtained from a polycrystalline YIG sample.

⁺VS = very strong; S = strong; M = medium; W = weak; VW = very weak.

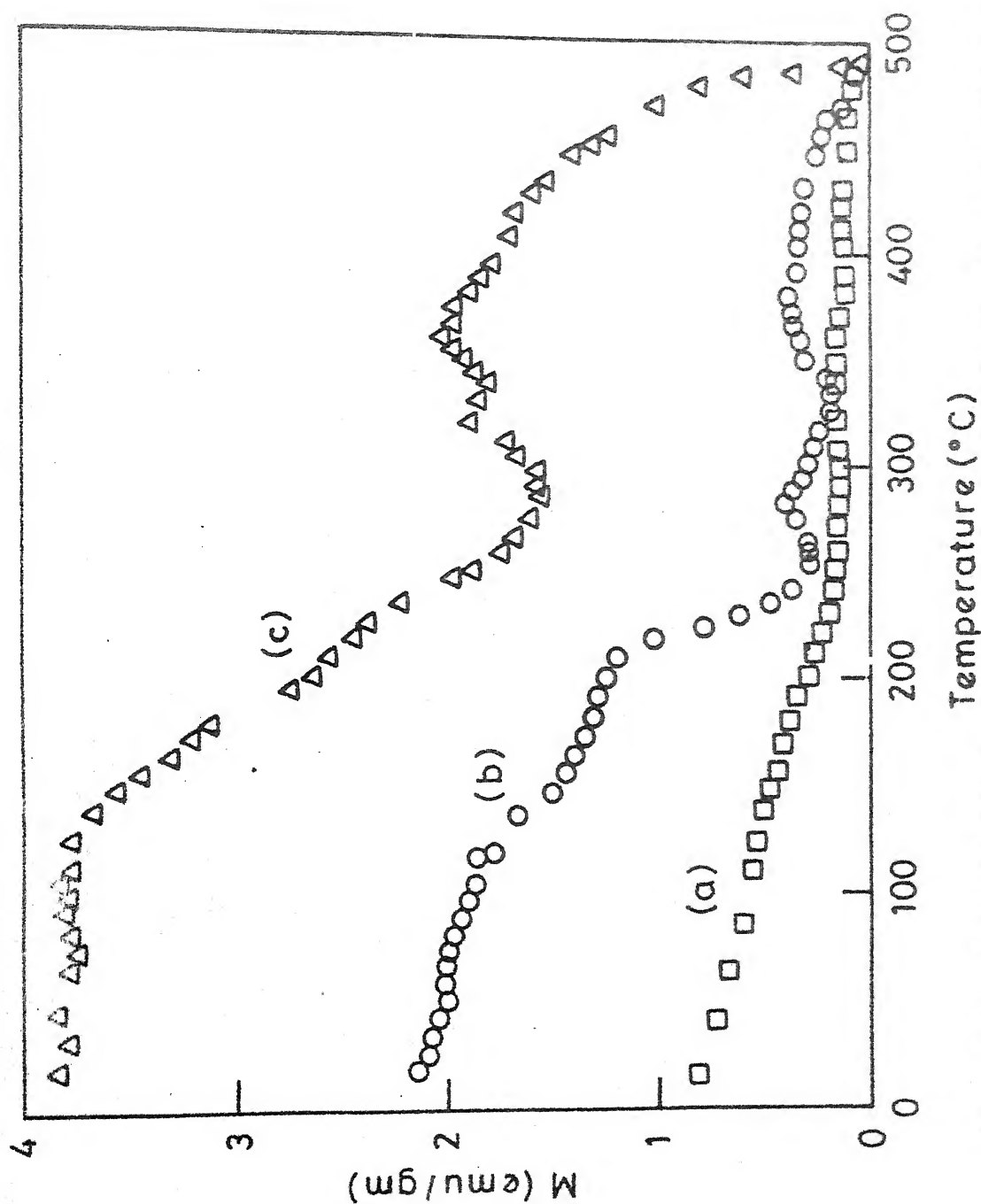


Fig. 3.14 Plot of magnetization versus temperature for the two-stage heat-treated samples. (a) Y9 (b) Y9 and (c) Y9F.

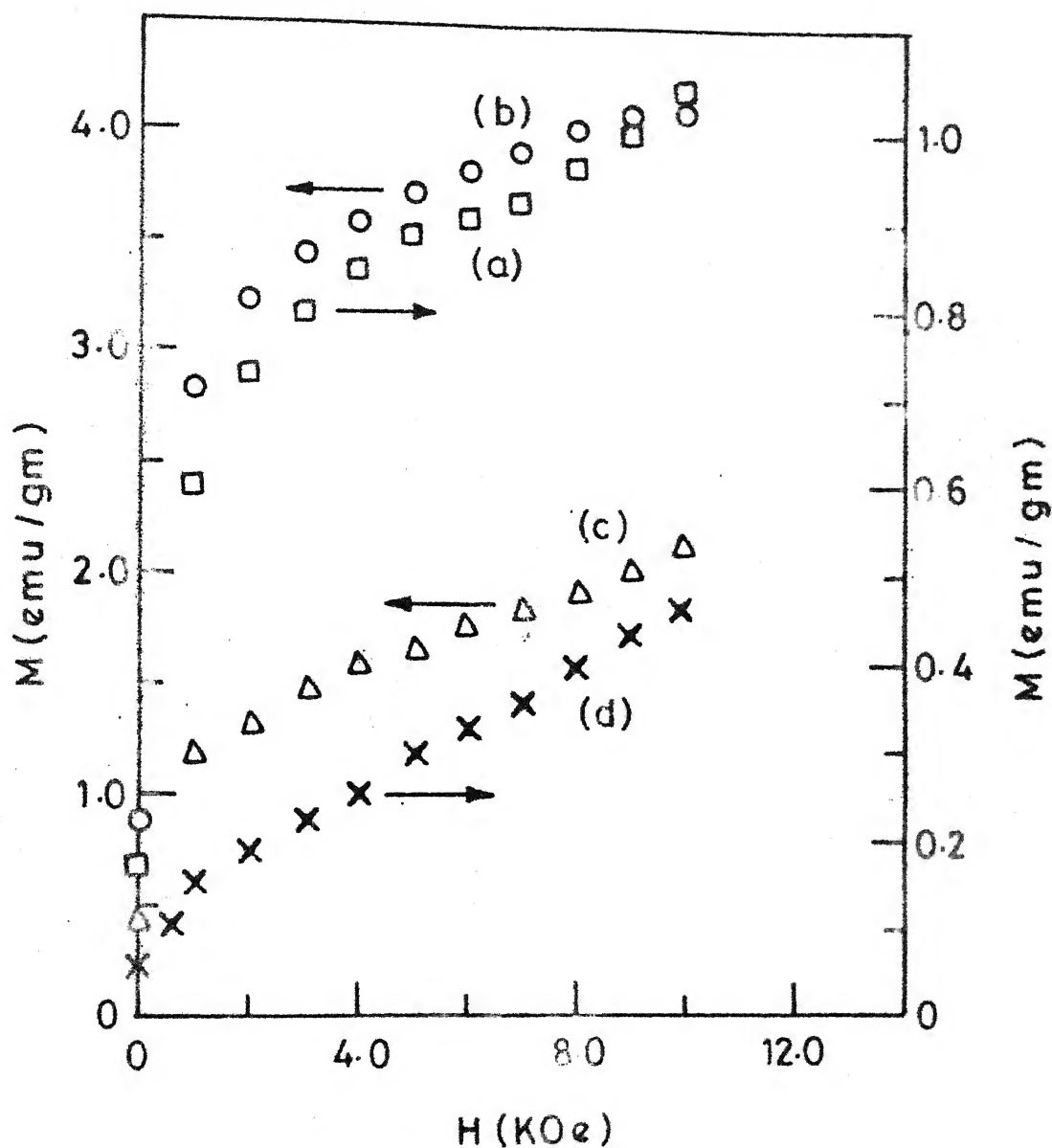


Fig. 3.15 Plot of magnetization versus field for the two-stage heat-treated samples. (a) Y9 (b) Y9P and (c) Y9T and (d) Y6P at room temperature.

the nucleating agents, especially P_2O_5 . In the case of the other phase the Curie temperature appears to be around $475^\circ C$. No saturation is observed for the samples upto the field of 10 KG (Fig. 3.15). The absence of saturation could be due to the superparamagnetic particles.

Mössbauer spectra of all the as-prepared samples (Y9, Y6P, Y9T and Y9P) taken at room temperature (RT) are shown^{*} in Fig. 3.16 and they all display quadrupole splitting. The values of the corresponding Mössbauer parameters are given in Table 3.7. Similarly the Mössbauer spectra and the Mössbauer parameter of the samples Y9, Y6P and Y9P heat-treated at $(720^\circ C + 820^\circ C)$ for 2 h each and Y9P heat-treated at $800^\circ C$ for 40 h are given in Fig. 3.17 and Table 3.8. All these spectra (Fig. 3.17) show magnetic hyperfine splitting. Fig. 3.18 show the Mössbauer spectra for the Y9P sample heat-treated for 2 h each at temperatures $(720^\circ + 750^\circ C)$, $(720^\circ + 775^\circ C)$, $(720^\circ + 800^\circ C)$ and $(720^\circ + 820^\circ C)$.

The isomer shift of all the as-prepared samples with respect to $\alpha\text{-Fe}$ (Fig. 3.16 and Table 3.7) is in the range $+(0.209 - 0.242) \text{ mm sec}^{-1}$ and is characteristic of Fe^{3+} . The linewidth (or peak width) of the individual peak in the

^{*}In Figs. 3.16, 3.17 and 3.18, the zero of the velocity scale refers to the centroid of $\alpha\text{-Fe}$ Mössbauer spectrum.

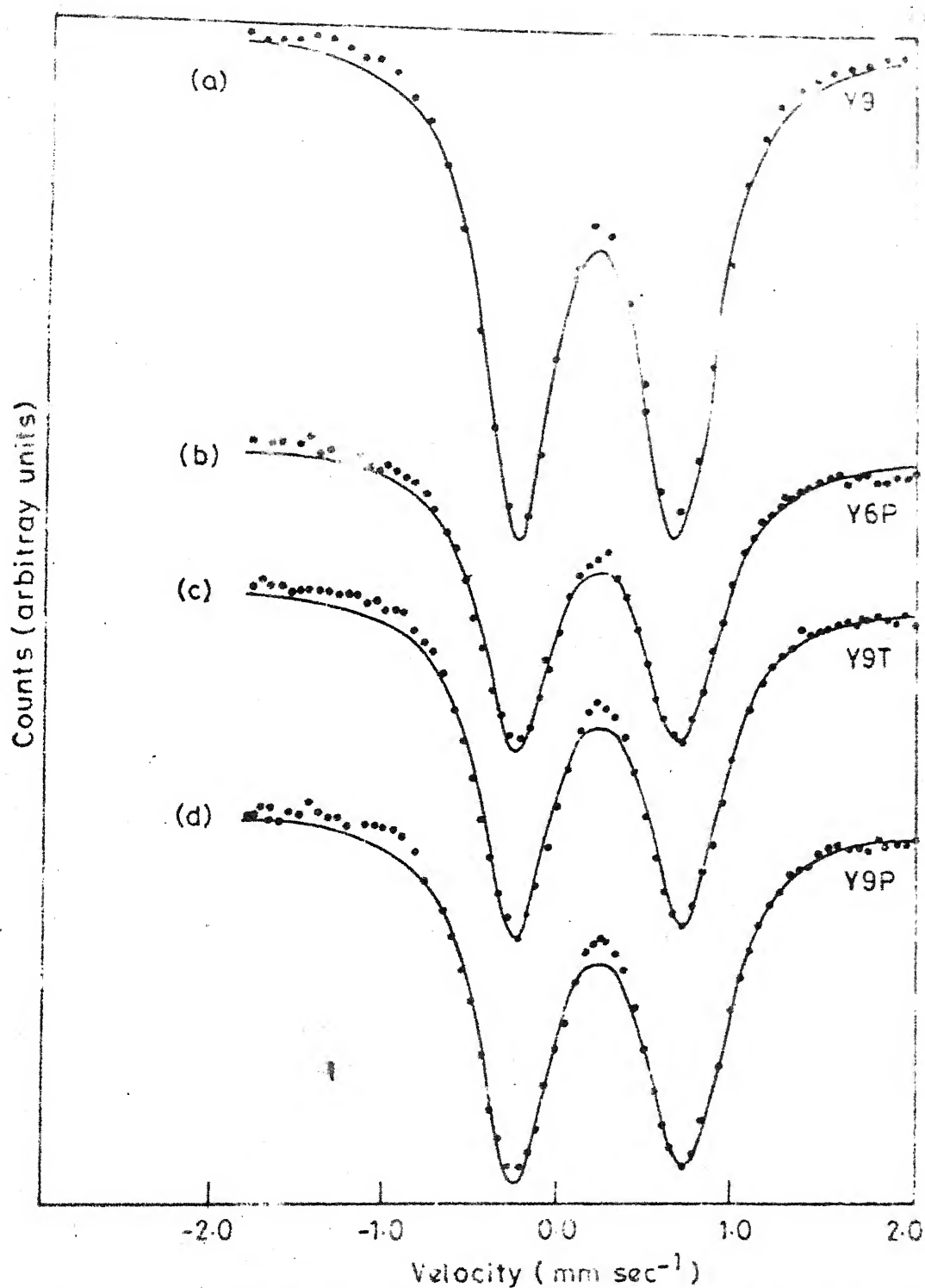


Fig. 3.16 Room-temperature Mössbauer spectra of the as-prepared samples Y9, Y6P, Y9T and Y9P. The zero of the velocity scale refers to the centroid of the α -Fe (absorber) Mössbauer spectrum.

TABLE 3.7

Mössbauer parameters of the as-prepared sample.

Sample	IS [*] mm sec ⁻¹	ΔE mm sec ⁻¹	Peak-width (mm sec ⁻¹)		EFG Distribution	
			I	II	ΔE (mm sec ⁻¹)	FWHM (mm sec ⁻¹)
Y9	0.209 \pm 0.008	0.900 \pm 0.006	0.49 \pm 0.01	0.49 \pm 0.01	0.88 \pm 0.02	0.42
Y6P	0.217 \pm 0.008	0.960 \pm 0.008	0.49 \pm 0.01	0.54 \pm 0.01	0.94 \pm 0.02	0.42
Y9T	0.232 \pm 0.008	0.978 \pm 0.008	0.48 \pm 0.01	0.53 \pm 0.01	0.98 \pm 0.02	0.44
Y9P	0.242 \pm 0.008	0.991 \pm 0.008	0.50 \pm 0.01	0.57 \pm 0.01	0.98	0.44

*Values with respect to α -Fe.

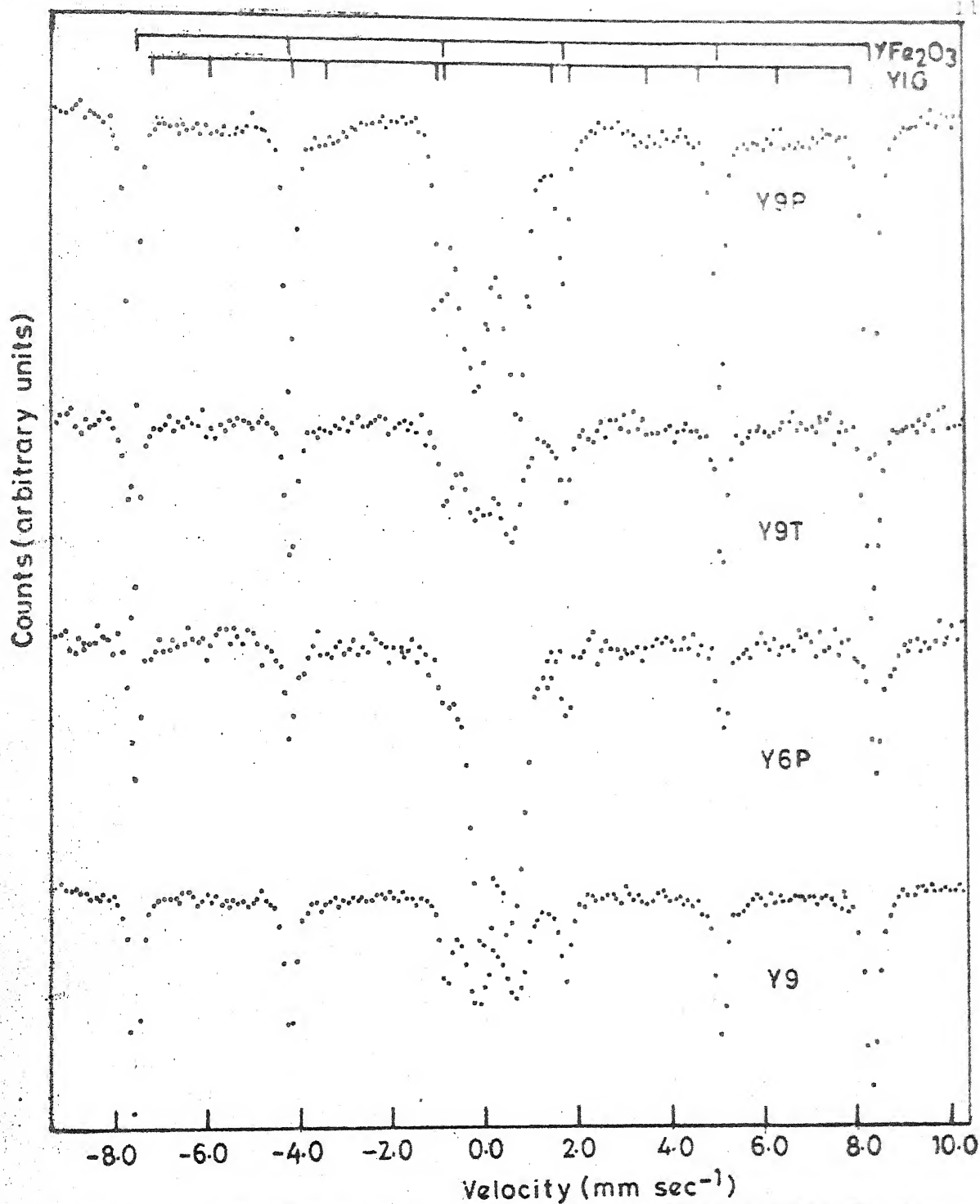


Fig. 3.17 Room-temperature Mössbauer spectra of the samples Y9, Y6P, Y9T heat-treated at 720°C and 820°C for 2 h each and sample Y9P heat-treated at 800°C for 40 h.

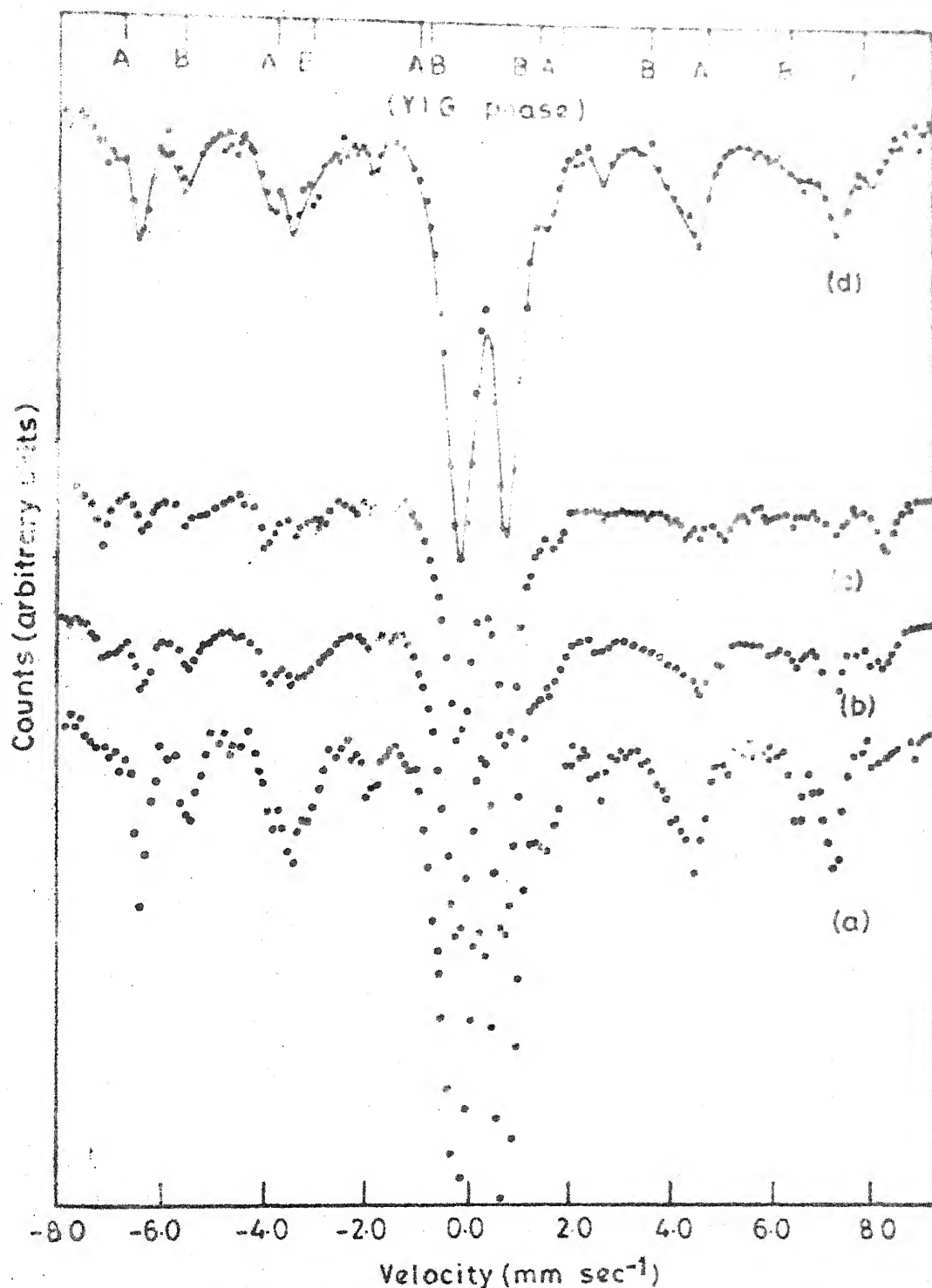


Fig. 2.18 Room-temperature Mössbauer spectra of the samples Y9P heat-treated different growing temperature (a) 720° + 750°C (b) 720° + 775°C, (c) 720° + 800°C and (d) 720° + 820°C for 2 h each.

TABLE 3.8

Mössbauer parameters for the sample with two-stage heat-treatment at temperature 720 °C + 820 °C
for 2 h each.

Sample	IS* (mm sec ⁻¹)	Quadrupole splitting		Magnetic hyperfine splitting		Ratio of area under magnetic hyperfine splitting and quadrupole splitting
		ΔE (mm sec ⁻¹)	Peak widths (mm sec ⁻¹)	IS* (mm sec ⁻¹)	H _{int} (kOe)	
Y9	0.25±0.02	0.83±0.02	0.57±0.04	0.44±0.01	509±5	2.07
Y6P	0.23±0.02	0.63±0.02	0.57±0.02	0.43±0.02	508±5	0.58
Y9T	0.16±0.03	0.72±0.05	0.85±0.14	0.39±0.02	507±5	1.78
Y9P	0.32±0.02	0.92±0.01	0.57±0.01	0.49±0.04	446±20	-
				0.23±0.04	414±20	-
				0.52±0.05	431±20	- These phases are not identified
Y9P ^a	0.29±0.02	0.92±0.02	0.73±0.03	0.35±0.05	250±20	-
			0.50±0.03	0.45±0.01	514±5	-

* IS w.r.t. α-Fe.

^a Heat-treatment given to this sample is 800 °C for 40 h

doublet spectra (quadrupole splitting in Fig. 3.16) is ~ 0.50 mm sec⁻¹ which is above the average linewidth usually observed. In order to investigate the reason behind this rather large linewidth we analyzed these spectra with the help of a computer programme (Sec. 2.8) to obtain the EFG distribution ($p|V|$). The results of this analysis are shown in Fig. 3.19 and they indicate that the EFG distributions show a single but broad peak centered around the corresponding ΔE value with a broad width (FWHM) of about 0.44 mm sec⁻¹ which is larger than that obtained in case of single iron site of sodium nitroprusside (≈ 0.20 mm sec⁻¹). These results indicate that the large peakwidth could be due to the presence of two sites for ⁵⁷Fe. However, the difference in them could be small because of the amorphous nature of the glass.

The value of ΔE (quadrupole splitting) for the as-prepared samples are all above 0.90 mm sec⁻¹ (Table 3.7). In case of each of the samples (Y9, Y6P, Y9T and Y9P), the effect of the two-stage heat-treatment is to lower the ΔE values (Table 3.8). A similar behaviour was observed for the Y6 sample (Table 3.3) as reported in the previous section. Komatsu and Soga [4] have reported a similar decrease in the ΔE values of silicate glasses upon heat-treatment. A possible explanation for this behaviour is already proposed in Sec. 3.2.3.

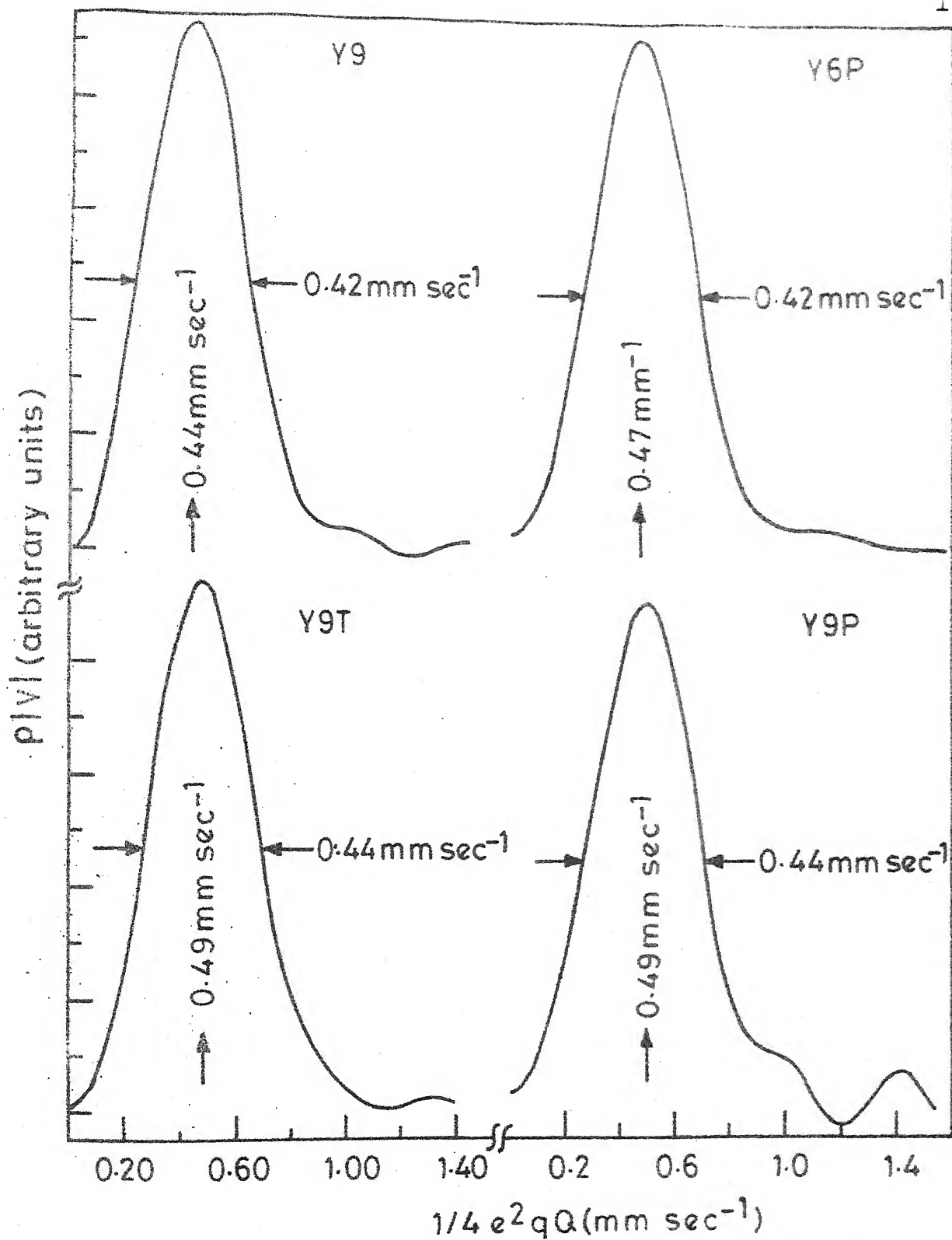


Fig. 3.19 EFG distribution for the as-prepared samples Y9, Y6P, Y9T and Y9P.

The results for the IS and ΔE values for the as-prepared samples have been plotted in Fig. 3.20 to bring out any systematic behaviour. The mole percentage of the Fe_2O_3 as well as of the nucleating agent ($\text{P}_2\text{O}_5/\text{TiO}_2$) is also shown on the x-axis to examine any possible correlations. The IS values appear to increase linearly due to combined (and complicated) effect of the mole percentage of Fe_2O_3 as well as the nucleating agent. In this connection it should be pointed out that the increase in the IS caused by P_2O_5 as a nucleating agent is more compared to that caused by TiO_2 (Fig. 3.20). Kurkjian and Sigety [12] have observed similar behaviour in their Mössbauer study of silicate and phosphate glasses and they suggested that trivalent iron prefers tetrahedral coordination in silicate glasses and octahedral coordination in phosphate glasses. Our present results on the IS data (Fig. 3.20) indicate that trivalent iron prefers tetrahedral coordination in our samples containing TiO_2 and octahedral coordination in samples containing P_2O_5 . It is seen from Fig. 1.7, taken from Kurkjian and Sigety [12], that IS values are higher in octahedral coordination compared to tetrahedral coordination.

The ΔE variation appears to be determined by the mole percentage of the nucleating agent, the presence of the nucleating agent seems to raise the ΔE value. This behaviour could arise due to the lowering of the symmetry after the addition of the nucleating agent.

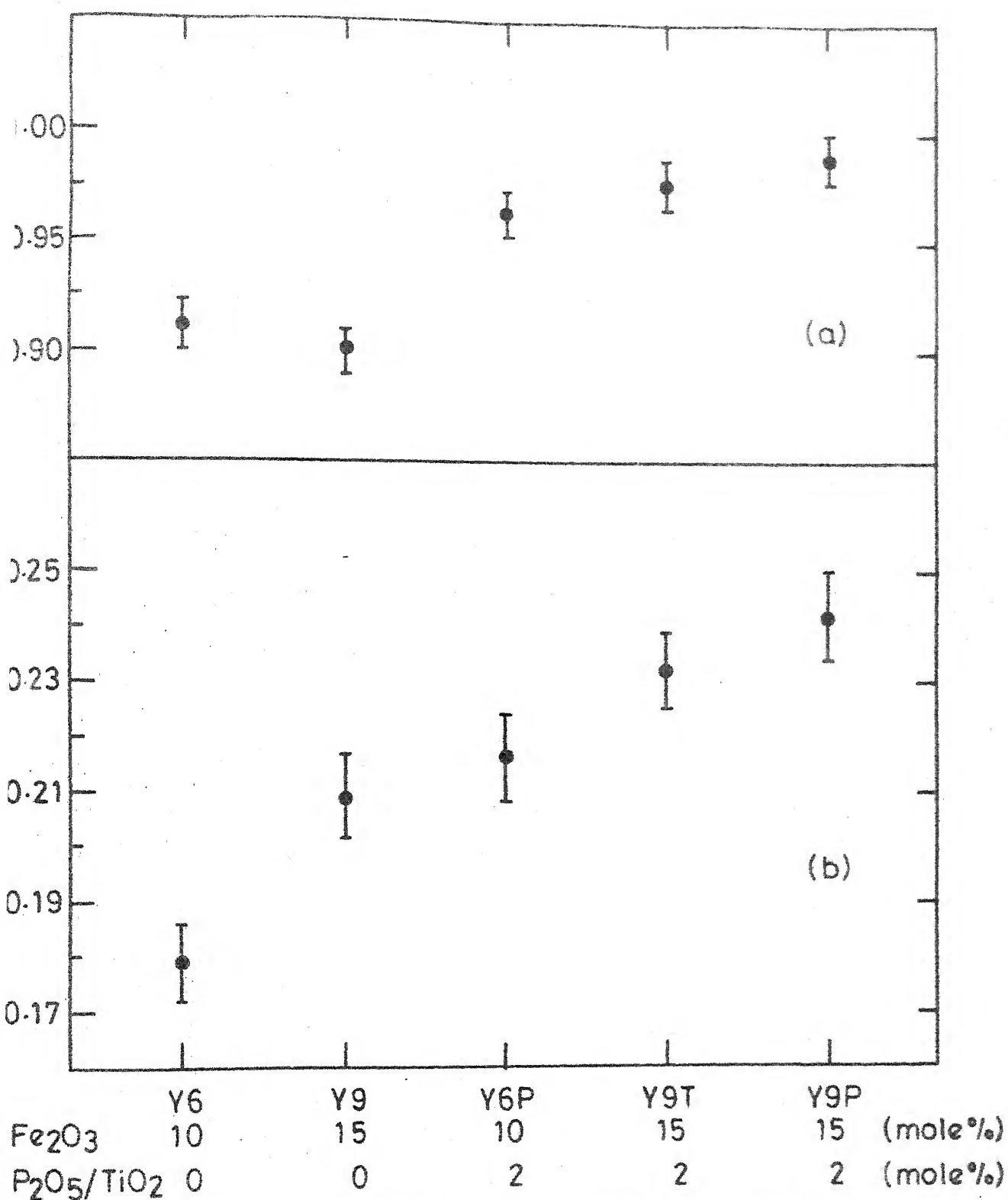


Fig. 3.20 Behaviour of the Mössbauer parameters, isomer shift (IS) and quadrupole splitting (ΔE), for the samples Y6, Y9, Y6P, Y9T and Y9P. The results for the sample Y6 have been taken from the previous section.

In the case of all the four samples (Y9, Y6P, Y9T and Y9P) heat-treated by a two-stage process at 720 °C and 820 °C for 2 h each the Mössbauer spectra show magnetic hyperfine splitting in addition to quadrupole splitting (Fig. 3.17). Examination of the IS-values determined from the doublet peaks (quadrupole splitting) of these spectra (Fig. 3.16 and Table 3.7) show that for each sample (except Y9T) the IS value for the heat-treated sample is higher than that for the as-prepared sample (Table 3.8). This behaviour can be understood, once again, by concluding that the trivalent iron prefers tetrahedral coordination in the samples containing TiO_2 and octahedral coordination in samples containing P_2O_5 .

It was observed (Fig. 3.17) that while the Mössbauer spectra of the heat-treated samples Y9, Y6P and Y9T could be resolved into one doublet (quadrupole splitting) and one sextet (corresponding to one magnetic hyperfine field), the Mössbauer spectrum for the heat-treated sample Y9P was quite complex and it had to be resolved into one doublet (quadrupole splitting) and four sextets (corresponding to four different magnetic hyperfine fields). The value of the relevant Mössbauer parameters determined from this analysis are given in Table 3.8.

The X-ray diffractograms of the two-stage heat-treated samples Y9, Y6P and Y9P observed by Bahadur et al. [22] showed the lines due to yttrium iron garnet (YIG) phase,

along with those due to other phases (e.g. spinels such as $\gamma\text{-Fe}_2\text{O}_3$ and $\alpha\text{-Fe}_2\text{O}_3$ etc.). However, the Mössbauer spectra observed by us for two-stage heat-treated samples Y9, Y6P and Y9T do not show lines due to YIG prominently (Fig. 3.17). We attribute this behaviour to the possibility that although the YIG phase is precipitated in these samples, the amount formed is small. The observed Mössbauer spectra for these samples, however, show lines which could be due to either $\alpha\text{-Fe}_2\text{O}_3$ or $\gamma\text{-Fe}_2\text{O}_3$ phase in agreement with the X-ray data (Table 3.6).

In the case of the two-stage heat-treated sample Y9P, the Mössbauer spectra has indicated the presence of one quadrupole splitting and four magnetic hyperfine splittings. Out of these, two magnetic hyperfine splittings correspond to the two (A and B) sites of the YIG phase with the IS values as $0.49 \pm 0.04 \text{ mm sec}^{-1}$ and $0.23 \pm 0.04 \text{ mm sec}^{-1}$ and the H_{int} values as $446 \pm 20 \text{ kOe}$ and $414 \pm 20 \text{ kOe}$ as determined by us from Fig. 3.18d. In order to confirm this assignment, we recorded a Mössbauer spectrum of polycrystalline YIG sample and observed values of IS for site A and B as $0.50 \pm 0.03 \text{ mm sec}^{-1}$ and $0.22 \pm 0.03 \text{ mm sec}^{-1}$ and for H_{int} as $469 \pm 15 \text{ kOe}$ and $405 \pm 15 \text{ kOe}$ respectively.

This observation along with the reported values by Kurkjian and Sigety [12] support our conclusion that the volume fraction of the YIG phase precipitated in the two-stage heat-treated sample is largest for the Y9P sample.

The other two hyperfine splittings observed in this sample (Fig. 3.18) appear to have the IS values as $0.52 \pm 0.05 \text{ mm sec}^{-1}$ and $0.35 \pm 0.07 \text{ mm sec}^{-1}$ and the H_{int} values as $431 \pm 40 \text{ kOe}$ and $250 \pm 40 \text{ kOe}$ respectively. These two could be due to the precipitation of some spinel phases such as a derivative of $\gamma\text{-Fe}_2\text{O}_3$.

In order to investigate the precipitation of the YIG phase in the Y9P sample, we subjected it to a two-stage heat-treatment at different growth (second stage) temperatures keeping the nucleation (first stage) temperature constant. This heating schedule consisted of

- (i) $720^\circ\text{C} + 750^\circ\text{C}$ for 2 h each,
 - (ii) $720^\circ\text{C} + 775^\circ\text{C}$ for 2 h each,
 - (iii) $720^\circ\text{C} + 800^\circ\text{C}$ for 2 h each
- and also
- (iv) 800°C for 40 h .

The Mössbauer spectra (at room temperature) for these samples (i), (ii) and (iii) are shown in Fig. 3.18 while the Mössbauer spectrum for the sample (iv) is shown in Fig. 3.17. In Table 3.9 we have shown the intensity of the outer peaks of the sextet (or six-peak Mössbauer spectrum) at the two sites A and B for each magnetic phase precipitated in these samples. For the sample heat-treated at 800°C the ratio of the peaks corresponding to the site A:B was observed to be 3:2 as is characteristic for the garnet phase [20]. We

TABLE 3.9

Sample Y9P : heat treatment at different temperatures

Percentage of the intensities of the A site and B
site.

Temperature of heat treatment (°C)	A site (%)	B site (%)	Unknown phase (%) (%)	
720 + 750	0.3	0.9	1.5	0.6
720 + 775	0.55	0.7	1.0	0.36
720 + 800	1.1	0.7	0.8	0.04
720 + 820	0.38	1.4	1.1	0.4

therefore conclude that 800 °C is the most optimum growth temperature for the most efficient precipitation of the YIG phase.

The Mössbauer spectrum for the sample Y9P heat-treated at 800 °C for 40 h shows the presence of small volume fraction of YIG and a larger fraction of the oxidation products of iron or their derivatives.

As mentioned earlier our main interest in this work was to study the crystallization of the YIG phase in different glass ceramics. However the observed variation in the pattern of Mössbauer spectra, X-ray and other data indicates the presence of other magnetic phases in the system. We propose the following explanation for the above observations. It is well-known that the different oxidation products of iron are interconvertible into one another under slightly different conditions [8]. It is, therefore, possible that we have more than one oxidation product of iron (or their derivatives) present in different glass ceramic samples studied by us. It is further possible that the relative concentration of these products (or their derivatives) may also vary from sample to sample depending on (i) the degree of the concentration of the constituents or (ii) the heat-treatment conditions or (iii) the presence of hydrogen ions. These oxidation products and their derivatives can be modified to $\gamma\text{-Fe}_2\text{O}_3$ (more favourably,

in the presence of moisture or hydrogen ions) or $\alpha\text{-Fe}_2\text{O}_3$ (more favourably, in dry atmosphere or at higher temperatures). The addition of P_2O_5 in the form of H_3PO_3 favours the formation of the spinel phase such as $\gamma\text{-Fe}_2\text{O}_3$ or their other derivatives. However it does not rule out the possibility of coexistence of the spinel or hexagonal phase of $\alpha\text{-Fe}_2\text{O}_3$. In fact the coexistence of these two oxidation products of iron is quite common.

3.3.4 Summary

The effect of nucleating agents such as 2 mole % of P_2O_5 or TiO_2 on the crystallization of yttrium iron garnet in $\text{Na}_2\text{O-SiO}_2\text{-Y}_2\text{O}_3\text{-Fe}_2\text{O}_3$ glass system has been studied using Mössbauer, X-ray diffraction, DTA and magnetization measurements. The effect was studied by giving two-stage heat-treatment (at the glass transition temperature, T_g , and crystallization temperature, T_c) to the samples. Mössbauer spectra as well as the X-ray diffractograms of all the glass samples show the presence of YIG (with various amounts of formation) and other magnetic crystalline phases. The results of Mössbauer studies agree with magnetization measurements. Results of Mössbauer measurements along with the magnetization and X-ray data indicate that P_2O_5 is a better nucleating agent than TiO_2 . The Mössbauer data also indicate that the trivalent iron prefers tetrahedral coordination in the samples containing TiO_2 and octahedral

coordination in samples containing P_2O_5 .

It is also indicated by the Mössbauer data that the volume fraction of the YIG phase precipitated in the two-stage heat-treated sample is largest for the Y9P sample. The present results also indicate that (i) 800°C is the most optimum growth temperature for the most efficient precipitation of the YIG phase in the Y9P sample, and (ii) the precipitation of the YIG phase is more efficient in the Y9P sample undergoing two-stage heat-treatment ($720 + 800^\circ\text{C}$) for 2 h each than in the single stage heat-treatment at 800°C for 40 h.

3.4 Study of $PbO-B_2O_3-Al_2O_3-Fe_2O_3-Y_2O_3$ Glass System

3.4.1 Introduction

As seen in the previous sections, controlled crystallization of glasses can be employed to produce glass ceramics with interesting magnetic and microstructural properties. Results of Mössbauer, EPR and other studies of the $Na_2O-SiO_2-Fe_2O_3-Y_2O_3$ glass system described previously have shown how the physical properties of the glass ceramic systems can be investigated. In an effort to develop and study novel magnetic glass ceramics we have studied the system $PbO-B_2O_3-Al_2O_3-Fe_2O_3-Y_2O_3$. The results of Mössbauer, magnetization, X-ray and other measurements of such glass ceramic samples heat-treated at different temperatures are reported below.

3.4.2 Experimental method

(a) Sample preparation

The glass samples were prepared from reagent grade chemicals by melting the mixture in an alumina crucible at about 1200 °C in an electrically heated furnace. The composition of the samples prepared was as follows : PbO (45 mol %), B₂O₃ (35 mol %), Al₂O₃ (4 mol %), Fe₂O₃ (10 mol %) and Y₂O₃ (6 mol %). Glass plates were cast by pouring the melt onto an aluminium mould. The as-cast sample was annealed in a furnace at 300 °C for about 2 h before further characterization.

(b) Measurements

The DTA, X-ray, magnetization and Mössbauer measurements were carried out by methods described earlier in section 3.2.2.

3.4.3 Results and discussion

The DTA data for the glass sample is shown in Fig. 3.21. From the DTA plot the glass transition (T_g) and crystallization (T_c) temperatures were estimated to be 560 and 660 °C respectively. X-ray diffraction measurements carried out with the glass sample heat-treated at 660 °C showed a number of diffraction lines most of which correspond to α -Fe₂O₃ phase (Table 3.10). No evidence for magnetic interaction was found for the as-prepared sample

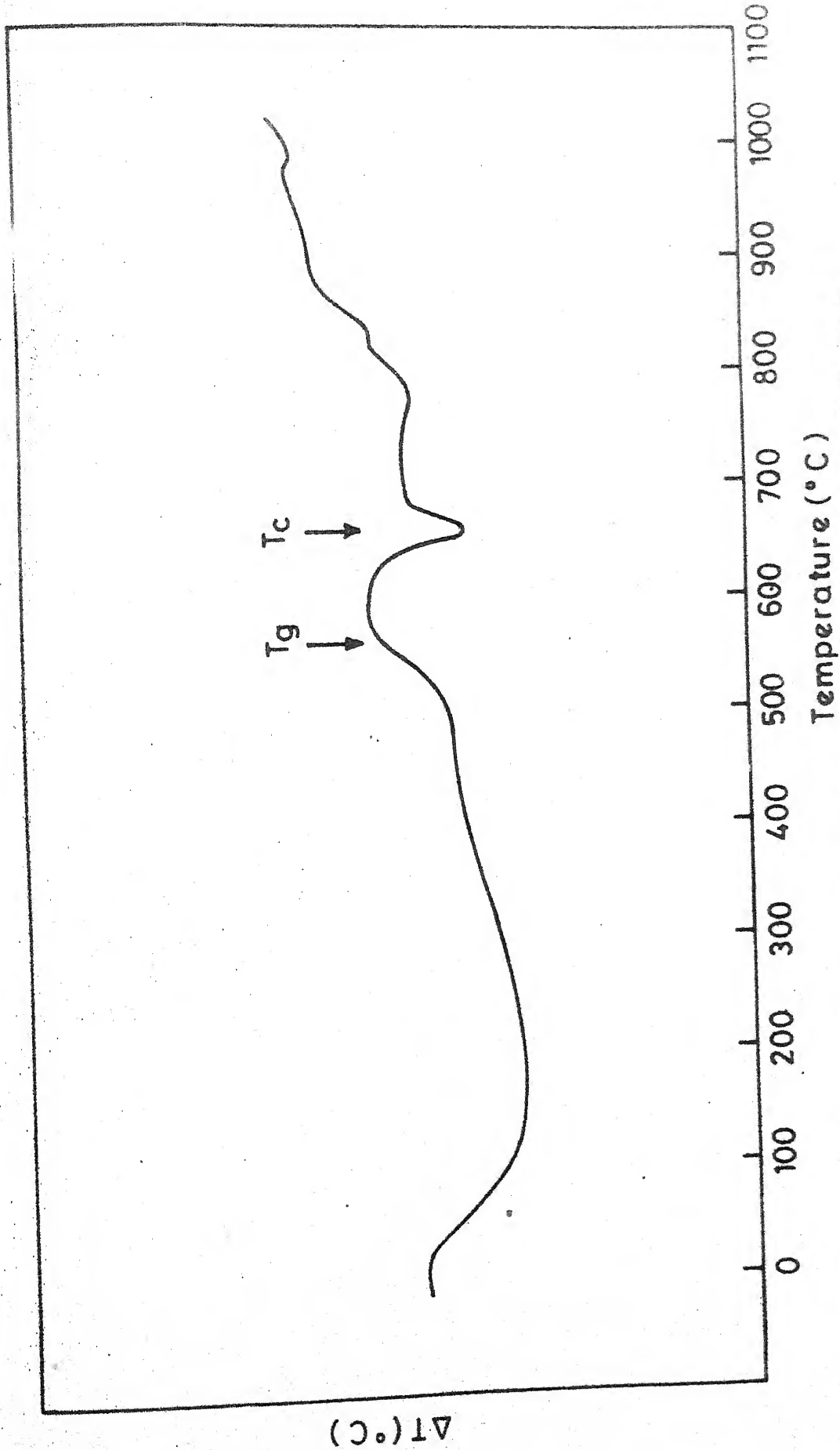


Fig. 3.21 DTA plot of the as-prepared sample $\text{PbO-B}_2\text{O}_3\text{-Al}_2\text{O}_3\text{-Pb}_2\text{O}_3\text{-Y}_2\text{O}_3$.

TABLE 3.10

X-ray diffraction data of the samples with different heat-treatment. T denotes the heat-treatment temperature.

T = 330°C			T = 660°C			Assignment
d (nm)	Intensity ⁺	hkl	d (nm)	Intensity ⁺	hkl	
			0.4055	VS	-	
			0.3613	VW	012	α -Fe ₂ O ₃
			0.3434	VW	211	γ -Fe ₂ O ₃
0.2690	M	104				α -Fe ₂ O ₃
0.2684	M	104				α -Fe ₂ O ₃
			0.2643	M	310	γ -Fe ₂ O ₃
0.2274	M	521	0.2255	W	-	-
			0.2177	VW	-	-
0.2074	M	400	0.2052	S	400	γ -Fe ₂ O ₃
		202			202	α -Fe ₂ O ₃
0.1868	VS	426				γ -Fe ₂ O ₃
			0.1819	W	024	α -Fe ₂ O ₃
			0.1765	M	-	-
0.1704	W	422				γ -Fe ₂ O ₃
0.1691	W	116				α -Fe ₂ O ₃
			0.1442	W	300	α -Fe ₂ O ₃
			0.1377	W	620	γ -Fe ₂ O ₃

⁺ VS = very strong; S = strong; M = medium; W = weak;
VW = very weak.

from the magnetization and preliminary EPR data. At a magnetic field of 6.10 kOe the values of magnetic moment observed for the as-prepared sample and the sample heat-treated at the crystallization temperature (660°C) were 6.15×10^{-2} emu/g and 2.07 emu/g. The plots of the magnetization versus magnetic field for the as-prepared sample and sample heat-treated at 300°C show typically paramagnetic behaviour while that for the sample heat-treated at T_c (660°C) shows a magnetic interaction with saturation effects (Fig. 3.22). In Fig. 3.23 is shown the plot of saturation magnetization versus temperature for the glass sample heat-treated at 660°C . Two transitions in the system are observed from this plot, one around 180°C and the other around 510°C . The transition at 180°C appears to be similar to a compensation temperature observed in the case of rare earth substituted garnets or some other ferrites. The effective moments calculated from the saturation magnetization is much less than what is expected from purely ferromagnetic interaction of iron ions. As discussed below, the iron ions have been assumed to be present in a +3 state on the basis of Mössbauer data reported in the following paragraph.

The Mössbauer spectra of the as-prepared glass sample as well as the samples heat-treated at 330, 500, 560, and 660°C are shown in Fig. 3.24. All these spectra were measured at room temperature. The values of the Mössbauer

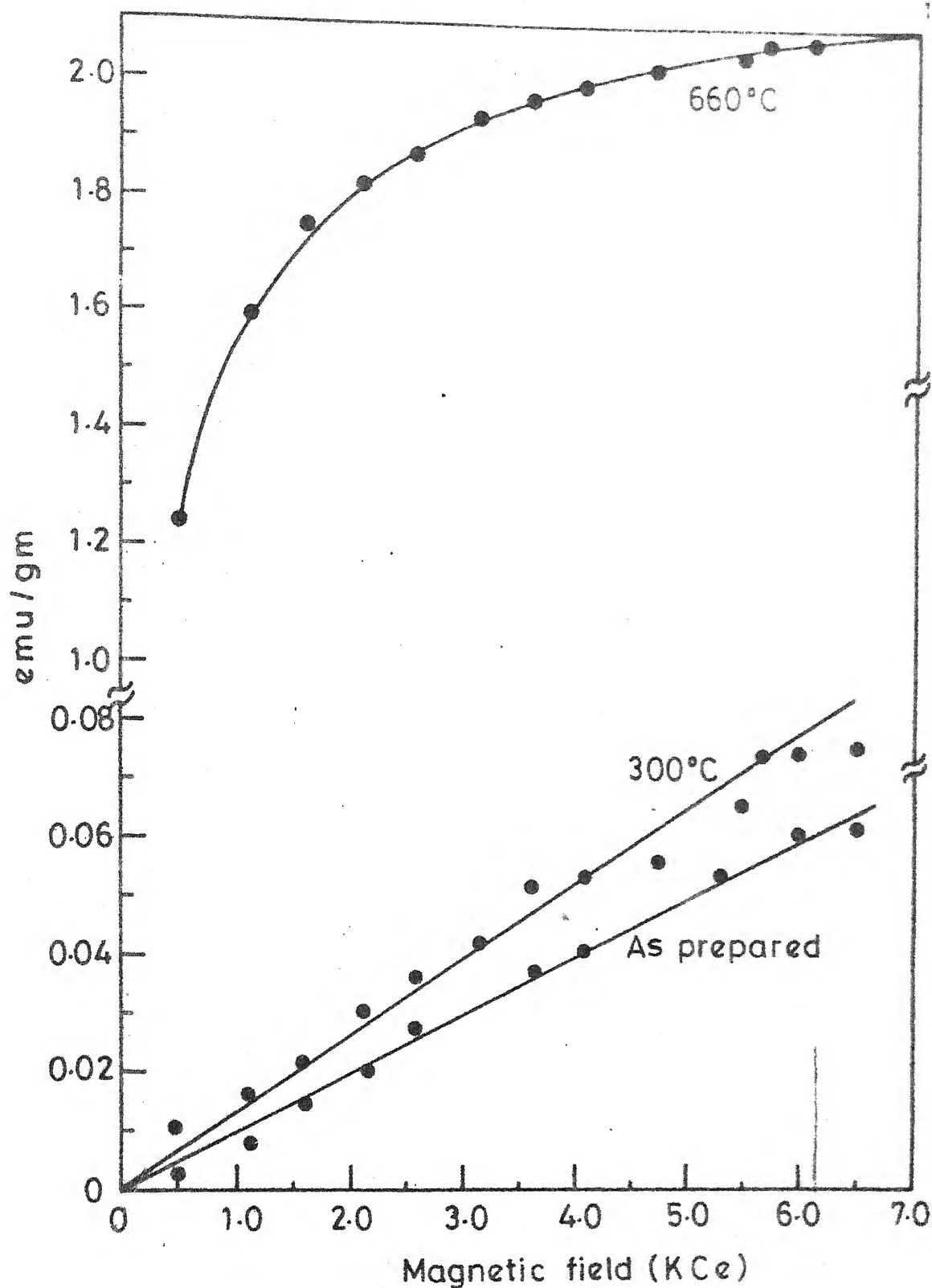


Fig. 3.22 Plot of magnetization versus magnetic field for the (a) as-prepared sample, (b) sample heat-treated at 300°C for 4 h and (c) sample heat-treated at 660°C for 4 h.

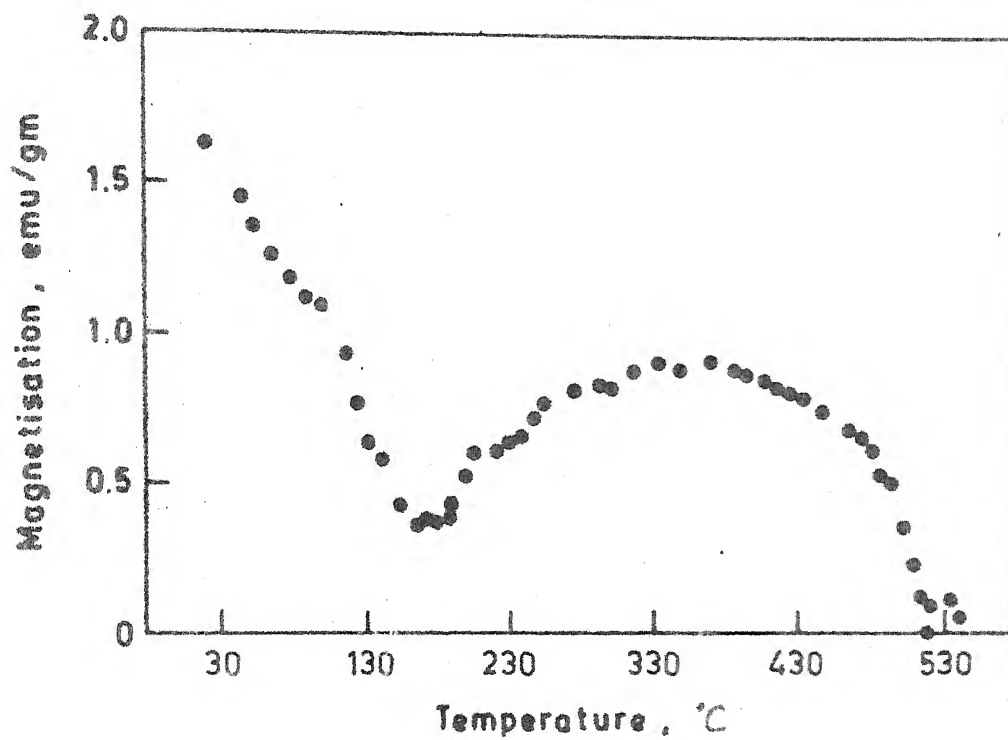


Fig. 3.23 Plot of magnetization versus temperature for the sample heat-treated at 660°C for 4 h.

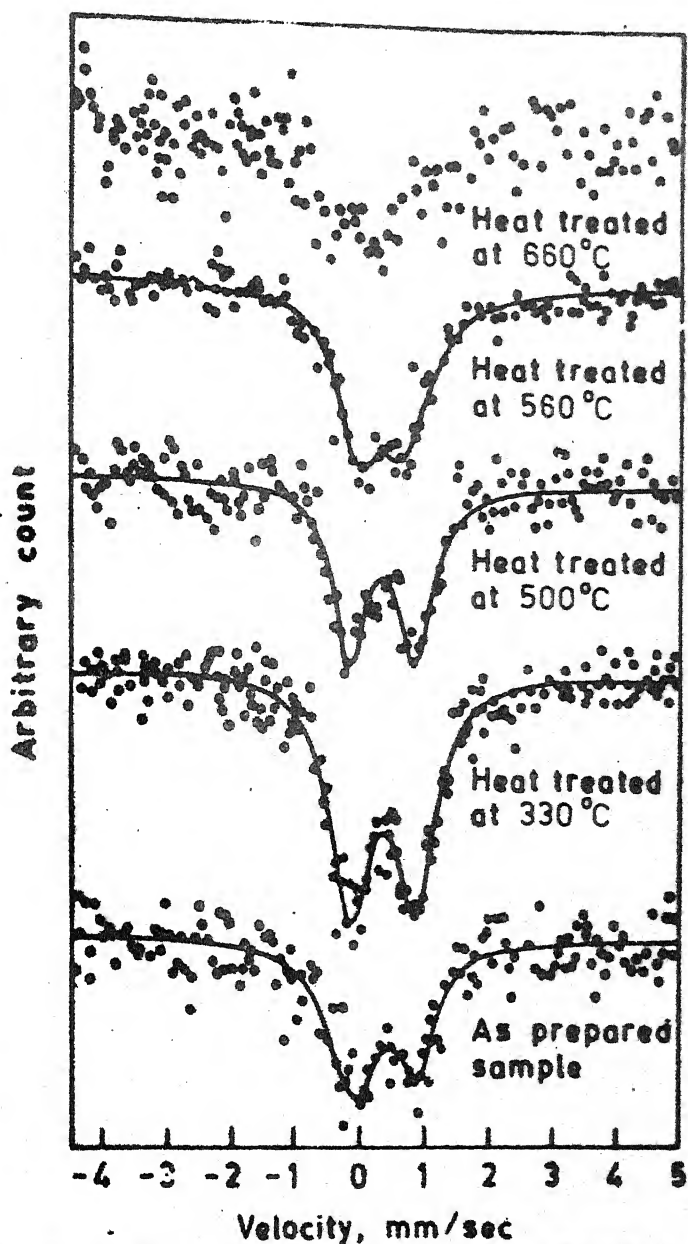


Fig. 3.24 Room-temperature Mössbauer spectra of the sample $\text{PbO-B}_2\text{O}_3\text{-Al}_2\text{O}_3\text{-Fe}_2\text{O}_3\text{-I}_2\text{O}_3$ heat-treated at different temperatures.

parameters determined from these spectra are given in Table 3.11. It will be noted that all the Mössbauer spectra (Fig. 3.24) except the one for the sample heat-treated at 660°C , show a doublet (i.e. quadrupole splitting only) structure. The Mössbauer spectrum for the sample heat-treated at 660°C shows a weak formation of a magnetic phase. The magnetic structure in this spectrum is not properly developed, although the recorded counts per channel in this spectrum were 2.2×10^6 counts as compared to 4×10^5 in the case of as-prepared sample. The development of magnetic hyperfine field is probably restricted due to the presence of lead ions which can give rise to a higher absorption of the Mössbauer gamma rays. The statistical fluctuation near the base line in the Mössbauer spectra of Fig. 3.24 is thus high and it might indicate poorly developed magnetic structure.

The values of the isomer shift (IS) for the four samples (as-prepared sample and the samples heat-treated for 4 h at 330 , 500 and 560°C) are all characteristic of Fe^{3+} ion [12]. The plot of the IS-values against the heat-treatment temperature is shown in Fig. 3.25 and the observed behaviour is similar to that for the $\text{Na}_2\text{O-SiO}_2\text{-Fe}_2\text{O}_3\text{-Y}_2\text{O}_3$ glass ceramic reported earlier (Fig. 3.4). The IS-value for the as-prepared glass sample is observed to be $0.372 \pm 0.076 \text{ mm sec}^{-1}$ with respect to $\alpha\text{-Fe}$ (Table 3.11). This IS-value corresponds to a value which is intermediate between octahedral and tetrahedral Fe^{3+} [12]. It is further

TABLE 3.11

Mössbauer parameters of as-prepared samples as well as sample heat-treated at different temperatures.

Heat-treatment Temperature	IS (mm sec ⁻¹)		ΔE (mm sec ⁻¹)	Peak-widths (mm sec ⁻¹)	
	w.r.t. Sodium nitroprusside	w.r.t. to α -Fe		I	II
As-prepared	0.636±0.076	0.372±0.076	0.970±0.076	0.95±0.12	0.62±0.12
330 °C for 4 h	0.625±0.029	0.361±0.029	1.052±0.029	0.83±0.05	0.77±0.05
500 °C for 4 h	0.569±0.043	0.305±0.043	1.028±0.044	0.62±0.07	0.67±0.07
560 °C for 4 h	0.511±0.088	0.247±0.088	0.699±0.088	0.67±0.12	1.16±0.12
660 °C for 4 h	0.278±0.254	0.014±0.254	0.788±0.254	0.41±0.37	1.92±0.39

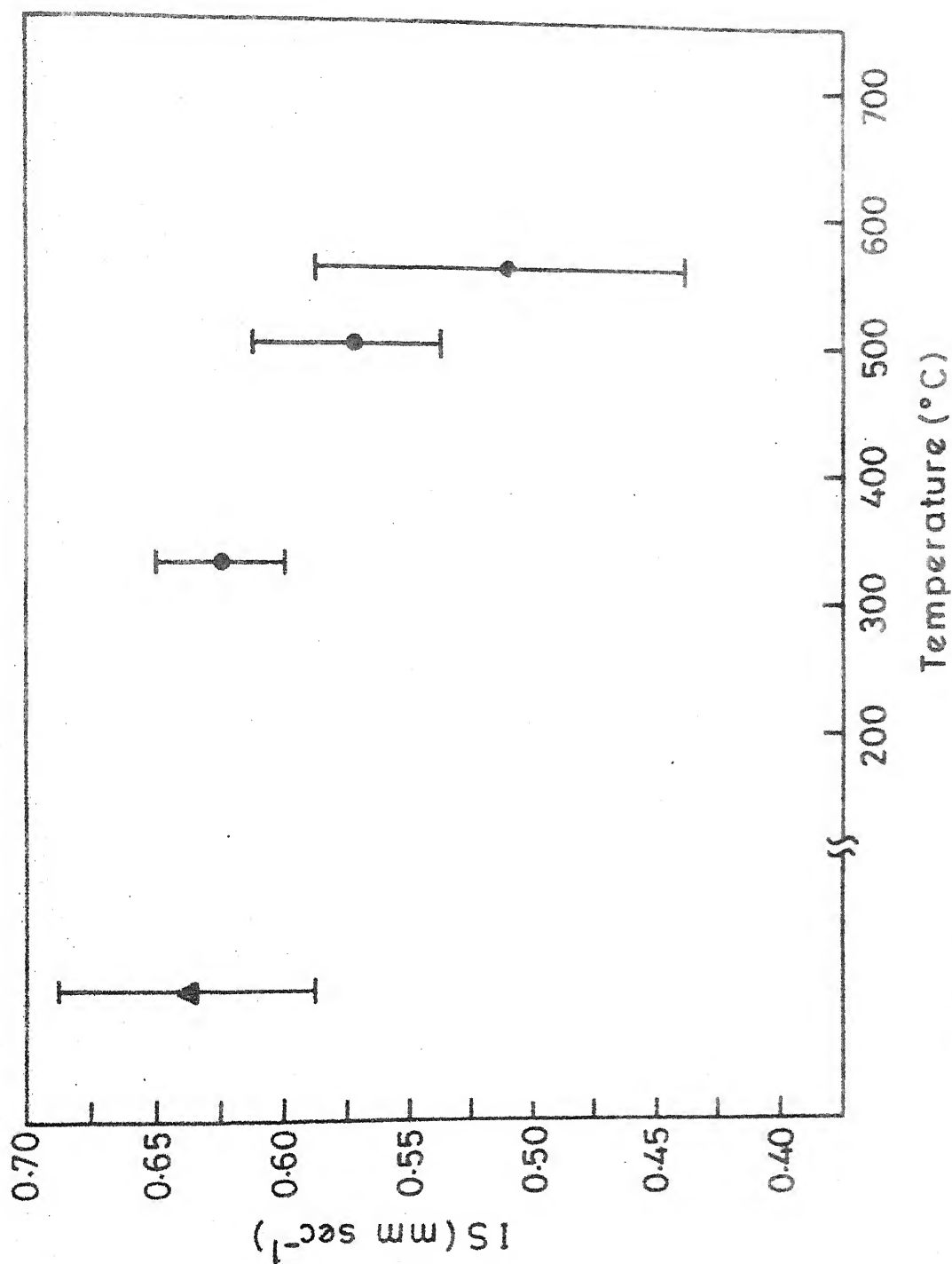


Fig. 3.25 Plot of the isomer shift (IS) against heat-treatment temperature. The isomer shift values are given relative to the sodium nitroprusside absorber. Point

observed that the linewidth of these doublet lines are rather large, thus indicating the presence of more than one doublet structure. To examine this aspect we analyzed the Mössbauer spectrum for the as-prepared sample by applying Window's method [11] for obtaining a fit of the EFG distribution $p(|V|)$ to the observed spectra. The resulting EFG distribution is shown in Fig. 3.26, and it supports the possibility of two doublet structures of different intensities. The presence of two different types of Fe^{3+} ions could be attributed to inequivalent tetrahedral and octahedral Fe^{3+} ions.

As observed earlier, the Mössbauer spectrum for the sample heat-treated at 660°C is complex in nature, the doublet structure existing together with a weakly developed magnetic structure. This explains the larger errors ascribed to the values of IS and ΔE (quadrupole splitting) for this sample (Table 3.11). This sample appears to consist of ferrimagnetic particles and this is supported by the magnetic data shown in Figs. 3.22 and 3.23.

The value of quadrupole splitting $\Delta E = 0.970 \pm 0.076$ observed for the as-prepared glass sample (Table 3.11) is about the same as that for the other glass ceramic $\text{Na}_2\text{O}-\text{SiO}_2-\text{Fe}_2\text{O}_3-\text{Y}_2\text{O}_3$ reported in Table 3.2. It is observed that the value of ΔE remains essentially constant upto the heat-treatment temperature of 500°C and it decreases for the sample heat-treated at $T = 560^\circ\text{C}$ (Fig. 3.27) the ΔE

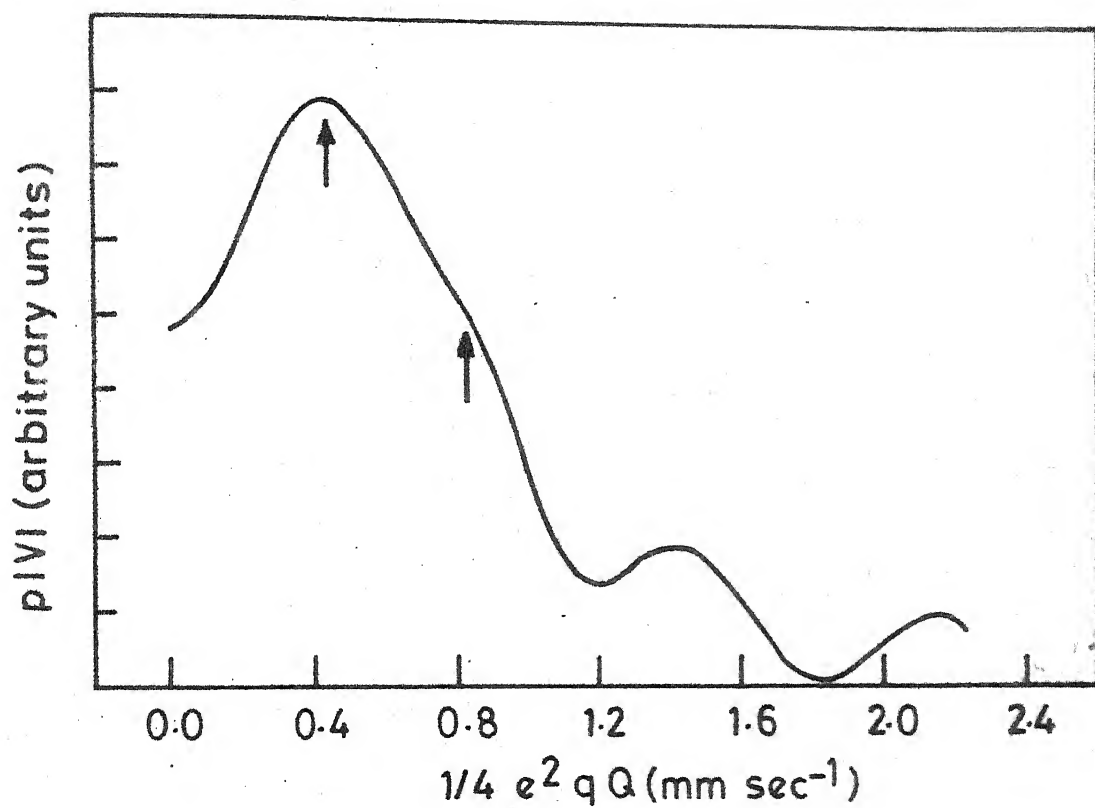


Fig. 3.26 EFG distribution for the as-prepared sample $\text{PbO-B}_2\text{O}_3\text{-Al}_2\text{O}_3\text{-Fe}_2\text{O}_3\text{-Y}_2\text{O}_3$.

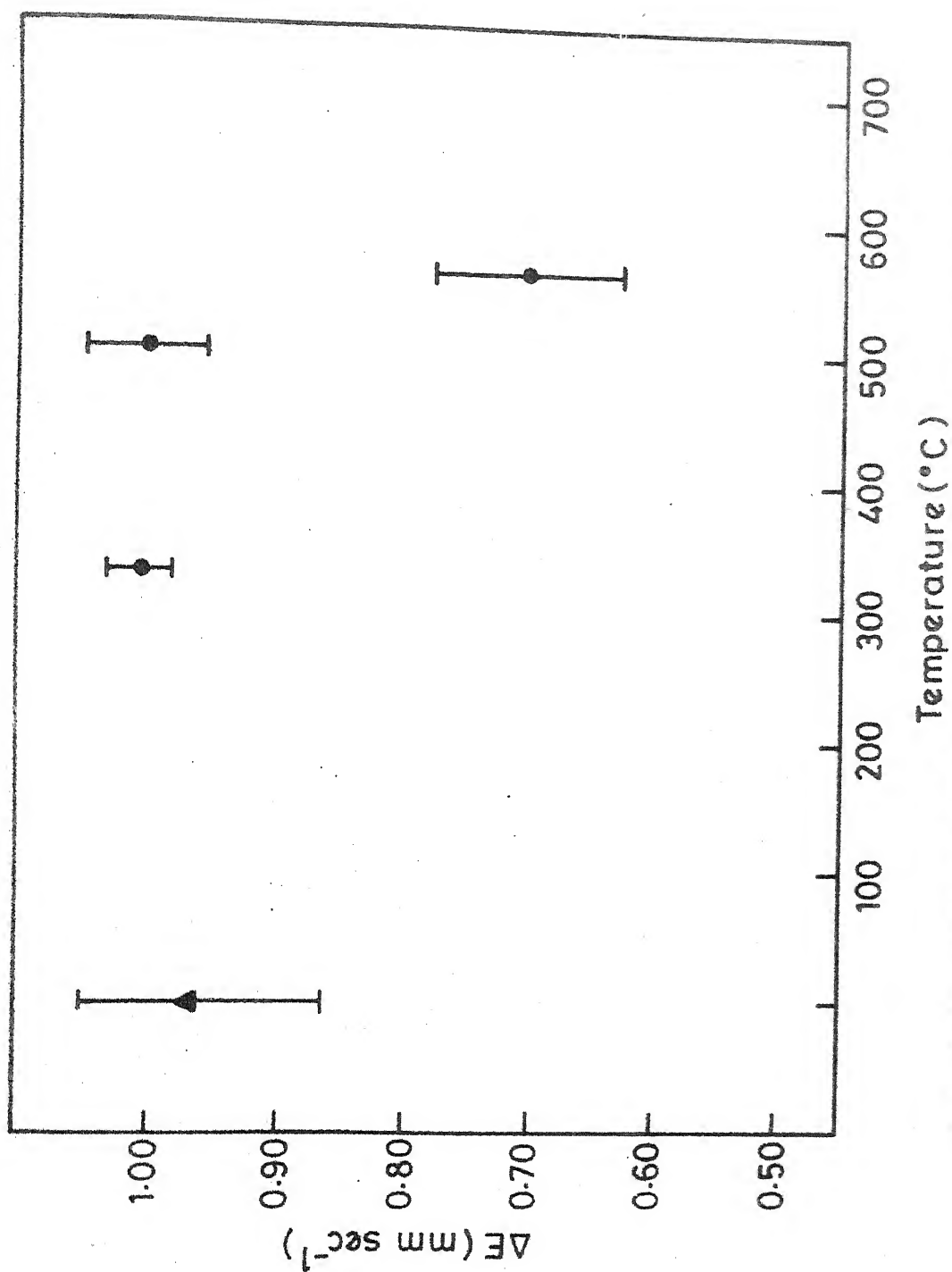


Fig. 3.27 Plot of the quadrupole splitting (ΔE) against the heat-treatment temperatures. Point marked as \blacktriangle refers to the as-prepared sample.

value for the sample heat-treated at 660°C (T_c) also shows a decrease although the associated error is relatively larger. This behaviour of the ΔE values with the heat-treatment temperature is similar to that observed for the $\text{Na}_2\text{O-SiO}_2\text{-Fe}_2\text{O}_3\text{-Y}_2\text{O}_3$ glass ceramic reported earlier (Fig. 3.6).

From the discussions in the preceding paragraphs, it is clear that Fe^{3+} ions are unequally distributed between octahedral and tetrahedral sites. This behaviour is usually observed in spinel and garnet structures. In the present case, X-ray diffraction lines (Table 3.10) clearly show the predominant phase to be $\alpha\text{-Fe}_2\text{O}_3$. Electron micrograph of the sample heat-treated at 660°C (Fig. 3.28) indicate the presence of two distinctly different particle sizes. The larger particles, which are around $0.4\text{ }\mu\text{m}$ in size, might arise from the $\alpha\text{-Fe}_2\text{O}_3$ phase because sharp diffraction lines are observed which correspond to $\alpha\text{-Fe}_2\text{O}_3$ phase. The smaller particles which are $< 100\text{ }\text{\AA}$ in size and are distributed around larger $\alpha\text{-Fe}_2\text{O}_3$ particles could probably be due to some spinel phase such as $\gamma\text{-Fe}_2\text{O}_3$. However, it is difficult to identify this phase from the X-ray data, probably because of its smaller size. On the other hand, the estimated Curie temperature is 510°C from the magnetization data (Fig. 3.23) which indicates the presence of some spinel phase $\gamma\text{-Fe}_2\text{O}_3$. However another transition around 180°C which is just like a compensation temperature is not clearly

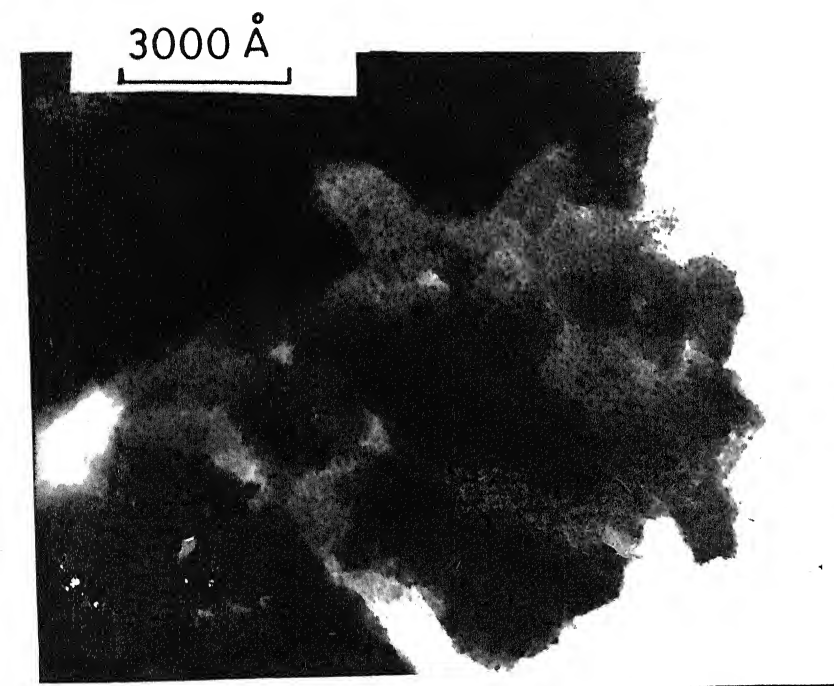


Fig. 3.28 Electron micrograph of the heat-treated sample at 660°C.

understood. We propose that this compensation temperature could be due to an exchange interaction between surface ions of $\alpha\text{-Fe}_2\text{O}_3$ particles and the ions of surrounding $\gamma\text{-Fe}_2\text{O}_3$ or substituted $\gamma\text{-Fe}_2\text{O}_3$ particles. In fact, it appears that $\alpha\text{-Fe}_2\text{O}_3$ particles form the inner core and the spinel phase forms a skin around the $\gamma\text{-Fe}_2\text{O}_3$ particles. A similar explanation has been put forward in the case of $\text{BaO-B}_2\text{O}_3\text{-Fe}_2\text{O}_3$ glass ceramics [1].

3.4.4 Summary

Mössbauer, X-ray diffraction and magnetization data of 45 PbO -35 B_2O_3 -4 Al_2O_3 -10 Fe_2O_3 -6 Y_2O_3 system heated at its crystallization temperature indicate the presence of large $\alpha\text{-Fe}_2\text{O}_3$ particles surrounded by smaller spinel particles. A compensation temperature observed at 180°C is ascribed to an exchange interaction of the surface ions of $\alpha\text{-Fe}_2\text{O}_3$ with the surrounding spinel phase.

REFERENCES

1. P.W. McMillan, Glass-Ceramics, Academic Press, London (1979).
2. Advances in Nucleation and Crystallization in Glasses, American Ceramic Society (1971).
3. T. Komatsu, N. Soga and M. Kunugi, J. Appl. Phys. 50, 6469 (1979).
4. T. Komatsu and N. Soga, J. Appl. Phys. 51, 601 (1980).
5. R.R. Shaw and J.H. Heasley, J. Amer. Ceram. Soc. 50, 297 (1967).
6. W.J.S. Blackburn and B.P. Tilley, J. Mater. Sci. 9, 1265 (1974).
7. B.T. Shirk and W.R. Buessem, J. Amer. Ceram. Soc. 53, 192 (1970).
8. E.P. Wohlfarth, ''Ferromagnetic Materials'' Vol. II, North-Holland, Amsterdam (1980).
9. D. Bahadur, B. Sharma and D. Chakravorty, J. Mater. Sci. Letters 1, 106 (1982).
10. G.C. Das, T.K. Reddy and D. Chakravorty, J. Mater. Sci. 13, 3211 (1978).
11. B. Window, J. Phys. B4, 401 (1971).
12. C.R. Kurkjian and E.A. Sigety, Phys.Chem.Glasses 9, 73 (1968).

13. J. Dannon in ''Chemical Applications of Mössbauer Spectroscopy'', edited by V.I. Goldanskii and R.H. Herber, Academic Press, New York (1968), p. 159.
14. J.J. Van Loef, Physica 32, 2102 (1966).
15. K.J. Kim, M.P. Maley and R.K. Macrone in Amorphous Magnetism, Vol. II, edited by R.A. Levay and R. Hasegawa, Plenum Press, New York (1977), p. 627.
16. W. Kündig, H. Bommel, G. Constabavis and R.H. Lindquist, Phys. Rev. 142, 327 (1966).
17. C.R. Kurkjian and E.A. Sigety, Phys. Chem. Glasses, 5, 63 (1964).
18. N.V. Nair, Ph.D. Thesis, Indian Institute of Technology, Kanpur (1981), Unpublished.
19. A.K. Bandopadhyaya, J. Zarzycki, P. Aurie and J. Chappert, J. Non. Cryst. Solids, 40, 353 (1980).
20. W.H. Von Aulock, ''Handbook of Microwave Ferrite Materials'', Academic Press, New York (1965).
21. D. Bahadur and K.N. Rai, Mater. Res. Bull. 15, 501 (1980).
22. D. Bahadur, P.K. Das and D. Chakravorty, J. Appl. Phys. 53, 7813 (1982).
23. M. Fahmy, M.J. Park, M. Tomozawa and R.K. MacCrone, Phys. Chem. Glasses, 13, 21 (1972).

CHAPTER - 4

MOSSBAUER SPECTROSCOPIC STUDIES OF THE METALLIC GLASS SYSTEM $\text{Fe}_{100-x}\text{B}_x$

4.1 Introduction

In recent years there has been a tremendous growth of interest in the study of metallic glasses because of the theoretical and technological interest in these solids [1-8]. The metallic glasses are similar to silicate glasses as far as the absence of long range periodicity is concerned. In both these types of glasses the correlations between the atomic positions are completely lost over distances of more than about 5 atomic spacings. However the metallic glasses are different from the familiar silicate glasses in other properties. Metal glasses are amorphous metallic alloys and interest in these systems grew after Duwez et al. [9] invented a practical way to quench a metallic melt at a rate of more than 10^6 K sec^{-1} . Metallic glasses can be prepared by two important methods. In the first method one quenches the metal so rapidly that there is insufficient time available for the crystallites to nucleate and grow,

while in the second method the amorphous alloy is obtained by depositing the vapour phase onto a cold substrate so that the atoms, during deposition, do not have sufficient time to arrange themselves in a long-range crystalline order.

Historically, Au-25 at.% Si alloy [9] was the first amorphous metal alloy developed and this was followed by the development of Pd-20 at.% Si. The subject of metallic glasses received a big boost after the development of iron- and nickel-bearing glasses which were found to be ferromagnetic. Gubanov [10] had, in 1960, predicted the possibility of ferromagnetism in glassy metals and the experimental confirmation of this prediction is an important milestone in the field of metallic glasses. For example, Duwez and Lin [11] found, in 1967, that the amorphous alloy $\text{Fe}_{75}\text{P}_{15}\text{C}_{10}$ was a typical soft ferromagnetic alloy with a large saturation magnetization of 7 KG but a relatively low coercive force of 3 Oe. A large number of amorphous metal glasses have been developed particularly in the last decade [1-8].

The study of the various metal glasses developed so far is inspired out of their theoretical as well as technological significance. The theoretical question to be answered is : how are the magnetic characteristics affected by the amorphous atomic structure? These magnetic properties include the magnetization, Curie temperature, temperature dependence of magnetization, magnetoresistance, spin waves, critical behaviour, anisotropy, hysteresis, coercive force,

Mössbauer parameters etc. Technological interest in the amorphous magnetic alloys arises mainly because of their potential as useful soft magnetic materials. Technologically interesting metallic glasses fall into two main categories : (a) The transition metal-metalloid (TM-M) alloys typically containing about 80 at % Fe, Co or Ni with the remainder being B, C, Si, P or Al. An example of the TM-M alloys is the $\text{Fe}_{100-x}\text{B}_x$ glasses studied presently. (b) The rare earth-transition metal RE-TM alloys, (e.g. Gd-Co alloys).

In recent years the practical significance of the magnetic properties of metallic glasses has centered on the possibility that metal glass, in wide sheet form, can replace the conventional grain-oriented iron-silicon laminations in power transformers. It is estimated that such a replacement, if carried out in the U.S.A., can lead to an annual saving upto 100-200 million dollars. Other possible applications making use of the magnetic properties of metallic glasses include audio tape-recorder heads, magnetic shielding, delay lines etc. [1,2].

The electrical properties of the metallic glasses include (i) higher residual electrical resistivity near $T = 0 \text{ K}$ compared to that of a crystalline metal (ii) smaller (and usually negative) temperature coefficient of resistivity as compared to a crystalline metal and (iii) a sharp minimum in the resistivity-temperature graph at low temperatures or a broad minimum at a high temperature. Regarding the

mechanical properties of the metallic glasses, the most important feature is that they are as strong as the oxide glass (Filament of $\text{Fe}_{80}\text{B}_{20}$ glass shows mechanical strength comparable to that of glass fibre). At the same time metal glasses, unlike oxide glasses, can undergo plastic deformation at ambient temperatures.

Besides the study of the magnetic, electrical and mechanical properties of metallic glasses considerable effort has gone into the study of their structure. Such structural information has been obtained by the diffraction studies (X-ray, neutron and electron diffraction) as well as by the Mössbauer, NMR and other indirect methods and it has provided a basis for the understanding of the physical properties of the glasses. Two types of structural models (i) dense random packing of hard spheres (DRPHS) model and (ii) cluster model have been used. We shall not go into the details of these models which are described in detail elsewhere [1-8].

Various glass-forming metallic alloys can be divided into well-defined categories. Following Cahn [1] we have shown this classification in Table 4.1.

In the present work we have studied the magnetic properties of the metallic glass system $\text{Fe}_{100-x}\text{B}_x$ ($13 \leq x \leq 26$) using Mössbauer spectroscopic techniques. Before we report our studies, we have given, in the next section, a brief review of the studies of $\text{Fe}_{100-x}\text{B}_x$ glasses carried out by

Table 4.1

Classification of glass-forming alloy systems

Category	Representative system	Typical composition range, at.%.
1. T^2 or noble metal + metalloid (m)	Au-Si, Pd-Si, Co-P, Fe-B, Fe-P-C, Fe-Ni-P-B, Mo-Ru-Si, Ni-P-Si	15-25 m
2. T^1 metal + T^2 (or Cu)	Zr-Cu, Zr-Ni, Y-Cu, Ti-Ni, Nb-Ni, Ta-Ni, Ta-Ir	30-65 Cu or T^2 or smaller range
3. A metal + B metal	Mg-Zn, Ca-Mg Mg-Ga	Variable
4. T^1 metal + A metal	(Ti,Zr)-Be	20-60 Be
5. Actinide + T^1	U-V, U-Cr	20-40 T^1

Key :

- T^2 : Late transition metal (Mn, Fe, Co, Ni Group)
 T^1 : Early transition metal (Sc, Ti, V Group)
A metal : Li, Mg groups.
B metal : Cu, Zn, Al groups.

other workers with the help of Mössbauer spectroscopy.

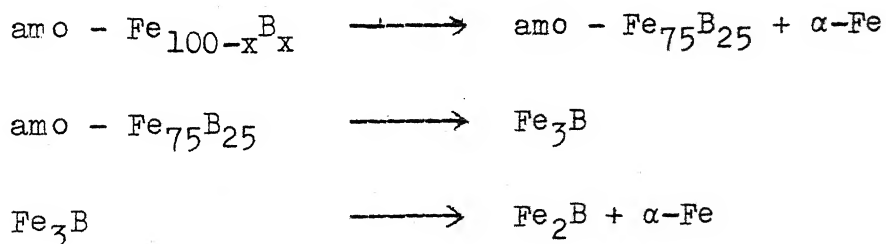
4.2 Review of Mössbauer Studies of $\text{Fe}_{100-x}\text{B}_x$ ($13 \leq x \leq 26$)

The crystallization process of the binary amorphous metal alloys $\text{Fe}_{100-x}\text{B}_x$ has been investigated by ^{57}Fe Mössbauer spectroscopy by many workers during the last few years. Chien [12] has reported ^{57}Fe Mössbauer spectroscopic studies of $\text{Fe}_{80}\text{B}_{20}$ from 4.2 to 1050 K. He reported sextet or six-line pattern at all temperatures, with broad width (FWHM) for the outer and middle lines. Using the Fourier series method developed by Window [13], Chien obtained a well defined hyperfine field distribution $p(H)$ which was analyzed in terms of temperature dependence and other aspects. The temperature dependence of the isomer shift in $\text{Fe}_{80}\text{B}_{20}$ was studied and compared with that of Fe_2B and $\alpha\text{-Fe}$.

In a subsequent paper Chien et al. [14] studied the magnetic properties of amorphous $\text{Fe}_{100-x}\text{B}_x$ ($14 \leq x \leq 28$) and crystalline Fe_3B by using ^{57}Fe Mössbauer spectroscopy and in some cases magnetization measurements. These authors determined the Curie temperature of the samples and the distribution of hyperfine fields from 4.2 K to the Curie temperature. In the case of $\text{Fe}_{76}\text{B}_{24}$, they found that the distribution $p(H)$ shifts to lower H values with increasing temperature. The shape of $p(H)$ was unchanged but the

width (ΔH) of $p(H)$ steadily decreased with increasing T . The various hyperfine fields exhibited almost similar temperature dependence. The isomer shift of the $Fe_{100-x}B_x$ samples at 4.2 K showed a smooth decrease with the decreasing value of x , the boron content. The hyperfine magnetic field H_{int} at 4.2 K showed a smooth increase with the decreasing values of x .

Kemeny et al. [15] studied the structure and crystallization of amorphous $Fe_{100-x}B_x$ ($12 \leq x \leq 25$) alloys using Mössbauer spectroscopy, differential scanning calorimetry and magnetization measurements. These authors found that the first stage in the crystallization process is the precipitation of α -Fe until the composition of the remaining glass reaches $Fe_{75}B_{25}$. During the second stage the remaining glass transforms into the Fe_3B intermetallic compound which decomposes into α -Fe and Fe_2B at higher temperatures. The crystallization sequence for the $Fe_{100-x}B_x$ ($12 \leq x \leq 25$) system as proposed by these authors is as follows :



where amo stands for amorphous phase.

Ruckman et al. [16] carried out X-ray crystallographic and Mössbauer spectroscopic studies of amorphous $Fe_{100-x}B_x$

alloy ($14 \leq x \leq 20$) annealed at 615 K for different annealing times. These studies were aimed at examining the kinetics of the crystallization process in $\text{Fe}_{100-x}\text{B}_x$ alloys. Formation of crystalline $\alpha\text{-Fe}$ and Fe_3B was observed as a result of the heat-treatment. Crystallization rates of the $\alpha\text{-Fe}$ phase were observed to be dependent on boron concentration and the annealing time.

Oshima et al. [17] and Oshima [18] also reported ^{57}Fe Mössbauer spectroscopy of $\text{Fe}_{100-x}\text{B}_x$ ($x = 12 - 15$) alloys and these results revealed the characteristic dependence of the H_{int} on x and this was interpreted in terms of the interactions between iron and boron atoms in different ways depending on the boron content and the microstructure of amorphous matrix. Similar observations were reported by Oshima and Fujita [19] in another paper.

Koshimura et al. [20] studied the temperature dependence of the internal field distribution in amorphous $\text{Fe}_{83}\text{B}_{17}$ and $\text{Fe}_{82}\text{P}_{18}$ alloys. The peak values of the internal field distribution $p(H)$ and the distribution of magnetic moments $W(m)$ were analyzed in terms of their temperature dependence. More recently Kemeny et al. [21] have studied the crystallization kinetics of $\text{Fe}_{100-x}\text{B}_x$ ($12 \leq x \leq 26$) alloys by Mössbauer spectroscopy and differential scanning calorimetry.

It is thus seen that the amorphous $\text{Fe}_{100-x}\text{B}_x$ alloys have been studied for different concentrations (x) of boron

by different authors by measuring their Mössbauer spectra at different temperatures. Although these studies have provided valuable information about the crystallization process in these metallic glasses, the kinetics of crystallization are not completely understood yet. In the present work our aim was to further characterize the crystallization process in the $\text{Fe}_{100-x}\text{B}_x$ alloys. To this aim we selected samples of amorphous $\text{Fe}_{100-x}\text{B}_x$ ($x = 13$ to 26) alloys and subjected them to heat treatment at 100 , 200 , 300 , 350 and 400°C for 1 h each and studied them by Mössbauer spectroscopy. The crystallization characteristics were also followed by differential thermal analysis (DTA) and transmission electron microscopy (TEM). The choice of the x values was made in the range $x = 13$ to 26 because these amorphous alloys show most interesting behaviour around $x = 20$ [22]. The heat-treatments were chosen so that one could follow the kinetics of crystallization throughout. Ruckman et al. [16] had annealed their samples of $\text{Fe}_{100-x}\text{B}_x$ ($14 \leq x \leq 20$) only at 615 K or 342°C . In our studies we have carried out the heat-treatment upto a temperature of 673 K or 400°C at which the crystallization is more or less complete. To examine the effect of the annealing time on the crystallization kinetics we have also studied two samples heat-treated at 350°C and 400°C for a period of 4 h. The details of the present measurements and the discussion of our results are presented in the following sections.

4.3 Experimental

4.3.1 Introduction

In the following we shall describe the experimental details of the measurements. These include the preparation of samples and measurements using the transmission electron microscopy (TEM), differential thermal analysis (DTA) and Mössbauer spectroscopy techniques.

4.3.2 Sample Preparation

The samples of the amorphous metallic alloys (or metallic glasses) $\text{Fe}_{100-x}\text{B}_x$ were obtained from the Allied Chemical Corporation, U.S.A. through the kind courtesy of Dr. R. Hasegawa. Six samples of $\text{Fe}_{100-x}\text{B}_x$ with $x = 13, 16, 18, 20, 22$ and 26 were used in the present work. These samples were prepared from the constituent elements of purity higher than 99.9 % by rapidly quenching from the melt using a chill casting technique [23]. The samples consisted of ribbons having a typical size $1.2 \text{ mm} \times 40 \text{ }\mu\text{m}$. Samples used in the TEM, DTA and Mössbauer measurements were formed in a suitable configuration (to be described later) according to the requirements of the experiment.

The 'as-obtained' or 'as-prepared' samples were given heat-treatment in a sealed tube containing argon gas for 1 h at 100, 200, 300, 350 and 400 °C and for 4 h at 350 and 400 °C. The heat-treated samples were allowed to

cool down slowly to room temperature before studying them with Mössbauer spectroscopy. In the following discussion we shall refer to a particular sample by its composition as well as the heat-treatment temperature and time period.

Thus a 300°C (1 h) sample of $\text{Fe}_{80}\text{B}_{20}$ will refer to a $\text{Fe}_{80}\text{B}_{20}$ sample heat-treated at 300°C for 1 h.

4.3.3 Measurement techniques

(a) Transmission electron microscopy

In order to carry out the transmission electron microscopy (TEM) studies, the samples were ground on emery paper to remove the surface layers. This was followed by electromechanical thinning using a Struers Tenupol unit. More details of the thinning treatment given to the samples for the TEM studies are described by Das [24] who carried out and reported these measurements. Following the thinning treatment the samples were studied with the help of a Philips EM 301 electron microscope operated at 100 KV. Crystallization studies were carried out by heating the bulk samples outside the microscope and then thinning them for electron microscopy, in a second set of experiments thin foil prepared from the amorphous material were heated inside the electron microscope using the hot stage.

(b) Differential thermal analysis

For carrying out the differential thermal analysis (DTA) the samples (in the form of ribbons) were cleaned mechanically using emery paper so that the oxide layer was removed from the surface. The ribbons were then cut into small pieces of 3 mm size and packed in a crucible for the DTA studies [24]. MOM Hungary Derivatograph was used with Al_2O_3 as a reference material. Other details are described by Das [24].

(c) Mössbauer spectroscopic measurements

The Mössbauer spectroscopic measurements were performed by using the constant acceleration spectrometer described in Sec. 2.3. Mössbauer absorbers were prepared from the $\text{Fe}_{100-x}\text{B}_x$ ribbons placed parallel and close to each other by pasting them over copper rings of 1 cm diameter. All Mössbauer spectra were recorded at room temperature. The velocity calibration and the data analysis of the Mössbauer spectra were performed by using the methods described in the earlier Chapters.

4.4 Results and Discussion

4.4.1 Results of transmission electron microscopy

The results of the investigations on thin samples of $\text{Fe}_{100-x}\text{B}_x$ using transmission electron microscopy are

discussed in detail by Das [24] who has also presented a number of micrographs and diffraction patterns corresponding to various annealing temperatures. These are summarized in Table 4.2 in terms of the transformations occurring during the crystallization. These interpretations are based on the TEM studies by Das [24]. The recent results of Das and Ramachandran [25] on the annealing of bulk materials [25] outside the electron microscope are also included in Table 4.2, along with the data about temperature and time period of heat-treatment as well as the interpretation proposed. The crystallization process in the bulk samples occurs in the temperature range $350^{\circ}\text{C} - 400^{\circ}\text{C}$ with the formation of $\alpha\text{-Fe}$ and Fe_3B . In the case of thin samples heated inside the electron microscope the temperature for the onset of crystallization is somewhat lower. Two factors are likely to contribute to the difference in the crystallization behaviour of the bulk samples and thin samples. The large surface area associated with the latter would cause heterogeneous nucleation of the crystals at temperatures lower than those encountered in bulk samples. On the other hand since the rate of heating of the thin foil inside the microscope is about $10 - 15^{\circ}\text{C}/\text{min}$, there would be an increase in the crystallization temperature compared to those encountered in prolonged isothermal treatments (such as those given in the bulk annealing of samples). The actual temperature of transformation would be the net

Table 4.2

Summary of the results obtained by the TEM, DTA, DTXD and Mössbauer studies of the $\text{Fe}_{100-x}\text{B}_x$ samples.

Sample and Composition	Transmission Electron Microscopy			DTA(a)			
	Thin Sample [24]	Bulk sample [25]		Rate of Heating ($^{\circ}\text{C}/\text{min}$)			
		T(b)	t(b)	1 [26] Peak I II		5 [24] Peak I II	
$\text{Fe}_{87}\text{B}_{13}$	amo $\underline{180^{\circ}\text{C}}$ $\alpha\text{-Fe+amo}$ \downarrow 560°C $\alpha\text{-Fe+Fe}_3\text{B}$	-	-	310	440	240	5
$\text{Fe}_{84}\text{B}_{16}$	amo $\underline{310^{\circ}\text{C}}$ $\alpha\text{-Fe+amo}$ \downarrow 450°C $\alpha\text{-Fe+Fe}_3\text{B}$	350	1h amorphous	360	405	300	4
$\text{Fe}_{82}\text{B}_{18}$	amo $\underline{350^{\circ}\text{C}}$ $\alpha\text{-Fe+amo}$ \downarrow 440°C $\alpha\text{-Fe+Fe}_3\text{B}$	350	1h amorphous	-	380	-	4
$\text{Fe}_{80}\text{B}_{20}$	amo $\underline{332^{\circ}\text{C}}$ $\alpha\text{-Fe+amo}$ \downarrow 405°C $\alpha\text{-Fe+Fe}_3\text{B}$	350	1h $\alpha\text{-Fe}$ just formed while large amount of amorphous phases still there	-	385	-	4
$\text{Fe}_{78}\text{B}_{22}$	amo $\underline{363^{\circ}\text{C}}$ $\alpha\text{-Fe+amo}$ \downarrow 400°C $\alpha\text{-Fe+Fe}_3\text{B}$	400	1h $\alpha\text{-Fe+Fe}_3\text{B}$	-	395	-	4
$\text{Fe}_{74}\text{B}_{26}$	amo $\underline{420^{\circ}\text{C}}$ $\alpha\text{-Fe+Fe}_3\text{B}$	-	-	-	415	-	4

(a) DTA = Differential Thermal Analysis. The temperature given in ($^{\circ}\text{C}$).

(b) T = temperature of heat-treatment (in $^{\circ}\text{C}$); t = time period of heat-treatment.

Contd.....

effect of these two opposing factors.

Electron-optical studies of previous investigators were mainly restricted to $\text{Fe}_{100-x}\text{B}_x$ samples having boron concentration $x = 16, 17, 20$ and 24 with $x = 20$ alloy receiving maximum attention. The present studies support primary crystallization of $\alpha\text{-Fe}$ in the $\text{Fe}_{100-x}\text{B}_x$ alloys for $x = 13, 16, 18, 20$ and 22 but not for $x = 26$. The primary crystallization temperature appears to increase with increasing boron content in thin samples, however this effect is not prominent in bulk annealed samples. The temperature at which the Fe_3B separates out in thin samples appears to decrease with increasing boron content. This behaviour is consistent with the prediction of the free energy composition diagram for these alloys. Formation of $\alpha\text{-Fe}$ in thin foils was observed to become weaker as the boron content increases from 13 to 22 as revealed by higher temperatures for primary crystallization. The tendency for the formation of Fe_3B is more in the concentrated alloys resulting in lower crystallization temperatures.

4.4.2 Differential thermal analysis

The differential thermal analysis (DTA) carried out on the $\text{Fe}_{100-x}\text{B}_x$ samples provide valuable information on the temperatures at which crystallization is initiated and the activation energy for the crystallization. The results of the DTA studies for the heating rate of $1^\circ\text{C}/\text{min}$ by Ray and Hasegawa [26] and of $5^\circ\text{C}/\text{min}$ by Das [24]

are summarized in Table 4.2. The labels I and II in Table 4.2 refer to the positions of first and second peaks observed in the DTA spectra, since some spectra showed two peaks. Differences observed in the results of Ray and Hasegawa [26] and Das [24] can be ascribed to the different rates of heating in the two measurements. The $x = 13$ and $x = 16$ samples show two peaks, one occurring at temperatures at about 300°C and the other at temperatures greater than 400°C . For the alloys having boron concentration of $x = 18, 20, 22$ and 26 , the DTA plots show only one prominent peak in the temperature range $460\text{--}490^{\circ}\text{C}$ for the heating rate of $5^{\circ}\text{C}/\text{min}$. The dependence of the temperature of occurrence of the DTA peak on the heating rate was used by Das to calculate the activation energy of the crystallization process and values of 36.9 K Cal/mole and 52.3 K Cal/mole were obtained for the 18 and 20% boron samples respectively.

4.4.3 Dynamic temperature X-ray diffraction

Recently Khan et al. [27] have studied the stability and crystallization behaviour of $\text{Fe}_{100-x}\text{B}_x$ alloys for $12 \leq x \leq 28$ by the dynamic temperature X-ray diffraction (DTXD) method. These authors have presented a plot [27] of the temperatures of first appearance of the phases found in $\text{Fe}_{100-x}\text{B}_x$ as a function of the boron concentration x . Their results, in terms of these temperatures are also shown in Table 4.2. The range of temperatures given for

Fe_3B and Fe_2B in Table 4.2 refers to the high and low temperature modifications discussed by Khan et al. [27].

In this way we have attempted to collate in Table 4.2 the available data, relevant to $\text{Fe}_{100-x}\text{B}_x$, obtained by TEM [24,25], DTA [24,26], DTXD [27] and Mössbauer studies. The Mössbauer spectroscopic results presented in Table 4.2 include those from the present work (to be discussed in Sec. 4.4.4) as well as those reported by Oshima and Fujita [19], Ruckman et al. [16] and by Franke and Rosenberg [28].

4.4.4 Mössbauer studies

The Mössbauer spectra for the sample $\text{Fe}_{87}\text{B}_{13}$, $\text{Fe}_{84}\text{B}_{16}$, $\text{Fe}_{82}\text{B}_{18}$, $\text{Fe}_{80}\text{B}_{20}$, $\text{Fe}_{78}\text{B}_{22}$ and $\text{Fe}_{74}\text{B}_{26}$ heat-treated at different temperatures are shown in Figs. 4.1 to 4.8 where the heat-treatment temperatures and its time-schedule (number of hours) are described in the caption for each figure. It is seen that for each of these six samples one observes a six-line (sextet) Mössbauer spectrum for the as-prepared sample as well as the samples heat-treated at 100, 200, 300 and 350 °C for 1 h each. However the width of each of these six line in these Mössbauer spectra is rather broad, the outer peaks showing a $\text{FWHM} \approx 1.2 \text{ mm sec}^{-1}$ and the innermost peaks showing $\text{FWHM} \approx 0.5 \text{ mm sec}^{-1}$, in agreement with Chien [12]. The observed broad width arises because of the amorphous nature of the alloys. A marked difference in the shape of the Mössbauer spectrum is seen in going from the heat-treatment

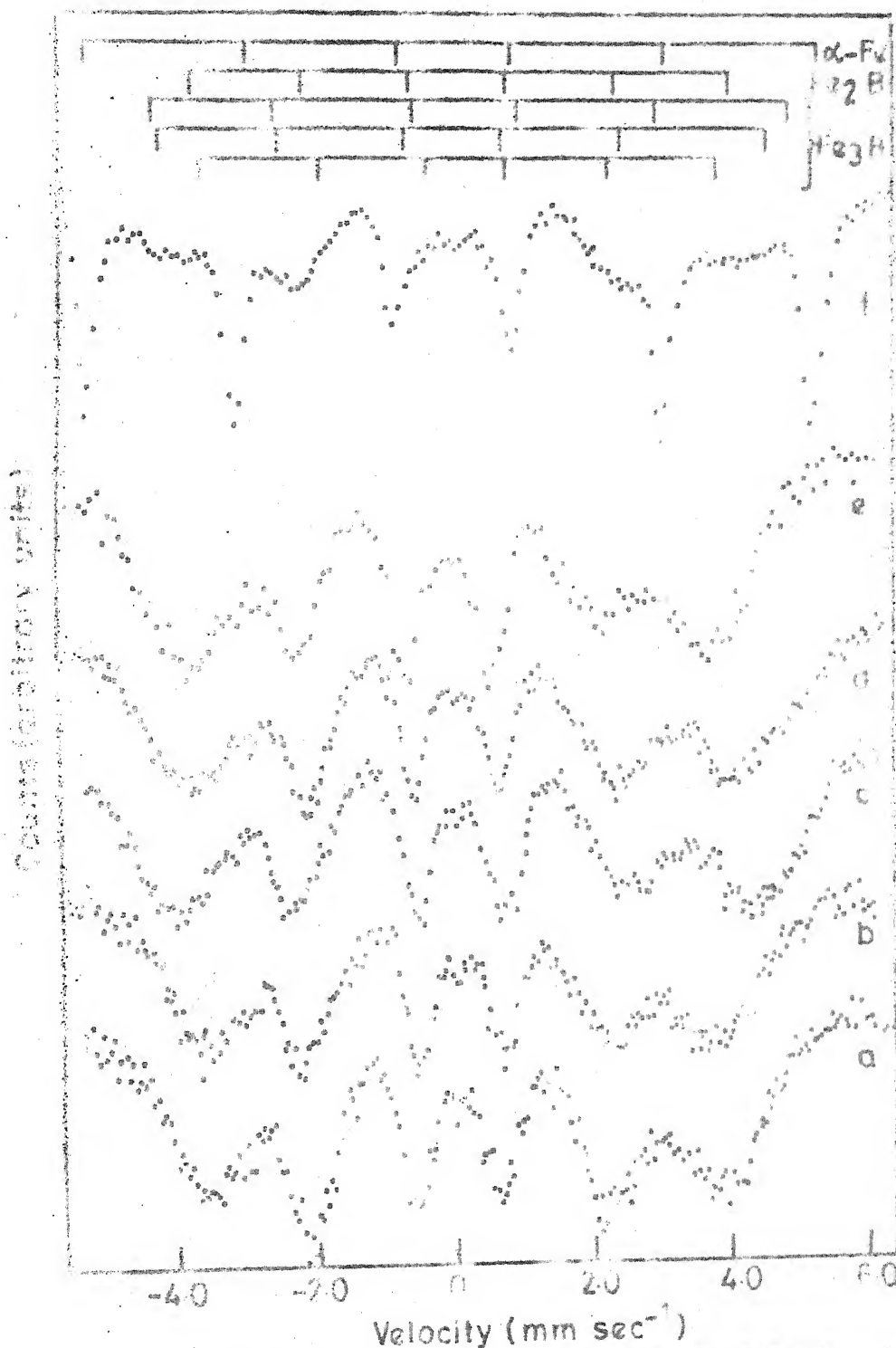


Fig. 4.1 Mössbauer spectra of $\text{Fe}_{23}\text{B}_{13}$ at room temperature. Spectrum a represents the results for the as-prepared sample while spectra b, c, d, e and f refer to samples heat-treated at $T = 100, 200, 300, 350$ and 400°C for 1 h each. The zero of the velocity scale refers to the centroid of the inner peaks of the $\alpha\text{-Fe}$ Mössbauer spectrum. The lines at the top indicate the characteristic peak positions in the Mössbauer spectra of $\alpha\text{-Fe}$, Fe_2B and Fe_3B (three sextets for Fe_3B).

Counts(arbitrary units)

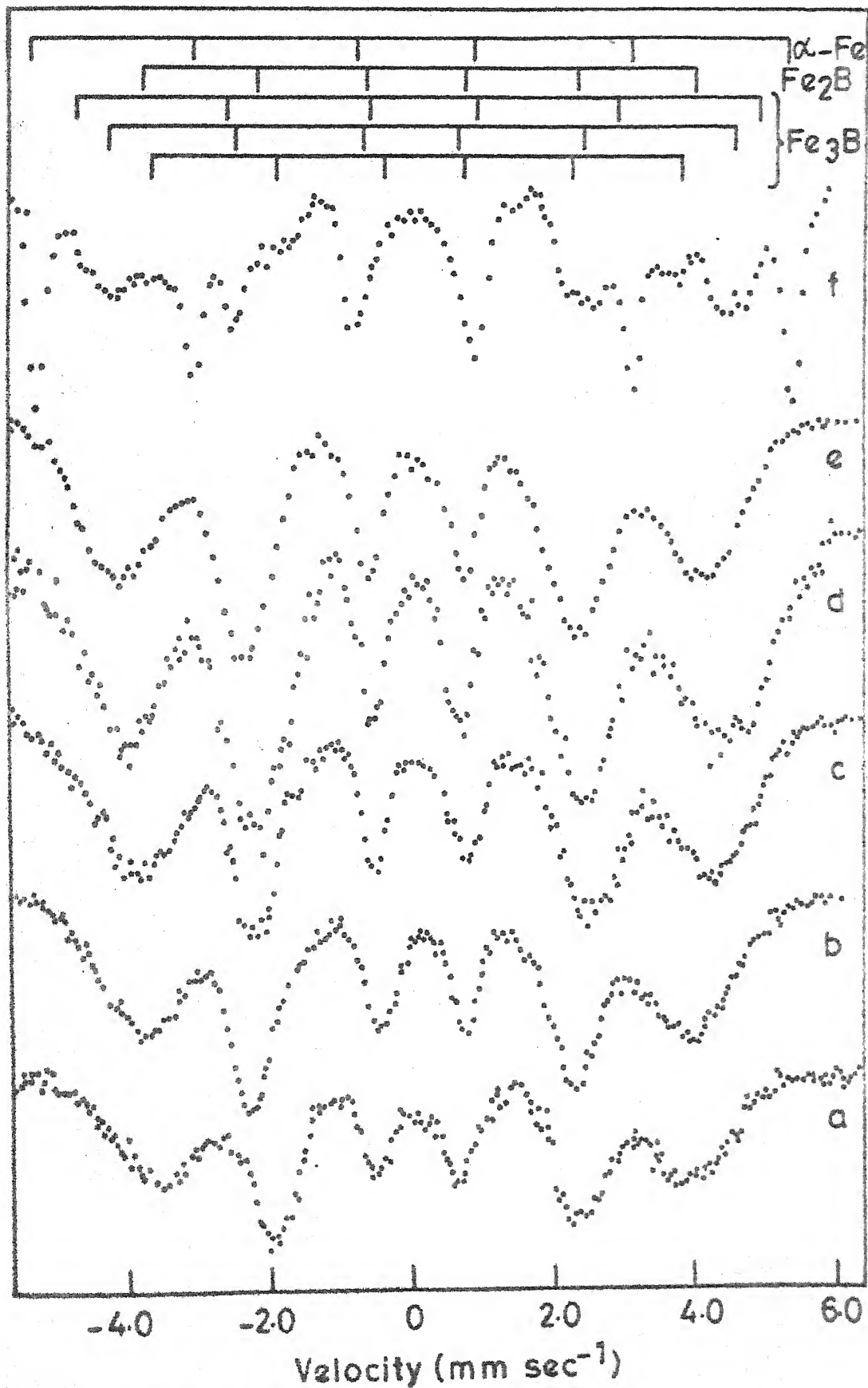


Fig. 4.2 Same as Fig. 4.1 but for $\text{Fe}_{84}\text{B}_{16}$.

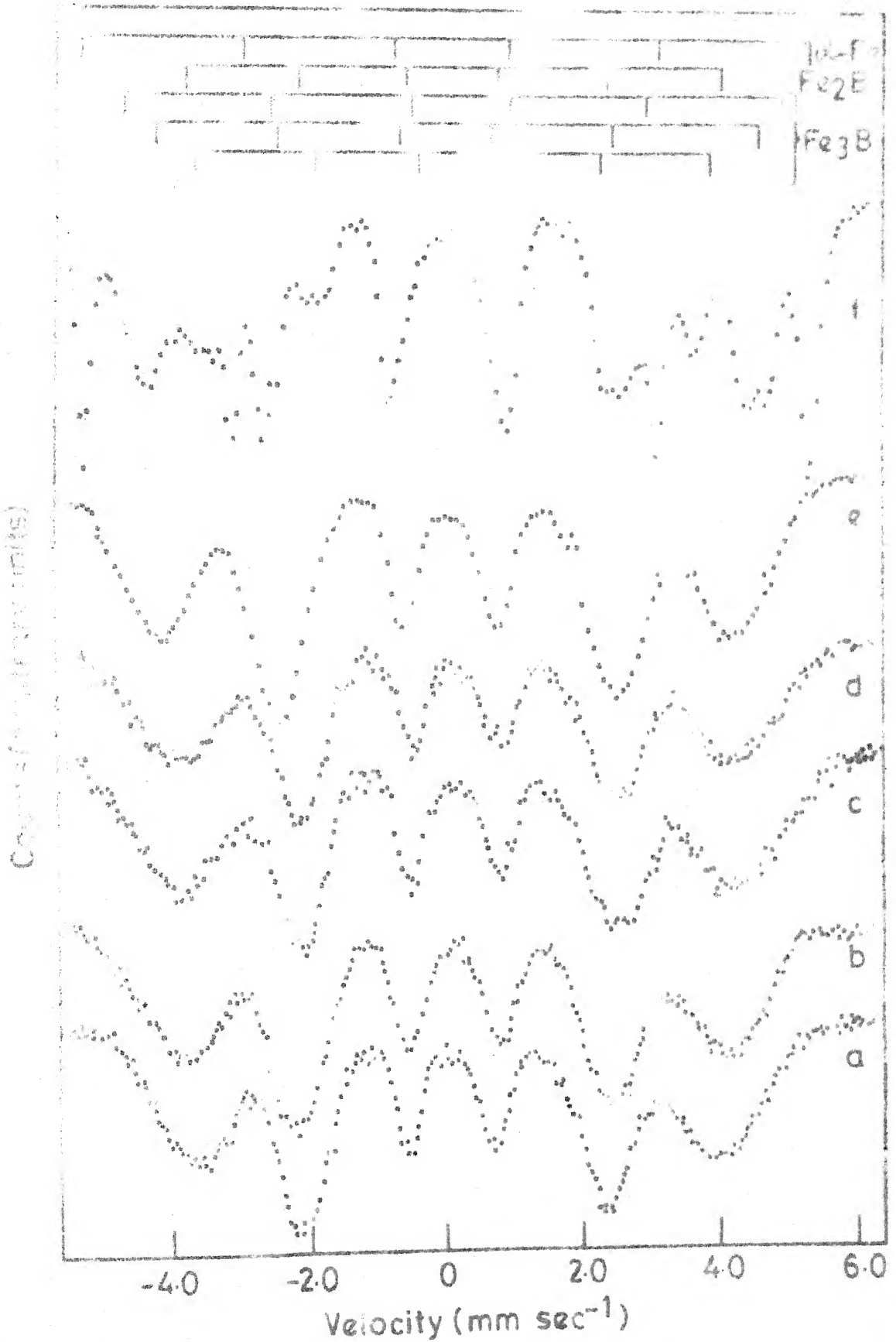


Fig. 4.3 Same as Fig. 4.1 but for Fe₈₂B₁₀.

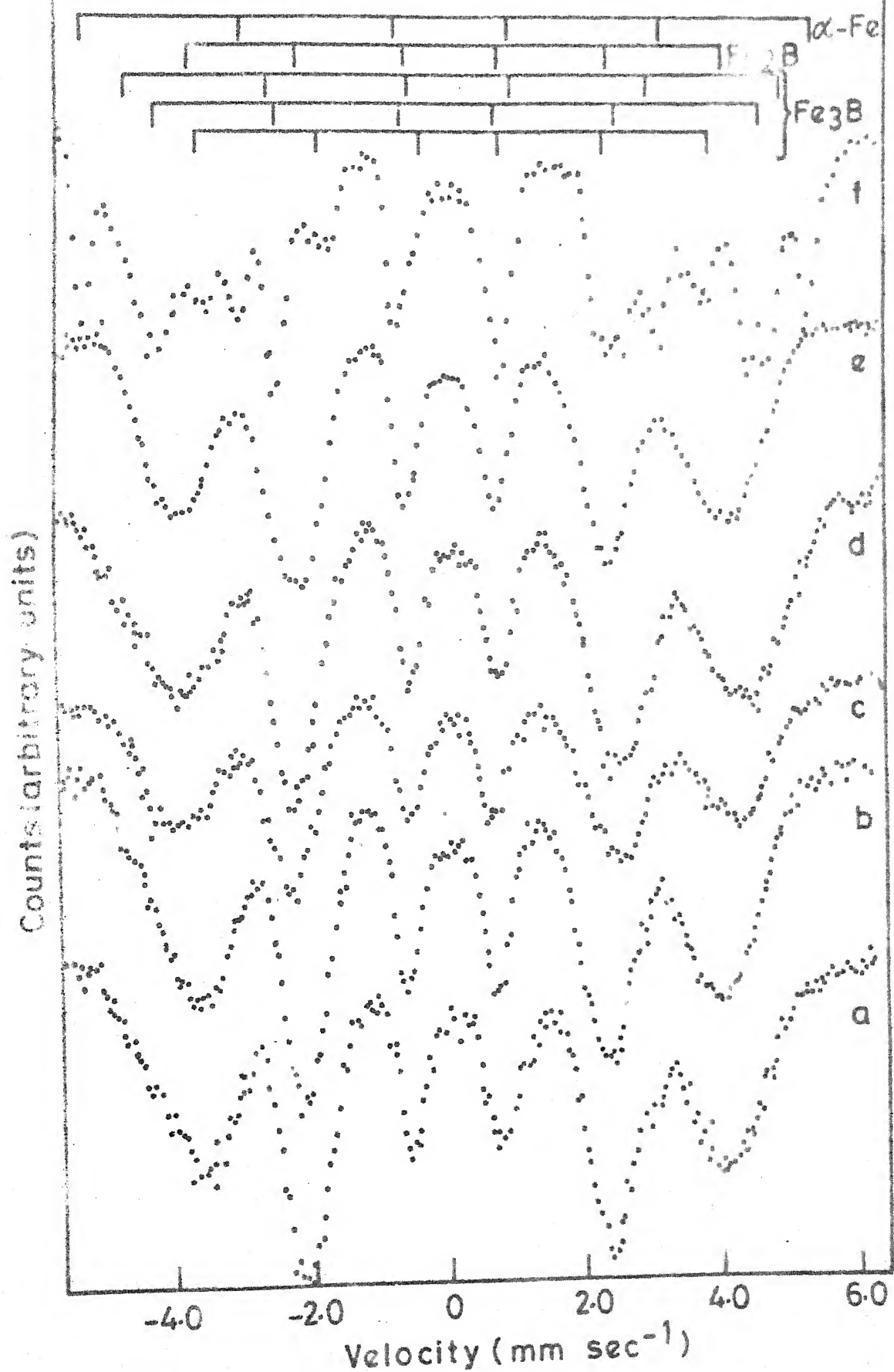
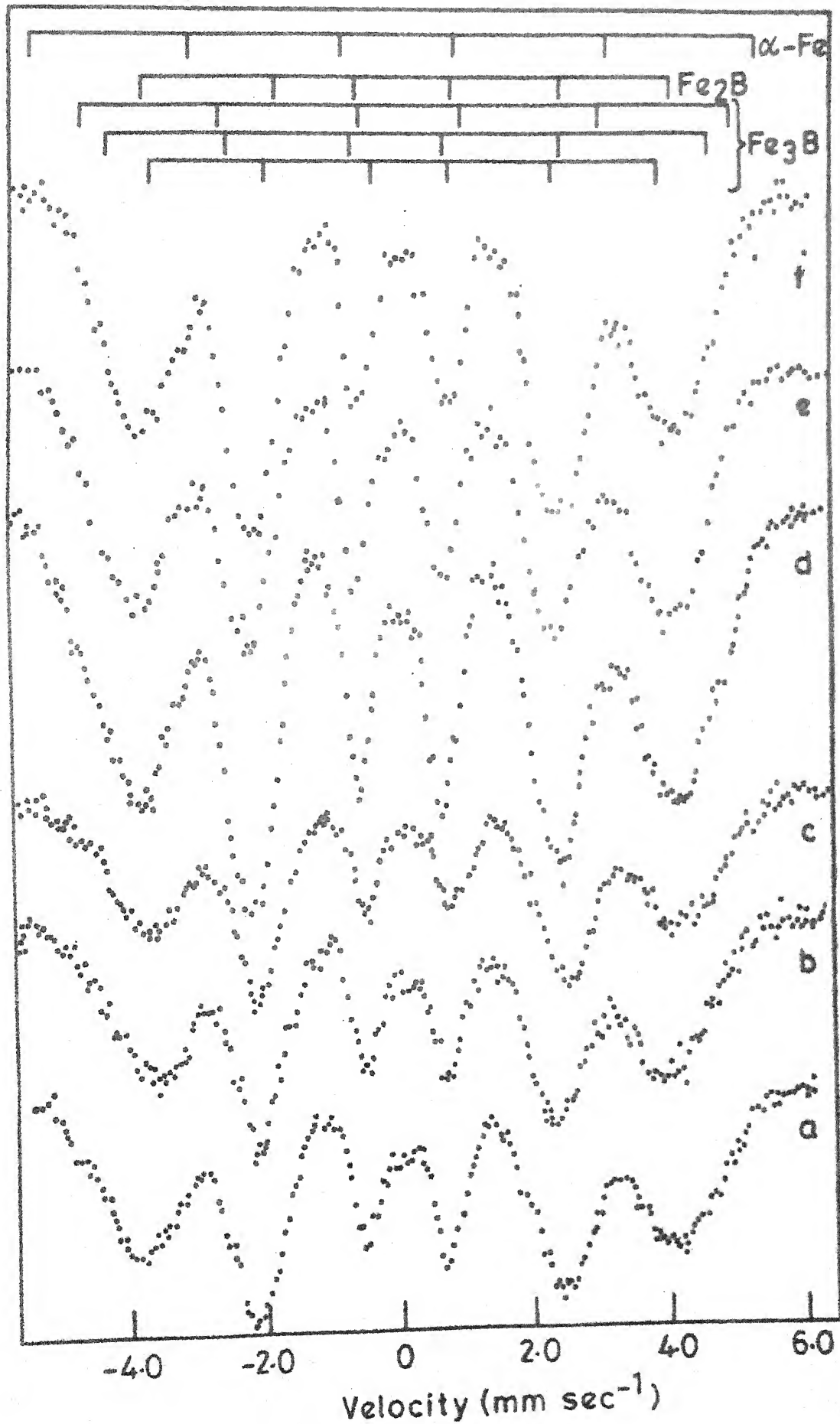


Fig. 4.4 Same as Fig. 4.1 but for $\text{Fe}_{60}\text{B}_{20}$.

Counts(arbitrary units)



-- was 4.1 but for $\text{Fe}_{78}\text{B}_{22}$.

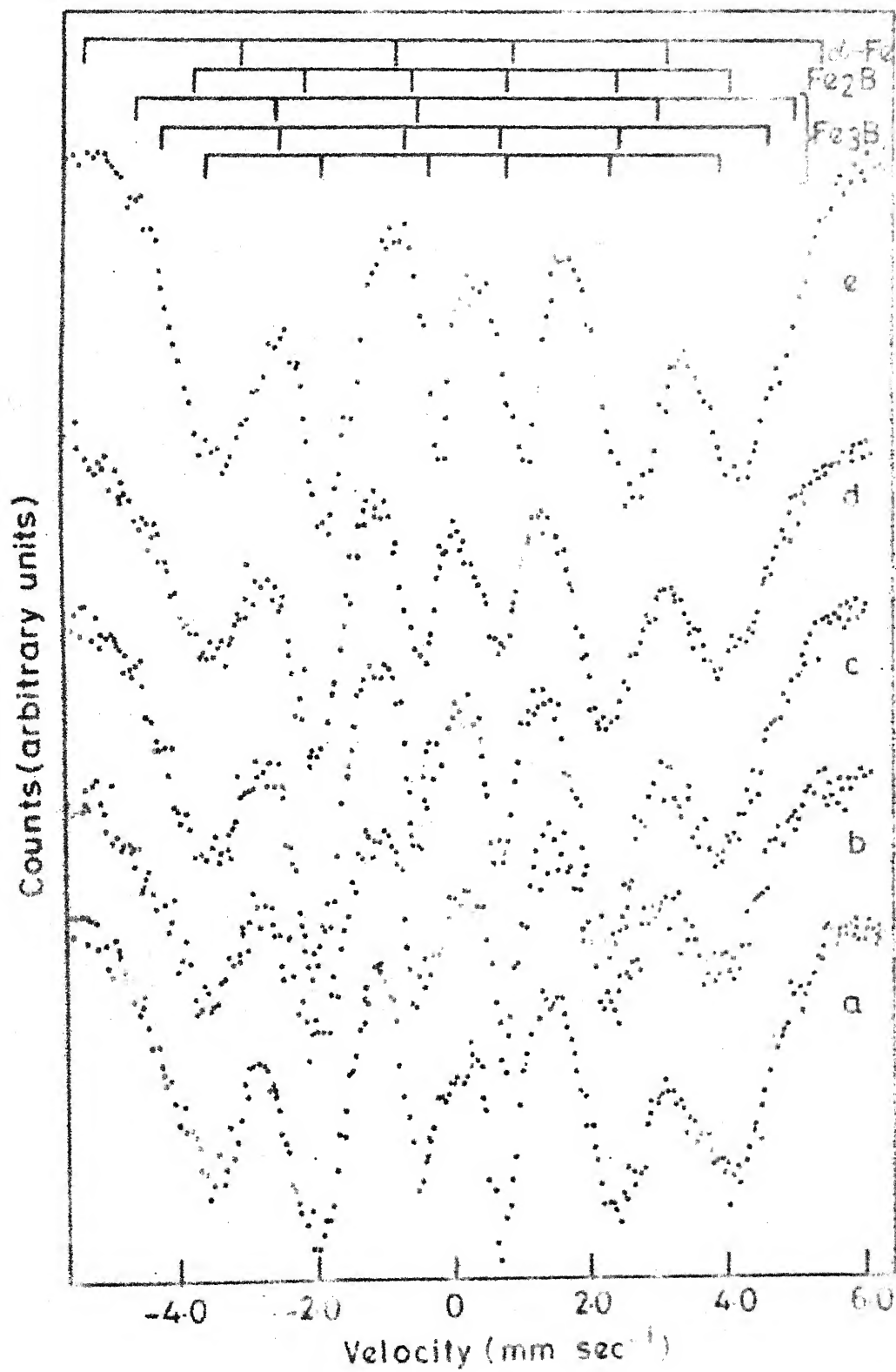


Fig. 4.6 Same as Fig. 4.1 but for $\text{Fe}_{24}\text{P}_{26}$.

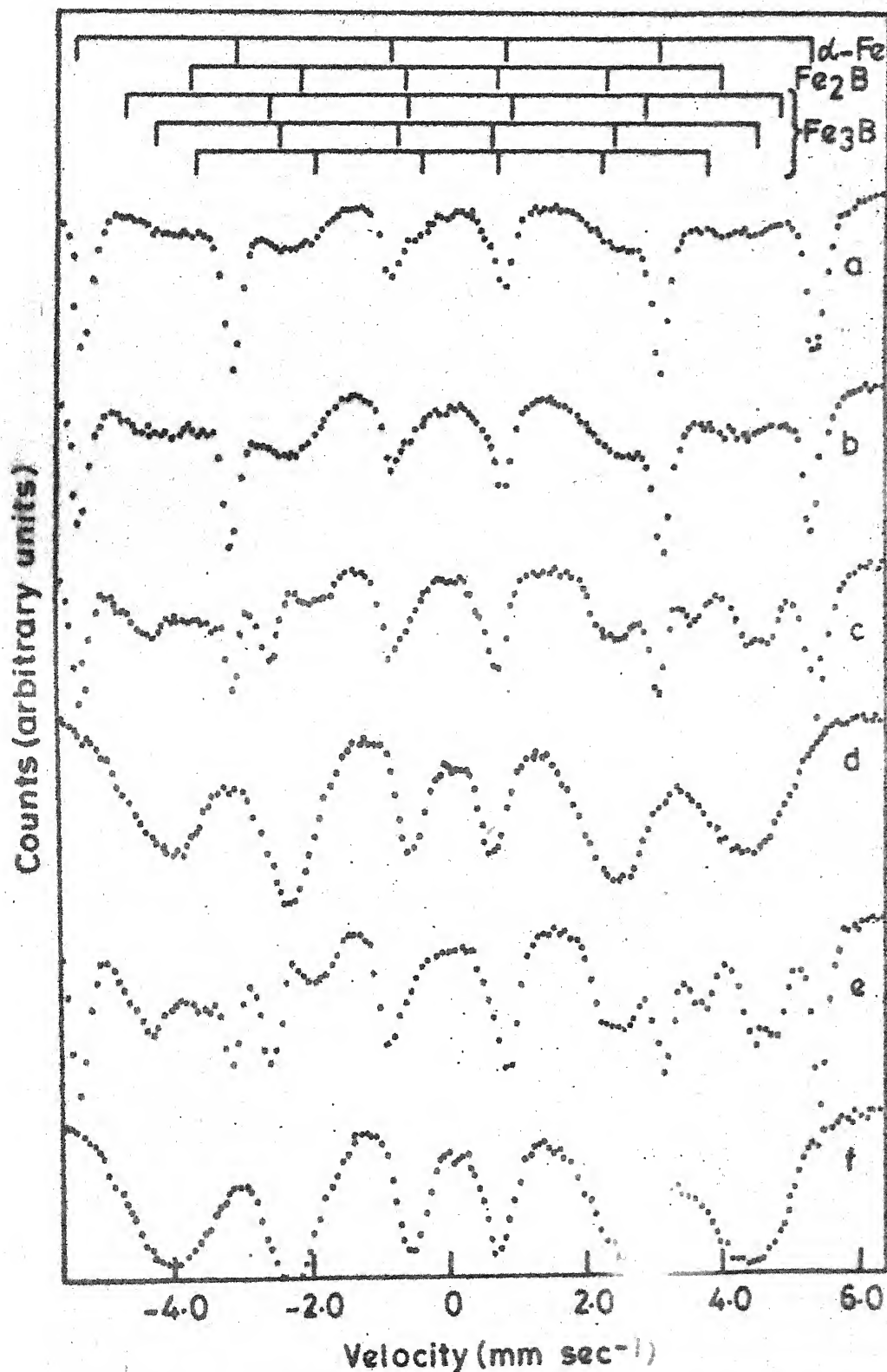


Fig. 4.7 Mössbauer spectra of $\text{Fe}_{100-x}\text{B}_x$ samples heat-treated for 4 h at different temperatures, T. $\text{Fe}_{87}\text{B}_{13}$: (a) 400 °C (b) 350 °C, $\text{Fe}_{84}\text{B}_{16}$: (c) 400 °C (d) 350 °C and $\text{Fe}_{82}\text{B}_{18}$: (e) 400 °C, (f) 350 °C.

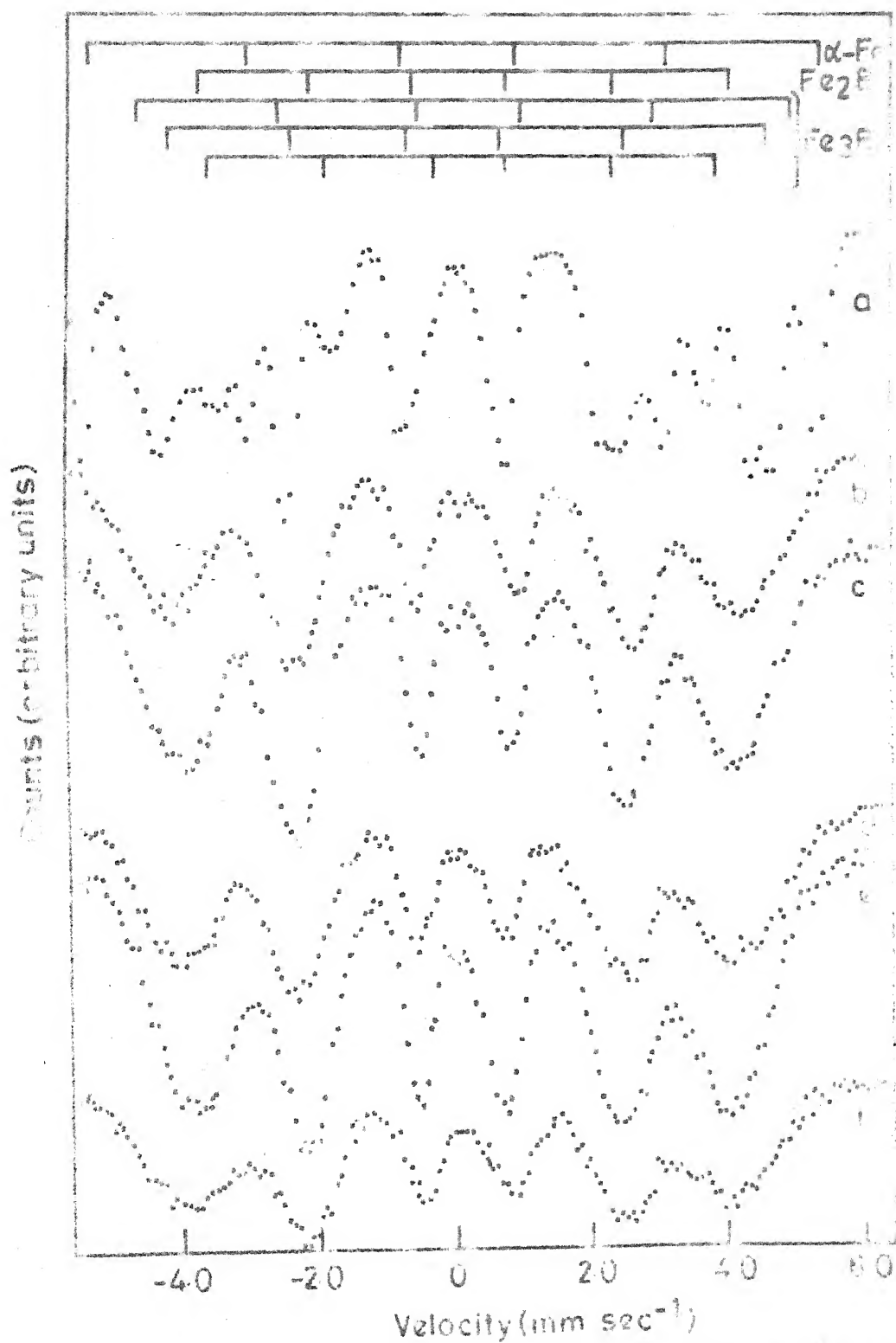


Fig. 4.8. Same as Fig. 4.7 but for $\text{Fe}_{75}\text{S}_{20}$: (a) 100 °C, (b) 200 °C, $\text{Fe}_{75}\text{S}_{20}$; (c) 300 °C, (d) 400 °C and (e) 500 °C.

temperature of 350 °C to 400 °C for the samples $\text{Fe}_{87}\text{B}_{13}$, $\text{Fe}_{84}\text{B}_{16}$, $\text{Fe}_{82}\text{B}_{18}$ and $\text{Fe}_{80}\text{B}_{20}$ (Figs. 4.1 to 4.4). In the case of the samples $\text{Fe}_{78}\text{B}_{22}$ and $\text{Fe}_{74}\text{B}_{26}$ the spectra for the 350 °C and 400 °C samples are similar. This behaviour will be discussed later.

It is observed from Fig. 4.7 and Fig. 4.8 that the Mössbauer spectra for the 400 °C (4 h) and 400 °C (1 h) are similar in the case of all the six samples, while the 350 °C (4 h) and 350 °C (1 h) are similar for all the samples except $\text{Fe}_{87}\text{B}_{13}$. We shall comment on this behaviour later on.

We carried out an analysis of the hyperfine magnetic field distribution $p(H)$ using Window's method described in Chapter 2. Plots of the $p(H)$ distributions for the different as-prepared samples ($x = 13, 16, 18, 20, 22$ and 26) are shown in Fig. 4.9 while Fig. 4.10 shows the plots of $p(H)$ for the $\text{Fe}_{74}\text{B}_{26}$ samples for different heat-treatment temperatures (time = 1 h). Using these results we have determined the peak values of the hyperfine magnetic field, H_{int} , as well as the FWHM of the $p(H)$ distributions, ΔH , and these are shown in Figs. 4.9 and 4.10. It may be pointed out that the values of H_{int} , determined by us from the least-square-fit analysis (fitting of Lorentzian curve as discussed in Chapter 2) were consistently higher than those determined from the $p(H)$ distributions (except for 2-3 cases) by 1-5 %. The values of H_{int} and ΔH obtained by us are shown in Table 4.3.

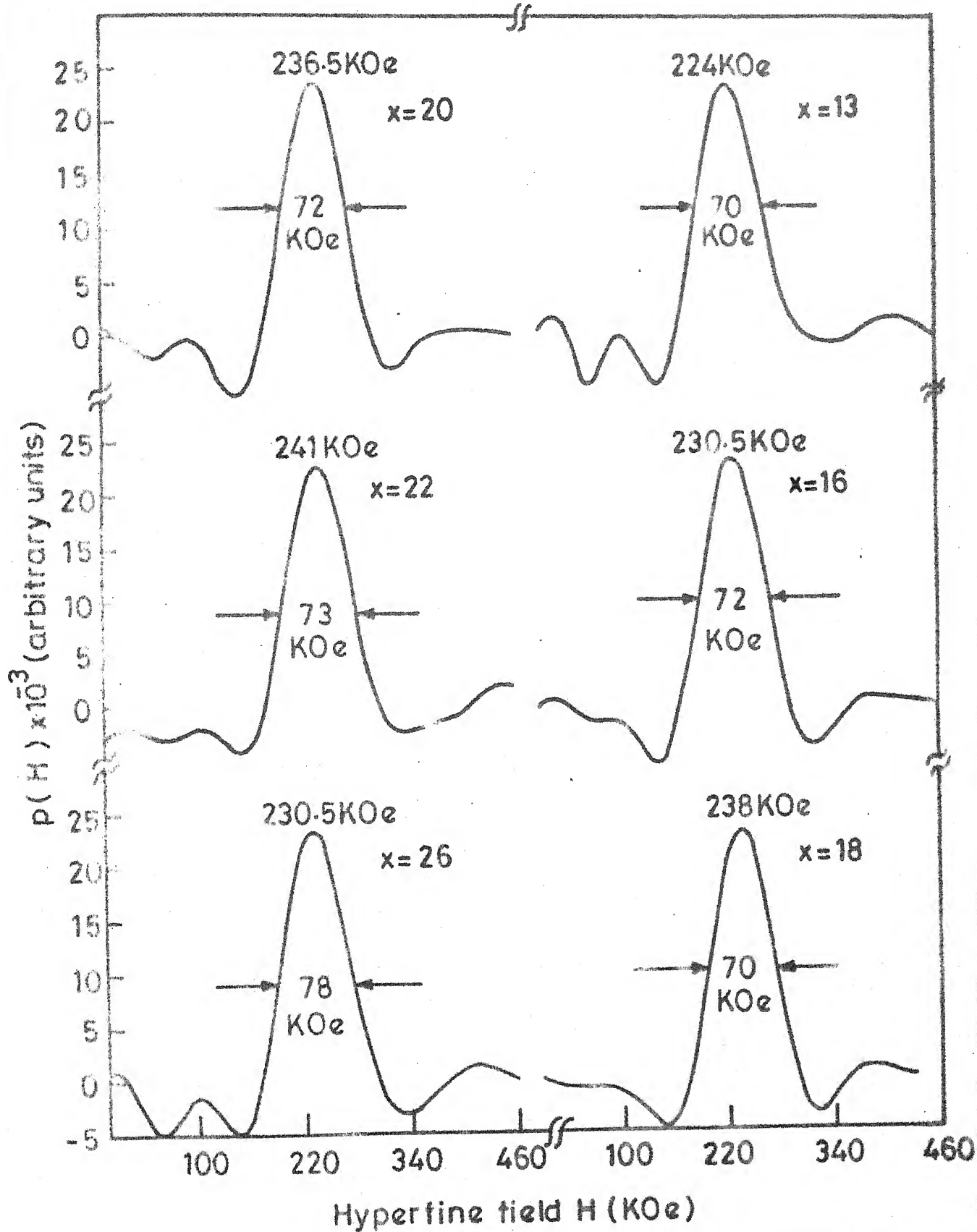


Fig. 4.9 Plots of the $p(H)$ distributions determined from the Mössbauer spectra of the as-prepared samples of $\text{Fe}_{100-x}\text{B}_x$ (taken at room temperature) for different x .

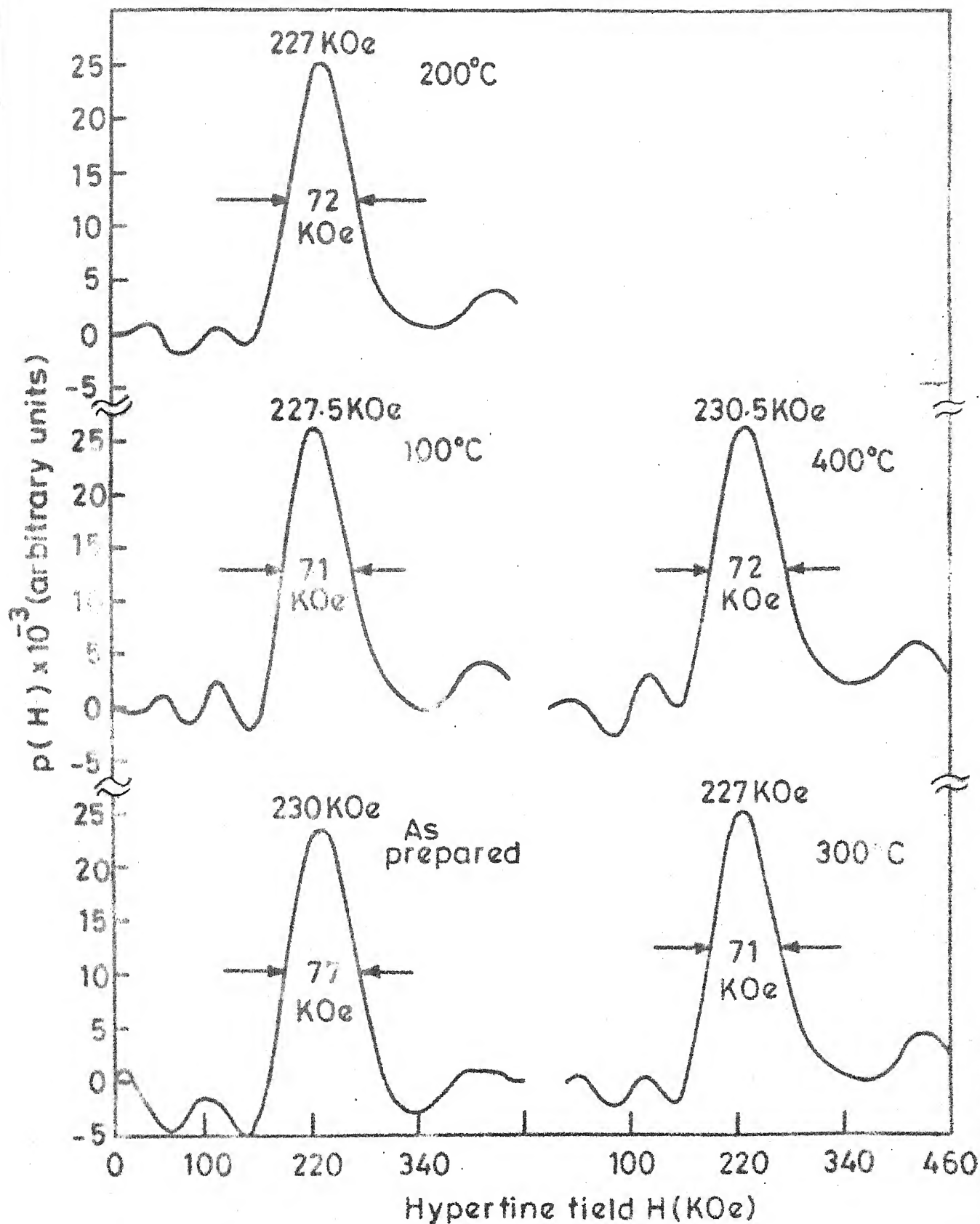


Fig. 4.10 Plots of the $p(H)$ distributions determined from the Mössbauer spectra of the $\text{Fe}_{75}\text{B}_{26}$ sample (taken at room temperature) heat-treated at 100, 200, 300 and 400 °C for 1 h.

Table 4.3

Behaviour of internal magnetic field, H_{int} , in the $\text{Fe}_{100-x}\text{B}_x$ alloys as a function of x at different heat-treatment temperatures.

Temperature t_{OC} (1 h)	$\text{Fe}_{74}\text{B}_{26}$				$\text{Fe}_{78}\text{B}_{22}$				$\text{Fe}_{80}\text{B}_{20}$			
	H		ΔH		H		ΔH		H		ΔH	
	(Ind)	(p(H))	(p(H))	(Ind)	(Ind)	(p(H))	(p(H))	(Ind)	(Ind)	(p(H))	(p(H))	(p(H))
As-prepared	233.5	230.5	77	239.6	241.0	73	243.5	236.5	72			
100	299.0	227.5	71	237.2	232.0	70	241.5	235.0	72			
200	234.4	227.0	72	247.9	242.0	72	256.8	250.0	71			
300	233.2	227.0	71	249.4	244.0	74	257.4	253.0	72			
350	-	-	-	243.4	239.5	71	256.3	244.0	70			
400	241.8	230.5	72	251.9	242.0	69	-	-	-			

Contd.....

Table 4.3 (Continued)

Temperature $^{\circ}\text{C}$ (1 h)	$\text{Fe}_{82}\text{B}_{18}$			$\text{Fe}_{84}\text{B}_{16}$			$\text{Fe}_{87}\text{B}_{13}$		
	H (Ind)	H (p(H))	ΔH (p(H))	H (Ind)	H (p(H))	ΔH (p(H))	H (Ind)	H (p(H))	ΔH (p(H))
As-prepared	243.5	238.0	70	236.0	230.5	72	233.9	224.0	70
100	243.0	244.0	71	234.4	240.0	72	234.5	229.0	71
200	254.2	247.0	71	253.8	245.5	69	246.1	248.0	72
300	252.3	247.0	72	252.8	247.0	70	244.4	233.0	67
350	267.2	253.0	70	259.5	249.0	70	238.6	225.0	68
400	-	-	-	-	-	-	-	-	-

These p(H) distributions were obtained from those Mössbauer spectra which shows only the amorphous phases.

N.B. The values of H_{int} were determined by using the following two methods.

Ind = value of H_{int} obtained from independent least-square curve-fitting using Lorentzian lineshapes.

p(H) = peak value, H_{int} , obtained from the p(H) distribution in Figs. 4.9 and 4.10.

It is observed that the general shape of the $p(H)$ distributions at room temperature is similar for different boron concentrations (Fig. 4.9). For the $Fe_{74}B_{26}$ sample the effect of heat-treatment on the $p(H)$ distributions is to bring an asymmetry in the $p(H)$ curves at higher temperatures (Fig. 4.10). The width (FWHM), ΔH , of the $p(H)$ curves is 77 KOe for the as-prepared sample. The values of ΔH shows marginal changes with x or with the temperature.

In order to bring out the systematic behaviour of the variation of the Mössbauer parameters like isomer shift (IS) and hyperfine magnetic field (H_{int}) we have analyzed the spectra in Figs. 4.1 to 4.6 and obtained the values of IS (relative to α -Fe) and H_{int} (in KOe) obtained by Lorentzian curve-fitting. These results are plotted in two ways. (i) In Fig. 4.11 and Fig. 4.12, we have plotted IS and H_{int} values for each x (percentage of boron in $Fe_{100-x}B_x$) as a function of the heat-treatment temperature (time = 1 h). (ii) In Fig. 4.13 and Fig. 4.14 the IS and H_{int} values for each heat-treatment temperature (time = 1 h) are plotted against x .

Examination of these results reveals that excepting $x = 26$, the H_{int} values increase with the heat-treatment temperature for the different ($13 \leq x \leq 22$) boron concentrations. The onset of such an increase in the H_{int} values appears to occur between $T = 100^\circ C$ and $T = 200^\circ C$ and indicates a distinct change in the atomic structure of

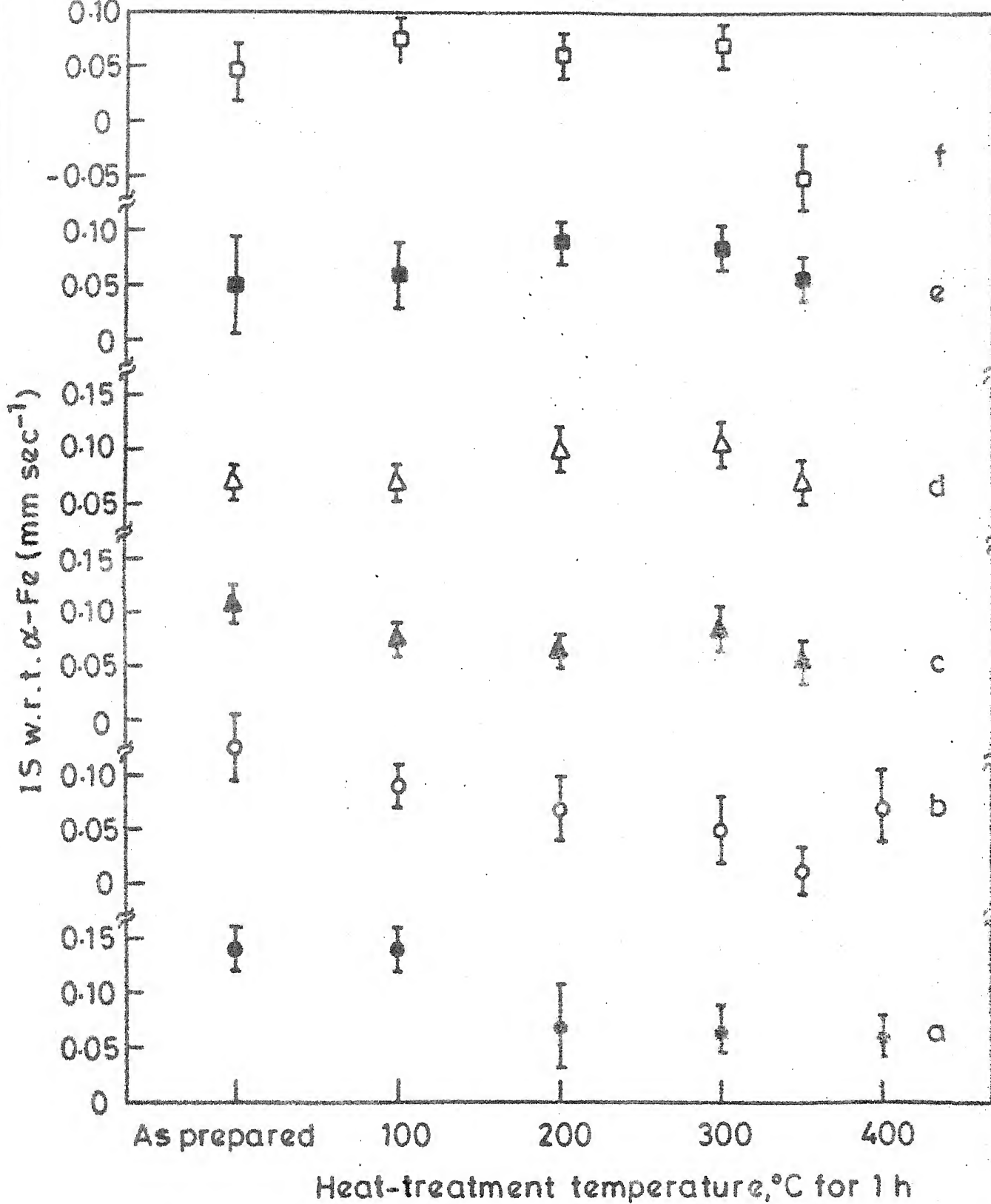


Fig. 4.11 Plot of the isomer shift (IS) data for $\text{Fe}_{100-x}\text{B}_x$ samples against the heat-treatment temperature, T.
 a : $x = 26$, b : $x = 22$, c : $x = 20$, d : $x = 18$,
 e : $x = 16$ and f : $x = 13$.

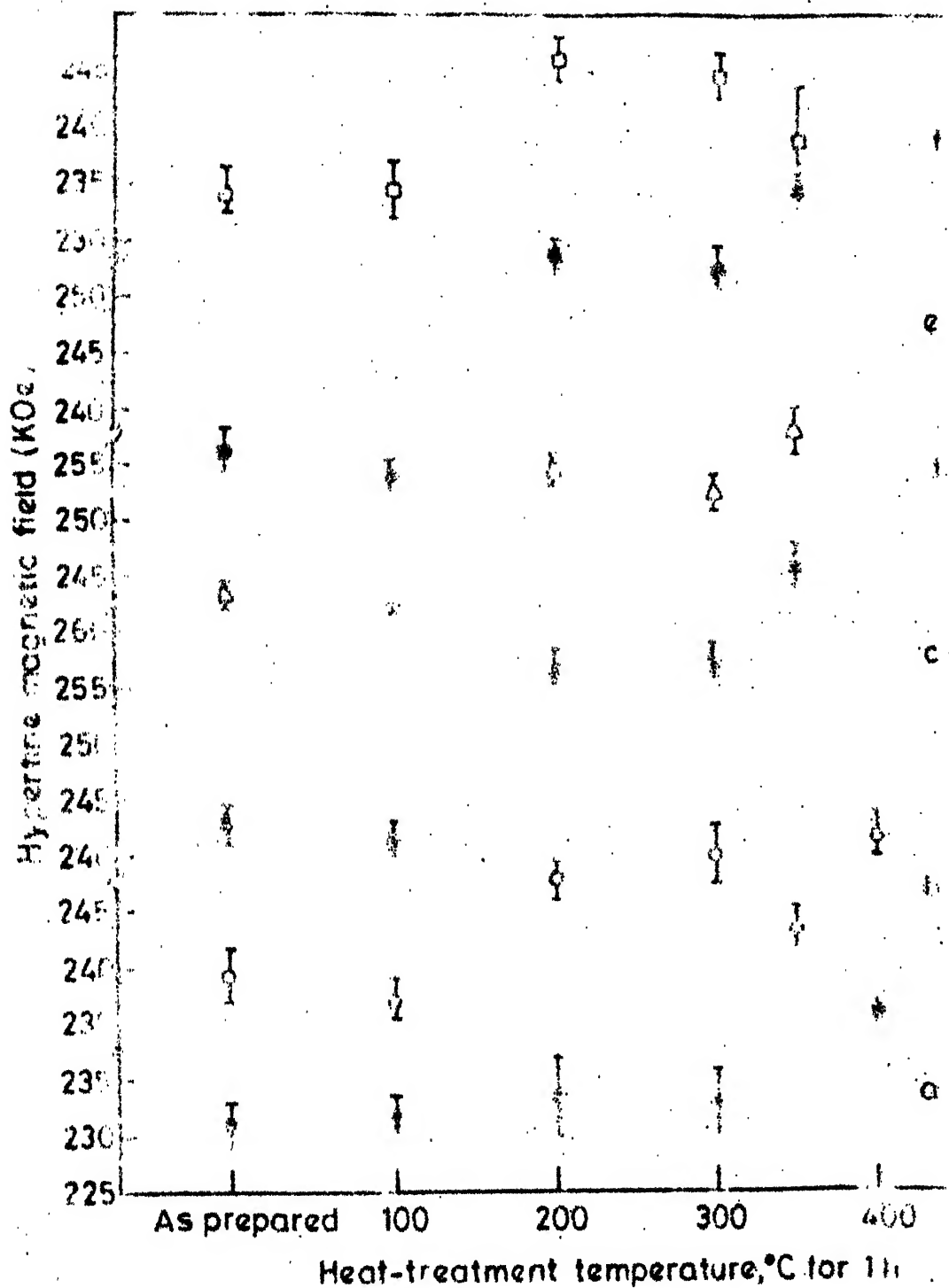


Fig. 4.12 Plot of the H_{hf} data for $\text{Fe}_{100-x}\text{B}_x$ samples against the heat-treatment temperature, T. a : $x = 26$, b : $x = 22$, c : $x = 20$, d : $x = 18$, e : $x = 16$, f : $x = 14$.

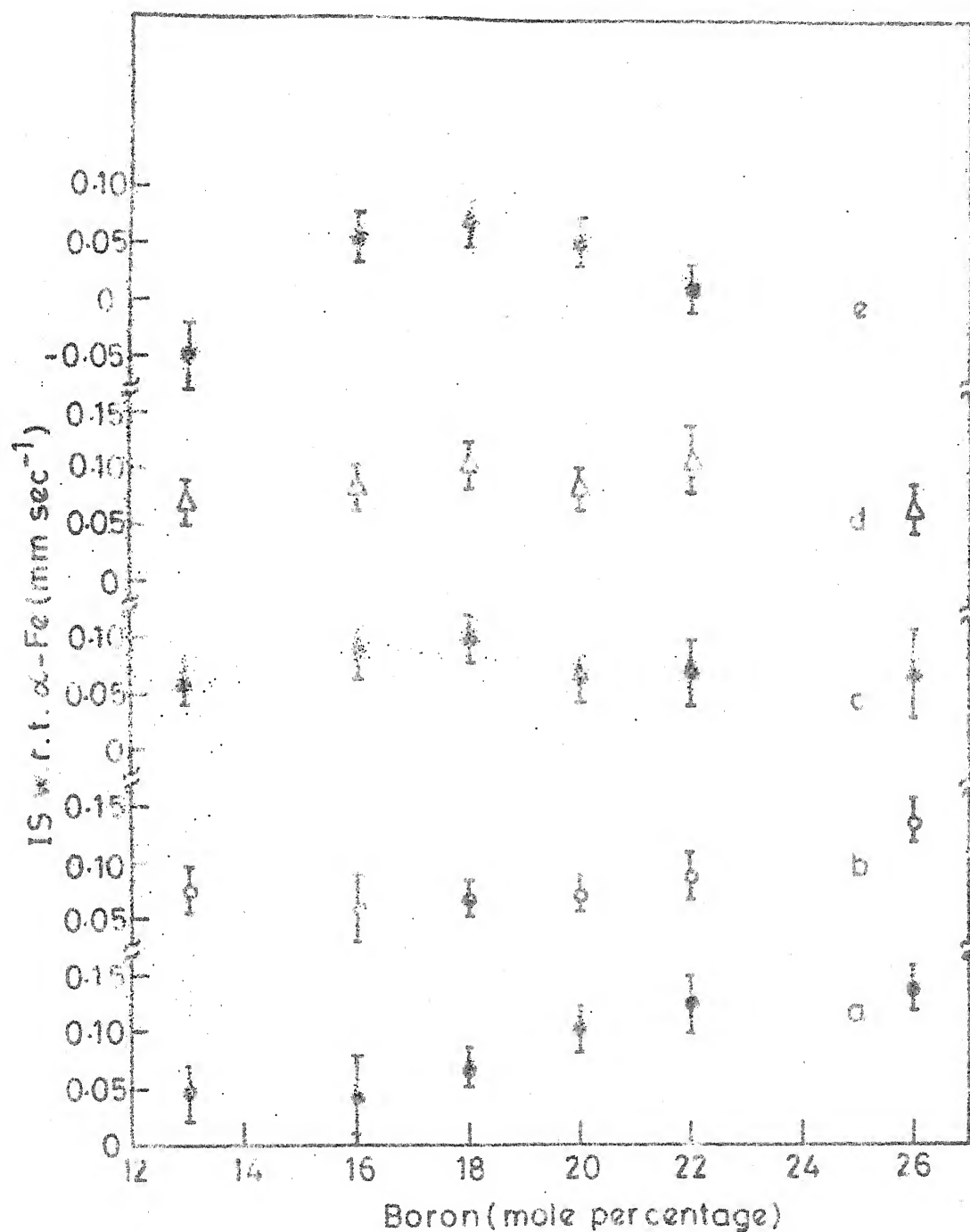


Fig. 1.13 Plot of the IS data for $\text{Fe}_{100-x}\text{B}_x$ samples against the boron concentration x . a : as-prepared, b : $T = 100^\circ\text{C}$, c : $T = 200^\circ\text{C}$, d : $T = 300^\circ\text{C}$ and e : $T = 350^\circ\text{C}$. (In each case $t = 1$ h).

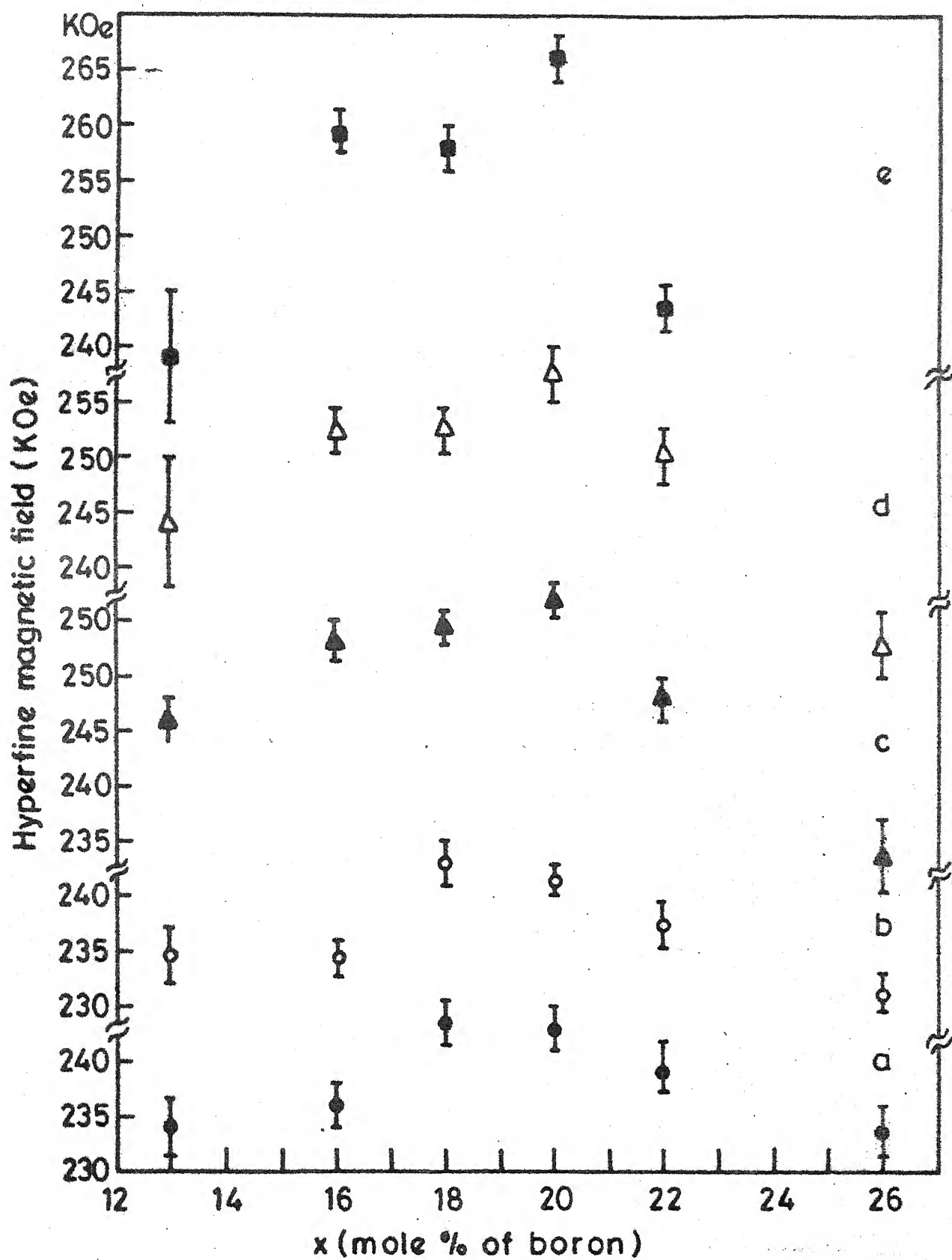


Fig. 4.14 Same as Fig. 4.13 but for the H_{int} data.

the glass systems between 100 °C and 200 °C. A further increase in the H_{int} value (excepting $x = 13$ and $x = 22$) accompanied by a more asymmetric nature of the $p(H)$ curve is observed after 300 °C. This behaviour is attributed to the formation of crystalline α -Fe and Fe_3B as observed by TEM studies (Table 4.2).

The variation of the H_{int} values with x for different heat-treatment temperatures show that for $T = 350$ °C, H_{int} increases from $x = 13$ to $x = 18$, remains unchanged between $x = 18$ and $x = 20$ and then decrease from $x = 20$ to $x = 26$ (Fig. 4.14). Similar behaviour was observed by Ruckman et al. [16]. For the samples heat-treated at 350 °C the H_{int} values are higher and show a sharp decrease after $x = 20$. These results show that as the boron percentage increases beyond $x = 20$, the behaviour of internal magnetic field changes sensitively. Such dependence of the properties of $Fe_{100-x}B_x$ alloy on the boron percentage has been observed earlier [16,22,24].

It is seen from Fig. 4.13 that the IS values do not show variation with x for the samples heat-treated at 100, 200 and 300 °C. In the case of the as-prepared samples the IS values decrease with x in agreement with Ruckman et al. [16]. The sample heat-treated at 350 °C shows an increase in the IS value from $x = 13$ to $x = 16$, followed by a flat behaviour upto $x = 22$. The lower IS value for the $x = 13$ sample could be due to the formation of α -Fe as suggested

in Table 4.2.

As explained earlier we have collated the data from Mössbauer and other studies of $\text{Fe}_{100-x}\text{B}_x$ in Table 4.2. The present Mössbauer spectroscopy results for $x = 13, 16, 18, 20, 22$ and 26 are shown in Table 4.2 for the heat-treatment temperatures (T) of 350 and 400°C for the treatment periods (t) of 1 h and 4 h. In Table 4.2 our results are summarized in terms of the identification of the Mössbauer lines due to amorphous phase, $\alpha\text{-Fe}$, Fe_3B and Fe_2B using the spectra and the characteristic line positions shown in Figs. 4.1 - 4.8. The relative contributions from the $\alpha\text{-Fe}$, Fe_3B and Fe_2B phases are indicated by the symbols S = strong, M = moderate and W = weak shown in the brackets and they were deduced from the intensities of the Mössbauer lines (Figs. 4.1 - 4.8). Also shown in Table 4.2 are the summarized results of other work on Mössbauer studies of $\text{Fe}_{100-x}\text{B}_x$. The results shown in Table 4.2 will now be discussed separately for each value of x (boron concentration). Data presented in Table 4.2 have to be kept in mind while following the discussion given below.

$\text{Fe}_{87}\text{B}_{13}$

Samples with this composition in the form of thin foils annealed inside the transmission electron microscope (TEM) crystallize at 180°C [24] with the $\alpha\text{-Fe}$ phase separating out and Fe_3B is observed to be formed at 560°C .

Differential thermal analysis (DTA) studies reveal peaks at 310 and 440 °C for the heating rate of 1 °C/min [26] and at 240 and 510 °C for 5 °C/min [24]. Results of the dynamic temperature X-ray diffraction (DTXD) measurements show the separation of α -Fe at 149 °C and of Fe_2B from 298 to 485 °C [27]. Mössbauer studies reported by Oshima and Fujita [19] show separation of α -Fe at 260 °C. The present Mössbauer spectroscopy results show (i) formation of α -Fe when the sample is heat-treated at $T = 350$ °C for $t = 1$ h, and (ii) weak formation of the Fe_3B and Fe_2B phases when the heat-treatment at 350 °C is prolonged for 4 h. It is to be noted that the crystallization of Fe_2B is indicated only in the DTXD and the present Mössbauer studies. The variation in the temperatures of appearance of the various phases as revealed by various techniques (viz. DTXD, DTA, TEM and Mössbauer) is an important feature of the results in Table 4.2 and is consistently observed with samples of other compositions. The present Mössbauer results (Fig. 4.1 and 4.7 and Table 4.2) support existence of amorphous phase for $T < 350$ °C and formation of α -Fe at $T \approx 350$ °C and $t = 1$ h with a weak formation of Fe_3B and Fe_2B at $T = 350$ °C, $t = 4$ h and at $T = 400$ °C with $t > 1$ h.

$\text{Fe}_{84}\text{B}_{16}$

Thin foil samples with this composition when examined by the TEM studies [24] show the separation of α -Fe at

$T = 310^{\circ}\text{C}$ and of Fe_3B at $T = 450^{\circ}\text{C}$. In contrast, the TEM studies of the bulk samples of $\text{Fe}_{84}\text{B}_{16}$ annealed at $T = 350^{\circ}\text{C}$ for $t = 1$ h still show [25] the amorphous structure and the formation of $\alpha\text{-Fe}$ and Fe_3B is seen only at $T = 400^{\circ}\text{C}$ for $t = 1$ h. The DTA results show peaks at 360 and 405°C for $1^{\circ}\text{C}/\text{min}$ (heating rate) [26] and at 300 and 482°C for $5^{\circ}\text{C}/\text{min}$ [24]. Results of the DTXD measurements [27] for this composition show the separation of $\alpha\text{-Fe}$, Fe_3B and Fe_2B at 242°C , $284 - 460^{\circ}\text{C}$ and 572°C respectively. Mössbauer studies reported by Ruckman et al. [16] indicate formation of $\alpha\text{-Fe}$ at $T = 342^{\circ}\text{C}$ for $t = 24$ h and crystallization of Fe_3B at $T = 342^{\circ}\text{C}$ when t is increased to $t = 360$ h. Present Mössbauer results show that $\text{Fe}_{84}\text{B}_{16}$ remains amorphous at $T = 350^{\circ}\text{C}$ when heating period is $t \leq 4$ h. We have observed strong formation of $\alpha\text{-Fe}$, accompanied by weak formation of Fe_3B and perhaps some Fe_2B when this sample is heated at $T = 400^{\circ}\text{C}$ for $t \geq 1$ h. The present Mössbauer results agree with the TEM results for the bulk samples [25].

$\text{Fe}_{82}\text{B}_{18}$

The TEM measurements carried out with thin foil samples of this composition reveal the separation of $\alpha\text{-Fe}$ at 350°C and of Fe_3B at 440°C [24] while those carried out with bulk samples show the separation of $\alpha\text{-Fe}$ and Fe_3B at 400°C [25]. Only one peak is observed in the DTA studies and it is observed at 380°C with the heating rate

of 1 °C/min [26] and at 460 °C with 5 °C/min [24]. Results of the DTXD measurements [27] show formation of α -Fe, Fe_3B and Fe_2B at temperatures $T = 282$ °C, 257-427 °C and 539 °C respectively. Mössbauer studies of $\text{Fe}_{82}\text{B}_{18}$ by Ruckman et al. [16] show results similar to those observed by them for $\text{Fe}_{84}\text{B}_{16}$. The present Mössbauer results show that $\text{Fe}_{82}\text{B}_{18}$ remains amorphous at $T = 350$ °C for $t \leq 4$ h and α -Fe (strong) and Fe_3B (moderate) is formed at $T = 400$ °C with $t = 1$ h while α -Fe (strong) Fe_3B (moderate) and Fe_2B (weak) is formed at $T = 400$ °C with $t = 4$ h. This behaviour agrees with the trend of Mössbauer results observed by Ruckman et al. [16] and the TEM results observed by Das [24] and Das and Ramachandran [25].

$\text{Fe}_{80}\text{B}_{20}$

The TEM studies carried out with thin foils [26] of $\text{Fe}_{80}\text{B}_{20}$ reveal crystallization of α -Fe at 332 °C and of Fe_3B at 405 °C, while the TEM studies with the bulk samples [25] show that at $T = 350$ °C for $t = 1$ h, the sample is still amorphous with some formation of α -Fe. The DTA studies show single peak at 385 °C with 1 °C/min [26] and 460 °C with 5 °C/min [24]. Results of the DTXD studies indicate formation of α -Fe, Fe_3B and Fe_2B at 312 °C, 243-427 °C and 563 °C respectively [27]. Mössbauer studies by Franke and Rosenberg [28] showed that $\text{Fe}_{80}\text{B}_{20}$ remains amorphous at $T = 327$ °C for $t = 10$ h, but

new phases appear at $T = 377^{\circ}\text{C}$, with $\alpha\text{-Fe}$ appearing for $t = 45$ min. They observed $\alpha\text{-Fe}$, Fe_2B and presumably a phase with a ratio $\text{Fe}:\text{B} \gg 3$ at $T = 427^{\circ}\text{C}$ for $t = 1$ h. Present Mössbauer results indicate that $\text{Fe}_{80}\text{B}_{20}$ remains amorphous at $T = 350^{\circ}\text{C}$ for $t \leq 4$ h, while $\alpha\text{-Fe}$ and Fe_3B are formed at $T = 400^{\circ}\text{C}$ for $t \geq 1$ h. Thus the present results show good agreement with the trend of the results observed by other Mössbauer [28], TEM [24,25], DTA [24,26] and DTXD [27] studies.

$\text{Fe}_{78}\text{B}_{22}$

The TEM measurements with the thin samples [24] of this composition show separation of $\alpha\text{-Fe}$ at 363°C and of Fe_3B at 400°C [25] while those with the bulk samples show separation of $\alpha\text{-Fe}$ and Fe_3B at $T = 400^{\circ}\text{C}$ for $t = 1$ h. The DTA studies show single peaks at 395°C with $1^{\circ}\text{C}/\text{min}$ [26] and at 458°C with $5^{\circ}\text{C}/\text{min}$ [24]. The DTXD measurements [27] show formation of $\alpha\text{-Fe}$, Fe_3B and Fe_2B at 355°C , $241\text{--}402^{\circ}\text{C}$ and 548°C respectively. We have not come across any reported study of $\text{Fe}_{78}\text{B}_{22}$ using Mössbauer technique. Our Mössbauer studies indicate that in the samples of $\text{Fe}_{78}\text{B}_{22}$ the amorphous phase remains stabilised upto $T = 400^{\circ}\text{C}$ even if t is raised to 4 h. At first sight these Mössbauer results may appear to contradict the results obtained by TEM [24,25], DTA [24,26] and DTXD [27] studies. However the temperatures at which different phases have

appeared in various studies (i.e. using different techniques) are consistently in disagreement (for all the samples) as pointed out earlier. We feel that this inconsistency, arising out of different experimental conditions etc., is causing the problem. If we look at the general trend of different results, it appears that α -Fe and Fe_3B is formed in $\text{Fe}_{78}\text{B}_{22}$ just after 400°C and our Mössbauer measurements failed to detect these phases because we did not go beyond $T = 400^\circ\text{C}$ and $t = 4$ h.

$\text{Fe}_{74}\text{B}_{26}$

In the case of $\text{Fe}_{74}\text{B}_{26}$ the TEM studies with thin samples show separation of α -Fe and Fe_3B at 420°C [24]. The DTA studies show single peak at 415°C with $1^\circ\text{C}/\text{min}$ [26] and at 490°C with $5^\circ\text{C}/\text{min}$ [24]. The results of the DTXD measurements [27] show separation of α -Fe, Fe_3B and Fe_2B at 369°C , 441°C and 302 – 583°C respectively. Again there are no reported Mössbauer studies of $\text{Fe}_{74}\text{B}_{26}$ known to us. The present Mössbauer measurements of $\text{Fe}_{74}\text{B}_{26}$ yield results similar to those for $\text{Fe}_{78}\text{B}_{22}$ in that only the amorphous phase is revealed upto $T = 400^\circ\text{C}$ and $t = 4$ h. We therefore propose the same explanation as given in the preceding paragraph and conclude that in $\text{Fe}_{74}\text{B}_{26}$ the phases like α -Fe, Fe_3B and Fe_2B are separated out only at $T > 400^\circ\text{C}$ with $t > 4$ h.

In the above we have discussed the results obtained by Mössbauer and other measurements for different

compositions of $\text{Fe}_{100-x}\text{B}_x$. Some general remarks will be made now. Firstly the present Mössbauer results show that at $T = 400^\circ\text{C}$ and $t = 4$ h, the amount of $\alpha\text{-Fe}$ formed decreases from $x = 13$ to $x = 20$ (Figs. 4.7 and 4.8 and Table 4.2) or as the iron-content is decreased. Similar behaviour was reported by Ruckman et al. [16] and Kemeny et al. [21]. The amount of formation of Fe_3B increases as the boron concentration is increased from $x = 13$ to $x = 20$ (Fig. 4.7 and 4.8 and Table 4.2). Secondly the present Mössbauer measurements indicate weak formation of Fe_2B at $T = 400^\circ\text{C}$ for $x = 13, 16$ and 18 . However one should remember that the Mössbauer lines originating from Fe_3B and Fe_2B lie quite close (e.g. Fig. 4.7) and they cannot be clearly resolved. Again Fe_2B can arise out of the thermal decomposition of Fe_3B requiring an extended period of heat-treatment before a substantial amount of Fe_2B can be formed. In our case this time period t was $t \leq 4$ h and hence the formation of Fe_2B was weak for $x = 13\text{--}18$. The same reason may explain why our Mössbauer results do not indicate formation of Fe_2B for $x > 18$.

Thirdly the present Mössbauer results for $\text{Fe}_{78}\text{B}_{22}$ and $\text{Fe}_{74}\text{B}_{26}$ have shown stabilization of the amorphous phase upto $T = 400^\circ\text{C}$ even with $t = 4$ h. We attribute this behaviour to the following. It has been shown by Chien et al. [14] that the magnetic ordering temperature (T_c) decreases sharply with increasing Fe concentration; from

487 °C for $\text{Fe}_{72}\text{B}_{28}$ to 279 °C for $\text{Fe}_{86}\text{B}_{14}$. It therefore appears that $T_c < 400$ °C for $\text{Fe}_{78}\text{B}_{22}$ and $\text{Fe}_{74}\text{B}_{26}$ and hence in our measurements at $T = 400$ °C and $t \leq 4$ h, α -Fe could not be crystallized for $x = 22$ and 26 . We might have observed clearer formation of α -Fe for the $x = 22$ and $x = 26$ samples if we had gone upto $T \simeq 450$ °C or above. Similar arguments can be given to explain the non-formation of Fe_3B (and Fe_2B) in $\text{Fe}_{78}\text{B}_{22}$ and $\text{Fe}_{74}\text{B}_{26}$ at $T = 400$ °C with $t < 4$ h. We feel that these two compositions ($x = 22$ and $x = 26$) should be further investigated by Mössbauer spectroscopy using $T > 400$ °C and $t > 4$ h.

The present investigations, along with other reported data, have provided further information about kinetics of crystallization in the $\text{Fe}_{100-x}\text{B}_x$ glasses, although they do not provide a complete picture yet. The foregoing discussion clearly points out that attempting a meaningful comparison of the results obtained on various samples and by using a variety of techniques is a difficult task. There is a reasonable agreement between the results obtained with samples annealed outside and then examined by TEM and Mössbauer techniques. It appears that further studies in this connection should be concerned with the annealing of bulk samples for various lengths of time at temperatures ranging between 300 and 400 °C and perhaps upto 450 °C.

REFERENCES

- [1] R.W. Cahn, *Contemp. Phys.* 21, 43 (1980).
- [2] F.E. Luborsky in Ferromagnetic Materials, ed. E.P. Wohlfarth (North-Holland Publishing Co. Amsterdam, 1980) Vol. 1, Chapter 6.
- [3] C. Hargitai, I. Bakonyi and T. Kemeny eds. Metallic Glasses : Science and Technology (Kultura, Budapest, 1981).
- [4] H.O. Hooper and A.M. de Graff, eds. Amorphous Magnetism, (Plenum, New York, 1973).
- [5] R.A. Levy and R. Hasegawa, eds. Amorphous Magnetism II (Plenum, New York, 1977).
- [6] B. Cantor, ed. Rapidly Quenched Metals III, Vol. 1 and 2 (Metal Society, London, 1978).
- [7] T. Masumoto and K. Suzuki, eds. Rapidly Quenched Metals IV, Vol. 1 and 2 (Japan Institute of Metals, Sendai, 1982).
- [8] J.J. Gilman and H.J. Leamy, eds. Metallic Glasses (American Society for Metals, Ohio, U.S.A. 1978).
- [9] P. Duwez, R.H. Willens and W. Klement, Jr., *J. Appl. Phys.* 31, 1136 (1960); W. Klement, R.H. Willens and P. Duwez, *Nature (London)*, 187, 869 (1960).
- [10] A.I. Gubanov, *Fiz. Tver. Tel.* 2, 502 (1960).
- [11] P. Duwez and S.C.H. Lin, *J. Appl. Phys.* 38, 4096 (1967).

- [12] C.L. Chien, Phys. Rev. 18, 1003 (1978).
- [13] R. Window, J. Phys. F 4, 401 (1971).
- [14] C.L. Chien, D. Musser, E.M. Gyorgy, R.C. Sherwood, H.S. Chen, F.E. Luborsky and J.L. Walter, Phys. Rev. B20, 283 (1979).
- [15] T. Kemeny, I. Vincze, B. Fogarassy and S. Arajcs, Phys. Rev. B20, 476 (1979).
- [16] M.W. Ruckman, R.A. Levy, A. Kessler and R. Hasegawa, J. Non-Cryst. Solids 40, 393 (1980).
- [17] R. Oshima, F.E. Fujita, K. Fukamichi and T. Masumoto, J. de Physique C2 Suppl. C2-132 (1979).
- [18] R. Oshima, Suppl. Sci. Rep. Res. Inst. Tohoku Univ. A, 8 (1980).
- [19] R. Oshima and F.E. Fujita, Japanese Journ. Appl. Phys. 20, 1 (1981).
- [20] M. Koshimura, Y. Abe, M. Takahashi, S. Inawashiro and S. Katsura (Private Commun.).
- [21] T. Kemeny, I. Vincze, A.S. Schaafsma, F. der Worde and A. Lovas, Nucl. Inst. Methods 199, 153 (1982).
- [22] R. Ray, R. Hasegawa, C.P. Chou and L.A. Davis, Scripta Met., 11, 973 (1977).
- [23] R. Hasegawa and R. Ray, J. Appl. Phys. 49, 7 (1978).
- [24] S. Das, M. Tech. thesis, Indian Institute of Technology, Kanpur - 208016, India (unpublished).
- [25] S. Das and T.R. Ramachandran (Private Commun.).

- [26] R. Ray and R. Hasegawa, J. Appl. Phys. 49, 4174 (1978).
- [27] Y. Khan, E. Kneller and M. Sostarich, Z. Metallkde. 72, 553 (1981).
- [28] H. Franke and M. Rosenberg, J. Magnetism and Mag. Mater. 7, 168 (1978).

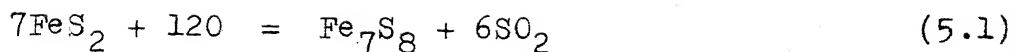
CHAPTER 5

STUDY OF THE ROASTING AND LEACHING PROCESS OF PYRITE MINERALS BY MÖSSBAUER SPECTROSCOPY

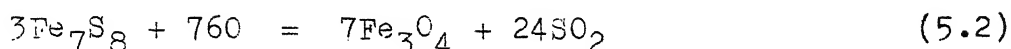
5.1 Study of the Roasting Process of Pyrite Mineral

5.1.1 Introduction

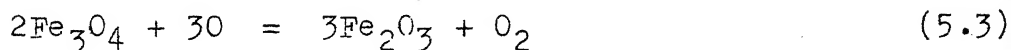
Various sulphides of iron provide important technological applications because of their interesting electrical and magnetic properties. Iron sulphides occur as minerals in nature and they may be beneficiated by different methods of ore dressing prior to extraction of their constituent elements. Among the six iron sulphide minerals (viz. pyrite, marcasite, pyrrhotite, mackinawite, greigite and smythite) pyrite (FeS_2) occurs abundantly among the coal deposits in nature as large cubic crystals. One of the ore dressing methods for separating many of the mixed sulphide and oxide ores utilizes high-power magnets. Some minerals are nearly non-magnetic and cannot be influenced by strongest magnets. In such cases, the minerals are rendered strongly magnetic by 'roasting' them under suitable conditions [1]. Such roasting of pyrite leads to formation of magnetic sulphides (e.g. pyrrhotite) Fe_{1-x}S , $0 \leq x \leq 0.125$ and oxides (e.g. Fe_3O_4 , Fe_2O_3 etc.). Such changes of pyrite into magnetic sulphide can be brought about by a short roast in air through a chemical change similar to



In (5.1) above only one suitable example is given but in the actual roasting process the nature of the exact sulphide formed is decided by the time period for which the roast is carried out. Thus in (5.1) above, the formation of Fe_7S_8 is limited to the surface of each grain with FeS_2 still forming the kernel. As the time period of roasting is increased the sulphide formation penetrates the grain while the sulphur on the outside is all removed. This leads to the formation of the magnetic oxide (magnetic-like Fe_3O_4) according to the chemical change



This change may continue until the whole grain of pyrite is changed into the strongly magnetic oxide, Fe_3O_4 . Upon carrying the roast further, iron takes up another atom of oxygen for every six atoms of Fe, to form Fe_2O_3 as shown below



It is well known that the Mössbauer spectra of pyrite, magnetic sulphide like pyrrhotite, magnetic oxide like Fe_3O_4 , Fe_2O_3 etc. show typical characteristics and their Mössbauer parameters like isomer shift (IS), quadrupole splitting (ΔE) and internal magnetic field (H_{int}) carry the individual identification of each compound. Earlier

studies of pyrite using Mössbauer spectroscopy have been aimed at studying the structural or electronic properties of this system [2-5]. We thought it interesting to study the kinetics of the roasting of pyrite by observing Mössbauer spectra of pyrite samples roasted for different intervals of time. In the following we report Mössbauer spectra of pyrite samples roasted at 610 ± 5 °C for a time interval $t = 0.0, 0.5, 1.0, 2.0, 5.0, 15.0, 30.0$ and 60.0 mins. The choice of temperature was made on the basis of existing literature data and the results obtained subsequently have justified the choice. The observed spectra are analyzed in terms of the particular compound that can be formed.

5.1.2 Experiment

a) Sample preparation

Powdered samples of pyrite were taken and roasted in a small porcelain boat at 610 ± 5 °C in controlled air stream for different time intervals $t = 0.0, 0.5, 1.0, 2.0, 5.0, 15.0, 30.0$ and 60.0 mins. After the roasting the sample material was quickly poured and quenched on alumina held at room temperature. After cooling, the sample material of about 50 mg was spread uniformly between two thin layers of sellotape to form absorbers for Mössbauer studies.

b) Mössbauer measurements

Mössbauer spectra from the pyrite samples were observed at room temperature with help of a constant acceleration. Mössbauer drive coupled to Nuclear Data Model ND60 multi-channel analyzer. A 20 mCi radioactive source of ^{57}Co in Rh matrix obtained from New England Nuclear Inc. USA was used for recording the spectra. The Mössbauer spectrometer was calibrated with the help of natural ^{57}Fe absorber. Parameters of the Mössbauer spectra were determined with the help of a computer program developed for least-squares curve-fitting analysis of the observed spectra.

c) Other measurements

To corroborate the results obtained by Mössbauer spectroscopy, we recorded the X-ray powder diffraction patterns of the samples by using Rich and Seifert ISO-Debyeflex 2002 diffractometer with a CrK_α target. These studies were performed at room temperature. Table 5.1 summarizes the X-ray data obtained for various samples together with the data obtained for pyrite. These results are also analyzed to identify lines due to $\alpha\text{-Fe}_2\text{O}_3$ and $\gamma\text{-Fe}_2\text{O}_3$. Examination of the X-ray data (Table 5.1) shows that the 0.5 min sample (i.e. sample roasted for 0.5 min) displays the X-ray lines of pyrite. On the other hand the X-ray lines due to pyrrhotite appear in the

TABLE 5.1

X-ray data for pyrite roasted for different time intervals.
The assignment is shown in the last column (page 199)

Sr. No.	Pyrite			0.5 minute heat-treatment			1.0 minute heat-treatment		
	d(nm)	Inten- sity	hkl	d(nm)	Inten- sity	hkl	d(nm)	Inten- sity	hkl
1.	-	-	-	-	-	-	-	-	-
2.	-	-	-	-	-	-	-	-	-
3.	0.3124	M	111	0.3124	M	111	0.3124	M	111
4.	-	-	-	-	-	-	0.2960	VW	101
5.	0.2704	VS	200	0.2704	VS	200	0.2699	VS	200
6.	-	-	-	-	-	-	0.2621	VW	112 224 404
7.	-	-	-	-	-	-	-	-	-
8.	-	-	-	-	-	-	-	-	-
9.	0.2423	S	210	0.2419	M	210	0.2419	VS	210
10.	-	-	-	-	-	-	-	-	-
11.	0.2210	S	211	0.2207	VS	211	0.2210	M	211
12.	-	-	-	-	-	-	-	-	-
13.	-	-	-	0.2053	VW	228	0.2052	VW	228
14.	-	-	-	-	-	-	0.2047	VW	228
15.	0.1913	M	220	0.1913	M	220	0.1911	M	220
16.	-	-	-	-	-	-	-	-	-
17.	-	-	-	-	-	-	-	-	-
18.	0.1632	VS	311	0.1632	VS	311	0.1630	VS	311
19.	0.1563	VW	222	0.1563	VW	222	0.1563	VW	222
20.	0.1501	W	230	0.1500	VW	230	0.1502	W	230
21.	-	-	-	-	-	-	-	-	-
22.	0.1447	W	321	0.1446	W	321	0.1447	M	321

Continued...

Table - 5.1 (Continued)

Sr. No.	2.0 minute. heat-treatment			5.0 minute heat-treatment			15.0 minute heat-treatment		
	d(nm)	Inten- sity	hkl	d(nm)	Inten- sity	hkl	d(nm)	Inten- sity	hkl
1.	-	-	-	-	-	-	0.3675	M	-
2.	-	-	-	-	-	-	0.3331	W	-
3.	0.3118	W	111	0.3124	S	111	-	-	-
4.	0.2960	W	101	0.2960	VS	101	0.2973	S	101
5.	0.2704	VS	200	0.2704	S	200	0.2689	VS	104
6.	0.2630	W	112 224 404	0.2621	VS	112 224 404	0.2635	S	112 224 404
7.	0.2526	VW	201	0.2522	VW	201	0.2517	VS	201
8.	-	-	-	-	-	-	0.2517	VS	110 311
9.	0.2419	S	210	0.2419	S	210	-	-	-
10.	0.2266	VW	1010	0.2269	VW	1010	0.2269	VW	101
11.	0.2210	S	211	0.2207	M	211	0.2207	M	113
12.	-	-	-	0.2074	VW	114 408	0.2074	VW	114 408
13.	0.2050	W	228	0.2053	VS	228	0.2058	W	228
14.	0.2037	W	228	-	-	-	-	-	-
15.	0.1911	W	220	0.1913	M	220	-	-	-
16.	0.1714	VW	300 201	0.1708	M	300 201	0.1719	M	300 201
17.	0.1691	VW	116	0.1693	W	116	0.1695	M	003 116
18.	0.1633	M	311	0.1630	S	311	-	-	-
19.	0.1563	W	222	0.1563	W	222	-	-	-
20.	0.1502	VW	230	0.1500	W	230	-	-	-
21.	-	-	-	0.1480	W	214 440	0.1480	W	214 440
22.	0.1447	W	321	0.1447	M	321	0.1433	S	433 530

Continued.....

Table - 5.1 (Continued)

Sr. No.	30.0 minute heat-treatment			60.0 minute heat-treatment			Assignment
	d(nm)	Int- ens- ity	hkl	d(nm)	Int- ens- ity	hkl	
1.	0.3665	S	012	0.3665	M	012	α -Fe ₂ O ₃
2.	0.3331	W	213	0.3331	VW	213	γ -Fe ₂ O ₃
3.	-	-	-	-	-	-	Pyrite (FeS ₂)
4.	-	-	-	-	-	-	Pyrrhotite (Fe _{1-x} S), Mackinawite(Fe ₉ S ₈)
5.	0.2694	VS	104	0.2704	VS	140	Pyrite in first five column and α -Fe ₂ O ₃ in las three column
6.	-	-	-	-	-	-	Troilite (FeS) and Pyrrhotite (Fe _{1-x} S)
7.	-	-	-	-	-	-	Troilite (FeS)
8.	0.2513	VS	110 311	0.2513	VS	110 311	α -Fe ₂ O ₃ γ -Fe ₂ O ₃
9.	-	-	-	-	-	-	Pyrite (FeS ₂)
10.	2.2657	VW	1010	-	-	-	Smythite (Fe ₉ S ₁₁)
11.	0.2200	S	113	0.2200	M	113	Pyrite in first five column and α -Fe ₂ O ₃ in las three column
12.	0.2078	VW	114 408	-	-	-	Troilite (FeS) Pyrrhotite (Fe _{1-x} S)
13.	-	-	-	-	-	-	Pyrrhotite (Fe _{1-x} S)
14.	-	-	-	-	-	-	Pyrrhotite (Fe _{1-x} S)
15.	-	-	-	-	-	-	Pyrite
16.	-	-	-	-	-	-	Troilite (FeS), Mackinawite (Fe ₇ S ₈)
17.	0.1693	VS	116	0.1693	S	116	α -Fe ₂ O ₃
18.	-	-	-	-	-	-	Pyrite (FeS ₂)
19.	-	-	-	-	-	-	Pyrite (FeS ₂)
20.	-	-	-	-	-	-	Pyrite (FeS ₂)
21.	0.1485	M	214 440	0.1484	S	214 440	α -Fe ₂ O ₃ γ -Fe ₂ O ₃
22.	0.1433	M	433 530	0.1433	W	433 530	Pyrite in first five column and γ -Fe ₂ O ₃ in the last three column

1.0 min sample and their intensity increases as the roasting time is increased from $t = 1.0$ min to $t = 5.0$ min. The intensities of the X-ray lines due to pyrite, however, decreases from $t = 1.0$ min to $t = 5.0$ min. This behaviour indicates conversion of pyrite into pyrrhotite from $t = 1.0$ min to $t = 5.0$ min. Beyond $t = 5.0$ min the X-ray data show that X-ray lines due to pyrite disappear in the 15.0 min, 30.0 min and 60.0 min samples while X-ray lines due to $\alpha\text{-Fe}_2\text{O}_3$ and $\gamma\text{-Fe}_2\text{O}_3$ make their appearance. The X-ray lines due to pyrrhotite are absent in the 30.0 min and 60.0 min samples. This behaviour suggests that the transformation $\text{pyrite} \longrightarrow \text{pyrrhotite} \longrightarrow \alpha\text{-Fe}_2\text{O}_3$ and/or $\gamma\text{-Fe}_2\text{O}_3$ is completed after $t = 30.0$ min.

5.1.3 Results and discussion

The Mössbauer spectra for the as-prepared pyrite sample and other samples for different time intervals (t) are shown in Fig. 5.1. The spectrum for the as-prepared sample shows a doublet structure (quadrupole splitting) and the observed values of isomer shift, $\text{IS} = 0.365 \pm 0.005$ mm sec⁻¹ (with respect to natural Fe) and quadrupole splitting, $\Delta E = 0.618 \pm 0.003$ mm sec⁻¹, agree satisfactorily with other results [2-5]. These observations are consistent with the known structure of pyrite involving covalent ferrous ion in distorted octahedral coordination. In pyrite, iron is in low-spin state and the quadrupole

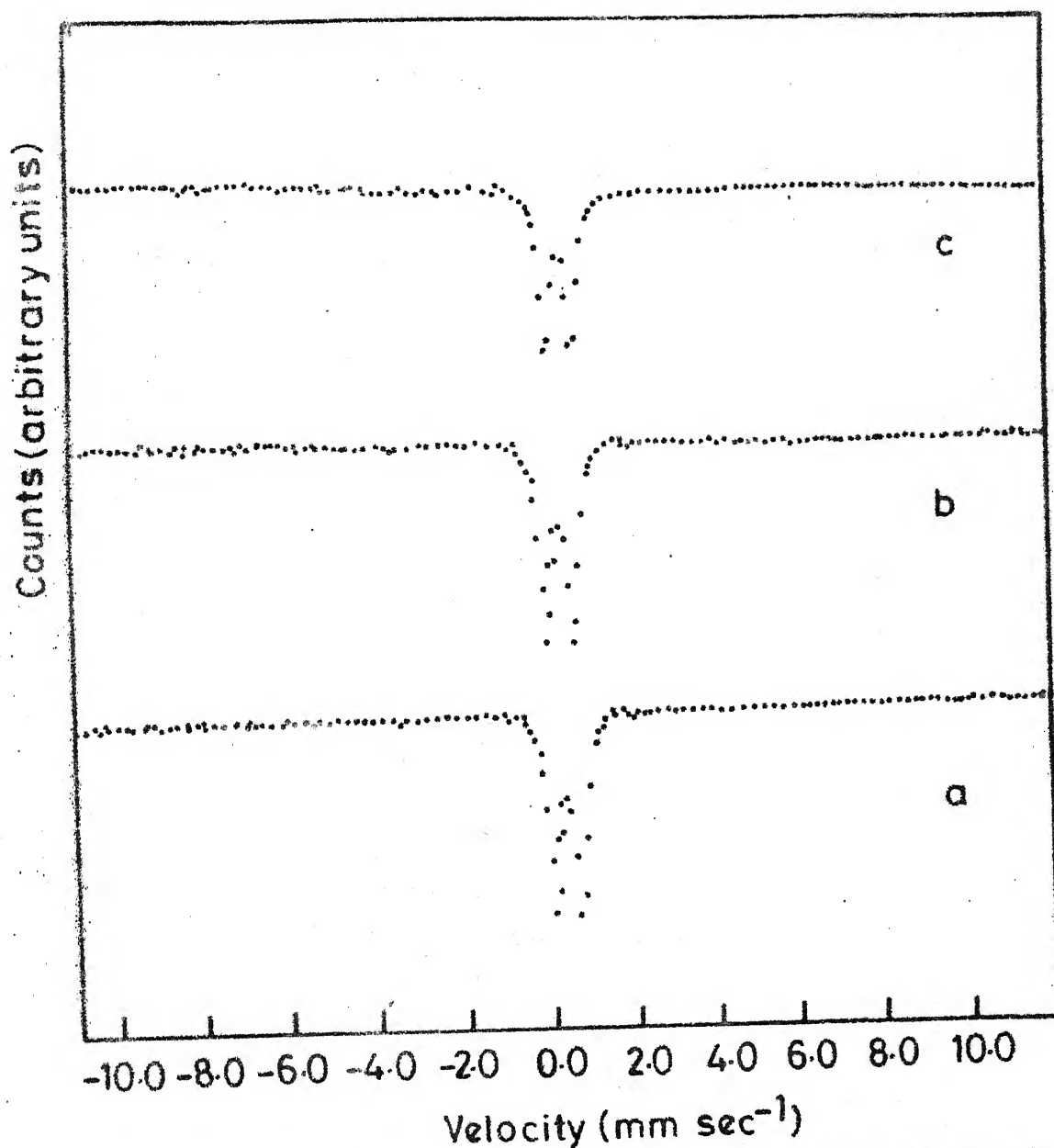


Fig. 5.1 Room temperature Mössbauer spectrum of pyrite roasted at $610 \pm 5^\circ\text{C}$ for different time intervals. a) 0.0 min, b) 0.5 min, c) 1.0 min, d) 2.0 min, e) 5.0 min, f) 15.0 min, g) 30.0 min and h) 60.0 min. The zero of the velocity scale refers to the centroid of the inner peaks of $\alpha\text{-Fe}$ Mössbauer spectrum. The lines at the top indicate the characteristic peak positions in the Mössbauer spectra of $\gamma\text{-Fe}_2\text{O}_3$, $\alpha\text{-Fe}_2\text{O}_3$, Fe_3O_4 , $\alpha\text{-Fe}$, FeS and pyrrhotite.

Fig. 5.1 Condt.

splitting arises because of the lattice effects [2]. As the time-period (t) of the roasting is raised, the Mössbauer spectra show interesting changes. No magnetic hyperfine splitting is observed upto $t = 1.0$ min and the Mössbauer parameters $IS, \Delta E$ and H_{int} shown in Table 5.2 do not show any significant changes from the values observed for the as-prepared pyrite samples. This behaviour indicates that roasting upto $t = 1.0$ min does not lead to any transformation of pyrite to other iron compounds. The Mössbauer spectra for $t = 2.0$ min shows the onset of magnetic hyperfine structure which is fully developed in the spectrum for $t = 30.0$ and $t = 60.0$ min. In order to identify the origin of this magnetic hyperfine structure we have shown the reported peak positions for pyrrhotite [2] in Fig. 5.2 and Fe_3O_4 [6], $\gamma-Fe_2O_3$, FeS and $FeSO_4 \cdot 2H_2O$ in Fig. 5.3. The peak positions for Fe_3O_4 and $\gamma-Fe_2O_3$ were confirmed by us by recording their Mössbauer spectra. By using these peak positions as guidelines we have proposed an identification which is shown in Table 5.2. The results shown in Fig. 5.1 and described in Table 5.2 are understood as follows. In this discussion and interpretation of the results the comments given in the column of Table 5.2 have to be taken into account.

During the roasting of pyrite, pyrrhotite appears to be formed at $t = 2.0$ min. The conversion from pyrrhotite to Fe_3O_4 seems to have been completed between $t = 5.0$ min and $t = 15.0$ min and, after

Table 5.2

Mossbauer parameters of pyrite sample roasted for different time intervals at temperature $610^{\circ} + 5^{\circ}\text{C}$.

Sr. No.	Time interval (t) of heat-treatment (mins)	Identification	IS(±) (mm sec ⁻¹)	ΔE (mm sec ⁻¹)	H _{int} (kOe)	Remarks
1	0.0 (as-prepared)	Pyrite (FeS ₂)	0.32±0.01	0.61±0.01	None	No hyperfine magnetic splitting is observed, Fe ²⁺ valence state with low spin. Structure has covalent bond Compared to pyrite the IS value does not change (within error) but ΔE shows slight decrease
2	0.5	Pyrite (FeS ₂)	0.32±0.01	0.61±0.01	None	
3	1.0	Pyrite (FeS ₂)	0.31±0.02	0.59±0.01	None	
4	2.0	Pyrite (FeS ₂) and some pyrrhotite	0.31±0.02 See under remarks	0.59±0.01 See under remarks	See under remarks	A weak contribution from pyrrhotite is observed. Statistics too low for good computer fit.
5	5.0	Pyrite (FeS ₂) and some pyrrhotite	Same as above	Same as above	Same as above	Same as above, except amount of pyrrhotite is more than for the case t = 2.0 min.

Table 5.2 (Continued)

Sr. No.	Time interval (t) of heat-treatment (mins)	Identification	IS(*) (mm sec ⁻¹)	ΔE (mm sec ⁻¹)	H _{int} (kOe)	Remarks
6.	15.0	Some pyrite, some pyrrhotite, some Fe ₃ O ₄ otherwise mostly γ -Fe ₂ O ₃	See under remarks	See under remarks	See under remarks	Spectrum is very complex. Identification done by using the reported values of the Mössbauer parameter for pyrrhotite [2], Fe ₃ O ₄ [6] and γ -Fe ₂ O ₃ [7]. Lines for α -Fe ₂ O ₃ not observed clearly.
7.	30.0	Mostly γ -Fe ₂ O ₃ , slight trace of α -Fe ₂ O ₃	0.45±0.02	None	497±6	Some trace of α -Fe ₂ O ₃ cannot be ruled out.
8.	60.0	Almost completely γ -Fe ₂ O ₃	0.45±0.02	None	497±6	Pyrite has been fully oxidized to γ -Fe ₂ O ₃

*Values with respect to α -Fe.

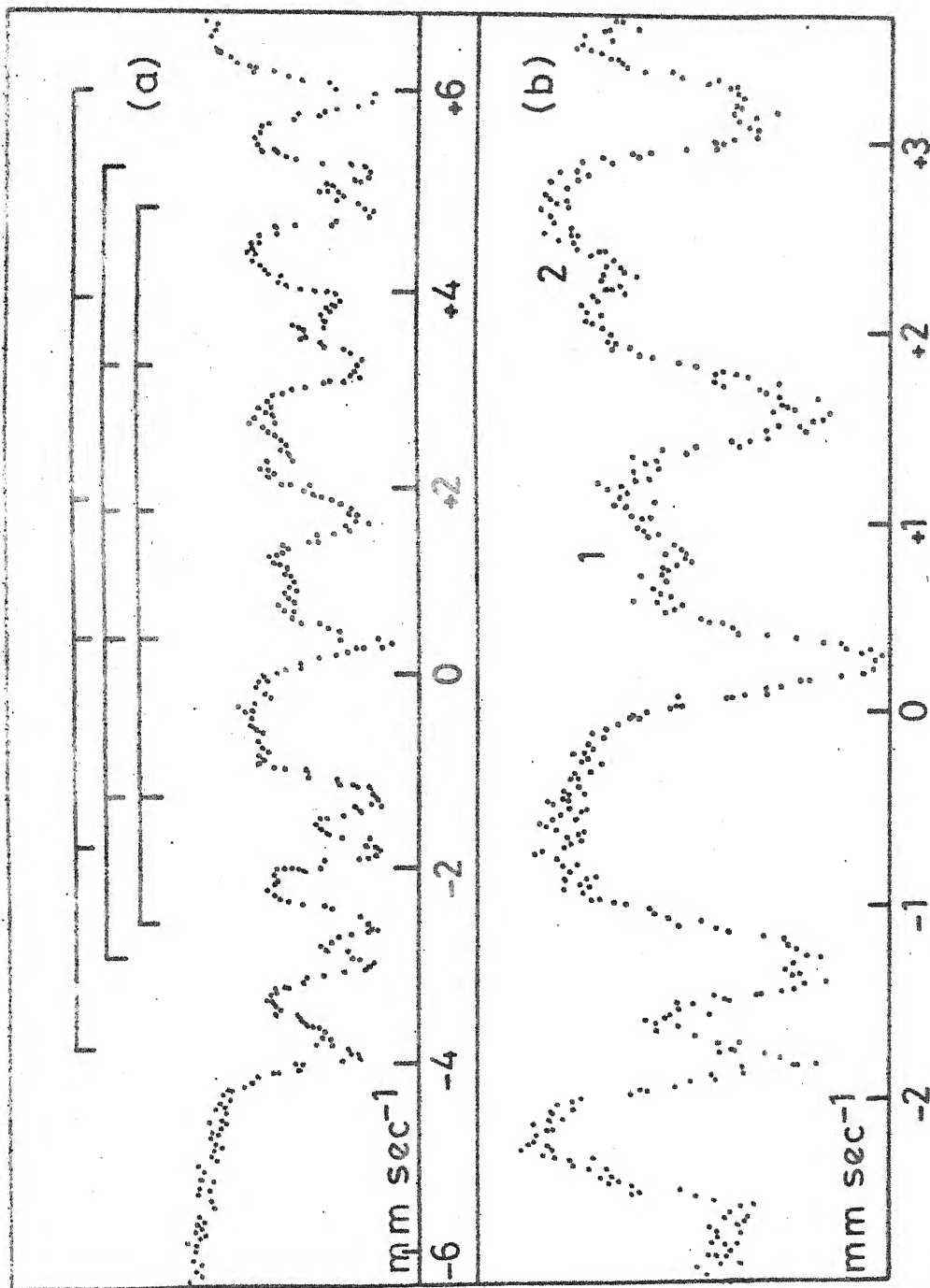


Fig. 5.2 Room temperature Mössbauer spectrum of a) pyrrhotite. Spectrum b shows the expansion of the inner peaks of the spectrum (a). The zero of the velocity scale refers to the centroid of the solid nitroprusside Mössbauer spectrum. In (b) 1 and 2 denote unidentified peaks [2].

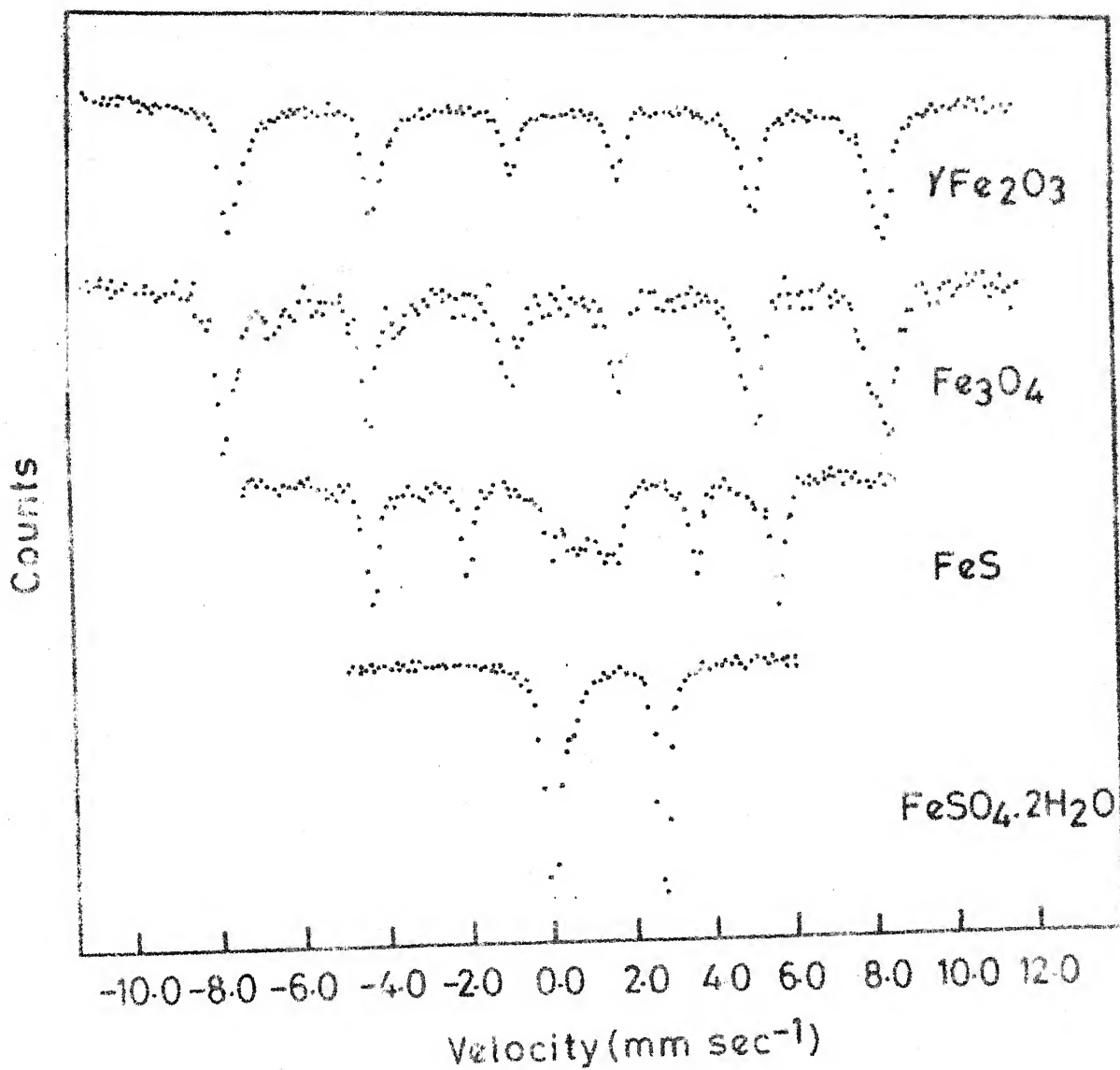


Fig. 5.3 Room temperature Mössbauer spectrum of $\gamma\text{-Fe}_2\text{O}_3$, Fe_3O_4 , FeS and $\text{FeSO}_4 \cdot 2\text{H}_2\text{O}$.

$t = 15.0$ min pyrite had been almost completely transformed into $\gamma\text{-Fe}_2\text{O}_3$. At about $t = 60.0$ min pyrite had been fully oxidized to $\gamma\text{-Fe}_2\text{O}_3$. These results are supported by our X-ray powder diffraction data. It should be noted that the onset of the formation of pyrrhotite or Fe_3O_4 appears to occur at different times (t values) from the Mössbauer results and the X-ray data. However, these differences are minor and could be due to the different sensitivity of the two techniques. In any case, same general trend is indicated by the results obtained with the two methods.

Based on the present results, roasting of the pyrite mineral can, therefore, be summarized as follows. Under heat-treatment pyrite transforms via pyrrhotite to the oxide of iron as a result of the reduction process. For the roasting period $t = 5.0$ min, pyrrhotite is formed in good amount with some pyrite still remaining. At $t = 15.0$ min pyrite disappears with pyrrhotite and Fe_2O_3 remains. It is conjectured that at some time intermediate between $t = 5.0$ and $t = 15.0$ min the sample consists mostly of pyrrhotite. For times $t \geq 30.0$ min there is a complete transformation into $\alpha\text{-Fe}_2\text{O}_3$ and $\gamma\text{-Fe}_2\text{O}_3$.

5.2 Study of the Leaching Process of the Pyrite Minerals

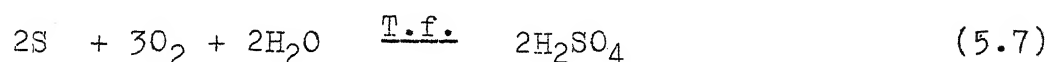
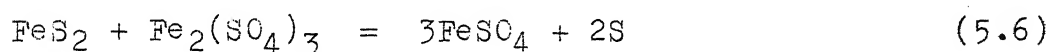
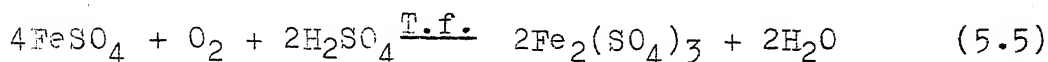
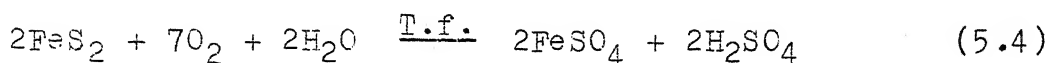
5.2.1 Introduction

In recent years micro-organisms have been increasingly used in the recovery of commercially valuable

minerals from low grade ores [8-11]. Use of bacteria has ushered revolutionary changes in the mining of metallic minerals. One group of such useful bacteria is called acidophilic thiobacilli and they thrive in an environment which consists of a solution of metals, particularly iron, in 0.05 M sulphuric acid and they can tolerate a range of temperature between 0 and 60 °C. For a mining engineer, the most important member of this group of bacteria is Thiobacillus ferrooxidans (usually abbreviated as T. ferrooxidans) which derives its energy by oxidising sulphur, sulphides and ferrous iron [12,13]. Although T. ferrooxidans is one of the earliest living micro-organisms on the earth, it was isolated only in 1947 [14] from the flood waters coming out from an abandoned coal mine in West Virginia . Historically, the presence of copper in mine drainage waters was noticed by mankind, for example by Phoenicians, Romans, Arabs, Spaniards etc. Although the earliest leaching of copper from copper sulphide-bearing materials was observed in 1942 at Pio Tinto in Spain, the presence of bacteria in the leach waters of these mines was not confirmed until 1962 [15].

Details of the morphology, physiology, chemical composition and structure of T. ferrooxidans are described in literature [9]. The activity of the bacteria is normally limited by the small quantities of substrate exposed to the atmosphere because of the requirement of abundant supply of oxygen. One of the most important growth substrates is

iron pyrites (FeS_2) which often occur together with other and more valuable minerals like copper, zinc and uranium. Pyrite is known to be almost insoluble under normal conditions but in the presence of T. ferrooxidans its dissolution rate may increase by as much as 10^6 . Although one does not know how T. ferrooxidans is able to attack the mineral, it is supposed that the interface between the mineral and the micro-organism consists of high local concentrations of ferric iron which results in rapid oxidation. The chemical reactions involved in the leaching process of the pyrite mineral are :



(T.f. indicates T. ferrooxidans).

Reactions (5.4), (5.5) and (5.7) take place enzymatically under the active participation of T. ferrooxidans whereas reaction (5.6) takes place chemically without any participation of the bacteria. Reactions (5.5) and (5.7) provide energy to T. ferrooxidans. In the absence of bacteria, reaction (5.4) occurs very slowly but it may be useful in providing the solution of

ferrous iron necessary to start the bacterial growth. The products of these reactions are thus ferric-sulphate and sulphuric acid, a mixture capable of oxidising and dissolving many minerals which are otherwise insoluble.

We have studied the bacterial leaching of pyrite by Mössbauer spectroscopy. The motivation of the present work was to establish the phases containing iron and the valency states of iron on the surface of pyrite particles as these are leached bacterially.

5.2.2 Experimental

a) Micro-organisms

The micro-organisms used in the leaching of pyrite were strains of Thiobacillus ferrooxidans obtained from (i) Bose Institute, Calcutta and (ii) National Chemical Laboratory (NCL), Pune. These organisms were routinely maintained on a modified 9K growth medium [16], in which the energy source (ferrous sulfate) was replaced by pure pyrite. Logarithmic phase cultures were used as inocula for subcultures and experimental systems.

b) Substrate

The pyrite sample was obtained from Alminrock Bangalore - 3 and was ground to a particle size $\leq 65 \mu\text{m}$ and used in all these leaching experiments.

c) Estimation of iron

Iron in leaching solutions was analyzed by atomic absorption spectrophotometry.

d) Experimental procedures

Initially, the strains were adapted to the pyrite in the iron-free medium and after three transfers, a 5.0 ml aliquot of the log phase culture was used as experimental inoculum. In the procedure, 1.0 g of pyrite was taken in a 250 ml extenmeyer flask containing 100 ml of iron-free medium and the pH was adjusted to 1.7 in case of the Bose Institute strain and 3.2 in case of the NCL strain. The flasks were sterilized at 15 psi (1.05 kg/cm^2) for 15 min. Then 5.0 ml of the log phase culture of T. ferrooxidans was inoculated and the flasks were agitated on a gyratory shaker at 25-27 °C. The samples were removed after 2, 6, 9, 12, 15, 20 and 45 days followed by filtration through commercial filter paper. The pH of the samples were also recorded after filtration and the iron content was analyzed by atomic absorption spectrophotometry.

e) Mössbauer measurements

The Mössbauer spectra of various samples were recorded by using the method described in Sec. 5.2.2.

5.2.3 Results and discussion

Mössbauer spectra of the untreated pyrite sample, as well as of the samples leached with the bacteria T. ferrooxidans for various time periods all show a doublet structure or quadrupole splitting. Two of such typical spectra are shown in Fig. 5.4. Results of the Mössbauer parameters isomer shift (IS) and quadrupole splitting (ΔE) are given in Table 5.3 for the bacteria obtained from the Bose Institute, Calcutta and the National Chemical Laboratory, Pune. It should be pointed out that the value of IS and ΔE obtained for the reference pyrite sample in the leaching studies were $IS = 0.37 \pm 0.01 \text{ mm sec}^{-1}$ and $\Delta E = 0.62 \pm 0.01 \text{ mm sec}^{-1}$ (Table 5.3) as against $IS = 0.32 \pm 0.01 \text{ mm sec}^{-1}$ and $\Delta E = 0.61 \pm 0.01 \text{ mm sec}^{-1}$ obtained for the reference pyrite sample used in the roasting studies (Table 5.2, Sec. 5.2). The difference observed in the two IS values are ascribed to the fact that the reference pyrite samples used in the two studies were not same. The pyrite sample used in the leaching studies was less pure and contained large amount of other sulphides such as marcasite, barnite, chalcopyrite etc. In addition the particle size of the pyrite samples used in the leaching studies was $\leq 65 \mu\text{m}$ as compared to the size $\leq 125 \mu\text{m}$ in the roasting studies.

The present studies have shown that the pyrite samples subjected to bacterial leaching for time periods

Table 5.3

Mössbauer parameters of pyrite samples leached for different days by using two different source of bacteria.

Time Period of le- aching (in days)	NCL [*]				BI [*]					
	IS(a)		ΔE (mm sec ⁻¹)	Peak Widths		IS(a)		ΔE (mm sec ⁻¹)	Peak Widths	
	(mm sec ⁻¹)	(mm sec ⁻¹)		I	II	(mm sec ⁻¹)	II		I	II
0	0.37±0.01	0.62±0.01	0.34±0.01	0.30±0.01	0.37±0.01	0.62±0.01	0.34±0.01	0.30±0.01		
2	0.33±0.02	0.63±0.01	0.46±0.01	0.40±0.01	0.33±0.02	0.63±0.01	0.39±0.01	0.36±0.01		
6	0.31±0.01	0.62±0.01	0.42±0.01	0.40±0.01	0.38±0.01	0.60±0.01	0.38±0.01	0.34±0.03		
9	0.38±0.02	0.63±0.01	0.36±0.01	0.33±0.01	0.38±0.01	0.63±0.01	0.36±0.01	0.33±0.01		
12	0.35±0.02	0.63±0.01	0.37±0.01	0.34±0.01	0.33±0.02	0.63±0.01	0.36±0.01	0.33±0.01		
15	0.33±0.01	0.63±0.01	0.36±0.01	0.33±0.01	0.33±0.02	0.63±0.01	0.39±0.01	0.36±0.01		
20	0.34±0.01	0.62±0.01	0.38±0.01	0.34±0.01	0.34±0.02	0.63±0.01	0.37±0.01	0.35±0.01		
45	0.33±0.01	0.63±0.01	0.37±0.01	0.34±0.01	0.35±0.02	0.62±0.01	0.38±0.01	0.35±0.01		

(a) Values are with respect to α -Fe.

* Indicates the source of the bacteria used. NCL = National Chemical Laboratory, Pune,
BI = Bose Institute, Calcutta.

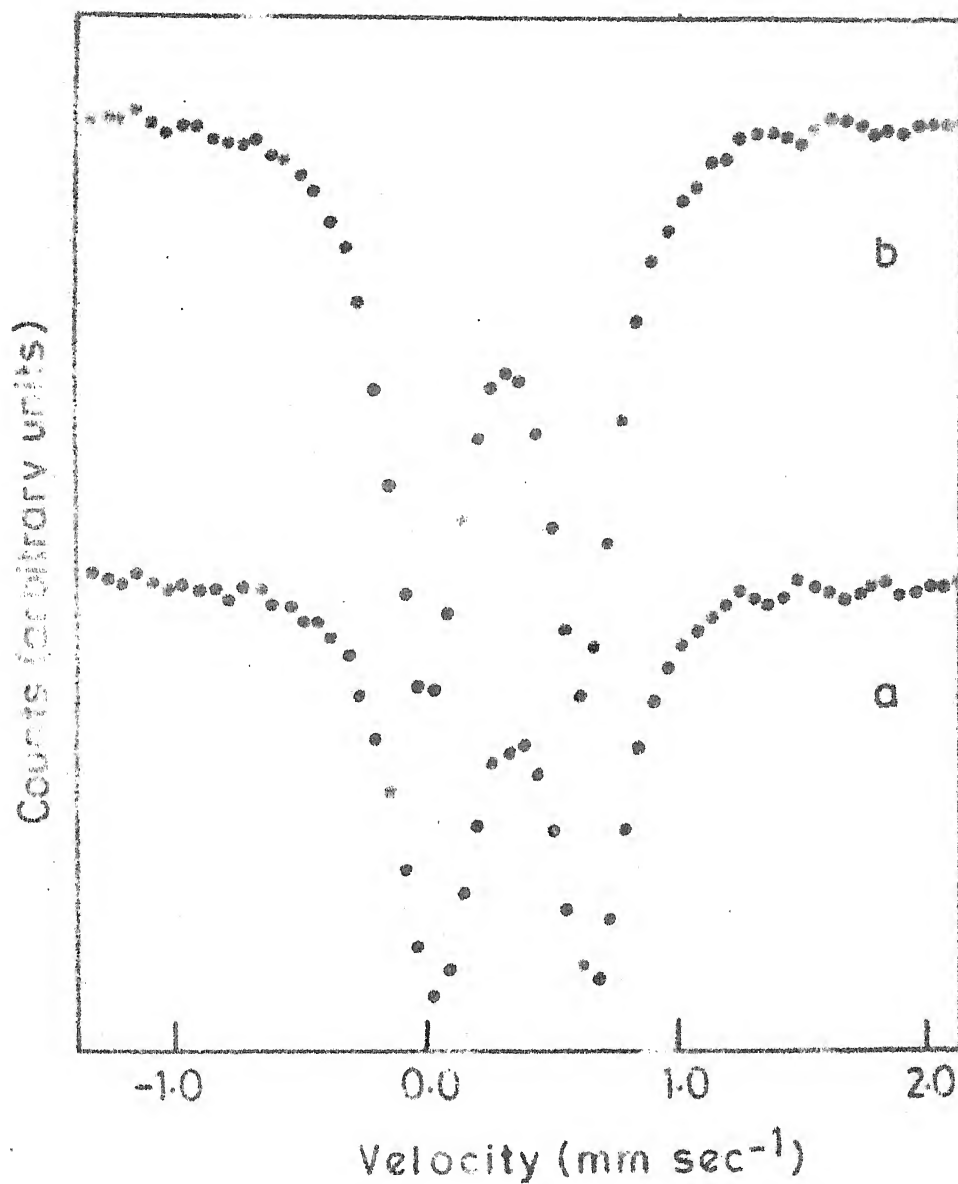


Fig. 5.1 Room temperature Mössbauer spectrum of (a) pyrite and (b) pyrite sample leached for 15 days.

varying from 2 days to 45 days continue to show doublet structure or quadrupole splitting and the Mössbauer parameters IS and ΔE (Table 5.3) do not change from the untreated pyrite sample. The peak-widths of the two lines also do not show significant changes. Similarly no differences were observed between the effects of bacteria obtained from the two sources (National Chemical Laboratory, Pune and Bose Institute, Calcutta).

The chemical reactions involved in the leaching process of pyrite, eqs. (5.4) to (5.7) indicate that we should observe iron sulphates $\text{Fe}_2(\text{SO}_4)_3$, FeSO_4 as a by-product after leaching. The Mössbauer parameters at room temperature IS and ΔE (at room temperature) for iron sulphates as reported by Danon [17] are shown in Table 5.4.

In the present analysis we examined the Mössbauer spectra and the parameters (Table 5.3) to look for the presence of the iron sulphate FeSO_4 and $\text{Fe}_2(\text{SO}_4)_3$ in the leached samples. From the Mössbauer parameters given in Table 5.4 it is obvious that the presence of the iron sulphates if existed could not have been missed. However our results ruled out the presence of these iron sulphates. This can be correlated with the formation of soluble ferrous sulphates formed from pyrite during leaching. This was also evident from the colour of the filtered sample.

Table 5.4

Isomer shift (IS) and quadrupole splitting (ΔE) for iron sulphates. The results are reported (for room temperature) by Danon [17].

Compound	IS (a) (mm sec ⁻¹)	ΔE (mm sec ⁻¹)
FeSO ₄	1.33	3.27
FeSO ₄ ·7H ₂ O	1.31	3.20
Fe ₂ (SO ₄) ₃	0.46	0.0
Fe ₂ (SO ₄) ₃ ·xH ₂ O	0.44	0.28

(a) Values with respect to α -Fe.

Our results do not indicate any major presence of other iron compounds, besides pyrite, after the leaching process. Ferrous/ferric salts being soluble in water do not stay on the surface. Slight variations of the IS and ΔE parameters observed by us could be due to the impurities involved. These investigations illustrate how Mössbauer spectroscopy can be used to study the leaching of minerals containing iron compounds.

REFERENCES

- [1] R.H. Richards and C.E. Locke, Textbook of Ore Dressing, McGraw Hill Book Company, New York, 1940, Chapter XIV, pp. 300-303.
- [2] J.A. Morice, L.V.C. Rees and D.T. Rickard, J. Inorg. Nucl. Chem. 31, 3797 (1969).
- [3] P.A. Montano and M.S. Seehra, Solid State Commun. 20, 897 (1976).
- [4] V.K. Garg, J. Appl. Phys. 52, 373 (1981).
- [5] V.K. Garg, Revisto Brasileira de Fisica 10, 535 (1980) and references therein.
- [6] Y. Fujio, Japanese J. Appl. Phys. 12, 1850 (1973).
- [7] W.H. Kelly, V.J. Folen, M. Hass, W.N. Schreiner and G.B. Beared, Phys. Rev. 124, 80 (1961).
- [8] R. Manches, Trends in Biochemical Science, 4, 77 (1979).
- [9] A.E. Torma in Advances in Biochemical Engineering 6, Editorst T.K. Ghose, A. Fiechter and N. Blakebrough, Springer-Verlag Berlin (1977) page 1-37.
- [10] P.A. Trudinger, M.R. Walter and B.J. Ralph Editors Biochemistry of Ancient and Modern Environments, Springer Verlag, New York (1980).
- [11] A.W. Fletcher, Trans. Inst. Mining Metallurgy Dec. 1970.
- [12] K.L. Temple and A.R. Colmer, J. Bact. 62, 605 (1951).
- [13] O.H. Tuovinen and D.P. Kelly, Z. Allg. Mikrobiol. 12, 311 (1974).

- [14] A.R. Colmer and M.E. Hinkle, Science 106, 253 (1947).
- [15] W.F. Razell and P.C. Trussell, J. Bacteriol; 85, 593 (1963).
- [16] M.P. Silverman and D.G. Lundgren, J. Bacteriol., 77, 642 (1959).
- [17] J. Danon, in Chemical Application of Mössbauer Spectroscopy Editors V.I. Goldanskii and R.H. Herber, Academic Press, New York (1968).